

Modelling Catastrophic Loss in the Mechanical Integrity of Pressurised Pipelines under Fire Attack

A thesis submitted to the University of London for the degree of
Doctor of Philosophy

By

Muhammad Umar Abbasi

Department of Chemical Engineering
University College London
Torrington Place
London WC1E 7JE

February 2007

UMI Number: U591272

All rights reserved

INFORMATION TO ALL USERS

The quality of this reproduction is dependent upon the quality of the copy submitted.

In the unlikely event that the author did not send a complete manuscript and there are missing pages, these will be noted. Also, if material had to be removed, a note will indicate the deletion.



UMI U591272

Published by ProQuest LLC 2013. Copyright in the Dissertation held by the Author.
Microform Edition © ProQuest LLC.

All rights reserved. This work is protected against
unauthorized copying under Title 17, United States Code.



ProQuest LLC
789 East Eisenhower Parkway
P.O. Box 1346
Ann Arbor, MI 48106-1346

ABSTRACT

This thesis describes the development of a mathematical model for simulating the loss in the mechanical integrity of pressurised hydrocarbon conveying pipelines under fire attack.

The model is based on the resolution of the conservation equations using the Method of Characteristics. It accounts for real fluid behaviour, pipeline mechanical strength, as well as phase and flow dependent transient heat transfer effects and frictional pressure losses. Failure is assumed to occur when any one of the simulated triaxial thermal and pressure stresses in the pipeline wall exceed its ultimate tensile strength.

Two types of failure scenarios both involving thermal loading of a pressurised pipeline are modelled and the consequences of failure are elucidated using hypothetical case examples.

The first deals with direct jet fire impingement in which a section of the pipeline is assumed to be completely enveloped by the fire. Here the results of the simulations show that the pipeline fails through bulging and buckling due to the prevailing tangential stresses. The efficacy of emergency depressurisation using different diameter relief valves as a means of protecting the pipeline mechanical integrity during fire attack is also quantitatively investigated.

The more complicated alternative failure scenario modelled involves the puncture of the pressurised pipeline and the immediate ignition of the escaping high pressure inventory. The impact of the resulting jet fire back radiation on the mechanical integrity of the depressurising pipeline is then modelled. An important precursor to the above is the presentation followed by linking of an appropriate jet flame model based on published literature describing the transient jet fire characteristics to the outflow model.

Application of the model to a 10mm puncture positioned at the downstream end of a hypothetical 0.5km, 0.395m dia. steel pipeline conveying natural gas at 110bara

shows that the pipeline fails in the tangential direction some 1070s following the initial release.

The size and location of the puncture during unisolated release are found to have a profound effect on delaying or circumventing catastrophic pipeline failure. The former was expected as increasing the puncture diameter results in a more rapid depressurisation rate thus resulting in a faster reduction of the accompanied pressure stresses which contribute to the pipeline failure. The significant effect of the location of the puncture on the fate of the pipeline was however somewhat unexpected. Here it is found that placing the puncture at the downstream end of the pipeline results in a discharge pressure and hence jet flame overall dimensions that are approximately double those compared to mid point puncture. The above is manifested in catastrophic pipeline failure due to the much more severe thermal loading in the case of downstream end puncture. The study concludes by investigating the effect of using different grades of carbon steel on the pressurised pipeline's resistance to withstand thermal loading.

DEDICATION

To ALLAH and none else Praise to be ALLAH, Lord of the Worlds, The all-Sufficing, The self-Sufficient, The Responder, The answer of Prayers, The Evolver, The Peace and the Source of Peace.

“To His noble prophets (PBUT) and those who follow them in upholding the cause of righteousness”

To my beloved Parents, my brothers and my supervisor

ACKNOWLEDGEMENTS

I owe all my work to ALLAH, the Almighty; undoubtedly these are his unlimited bounties that I have been able to complete this thesis.

Furthermore I would like to express my profound gratitude to the following people

To my very dear parents for your love, sincere prayers and faith in me.

My brothers Farooq and Haroon for your encouragement and support.

To my supervisor, Prof. Haroun Mahgerefteh; I am highly indebted for your guidance throughout the course of my work.

My mother and father-in-law to be for your prayers and love, I am truly grateful.

My dear friend Abdur Rehman for your silly jokes and true friendship.

The new addition to our family, my niece Rafia, for the joy and love you have brought with you.

My dear grandparents for your prayers, Hina and Hajra for the support.

The technical and admin staff of the department of Chemical Engineering, UCL.

To the ORS for the financial assistance.

To Dr Ade Oke, Dr Femi Atti and Dr to be Mr Garfield Denton for your help and assistance in the completion of this work. I'm truly thankful.

Lastly I would like to thank Ari, Huw, Nadeem, Shahryar, Abid, Thien, Sayeh, John and all the rest of my colleagues, both past and present with whom we shared the same office. It was a pleasure meeting you all.

LIST OF CONTENTS

ABSTRACT	2
DEDICATION	4
ACKNOWLEDGEMENTS	5
CHAPTER 1	
INTRODUCTION	10
CHAPTER 2	
LITERATURE REVIEW	15
2.1 Introduction	15
2.2 Review of Pipeline Outflow Models	15
2.2.1 OLGA	16
2.2.2 PLAC	18
2.2.3 Imperial College London Models (BLOWDOWN)	20
2.2.3.1 Haque et al., 1990, 1992 a,b, Richardson et al., 1991, 1996 a,b	20
2.2.3.2 Chen et al., 1992, 1995 a,b (HEM, MSM)	22
2.2.4 UCL Models.....	26
2.2.4.1 Mahgerefteh et al., 1997-2000	26
2.2.4.2 Vahedi, 2003	27
2.2.4.3 Oke et al., 2003; Oke, 2004	30
2.2.4.4 Mahgerefteh and Atti, 2006	32
2.2.4.5 Other Models.....	36
2.3 Modelling Work on Thermal Response on Pressurised Vessels and Pipework to Fire Attack	38
2.3.1 Mahgerefteh et al., 2002	38
2.3.2 Mahgerefteh and Falope, 2003	42
2.3.3 Blast and Fire Engineering for Topside Structures (Roberts et al., 2000)	43
2.3.4 Russo et al., 1995	44
2.3.5 Other Models	46

2.4	Tank Fires	47
2.5	Jet Flame Models	47
2.5.1	Kalghatgi, 1983	48
2.5.2	Chamberlain, 1987	49
2.5.2	Johnson et al., 1995	51
2.5.2	Carter (1991)	52
2.6	Conclusion.....	56

CHAPTER 3

PIPELINE OUTFLOW MODELLING.....	57	
3.1	Introduction	57
3.2	Outflow Model Assumptions.....	58
3.3	Equations of outflow Modelling.....	58
3.4	Quasilinear Partial Differential Equations.....	60
3.4.1	Hyperbolic Quasilinear Partial Differential Equations.....	61
3.4.2	Solution of Hyperbolic System of Equations	62
3.5	Method of Characteristics (MOC).....	63
3.5.1	Mathematical Formulation of MOC.....	65
3.5.2	Finite Difference Solution of the Compatibility and Characteristic Equations	68
3.6	The Intact Point Calculation.....	72
3.7	Rupture Plane Calculation.....	74
3.8	Discharge Rate Calculation.....	76
3.9	Cubic Equation of State (CEoS)	78
3.10	Hydrodynamic and Thermodynamic Correlations	79
3.11	Calculation of Fluid and Wall Temperature	83
3.11.1	Fluid/Pipeline Wall Heat Transfer.....	87
3.11.2	Ambient/Pipeline Wall Heat Transfer	88
3.12	Validation	90
3.12.1	P40 Simulation	91
3.12.2	P42 Simulation	92
3.13	Conclusion	92

CHAPTER 4

MODELLING THERMAL RESPONSE OF PRESSURISED PIPELINES

UNDER JET FIRE IMPINGEMENT.....	100
4.1 Introduction	100
4.2 Fire Scenarios	101
4.3 Wall Resident Stresses	102
4.4 Effect of Thermal Impact	103
4.5 Model Development	104
4.5.1 Pressure and Thermal Stresses	104
4.5.1.1 Thermal Stresses across Pipewall	105
4.5.1.2 Pressure Stresses across Pipewall	106
4.5.2 Pipeline Material of Construction.....	106
4.6 Case Study	109
4.6.1 Isolated Pipeline	109
4.6.2 Pressure Relief Valve	112
4.6.3 Unisolated Pipeline.....	113
4.7 Effect of Pipe Material of Construction	115
4.8 Conclusion	115

CHAPTER 5

MODELING SECONDARY FAILURES IN PRESSURISED PIPELINES

FOLLOWING THE IGNITION OF A RELEASED INVENTORY	145
5.1 Introduction.....	145
5.2 Diffusion Flame.....	145
5.3 Radiation	145
5.4 Flame Emissivity.....	147
5.5 Atmospheric Transmissivity	148
5.6 View Factor.....	148
5.7 Model Development	149
5.8 Validation of Chamberlain (1987) Jet Flame Model.....	161
5.9 Case Study.....	161
5.10 Conclusion	166

CHAPTER 6

CONCLUSIONS AND SUGGESTED FUTURE WORK 182

6.1 Conclusions 182

6.2 Suggestions for Future Work 187

REFERENCES 189

CHAPTER 1

INTRODUCTION

In recent years, pipelines have gained significant popularity as a means of transporting large amounts of pressurised hydrocarbons across the globe. These provide extraordinary quantities of energy products to industry and consumers, literally fuelling economies and ways of life. However, their increasing use coupled with operation under more extreme conditions such as high pressures in order to maximise throughput have inevitably resulted in a significant rise in their failure frequency. Such accidents have often resulted in large number of casualties, including fatalities and significant environmental damage (see for example Bond, 2002).

In the US there are more than 2.3 million miles of natural gas and hazardous liquid pipelines. These run under homes, near schools and offices. Since 1986 there have been 5,700 pipeline accidents resulting in 325 deaths, 1,500 injuries and more than \$850m environmental damage. On average, there is 1 pipeline accident every day. According to the US Office for Pipeline Safety (<http://ops.dot.gov/>) every year more than 6 million gallons of hazardous material are spilled through pipelines.

The Belgium pipeline rupture incident on 30th July 04 resulting in 27 deaths and 120 injuries (HInt Dossier, 2005) has since changed the historical perception that such incidents are mainly confined to outside of the European Union.

In the UK, more than 28000km of pressurised pipelines pass through both rural and populated areas. Of these approximately 20000km transport high-pressure natural gas above 7bar, 7000km multi-component liquids such as gasoline and over 1000km carry ethylene. Hundreds of kilometres of additional pipelines are currently being added to the UK pipeline infrastructure.

By the end of 2007, in order to address the UK's growing energy needs, the government plans to import large amounts of Liquefied Natural Gas (LNG) using marine tankers. Once treated and converted to its natural state, the gas is to be

distributed across the UK using pressurised pipelines. It is estimated that up to £4 billion worth of gas will be fed into the UK's supply over the next 15 years through this route.

The above has given rise to major public concern leading to several civil lawsuits awaiting hearing in the high court. This is set against the background of December 2005 massive Buncefield hydrocarbon tank fire explosion (subsequently described as the largest incident of its kind in peace time Europe:

http://www.bbc.co.uk/threecounties/read_this/buncefield_explosions), which caused extensive damage to property and the environment, as well as several injuries.

Indeed a recent EU commissioned study (Major Accident Hazards Bureau, Italy, 1999) recognises pipelines as a 'major-accident hazard'. Despite this, a greater use of pipelines is being promoted within the European Union, including the development of major European pipeline networks. In response to this, a new European Directive (Major Accident Hazards Bureau, Brussels, 2004) expected to come into effect by 2008, will require the hazard assessment of all pressurised pipelines containing appreciable amounts of hazardous materials. In the US the above is already enacted in the US Pipeline Safety Act 2000 (<http://ops.dot.gov/>). The Act goes on to require integrity management procedures that will reduce such risks to acceptable levels.

A major credible hazard involving pressurised pipelines is loss of mechanical integrity due to thermal loading during fire attack. In such circumstances, the determination of the subsequent discharge rate following outflow is important since it dictates all the major consequences associated with pipeline failure including fire, explosion, dispersion and environmental pollution. All of these parameters are key features of the safety case prepared by the pipeline operators. Safety authorities on the other hand use such data as the basis for controlling the risks to populated areas.

Ironically, despite the fact that pipelines pose a significantly greater hazard as opposed to pressurised vessels, the vast majority of studies reported in the literature concerning the modelling of the impact of fire loading have been exclusively confined to the latter (see for example Beynon et al., 1988; Ramskill, 1988, and Mahgerefteh et al., 2002). This is partly due to the more complicated nature of the large number of

interacting processes involved during unsteady state flow in a pressurised pipeline as opposed to those for a fluid confined in a fixed volume vessel.

In this thesis, the development of a mathematical simulation for modelling the loss in the mechanical integrity of pressurised pipelines during jet fire loading is presented. The model is based on the resolution of the conservation equations using the Method of Characteristics. It accounts for real fluid behaviour, pipeline mechanical strength, as well as phase and flow dependent transient heat transfer effects and frictional pressure losses. Failure is assumed to occur when any one of the simulated triaxial thermal and pressure stresses in the pipeline wall exceed its Ultimate Tensile Strength (UTS).

Two types of failure scenarios both involving thermal loading of a pressurised pipeline are modelled and the consequences of failure are elucidated using hypothetical case examples.

The first deals with the effect of direct jet fire impingement in which a section of the pipeline is assumed to be completely enveloped by the fire. The second failure scenario modelled involves the puncture of the pressurised pipeline and the immediate ignition of the escaping high pressure inventory. The impact of the resulting jet fire back radiation on the mechanical integrity of the depressurising pipeline is then mathematically assessed.

For better organisation, this thesis has been divided into 6 Chapters:

Chapter 2 firstly deals with a review of previous work on outflow modelling of pressurised pipelines following their rupture. The review highlights the theoretical basis, and where applicable, validation by comparison with experimental data.

It then goes on to review work relating to the effect of fire on the mechanical integrity of pressurised pipework and vessels. Also discussed is work done on simulating tank fires with particular emphasis on escalation. This type of work is presented to investigate the effect of fire on the adjacent structures.

The chapter concludes by reviewing literature on jet flame modelling. This culminates in the choice of an appropriate model used in this study for determining the characteristics of the ensuing fire following the immediate ignition of the escaping inventory from a punctured pipeline.

Chapter 3 presents the conservation equations governing the unsteady state flow following outflow of pipelines. The Method of Characteristics (MOC) is presented as the numerical tool adopted in this study to solve the conservation equations, which are proved to be quasilinear hyperbolic in nature. The Peng Robinson Equation of State (EoS) employed along with the other thermodynamic and hydrodynamic correlations are shown next. The more accurate 2-dimensional heat transfer approach as opposed the previous lumped capacitance method for determining the temperature profile in the pipewall is presented. The chapter ends with the validation of the developed outflow model with the Isle of Grain (IOG) experimental data.

Chapter 4 presents an important extension of the above work by modelling the effect of thermal loading on the mechanical integrity of a pressurised pipeline. The particular failure scenario simulated involves the localised heating of a section of the pipeline under direct jet fire impingement.

Both isolated and unisolated releases are modelled, the former deals with simulating the loss in mechanical integrity of an intact pipeline. The unisolated case on the other hand quantitatively accounts for the role of emergency depressurisation using different diameter relief valves on preserving the mechanical integrity of the pipeline during direct jet fire impingement.

The simulated pipewall temperature profile in conjunction with the appropriate stress equations, presented later in the chapter are used to simulate the transient triaxial thermal and pressure stress yield propagations. Failure is assumed to occur when any of the total stresses exceed the ultimate tensile strength of the pipeline material. The model is tested by its application to a hypothetical, nevertheless a realistic pressurised pipeline under fire attack.

Chapter 5 presents an alternative failure scenario involving the puncture of the pressurised pipeline and the immediate ignition of the released inventory. The impact of the resulting jet fire back radiation on the mechanical integrity of the depressurising pipeline is then modelled. An important precursor to the above is the presentation followed by utilisation of an appropriate model based on published literature describing the transient jet fire characteristics including its overall dimensions and radiation heat flux.

The chapter concludes with the comprehensive analysis of the results relating to the application of the transient jet fire model to the hypothetical failure of a natural gas pipeline.

Chapter 6 deals with general conclusions and suggestions for future work.

CHAPTER 2

LITERATURE REVIEW

2.1 Introduction

The layout of the work presented in this thesis was described in chapter 1. This chapter first deals with a review of previous work on outflow modelling of pressurised pipelines following their rupture. The review highlights the theoretical basis, and where applicable, validation by comparison with experimental data. It then goes on to review work relating to the effect of fire on the mechanical integrity of pressurised pipework and vessels. Also discussed is work done on simulating tank fires with particular emphasis on escalation. This type of work is presented to investigate the effect of fire on the adjacent structures.

The chapter concludes by reviewing literature on jet flame modelling. This culminates in the choice of an appropriate model used in this study for determining the characteristics of the ensuing fire following the immediate ignition of the escaping inventory from the punctured pipeline.

2.2 Review of Pipeline Outflow Models

The safety of pipelines used in the oil and gas industries became the subject of much debate when the US Department of Transportation (Office of Pipeline Safety, 2005), reported that incidents involving Natural Gas pipelines resulted in 22 fatalities and a total property damage of over \$160m during January 2000 to June 2005.

In the United Kingdom, the Offshore Installations (Safety Case) Regulations, 1992 (www.hse.gov.uk/ria/offshore) set requirements for demonstration, by reference to the results of a suitable and sufficient quantitative risk assessment, that the measures taken or to be taken by operators of offshore installations will reduce the risks to the health and safety of persons to 'As Low As Reasonably Practicable'. The assessments

of fire and explosion risks have become the essential first step in the effective management of such risks throughout the life of an installation.

The stricter safety design regulations and harsher penalties on pollution resulting from pipeline failure have promoted research into the modelling of accidents involving failure of pressurised pipelines.

The models discussed in this section are publications/products by four groups, two from industry (OLGA and PLAC) and two from academia (Imperial College and UCL) that represent the state of the art in this field. Later in this section, other less robust models developed for outflow in pipelines are also briefly discussed in terms of the methodology used and their limitations.

2.2.1 OLGA (Industry)

The commercially available pipeline model, OLGA was developed for simulation of multiphase transport in pipelines. It was initially conceived and developed in 1983 for the hydrocarbon industry by Statoil to simulate slow transients associated with terrain-induced slugging, pipeline start-up, shut-in and variable production rates. OLGA was very successful in simulating bubble/slug flow regime for small diameter low-pressure air/water flow; however the model was incapable of simulating stratified/annular flow regime. Further developments publicised in Bendiksen et al., (1991) addressed this problem and extended its use to hydrocarbon mixtures.

Limitations in OLGA's numerical methods and 2-phase models were discussed by Chen et al., (1993). The findings showed OLGA did not incorporate proper phase behaviour into its fluid description.

Two validations of OLGA were published by Bendiksen et al., (1991) and Shoup et al., (1998). Bendiksen et al., (1991) presented data using naphtha/diesel systems. The results gave good agreement with laboratory data but were confined to steady state conditions when comparing pressure drops, liquid hold up and flow regime transitions. Shoup et al., (1998) investigated OLGA under transient conditions. The results were compared with field data for 'slow' and 'rapid' blowdown of an onshore gas condensate pipeline. It was found that under 'slow' blowdown conditions results

showed reasonable agreement with field data. However, when simulating 'rapid' blowdown, the model performed relatively poorly. Figures 2.1 and 2.2 respectively show examples of the variations of simulated and measured release pressures with time.

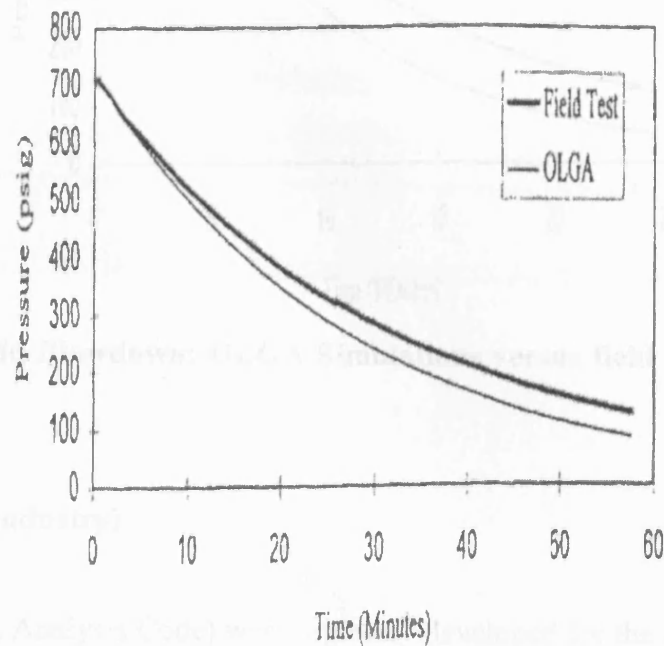


Figure 2.1: Slow blowdown: OLGA Simulations versus field test data (Shoup et al., 1998).

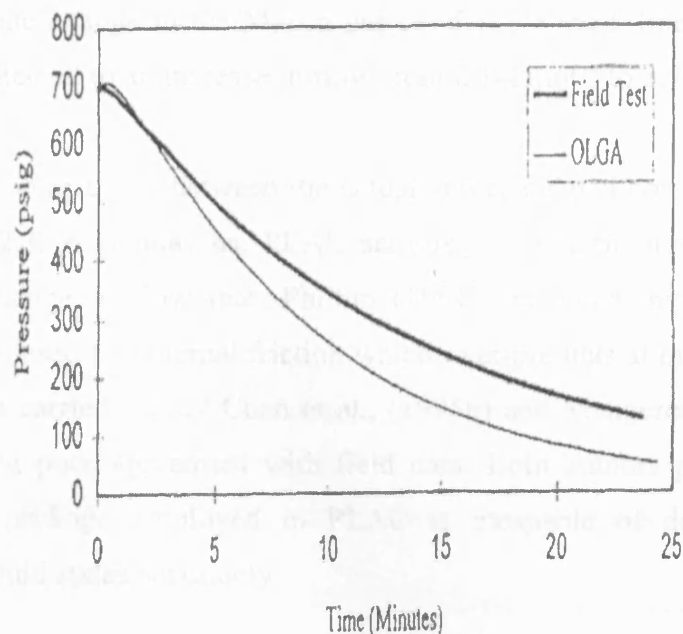


Figure 2.2: Rapid Blowdown: OLGA Simulations versus field test (Shoup et al., 1998).

2.2.2 PLAC (Industry)

PLAC (Pipe Line Analysis Code) was originally developed for the nuclear industry to simulate rapid transients within the cooling system pipework following prescribed failure scenarios (Peterson et al., 1985). Regarded as a general transient two-phase model, PLAC's initial purpose was to model terrain induced slugging of pipelines. It is claimed (Philbin 1991; Hall et al., 1993) that PLAC has the capacity to stimulate transients resulting from start-up, shutdown, ruptures and severe slugging.

With the recent upgrade of PLAC to PROFES (Produced Fluids Engineering Software -Hyprotech, 2001) the model is said to have the additional capability of simulating leaks from pipelines, however, no validation of these capabilities or theory has yet been made publicly available.

Several assessments of PLAC's performance in predicting pipeline rupture outflow data have been carried out including those by Chen et al., (1995b), Mahgrefteh et al., (1999) and Philbin (1991). Figure 2.3 shows the results obtained by Philbin (1991). The author compared PLAC's predictions with data obtained by Cunliffe (1978) for

the production rate change in the Marlin gas condensate trunk line near Melbourne. The line was subjected to an increase in flow from 2.14kmol/s to 3.75kmol/s.

Philbin's (1991) comparison between the actual and calculated condensate outflow is given in figure 2.3. As it may be, PLAC seriously underestimates the initial surge following the change in flow rate. Philbin (1991) attributed this to a correlation (Andritsos, 1986) used for internal friction which over-predicts at high pressures. The later assessments carried out by Chen et al., (1995b) and Mahgerefteh et al., (1999) also demonstrated poor agreement with field data. Both authors point out that the thermodynamic package employed in PLAC is incapable of determining phase boundaries and fluid states accurately.

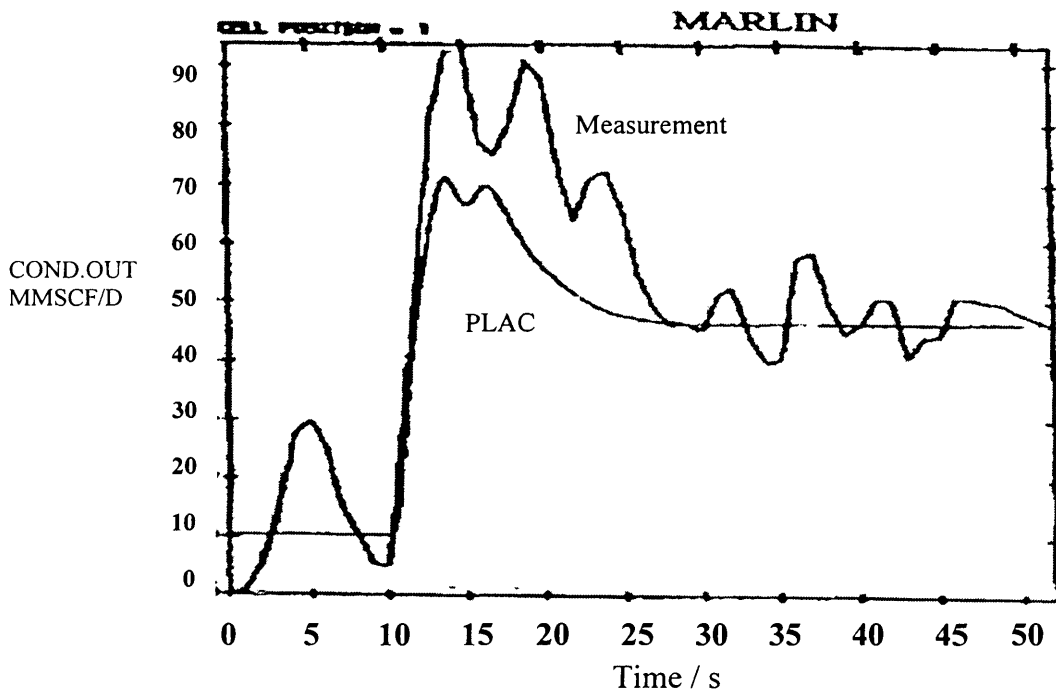


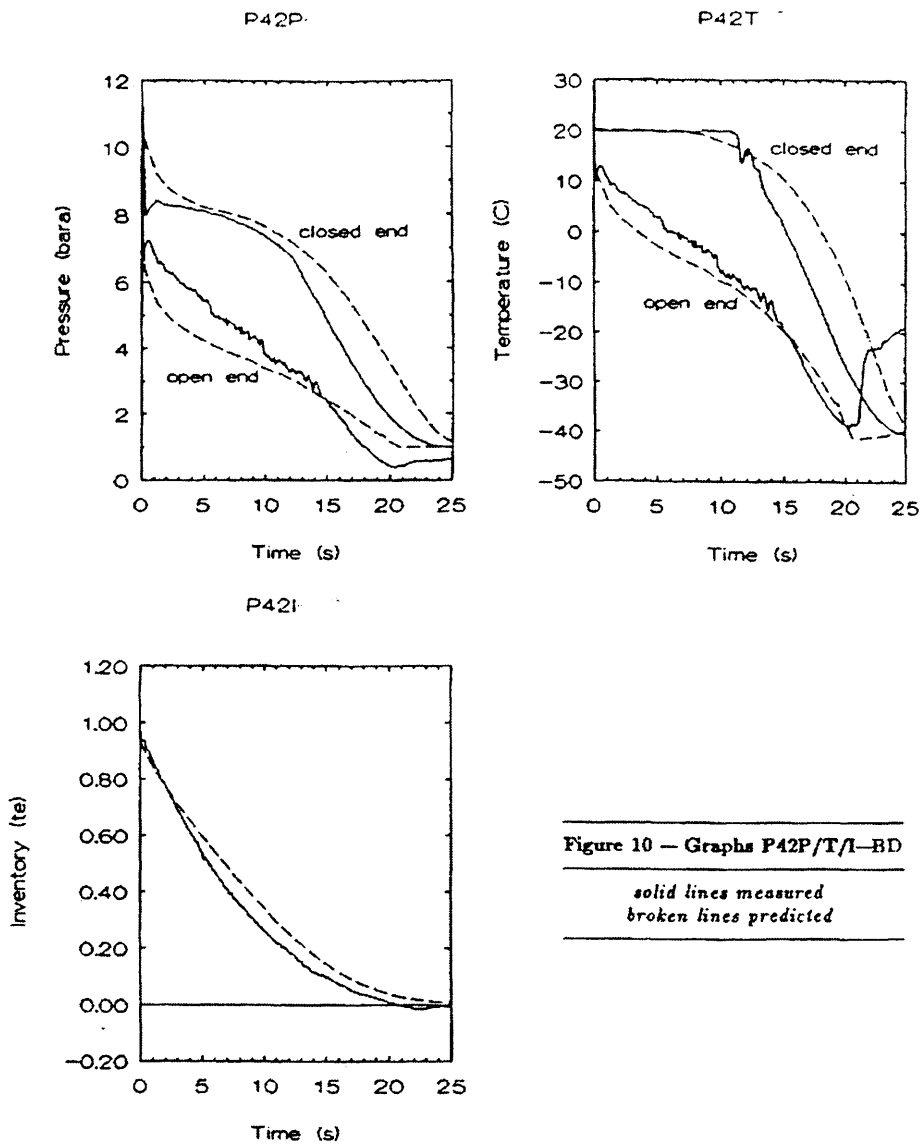
Figure 2.3: Condensate flow rate out versus time for the Marlin gas condensate trunk line (Philbin, 1991).

2.2.3 Imperial College Models: BLOWDOWN

2.2.3.1 Haque et al., (1990, 1992a, b); Richardson and Saville (1991, 1996a, b)

The BLOWDOWN simulation software was developed by Imperial College for simulating the quasi-adiabatic expansion process following the blowdown of pressure vessels. BLOWDOWN simulates the fluid and vessel wall temperatures during blowdown, allowing an evaluation of the likelihood of brittle vessel fracture due to low temperatures. Presently, BLOWDOWN is considered as the most comprehensive method available for depressurisation of vessels although, Mahgerefteh and Wong (1999) recently introduced a modification incorporating various equations of state.

The extended pipeline version of BLOWDOWN was validated with a reasonable degree of accuracy when compared with data from a series of LPG blowdown tests conducted jointly by Shell Oil and BP on the Isle of Grain. However, there were large discrepancies in temperature profiles towards the end of the blowdown this can be observed by the data shown in figure 2.4 a-c below. The data (figure 2.4 a-c) show the variation of the fluid temperature, pressure and inventory with time. As may be observed, reasonable agreement is obtained between the measured and experimental data although relatively large discrepancies in temperature profiles are observed towards the end of the blowdown. In addition, the predicted inventory remaining in the pipeline is consistently greater than the measured value. This, according to the authors, may be as a result of the quasi-steady and homogeneous flow assumption made in BLOWDOWN.



Figures 2.4 (a - c): Results of blowdown of pipeline containing LPG mixture; Isle of Grain depressurisation tests P42 (Richardson and Saville 1996b).

2.2.3.2 Chen et al., (1992, 1995a, b)

Chen et al., (1992) presented a numerical simulation for full-bore rupture (FBR) of pipelines containing perfect gases based on the solution of the conservation equations using the Method of Characteristics (MOC). A brief description of the MOC is given later (chapter 3). The ideal gas blowdown simulation results were validated against field data obtained during Piper Alpha tragedy following the FBR of the subsea gas pipeline between the Piper Alpha and MCP-01 platforms (Richardson and Saville, 1991). The results obtained were found to be in poor agreement with actual data, with the discrepancy being attributed to ignoring real fluid behaviour.

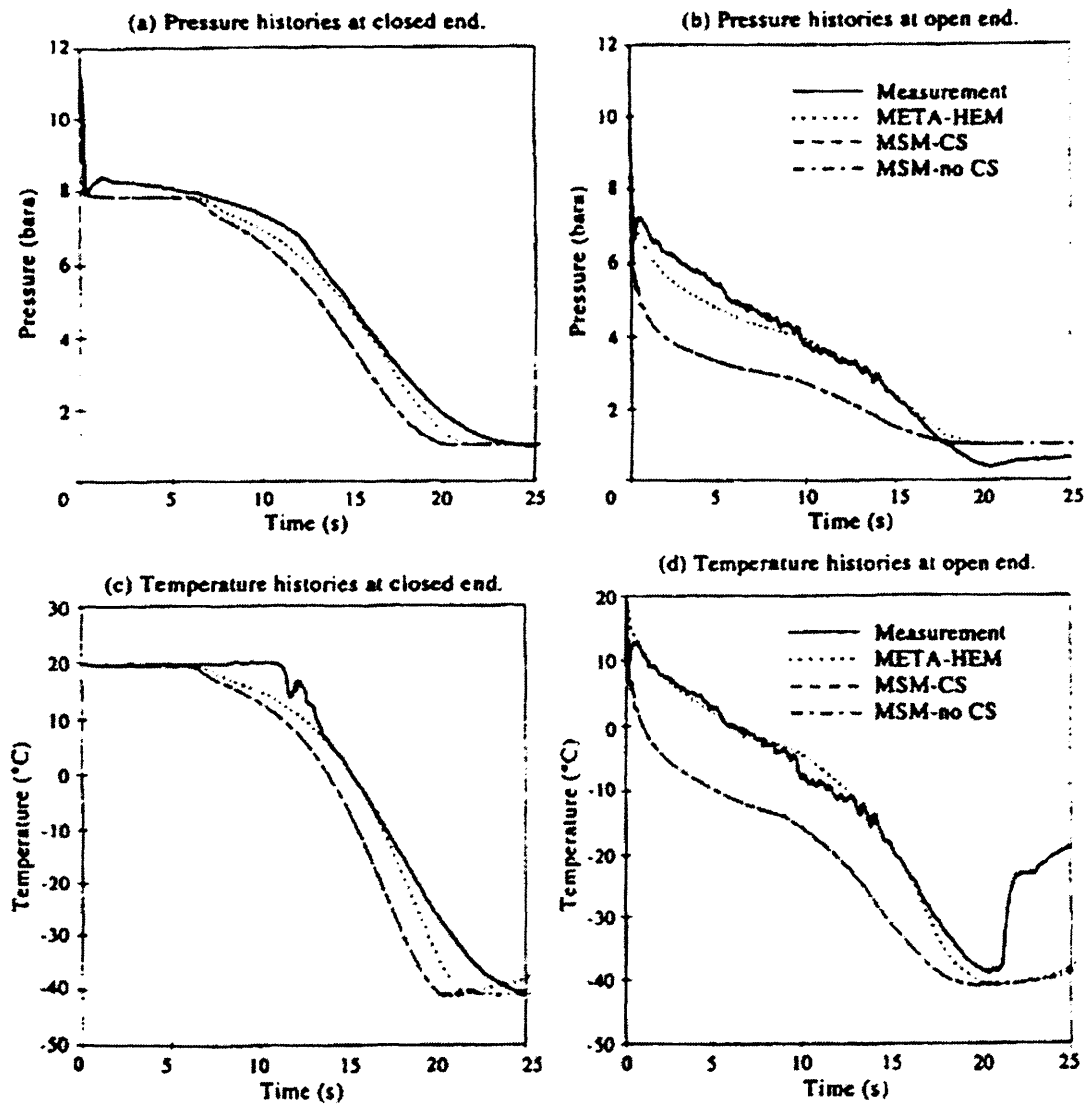
Chen et al., (1995a, b) accounted for real fluid behaviour using an in-house computer program-PREPROP. The authors also investigated the effects of assuming homogenous equilibrium as compared to heterogeneous equilibrium between the constituent phases on the accuracy of their simulations. As opposed to heterogeneous equilibrium, homogenous equilibrium assumes that all phases are at thermal and mechanical equilibrium, and move at the same velocity. This assumption ensures the maximum possible mass transfer rate during any phase process, significantly simplifying the requirement of modelling the interfacial heat/mass transfer processes into a simple phase equilibrium calculation.

Using the heterogeneous equilibrium model, the authors also investigated the effects of assuming stratified (liquid at the bottom with vapour at the top) as opposed to bubbly flow on the blowdown results.

The flow regime transitions are specified empirically by using a flow regime map. The flow channel is discretised using staggered meshes where the flow velocity is defined at the cell edge and all other variables defined at cell centre. Furthermore, the density in the mass conservation equation is eliminated using a locally linearised equation of state so that the discretised conservation laws can be reduced to two difference equations in terms of mixture enthalpy and pressure only.

Figures 2.5 a-d show the results of the heterogeneous equilibrium model, referred to as META-MSM (META Marginal Stability Model, with META referring to the name

of the main computer program) as well as homogenous equilibrium model (HEM) as compared to the Isle of grain depressurisation test P42 data. (See section 3.12; table 3.2, for full depressurisation conditions).



Figures 2.5 (a - d): Results of blowdown of pipeline containing LPG mixture (Isle of Grain depressurisation tests P42) (Chen et al., 1995b).

Good agreement between META-HEM and field data is obtained. This agreement is in fact better than those obtained using either of the non-equilibrium-based models (MSM-Concentration Stratification [CS] and MSM-no CS). The poor performances of heterogeneous models are probably as a consequence of the uncertainties associated with the large amount of empirical correlations used for the generation of the hydrodynamic data for the various flow regimes.

Based on the reasonably good performance of the HEM, it can be concluded that the homogenous equilibrium assumption is valid in the case of the FBR depressurisation of long (>100 m) pipelines.

Furthermore, agreement between the MSM-CS and MSM-no CS models indicates that the effect of concentration stratification can be ignored.

Figure 2.6 shows the performance of PLAC against the META-HEM, MSM-CS (Marginal Stability Model-Concentration Stratification) and BLOWDOWN codes for the variation of the total line inventory with time for LPG blowdown test P42. META-HEM, MSM-CS and BLOWDOWN agree relatively well in comparison to field data, with PLAC performing quite poorly.

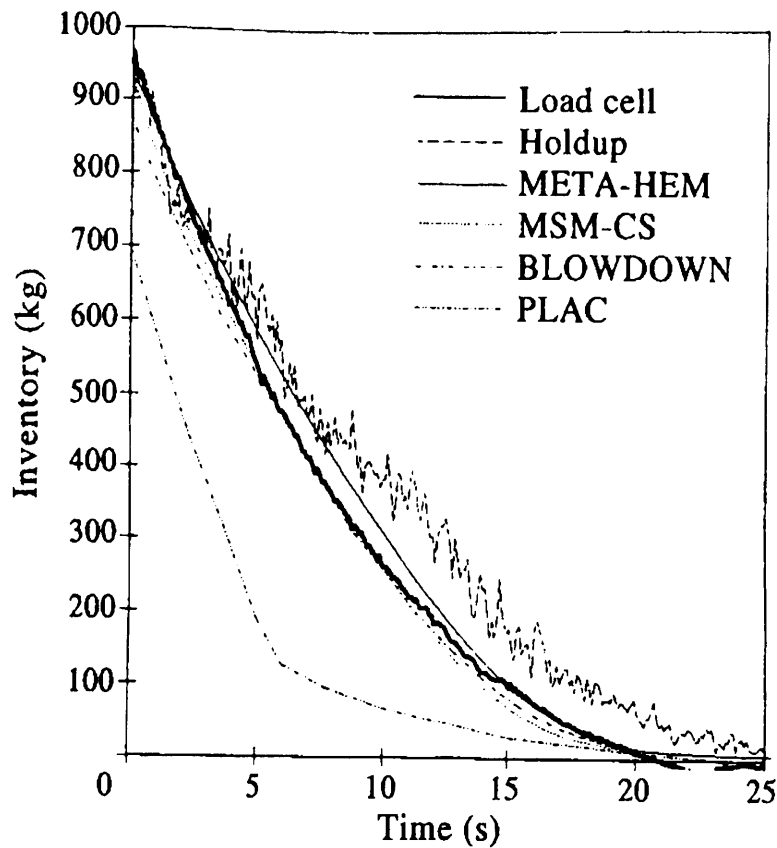


Figure 2.6: Comparison of results of HEM, MSM, BLOWDOWN and PLAC with the Isle of Grain depressurisation test P42 (Chen et al., 1995b).

25 uniform meshes were used in the simulation of the Isle of Grain depressurisation tests on a DEC 5000/240 workstation. The corresponding computation time for the META-MSM and the HEM model was ca. 20 hrs and 8 hrs respectively. Hence it is expected that the application of the above models (MSM and HEM) in simulating the complete blowdown of long pipelines would take many days to execute.

2.2.4 UCL Models

2.2.4.1 Mahgerefteh et al., (1997-2000)

Between 1997 and 2006, Mahgerefteh et al., published a number of papers relating to transient modelling of outflow following pipeline rupture based on the homogenous equilibrium flow assumption.

In the first publication, Mahgerefteh et al., (1997) using the Method of Characteristics (MOC) deal with the modelling of dynamic response of emergency shutdown valves following FBR of long pipelines containing perfect gases. This model was later extended by Mahgerefteh et al., (1999) to simulate pipelines containing two-phase hydrocarbon mixtures. In a further publication, Mahgerefteh et al., (2000) employed a real fluid model to predict the effect of phase transition on the dynamic behaviour of emergency shutdown valves.

The authors concluded that a transition from gas to two-phase flow during blowdown results in a delay in valve activation time as well as an increase in the total amount of inventory released prior to pipeline isolation.

The initial validation of the Mahgerefteh et al's., (2000) model was limited in its application to the rupture of the Piper Alpha riser (Richardson and Saville, 1991). A range of different hypothetical emergency shutdown scenarios involving ball valves and check valves were considered. To clarify the differences in behaviour between gas and two-phase transmission pipelines, the inventory was treated as a permanent gas as well as a real fluid experiencing phase change.

Figure 2.7 illustrates the variation of release rate at the rupture plane with time subsequent to valve closure for a range of delays in shutdown for a check valve placed 300m from the FBR plane. It is clear from the data that the predicted release rates in the case of the condensable gas mixture are notably higher than those for the permanent gas following emergency isolation of the pipeline. It is also important to note the depressurisation time is also longer for each closure delay.

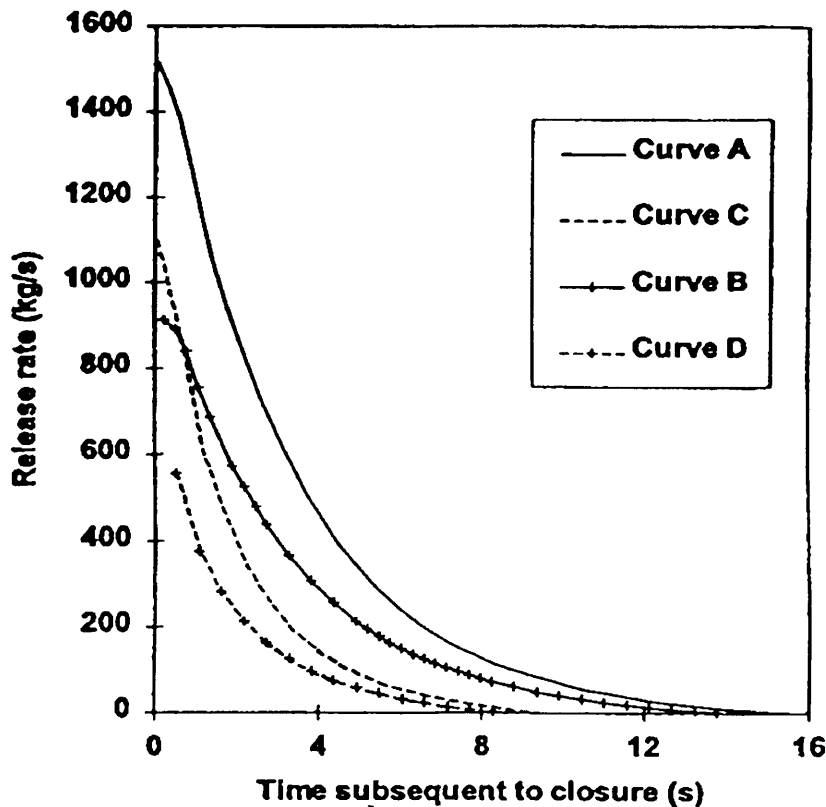


Figure 2.7: Variation of release rate with time subsequent to check valve closure for various arbitrary delays in valve shutdown (Mahgerefteh et al., 2000).

Curve A: Two-phase; valve closure delay after passage of flow reversal = 1.37s

Curve B: Two-phase; valve closure delay after passage of flow reversal = 6.47s

Curve C: Permanent gas; valve closure delay after passage of flow reversal = 1.37s

Curve D: Permanent gas; valve closure delay after passage of flow reversal = 6.47s

2.2.4.2 Vahedi (2003)

Vahedi (2003) developed a model based on the Method of Characteristics to determine the effects of inclination and pipeline enlargement (non-uniform pipe diameter) on outflow characteristics. A comparison was made between the results generated using linear as opposed to curved characteristics. The author also studied the effect of using different friction factor correlations on the simulated results. Fluid thermodynamic properties were calculated with the aid of the Peng-Robinson

equation of state (Walas, 1987) and the fluid phases were assumed to be in homogenous equilibrium.

Vahedi's (Vahedi, 2003) pipeline rupture model was validated against the Isle of Grain experimental data and those recorded during the Piper Alpha tragedy. Good agreement between field and experimental data was obtained.

A hypothetical scenario involving the rupture of an enlarged pipeline, containing methane at an initial pressure of 50bara was also investigated. Figure 2.8 gives a schematic representation of the pipeline and the rupture location.

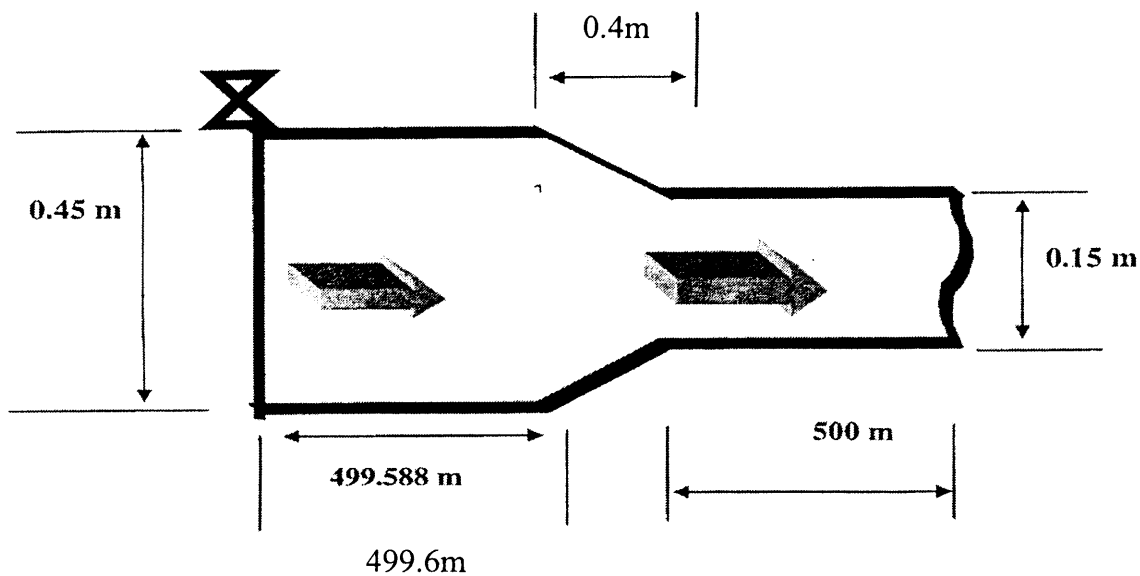


Figure 2.8: Schematic representation of enlarged pipeline simulation (Vahedi, 2003).

The simulation results for the above configuration were then compared against those obtained using a uniform diameter pipeline of the same length, containing the same amount of inventory and composition.

Figure 2.9 shows the variation of pipeline inventory with time following the rupture of the uniform and the enlarged pipeline. As it may be observed from the data, the

enlarged pipeline depressurises at a significantly slower rate as compared to the uniform diameter pipeline. The author concludes that reducing the pipeline diameter or ‘bottlenecking’ may be used as an effective way of reducing hazards following FBR by reducing the discharge rate.

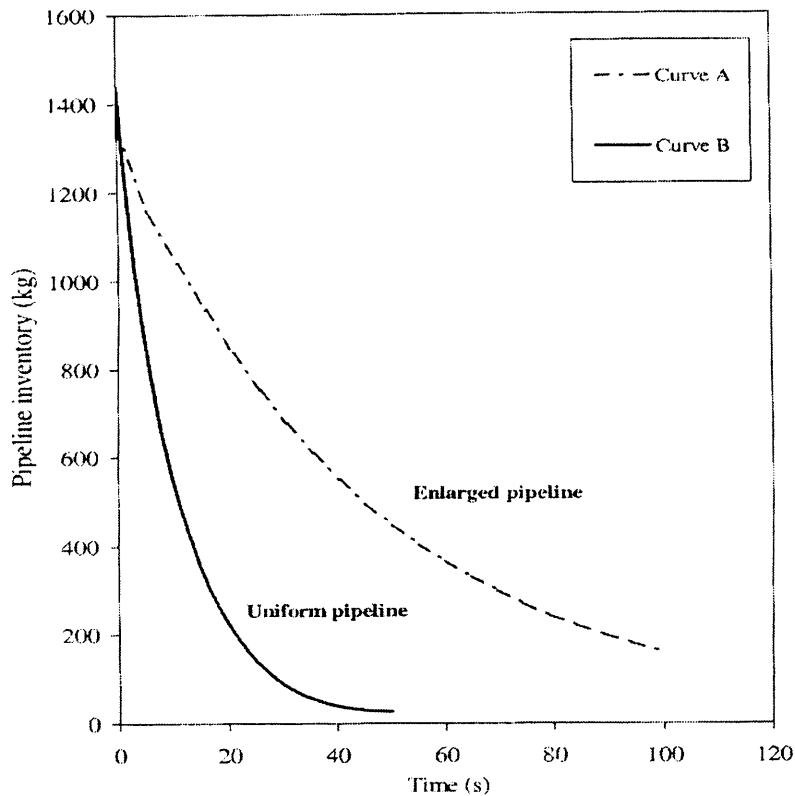


Figure 2.9: Pipeline inventory variation with time for methane following FBR (Vahedi, 2003).

Curve A: Enlarged pipeline.

Curve B: Uniform pipeline.

Other investigations made by Vahedi (2003) include the use of curved as opposed to linear characteristics on the simulation accuracy and CPU run times. It was observed that for 2 phase flows, the linear characteristics (see section 3.5.1) provide consistently better predictions and executed faster in comparison to curved characteristics (Vahedi, 2003). However, for gaseous media either methodology yields practically the same result with similar computational run times.

On the study of the effect of pipeline inclination, the author concludes that the pressure wave propagation during top end rupture is slower in inclined pipelines as compared to horizontal pipelines, with the converse holding for bottom end rupture.

2.2.4.3 Oke et al., 2003; Oke, 2004

The models developed by Oke et al. (2003) and Oke (2004) tackled the outflow characteristics following the puncture and rupture of pipeline networks. The model is based on the MOC and assumes homogenous equilibrium between phases. The conservation equations were modelled in terms of pressure, enthalpy and velocity (PHU) in contrast to the conventional pressure, density and velocity (PDU) formulation used by previous workers (Zucrow and Hoffmann, 1976; Tiley, 1989; Chen et al., 1992; Mahgerefteh et al., 1997-2000, etc). A pressure, entropy and velocity (PSU) based formulation was also presented and all three (PDU, PHU and PSU) models were compared in terms of accuracy and CPU run times.

Oke's (2004) model was validated against the Isle of Grain and Piper Alpha pipeline rupture data. The PDU, PHU and PSU based conservation equations were used to simulate the Isle of Grain depressurisation tests in order to investigate the effect of the choice of primitive variables on model accuracy and computational run time. Figure 2.10 shows the variation of discharge pressure with time for the Isle of Grain test P40 as compared to the simulation results. As it may be observed, in general, the PHU model performs best in terms of accuracy, followed by the PSU and PDU models. The PHU model also required the least CPU run time, requiring 12 minutes to execute, while the PSU and PDU models required 13 minutes and 86 minutes respectively on an IBM Pentium IV 2400MHz PC. Based on these results, the PHU model was thus used for all the subsequent simulations presented.

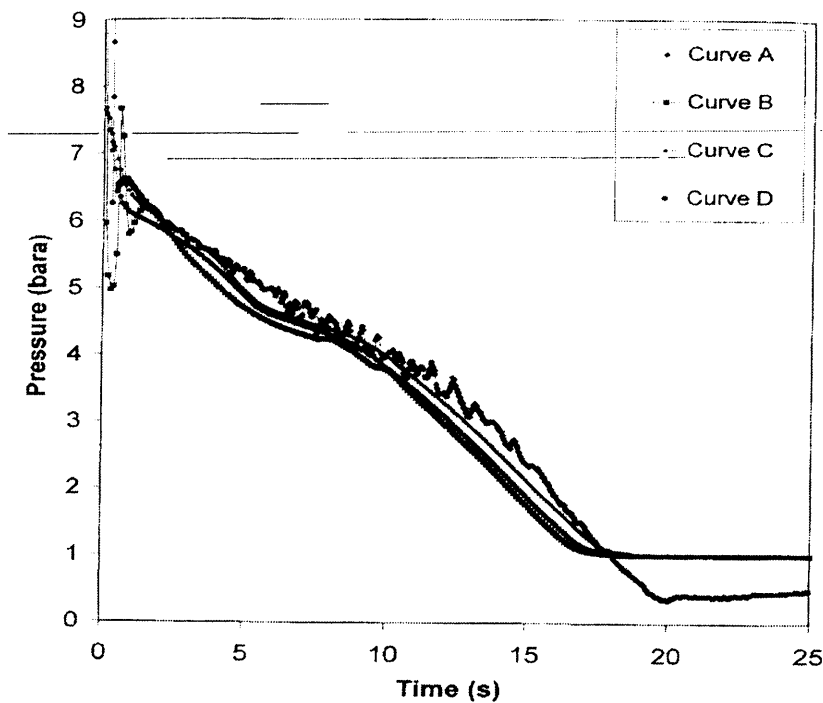


Figure 2.10: FBR pressure-time profiles at open end for test P40 (LPG) showing the effect of primitive variables on simulated results (Oke, 2004).

Curve A: Open end measurement.

Curve B: Open end simulation results using the PDU model.

Curve C: Open end simulation results using the PHU model.

Curve D: Open end simulation results using the PSU model.

Oke's model (2004) was then employed to simulate the blowdown of various configurations of pipeline networks having the same total length of 25km. The fluid inventories and conditions were the same as those used in the Piper Alpha simulation. From the simulations, it was concluded that the depressurisation of a pipeline network is strongly influenced by the overall distance travelled by the expansion waves from the rupture plane to the intact end. The shorter the distance travelled, the faster the depressurisation.

The fluid dynamics following the puncture of a hypothetical pipeline was discussed in the model presented by Oke et al., (2003). The PHU model was used in the simulation with the pipeline assumed to be isolated downstream upon puncture. Figure 2.11

shows a pictorial timeline simulation of the fluid flow pattern following puncture as presented by Oke et al., (2003).

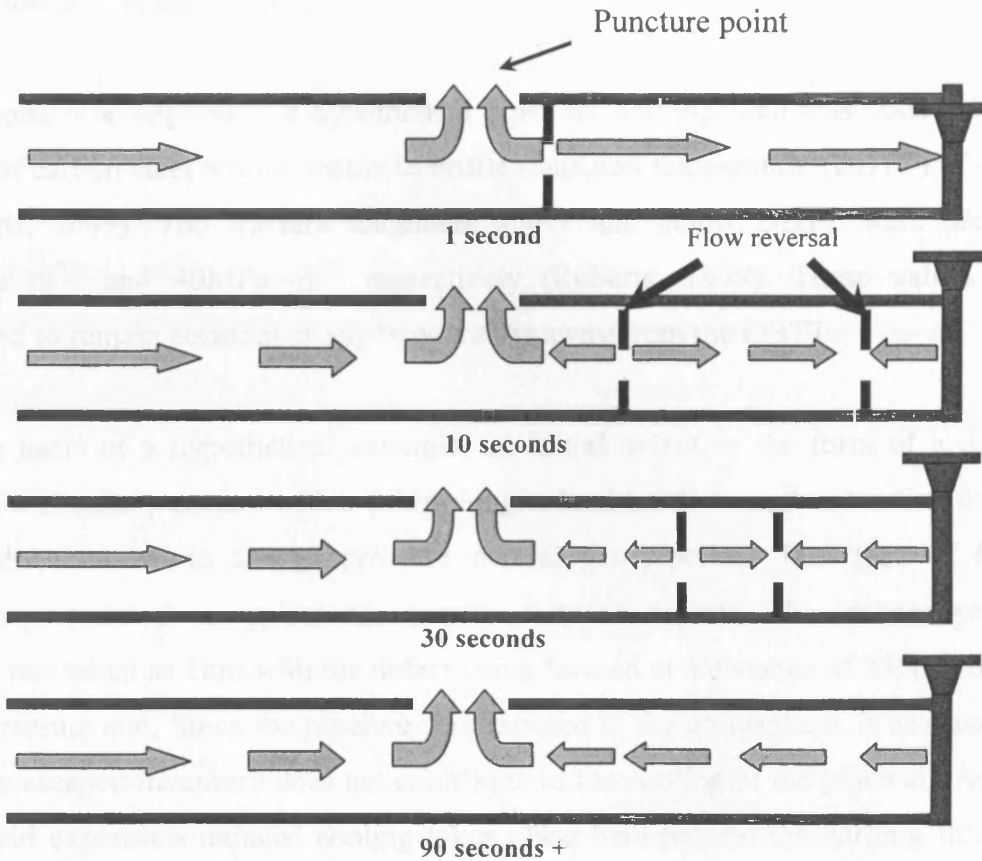


Figure 2.11: Schematic representation of flow patterns in the pipeline following puncture (Oke et al., 2003).

It is worthy to note that heat transfer modelling was based on a lumped capacitance approach (Oke, 2004) where the pipewall was treated as a heat sink between the ambient and the fluid. The model ignored the heat conduction in the radial and tangential direction.

2.2.4.4 Mahgerefteh and Atti (2006)

Mahgerefteh and Atti (2006) extended the puncture model to simulate the progression of a defect in the pipeline into a running fracture.

The crack propagation model invoked fracture mechanics principles and accounted for the important processes taking place during depressurisation including the thermal, and pressure stresses in the pipewall to simulate the progression of a simple defect into a running fracture.

The model was applied to a hypothetical pipeline. The pipewall was assumed to be made of carbon steel with a ductile to brittle transition temperature (DBTT) of -15°C (Roberts, 1999). The fracture toughness above and below DBTT were taken as $95\text{MPa m}^{0.5}$ and $40\text{MPa m}^{0.5}$ respectively (Roberts, 1999). These values were assumed to remain constant at any temperature away from the DBTT.

As the basis of a hypothetical example, an initial defect in the form of a 0.005m diameter circular puncture with a 0.05m longitudinal hairline crack extending from its side was assumed in a high pressure natural gas pipeline. This type of failure geometry is stated as typical of corrosion-induced defects. The isolated pipeline length was taken as 1km with the defect being formed at a distance of 250m from the high-pressure end. Since the pipeline was exposed to the atmosphere, it was assumed that the escaped inventory does not contribute to the cooling of the pipewall. As such any fluid expansion induced cooling takes place between the discharging fluid, the pipewall and the puncture plane.

Figure 2.12 shows the variation of the radial temperature profile (across the pipeline thickness) at the puncture plane at different time intervals during the depressurisation for an isolated failure scenario (no pumping). For the conditions tested, the data indicate that the temperature variation across the pipewall thickness is negligible. The maximum temperature drop of only 5K following depressurisation was recorded. Consequently, the associated thermal stresses due to temperature change in the radial direction were considered to be minimal.

In figure 2.13 the authors show the corresponding transient axial pipewall temperature profiles at different time intervals in the proximity of the puncture plane for the isolated failure scenarios. The corresponding DBTT is also indicated for reference. Referring to the data (figure 2.13), it is clear that the rapid expansion of the escaping

inventory results in significant cooling of the pipewall with the effect becoming more pronounced with time and distance towards the puncture plane.

The authors showed the transient variation of defect length with time following puncture for the isolated release. This data is shown in figure 2.14. The defect length was taken as the summation of the crack length and the puncture diameter. Curve A shows the actual defect length whereas curve B shows the corresponding critical defect length required to cause catastrophic failure. As it may be observed, depressurisation of the pipeline results in a significant and rapid increase in defect length. Catastrophic failure corresponding to the point of intersection for curves A and B occurs some 2,100s following puncture as indicated in figure 2.14.

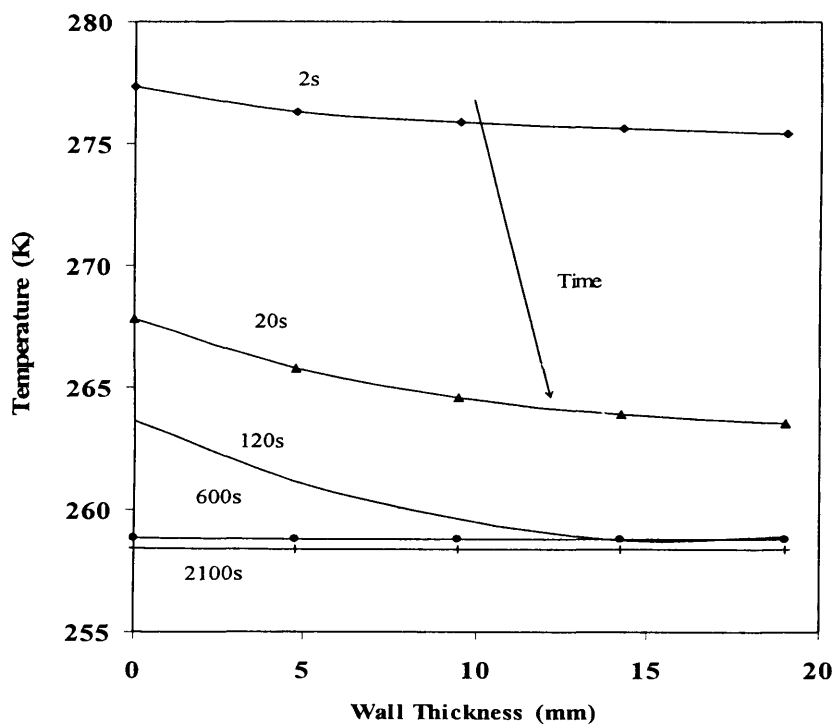


Figure 2.12 Transient variation of the radial temperature profile at the crack tip at different time intervals following depressurisation for isolated release (Mahgerefteh and Atti, 2006).

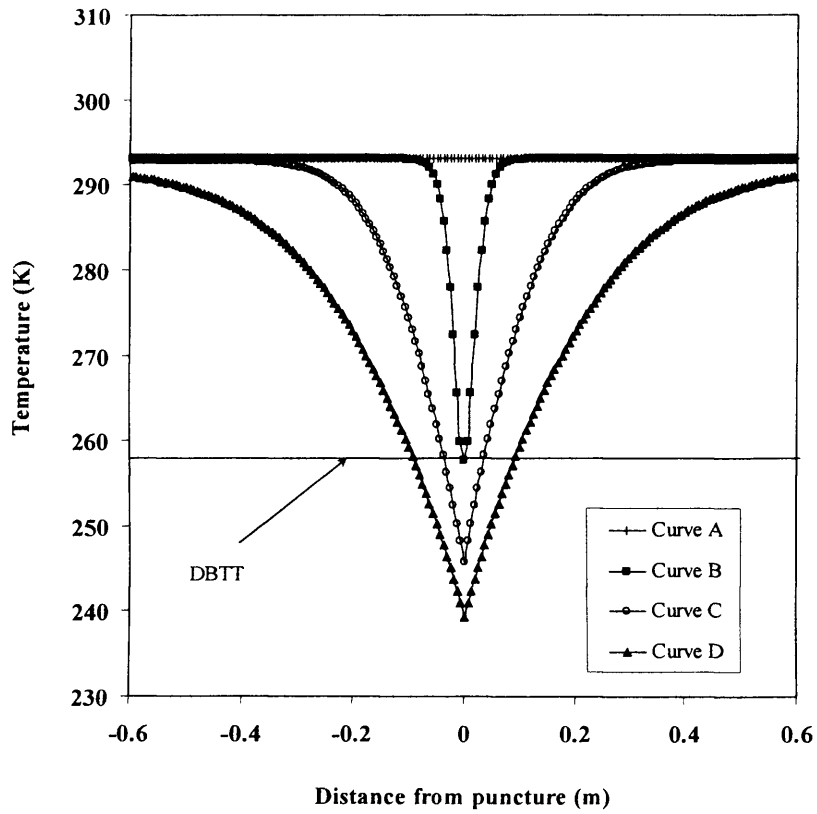


Figure 2.13 Transient variation of the axial temperature profile in the vicinity of the puncture plane (Mahgerefteh and Atti, 2006).

Curve A: 0s; **Curve B:** 30s; **Curve C:** 600s; **Curve D:** 2700s.

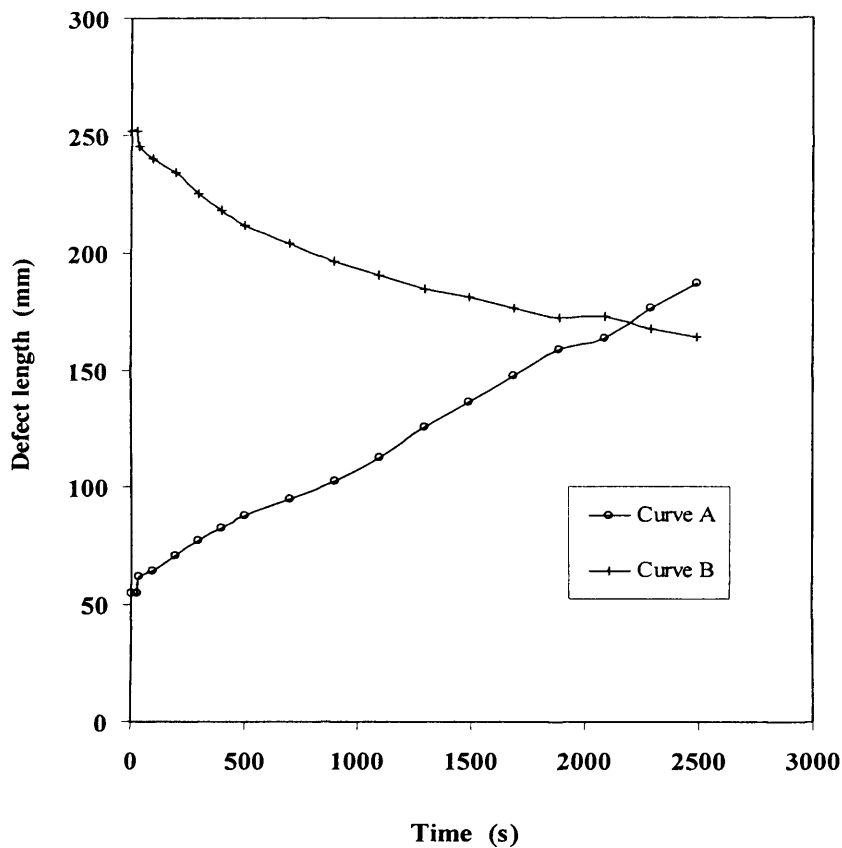


Figure 2.14: The variation of defect length with time (Mahgerefteh and Atti, 2006).

Curve A: Actual defect length

Curve B: Defect length required to cause a running (experimental data)

The above study for the first time quantitatively highlighted the importance of taking into account the expansion induced cooling effects as a credible failure scenario when undertaking safety assessment of pressurised pipelines.

2.2.5 Other Models

For the sake of completeness, the following is a review of the less rigorous models reported in the literature for pipeline rupture outflow simulation.

Sens et al., (1970) used an explicit finite difference method for the numerical solution of the partial differential equations to simulate transient flow in a gas pipeline a few seconds after rupture. The model is intrinsically one-dimensional and assumes perfect

gas behaviour. The formulation ignores the highly probable condensation of the fluid inventory due to its rapid expansion induced cooling at the rupture plane.

Jones and Gough (1981) developed a model; DECAY for analysing high pressure natural gas decompression behaviors following pipeline rupture. Assuming the pipeline to be horizontal, the model is based on isentropic and homogeneous equilibrium fluid flow assumption employing the Soave-Redlich-Kwong equation of state (SRK EoS). Although good agreement was obtained with experimental data, the performance of the model is uncertain with respect to the blowdown of long pipelines, including those conveying flashing fluids.

Flatt (1985-1989) studied the use of the Method of Characteristics for the analysis of unsteady compressible flow in long pipelines following rupture. The author discarded the simplifying assumptions of isothermal flow often applied in the case of unsteady compressible flow in pipelines. To improve accuracy, higher-order polynomials and an assumption of curved characteristic lines were employed. However, the model is one-dimensional and assumes single-phase gas discharge.

Picard and Bishnoi (1988) applied their three models namely the Perfect-gas Isentropic Decompression (PID) model, Real-fluid Isentropic Decompression (RID) model and Real-fluid Non-isentropic Decompression (RND) to investigate the importance of real-fluid behaviour in the modelling of high-pressure gas pipeline ruptures. The models are based on the MOC and assume the flow is one-dimensional. For the RID model, either the Soave-Redlich-Kwong (SRK) or the Peng-Robinson equation of state was employed. The authors observed that the PR-EoS gave better predictions of the fluid rupture data when compared to the SRK-EoS. The results also showed that the perfect-gas model (PID) could introduce significant errors as it underestimated the fluid pressure by as much as 20% when compared with the real fluid model (RID).

Zhou et al., (1997) tackled the problem of releases from high-pressure pipelines using three-dimensional computational fluid dynamics. This model was designed to incorporate geometric and physical complexities that may exist in the pipe system, and handle the modelling of punctures located and oriented at different angles at any

point along the walls of a pipeline. Whilst this model gives an exhaustive description of the fluid mechanical and thermodynamic properties, it nonetheless is based on steady state conditions and assumes steady state discharge.

2.3 Modelling Work on Thermal Response of Pressurised Vessels and Pipework to Fire Attack

Recently a considerable amount of work has been undertaken to understand the nature of the processes involved when pressurised equipment is exposed to external fire impingement. The main incentive of such studies arises from the safety issues associated with the storage and transport of highly flammable, pressurised inventory, brought about by the considerable increase in the use of pressure-liquefied fuels (e.g. butane and propane).

Most of the work done on fire modelling in the last 3 decades has been associated with vessels elucidating the important processes taking place during the blowdown of pressurised vessels under fire attack. This section presents the development of a robust model developed by Mahgerefteh et al., (2002) and Mahgerefteh and Falope (2003) to determine failure in pressurised vessels following fire attack. A detailed study carried out by HSE (Roberts et al., 2000) on the effects of vessels and pipework to fire attack is presented and lastly work done by Russo et al., (1995) in terms of expressing transient stresses in pipelines is described. These models form the basis of the work presented later in the thesis (Chapter 4). Other work on fire impingement modelling is also discussed in this section.

2.3.1 Mahgerefteh et al., (2002)

Mahgerefteh et al., (2002) presented the development of a robust numerical simulation for predicting the risk of rupture following blowdown of pressurised cylindrical vessels containing multi-component hydrocarbon mixtures under fire attack.

The model accounted for non-equilibrium effects between phases, heat transfer between each fluid phase and their corresponding sections of vessel wall, interphase

fluxes due to evaporation and condensation, as well as the effects of sonic flow at the orifice.

Using their model, Mahgerefteh et al., (2002) observed that in the case of a two-phase gas/liquid inventory, the much higher heat transfer coefficient in the liquid phase as compared to the vapour resulted in a relatively low inside wall temperature thus exposing the wetted vessel wall to significant thermal stresses. On the other hand, the vapour being a rather poor medium of heat transfer exposes the dry walls to significantly lower temperature gradients but much higher mean temperatures. The latter resulted in significant mechanical weakening of the vessel wall.

The transient tangential, radial and longitudinal thermal stress equations in a hollow cylinder given by Timoshenko and Goodier, (1987) and corresponding equations for pressure stresses for a thick-walled cylinder given by (Popov, 1999) were used in the model. The simulated stresses were then compared with vessel material's tensile stress data for precise evaluation of the risk of failure.

Figure 2.15 shows the predicted pressure and inventory against time profiles during blowdown under fire loading (curves A and D) and ambient surroundings (curves B and C). The authors observed a marked reduction in the rate of drop in pressure under fire. For example even after 1200s following blowdown, the residing pressure in the vessel is 10Bara. The authors claimed this to be due to the significant amount of liquid boiling and evaporation, which are in turn manifested in a corresponding increase in the rate of loss in inventory.

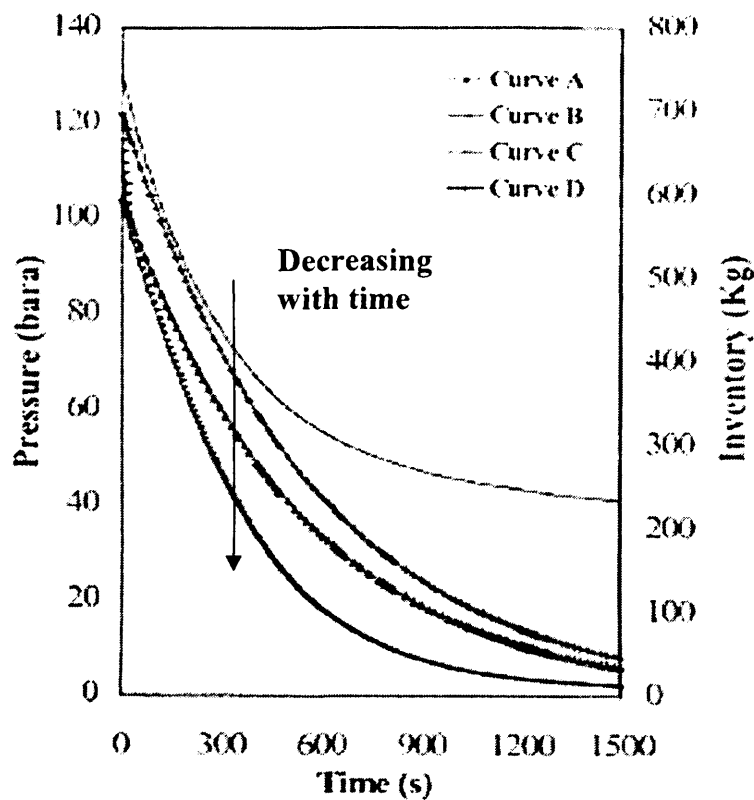


Figure 2.15: Pressure and inventory with time under fire and at ambient conditions. (Mahgerefteh et al., 2002).

Curve A: Pressure, fire; **Curve B:** Pressure, ambient; **Curve C:** Inventory, ambient; **Curve D:** Inventory, fire.

Figure 2.16 shows the variation of the temperature difference between the inner and outer walls for the wetted (curve A) and unwetted sections (curve B) of the vessel during blowdown under fire predicted by the model (Mahgerefteh et al., 2002). The authors state that the vessel wall in contact with the liquid inventory experiences a much larger temperature gradient compared to that exposed to the vapour. This is once again primarily a consequence of the much larger heat transfer coefficient in the liquid phase, which in turn results in the rapid removal of heat from the inner vessel wall to the bulk liquid. The fact that the temperature gradient increases in magnitude with time is indicative of improved rate of heat transfer in the liquid phase as blowdown proceeds.

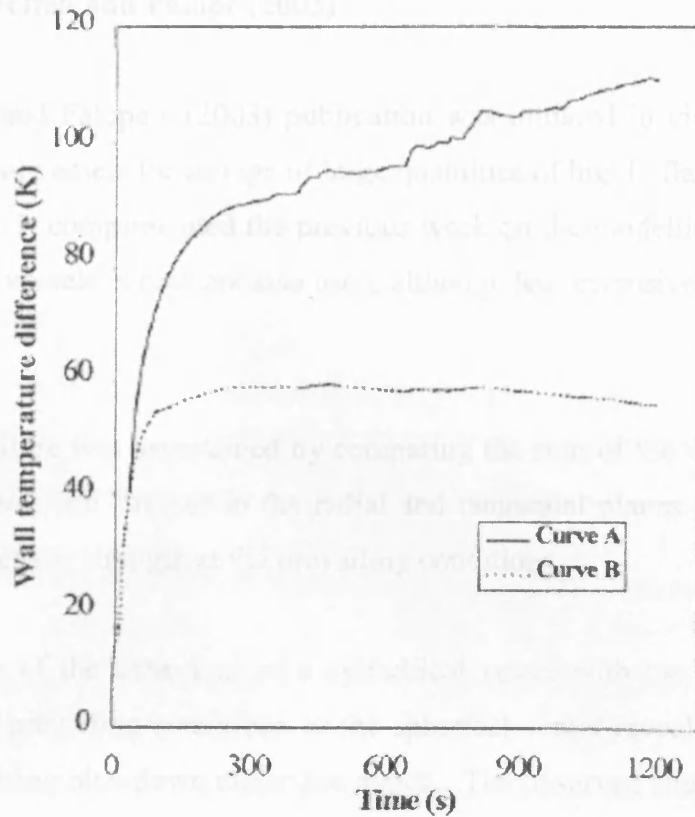


Figure 2.16 variation of wetted and unwetted wall temperature difference with time during blowdown under fire (Mahgerefteh et al., 2002).

Curve A: Wetted wall; **Curve B:** Unwetted wall.

Apart from predicting the precise mode of vessel failure, the simulation was used as an investigative tool for elucidating the role of a number of competing processes (transient thermal loading on the wetted and unwetted vessel wall) that ultimately lead to vessel rupture. In addition, some fundamental differences in the failure risks during blowdown under fire as opposed to that conducted under ambient conditions were highlighted.

2.3.2 Mahgerefteh and Falope (2003)

Mahgerefteh and Falope's (2003) publication was initiated in view of the extensive use of spherical vessels for storage of large quantities of highly flammable pressurised hydrocarbons. It complimented the previous work on the modelling of the behaviour of cylindrical vessels, which are also used, although less extensively for the storage of hydrocarbons.

The risk of failure was ascertained by comparing the sum of the vessel wall transient thermal and pressure stresses in the radial and tangential planes with its material of construction tensile strength at the prevailing conditions.

A comparison of the behaviour of a cylindrical vessel with the same volume, wall thickness and prevailing conditions as the spherical vessel revealed little differences in response during blowdown under fire attack. The observed slightly shorter time to reach failure in the case of the spherical vessel was stated to be attributed to its larger wall heat transfer area, which ultimately leads to the complete evaporation of the two-phase inventory. As a consequence, the amount of inventory present at the time of failure was observed to be smaller than that in the cylindrical vessel. In the latter case, the inventory remained in the two-phase region throughout the blowdown process.

Table 2.1 is a summary of the main differences in behaviour between the two vessels during blowdown under fire attack as highlighted by the authors.

	Spherical vessel	Cylindrical vessel
Time of failure following blowdown (s)	1070	1120
Failure mode	Tangential shear in the vapour space	Tangential shear in the vapour space
Vessel pressure at time of failure (bara)	18.10	12.90
Inventory remaining in vessel at time of failure (kg)	37.5	91.2

Table 2.1: A comparison between the behaviour of spherical and cylindrical vessels during blowdown under fire attack (Mahgerefteh and Falope, 2003)

2.3.3 Blast and Fire Engineering for Topside Structures (Roberts et al., 2000)

In 1991, the Health and Safety Executive UK, with the participation of the offshore industry, completed Phase 1 of a Joint Industry Project on Blast and Fire Engineering for Topside Structures. This comprehensive project included the thermal response of vessels and pipework exposed to fire and other closely related topics. The study resulted in the 'Interim Guidance Notes for the Design and Protection of Topside Structures against Explosions and Fire'. Following this, an HSE review was carried out by Roberts et al. (2000). It aimed to investigate the response of pressurised process vessels and equipment to fire attack by reviewing the current knowledge and available analysis techniques relating to it, and identify any gaps in knowledge that may need to be filled before new and comprehensive guidance can be given.

The report reviewed the types of fires that may occur on offshore installations and threaten equipment. The report provided new information on jet fires and pool fires.

It was suggested that failure of a pressurised pipeline/vessel subjected to fire attack is related to its strength at elevated temperature. The variation of mechanical and thermal properties with temperature for steels used for pressurised systems was

discussed. It was found that there are insufficient data available to fully describe the temperature dependant property of steels used in the manufacture of pressure vessels and pipework used offshore. Such information is essential for the development of validated criteria used to define failure of vessels subjected to fire loading.

The report elaborated the methods for predicting the thermo-mechanical response of pressurised systems attacked by fire. The study stated that failure of a vessel/pipeline normally occurs when the combined stress in the vessel/pipewall exceeds its strength. However this may not be the mode of failure if the vessel/pipeline is also stressed by connections and constraints or if there is severe non-uniform heating.

Dealing with the design of pressure relieving and depressurising systems, the methods of sizing pressure relief systems and depressurising systems both with and without fires were presented.

Predictive methods and experimental data available for assessing the thermal response of pressure systems when subjected to external fire were examined. Although not leading to the development of a mathematical model, the report pointed out the absence of any validated models for the emergency depressurisation of vessels or pipelines under fire loading highlighting the need for such models.

2.3.4 Russo et al., (1995)

Russo et al., (1995) presented the solutions for stress distributions in hollow spheres and cylinders in which the temperature is a function of radius and time.

Nine types of thermal boundary conditions, as given by Osizik (1980), were considered for spheres and cylinders, including: insulated interior or exterior surfaces; convection on the inside or outside boundaries; sudden cooling or heating of surface, etc. The worse-case scenario of a thermal shock was also presented.

The equations of stress for a sphere and cylinder due to radial temperature variation given by Timoshenko and Goodier (1987) were used. These stress equations may be used if the radial temperature is varying with time.

Russo et al., (1995) claimed that the worse-case scenario for thermal stress is that of a thermal shock, which would occur when the convective heat transfer coefficient is very large, thus causing the surface temperature to change very rapidly. The thermal conduction resistance was termed to be negligible. The maximum shock stress was stated to occur at the surface at the instant of sudden temperature change and was given by

$$\sigma_g = \sigma_L = \frac{E\alpha\Delta T}{1-\mu} \quad (2.1)$$

Where,

σ_g	=	tangential stress
σ_r	=	radial stress
E	=	modulus of elasticity
α	=	coefficient of thermal expansion
ΔT	=	temperature
μ	=	Poisson's ratio

Solutions for stress distributions in hollow spheres and cylinders undergoing radial and temporal changes were presented. The study was aimed at typical applications including a pressure vessel or pipeline in a polar environment or other low temperature service that is subjected to sudden hot process flow. The authors stated that failure modes may be determined by the substitution of the derived thermal stresses along with the pressure-induced stresses, into the usual failure criteria.

The derived method for determining the stresses in vessels and pipelines was not implemented in the form of a model. The study considered hollow spheres and cylinders and ignored the effect of flow.

2.3.5 Other Models

In considering the failure hazard during blowdown due to stress effects, Overa et al., (1994) used a hoop stress model for predicting the vessel burst pressure. The same hoop stress model was adopted in the ENGULF models (Ramskill, 1988). The HEATUP (Beynon et al., 1988) and PLGS-1 models (Aydemir et al., 1988) do not simulate the stress distribution within the vessel wall and hence do not allow the evaluation of the risk and mode of failure. The TCTCM computer model (Birk, 1988) considers the wall temperature distribution, however little detail on the formulation of the wall triaxial pressure and thermal stresses is given and hence the co-ordinate stress component responsible for rupture is unknown.

The US department of transport (Birk, 1989) conducted severe torch tests from propane jets fires with effective heat transfer coefficients of approximately $180\text{Wm}^{-2}\text{K}^{-1}$ being reported. With fire temperatures of 1300K, heat fluxes of 230kWm^{-2} were stated to be possible.

Birk and Cunningham (1994a) demonstrated the above with tests on 400L tanks (0.6m diameter, 3 or 6mm wall thickness) where a torch fire was applied at the tank top. In some cases, the tanks failed catastrophically resulting in BLEVEs even though the average liquid temperature did not rise above the ambient temperature of 20°C.

The Health and Safety Limited Laboratory (Roberts and Becket, 1996) undertook four failure mode trials involving unprotected, two-tonne, vessels containing various fills of propane. In each trial, a vessel was charged with propane to the required level. The vessel, located in the remote site was engulfed with a flashing liquid propane jet fire until it failed. The mass of the contents and temperature and pressure were measured up to the point of vessel failure. It was found that the temperature of the tank walls increased to between 700 to 800°C at failure. All the tanks failed catastrophically after no more than 5 minutes of fire engulfment.

Although significant work has been done to account for thermal effects following fire attack on pressurised vessels, there is little or no work done to account for fire engulfment or jet fire impingement on pressurised pipelines.

2.4 Tank Fires

Another plausible scenario in terms of fire modelling is evaluating the risk of loss of mechanical integrity of neighbouring or adjacent structures from fire. This type of work has been considered for oil tanks, where the fire from a tank is modelled to evaluate the resulting radiation effects on the adjacent tanks. Such a scenario would involve modelling the characteristics of the fire such as flame shape, flame length, flame area, surface emissive power (See chapter 5) and resulting radiative flux from the fire.

Once the radiative flux is simulated the impact of the received heat flux on the adjacent structure can be assessed. The resulting stress load may in turn lead to a structural collapse or rupture.

The frequency of fires in volatile hydrocarbons containing fixed roof tanks has been estimated by Kletz (1971). The quantities of material involved in a tank fire, and consequently the losses have been discussed in Fire Protection Manual for Hydrocarbon Processing Plants (Vervalin, 1964a, 1974a). The work on tank fires has also been presented by Burgoyne (1950).

Baum and McGrattan, (1999) developed a model for simulation of oil tank fires at the National Institute of Standards and Technology, USA. A methodology for simulating the dynamics of large industrial fires in an outdoor environment was presented. The simulation technique developed by the authors and their collaborators were used to simulate fire scenarios involving a large oil storage tank adjacent to several neighbouring tanks.

2.5 Jet Flame Models

The immediate ignition of the pressurised released inventory from a puncture in the pipewall leads to a jet flame. This section deals with a review of relevant jet fire models reported in the open literature with particular emphasis on investigating their suitability in predicting flame size, shape and heat radiation characteristics.

This study deals with the development of an empirically based jet flame model. This is chosen due to its simplicity as compared to a more complicated CFD based jet flame model which would be beyond the scope of this work.

Kalghatgi (1983, 1984) and Chamberlain (1987) carried out the pioneering work on empirical jet fire modelling. The authors approximate the visible flame to a frustum of a cone, defined by various characteristic dimensions. Both model predictions have been validated extensively against experimental data for single-phase gaseous discharge. However, while Kalghatgi's (1983) model was validated against wind tunnel experiments, Chamberlain's (1987) was validated using both wind tunnel and large-scale field data. Both models along with Johnson et al., (1995) are presented in the following section.

Carter's (1991) study on predicting incident heat fluxes following the formation of a jet fire ensuing from a pressurised pipeline is also discussed.

2.5.1 Kalghatgi (1983, 1984)

For hydrocarbon flames issuing into a crosswind, Kalghatgi (1983) conducted an experimental study to investigate the flame shape. Three lengths and two angles defined the frustum describing the flame. The distance between the burner tip and the point of intersection between the frustum and burner axis; the lift-off distance, though initially ignored was later accounted for in a later work (Kalghatgi, 1984). Jet fire experiments were carried out at different crosswind speeds ranging between 2.7 - 8.1m/s, and at different burner exit velocities in the range 15 – 220m/s. Empirical formulas for each of the five jet flame parameters were obtained.

Kalghatgi (1983) considered the length, L_B to be the characteristic dimension of the flame. At the flame tip, the fuel gas concentration was assumed to have reached the stoichiometric mass fraction, C , with L_B determined from the rate of air entrainment required to bring about this. The entrainment rate was further mentioned to be dependent on the momentum flux ratio, M_f given by:

$$M_f = \frac{\rho_\infty u_\infty}{\rho_j u_j} \quad (2.2)$$

where,

- u_∞ = velocity of free stream fluid
- u_j = jet velocity at nozzle
- ρ_∞ = density in free stream fluid (air)
- ρ_j = jet density

The entrainment rate was also dependent on the burner source diameter, D_s given as

$$D_s = D \left(\frac{\rho_j}{\rho_\infty} \right)^{0.5} \quad (2.3)$$

where D is the actual burner diameter.

The author showed that the shape and size of the flame are independent of the stoichiometric mass fraction, C for the small range of C (0.063 – 0.055) considered. In the presence of crosswind, buoyancy is not important and the flame size is independent of the Richardson number (defines the ratio between buoyancy and momentum forces) which ranged from 1.5 to 11.6. The crosswind was observed to be the dominant factor in the entrainment of air into the fuel jet, which shortened the flame length considerably.

2.5.2 Chamberlain (1987)

Chamberlain (1987) presented a well-accepted and widely used model for the prediction of flame shape and radiation fields. The model was developed from several years of research at Shell Research, Thornton. It was extensively validated against wind tunnel experiments and field trials both on and offshore. Chamberlain (1987) represents the flame as a frustum of a cone radiating as a solid body with uniform Surface Emissive Power (SEP), figure 2.17. Different flame shape characteristics

were defined. Various correlations describing the variation of flame shape and surface emissive power under a wide range of ambient and flow conditions were developed.

Once the shape, orientation and surface emissive power are known, the radiation level at any point may be calculated without further approximation using the formula:

$$q = VF \times SEP \times \tau \quad (2.4)$$

where

q	=	radiation level
VF	=	view factor of the flame from the receiver surface
SEP	=	surface emissive power (defined later)
τ	=	Atmospheric transmissivity

The exact value of the view factor was calculated from the known orientation of the receiver and the shape and orientation of the frustum (Sparrow and Cess, 1966). The surface emissive power on the other hand was derived empirically. It was found to be dependent on the combustion heat intensity, which was in turn a function of gas composition, flame size and fraction of heat radiated from the surface. Chamberlain's (1987) model requires five basic parameters to define the frustum size. These include the flame length (frustum length) R_L , tilt angle, α the lift-off distance, b frustum base width, W_1 and frustum tip width W_2 .

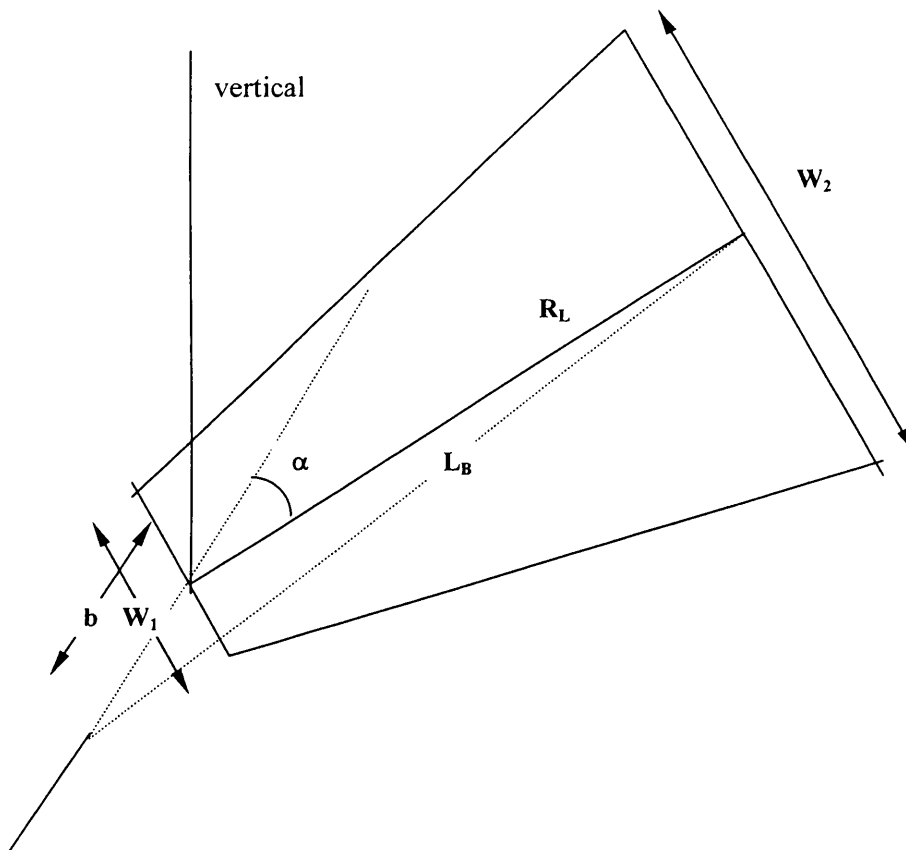


Figure 2.17 Diagram of the cone frustum parameters (Chamberlain, 1987).

Since Chamberlain's model has been extensively validated with experimental data and takes account of the important parameters for jet flame modelling, the correlations are used in the development of a jet flame model shown later in the thesis (chapter 5).

2.5.3 Johnson et al., (1995)

Johnson et al., (1995) developed a jet fire model, which in many ways was similar to that of Chamberlain (1987) including the representation of the flame by a frustum of a cone. However, a more detailed analysis was carried out to account for the effect of wind, vertical jet momentum fluxes, and the balance between them. In representing the total Surface Emissive Power (SEP), different values were predicted resulting from the side of the flame and for the ends of the flame. In comparing the radiation levels obtained from their model with experiments, the model developed was

considered to be accurate to within 15-20%. Johnson et al's., (1995) consideration was however only for horizontally released flames.

2.5.4 Carter (1991)

A model for the thermal radiation incident on a target from a jet flame on a gas pipeline was given by Carter (1991). The flame shape assumed is shown in figure 2.18. Its dimensions were established based on its state 30s after release. Carter (1991) states that the flame model itself was based on Chamberlain's (1987) model, but otherwise gave no further details.

Carter's (1991) model assumed that the shape of the jet flame is a cone of a known location, length, tilt and mass-burning rate. The emission of thermal radiation from discrete sections of the flame is represented by a number of simple point sources, each consuming fuel in proportion to the volume of the flame at that section; figure 2.18. Each point source contributes to the total radiation in accordance with the equation for thermal radiation received at a distance of x (m):

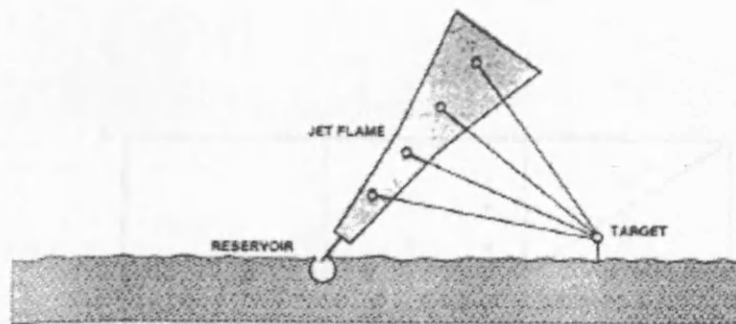


Figure 2.18 Multiple point source jet flame model (Carter, 1991).

The incidence heat received (kW/m^2) on the target is given by,

$$q = \frac{F_r (-\Delta H_c) m \tau}{4\pi x^2} \quad (2.5)$$

with

$$\tau = 1 - 0.0565 \ln x \quad (2.6)$$

Where F_r is the fraction of heat radiated. $-\Delta H_c$ is the heat of combustion (kJ/kg), m is the mass flow (kg/s), x is the distance from the source to the target (m) and τ is the atmospheric transmissivity.

The author presented a graphical representation of the radiation field around the flame, the received thermal radiation at any point, as well as the accumulated thermal radiation that would be received by a target as a function of distance from the flame. It is this latter value that is used in the risk assessment method.

The model was compared with published data for thermal radiation for gas flares with reasonably good agreement as shown in figure 2.19.

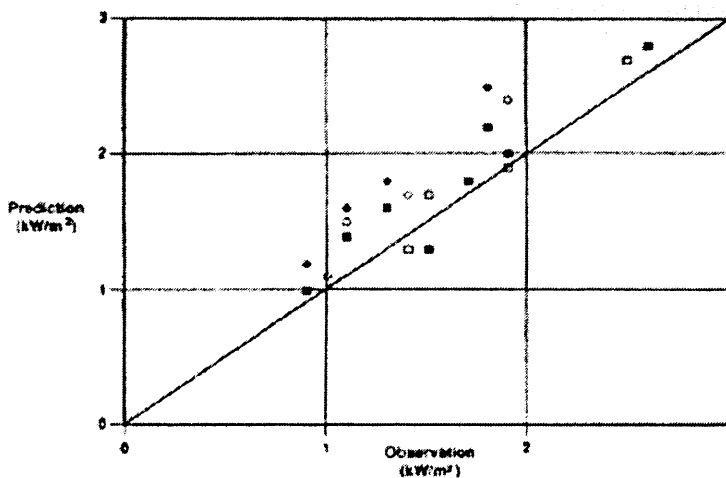
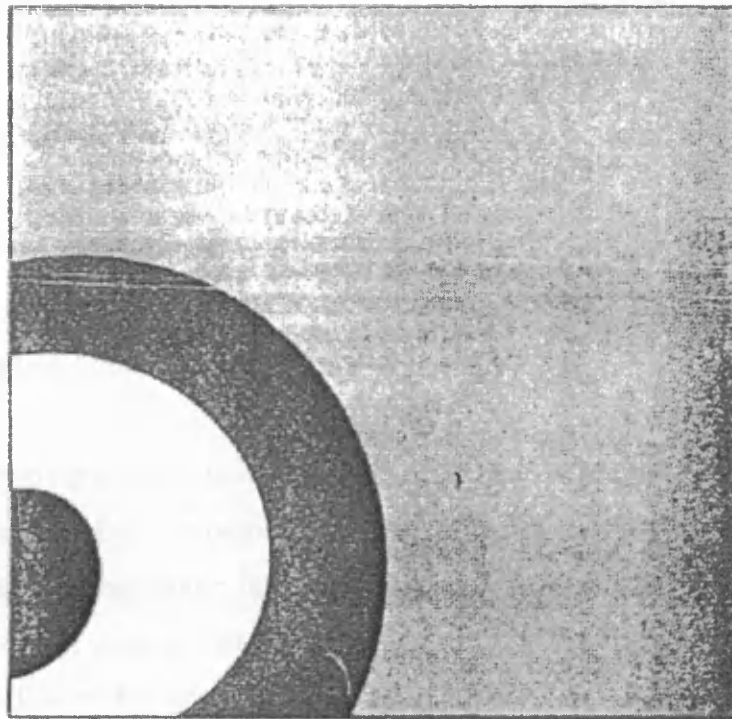


Figure 2.19 Comparison of Carter's flame model with published data (Carter, 1991).

Carter's (1991) model was applied to the predicated release rate from a puncture of the 9-inch, 100bar ethylene pipeline with wind speeds of 5 and 2m s⁻¹. The contours of incident heat are shown in figure 2.20.

The author used a rigorous approach to predict the thermal radiation on a target area, which involved the emission of thermal radiation from isolated sections of the flame represented by a number of simple point sources, each consuming fuel in percentage to the volume of the flame at that section. The model was useful for risk assessment as it obtained the radiation effect on a target travelling away from the source. The model however did not account for the temperature changes or the thermal effects on the pipeline itself under the influence of the flame.

In the present study, for simplification a single heat source flame is used for predicting the resulting temperature profile in the pipewall. Carter's (1991) approach of using a multiple point source model is considered too complicated as it would involve accounting for the transient variation of incident heat flux with distance along the length of the pipeline in addition to the effect of the drop in the line pressure as a result of loss of inventory.



100 Metres Sq.

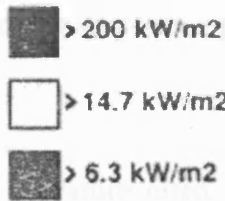


Figure 2.20 Application of Carter's model to predicted release rate: height of release above ground, 0m; mass discharge rate, 43.7kg/s; heat of combustion, $4.77E + 7J/kg$; fraction of heat radiated, 0.1284; total flame length, 39.04m; flame tilt from vertical, 11.5° (Carter, 1991).

2.6 Conclusion

This chapter reviewed past work done in three fields;

- Pipeline outflow modelling
- Thermal effects on process equipment under fire attack
- Jet flame modelling

A number of pipeline outflow models were reviewed. These were found to be limited to outflow under ambient conditions. To date no work accounting for thermal effects on pressurised pipelines under fire attack has been reported. Carter (1991) deals with jet flames resulting from the puncture of pressurised pipelines. However, apart from modelling the flame characterises, neither the transient variation of the flame overall dimensions as a result of the reduction in the line pressure nor the subsequent mechanical response of the pipewall under the influence of thermal loading are simulated.

Based on the literature cited, the pipeline outflow model developed by Oke et al., (2003) was found to be the most comprehensive having been validated against field data. In the present study, this model will be adopted as the basis for simulating the failure of pressurised pipelines under fire attack

Next the section reviewed work accounting for thermal effects following fire loading on process vessels and pipework. The chapter also discussed modelling work undertaken on storage tank fires highlighting the necessity to assess the risks involved from fires on adjacent structures. Once again, no parallel studies relating to pressurised pipelines have been reported.

A literature review relating to jet fire modelling was presented. The widely used Chamberlain (1987) flame model along with Kalghatgi (1983) and Johnson et al., (1995) received special attention due to their comprehensive nature. In the proceeding chapters, different aspects of these models will be adopted for predicting the jet flame characteristics of the ensuing fire from the punctured pipeline.

CHAPTER 3

PIPELINE OUTFLOW MODELLING

3.1 Introduction

The development of a robust mathematical model for simulating the thermal effects in pressurised pipelines under fire attack requires the formulation of an appropriate fluid outflow model.

The above entails the following:

- i) Formulation of the conservation equations for simulating unsteady state flow in the pipe and the prevailing assumptions
- ii) Solution of the resulting hyperbolic equations using a suitable numerical technique
- iii) Utilization of a suitable equation of state for predicting the appropriate vapor/liquid equilibrium data
- iv) Modelling of the accompanying fluid/wall/ambient heat transfer effects and the fluid/wall frictional pressure losses
- v) Validation against experimental data

This chapter entirely deals with steps (i) – (v) above. The modelling of the accompanying thermal and pressure stresses in the pipewall, which ultimately govern the mechanical integrity of the pipeline during fire attack is given in the next chapter.

3.2 Outflow Model Assumptions

The following assumptions are made in the development of the outflow model:

- Flow within the pipeline is assumed to be one-dimensional (rate of change of fluid properties normal to the streamline are negligible compared to the rate of change along the stream line)
- For two-phase flow situations a homogeneous equilibrium model (HEM) is adopted. This assumes that the two phases travel at the same velocity and are in thermodynamic equilibrium with one another. Previous studies (see for example Chen et al., 1995; Mahgerefteh et al., 1999) have validated this assumption through comparison of model data against real measurements
- The pipeline is assumed to be inelastic and rigidly anchored; hence vibrations and other associated fluid-structure interaction effects are ignored

3.3 Equations for Outflow Modelling

The conservation equations are the elemental components for formulating the flow process. These equations are sometimes called the equations of change, in as much as they describe the change of velocity and temperature with respect to time and position in the system (Rohsenow et al., 1998). The conservation equations are derived for a control volume. They are derived from the mathematical expressions of mass, momentum and energy conservation laws.

As demonstrated by Oke (2003) the conservation equations employed in the outflow model are:

$$[\rho T + \varphi] \left(\frac{\partial P}{\partial t} + u \frac{\partial P}{\partial x} \right) - \rho \varphi \left(\frac{\partial h}{\partial t} + u \frac{\partial h}{\partial x} \right) + \rho^2 a^2 T \frac{\partial u}{\partial x} = 0 \quad (3.1)$$

$$\rho \frac{\partial u}{\partial t} + \rho u \frac{\partial u}{\partial x} = - \frac{\partial P}{\partial x} - \rho g \sin \theta + \beta_x \quad (3.2)$$

$$\rho \frac{dh}{dt} - \frac{\partial P}{\partial t} - u \frac{\partial P}{\partial x} = q_h - u \beta_x \quad (3.3)$$

where, $\beta_x = -\frac{2f_w \rho \cdot u \cdot |u|}{D}$ and by definition:

$$\left(\frac{\partial P}{\partial \rho} \right)_s = a^2 \quad a = \text{speed of sound}$$

$$\left(\frac{\partial P}{\partial s} \right)_\rho = \varphi$$

At any time t , P, ρ, H, h, u, s and T represent the absolute pressure, density, total and specific enthalpies, velocity, entropy and temperature of the fluid respectively. D is the diameter and f_w the fanning friction factor. The modulus of the velocity, $|u|$ is introduced so that the friction force will change sign with change in flow direction and q_h is the heat transferred to the fluid element per unit volume.

Equation (3.1) is the form of the mass conservation equation employed, in which the total derivative of density with time has been expressed in terms of fluid pressure and enthalpy.

Equation (3.2) on the other hand is the form of the momentum equation employed in this study. The equation is derived from the application of Newton's second law of motion for a stationary volume element. The fanning friction factor determination is shown later.

Equation (3.3) is the energy conservation equation expressed in terms of fluid enthalpy. The energy conservation equation is derived from the application of the first law of thermodynamics, which states that the change in the total energy of a system is due to the heat transmitted and the work done on the system.

3.4 Quasilinear Partial Differential Equations

A partial differential equation is said to be quasilinear if all the derivatives of the dependent function $f(x, t)$ are linear, while their corresponding coefficients contain at least a term that is either a linear or non-linear function of, f (Prasad and Ravindran, 1985). This is illustrated by equation (3.4) below:

$$a(x, t, f)f_t + b(x, t, f)f_x = c(x, t, f) \quad (3.4)$$

where f_t, f_x are the partial derivatives of the function f in terms of t and x respectively. Equation (3.4) is quasilinear because its derivative terms (f_t, f_x) are linear while at least one of their corresponding coefficients [$a(x, t, f), b(x, t, f)$] contain terms that are functions of f . The partial derivatives in the system of conservation equations can be written as:

$$[\rho T + \varphi](P_t + uP_x) - \rho\varphi(h_t + uh_x) + \rho^2 a^2 T(u_x) = 0 \quad (\text{Continuity}) \quad (3.5)$$

$$\rho(u_t + uu_x) + (P_x) = \alpha \quad (\text{Momentum}) \quad (3.6)$$

$$\rho(h_t + uh_x) - (P_t + uP_x) = \psi \quad (\text{Energy}) \quad (3.7)$$

Where:

$$\alpha = -\rho g \sin \theta + \beta_{wx} \quad (3.8)$$

$$\psi = q_h - u\beta_{wx} \quad (3.9)$$

$\beta_{wx} = \beta_x$ (this re-annotation serves to avoid confusing β_x (a non-derivative term) with other derivative terms such as P_x).

From the definition given above for the quasilinear equations, the system of conservation equations represented by equations (3.5-3.7) can be seen to be quasilinear. This is because all the partial derivative terms are linear. Furthermore, terms that are coefficients of the partial derivatives, such as density [$\rho(P, h)$] or flow velocity (u) are functions of some of the dependent functions ($P, h, \text{ and } u$). These

attributes render the system of equations quasilinear.

In general, the system of equations (i.e., equations (3.5-3.7)) presented above can be broadly expressed as:

$$Am_t + Bm_x = C \quad (3.10)$$

In matrix form, A , m_t , B and m_x in equation (3.10) are given by:

$$A = \begin{bmatrix} \rho T + \varphi & -\rho\varphi & 0 \\ 0 & 0 & \rho \\ -1 & \rho & 0 \end{bmatrix} \quad m_t = \begin{bmatrix} P_t \\ h_t \\ u_t \end{bmatrix}; \quad B = \begin{bmatrix} (\rho T + \varphi)u & -\rho\varphi u & \rho^2 a^2 T \\ 1 & 0 & \rho u \\ -u & \rho u & 0 \end{bmatrix} \quad m_x = \begin{bmatrix} P_x \\ h_x \\ u_x \end{bmatrix}$$

$$C = \begin{bmatrix} 0 \\ \alpha \\ \psi \end{bmatrix} \quad (3.11)$$

3.4.1 Hyperbolic Quasilinear Partial Differential Equations

A quasilinear system of partial differential equations as given by equation (3.10) is said to be hyperbolic if the eigenvalue (λ), satisfying equation (3.12) given below, has real and distinct roots (i.e., $\lambda_1, \lambda_2, \lambda_3$ are real and distinct) (Prasad and Ravindran, 1985):

$$|B - \lambda A| = 0 \quad (3.12)$$

Thus, for the conservation equations with partial derivatives in terms of pressure, enthalpy and velocity, equation (3.12) can be expressed as:

$$|B - \lambda A| = \begin{vmatrix} u - \lambda & -u\psi + \lambda u & \rho a^2 \\ 1 & 0 & \rho u - \lambda \rho \\ 0 & \rho T u - \lambda \rho T & 0 \end{vmatrix} \quad (3.13)$$

Solving equation (3.12) to obtain the roots of λ gives:

$$\lambda_1 = u \quad (3.14)$$

$$\lambda_2 = u - a \quad (3.15)$$

$$\lambda_3 = u + a \quad (3.16)$$

From equations (3.14 – 3.16), it can be seen that the roots of the Eigen value (λ) that satisfy equation (3.12) are real and distinct. Thus, the systems of quasilinear partial differential equations for mass, momentum and energy conservation are hyperbolic, as they possess three real and distinct eigen values. This implies that the behaviour and properties of the physical system described by these equations will be dominated by wave-like phenomena (Prasad and Ravindran, 1985).

3.4.2 Solution of Hyperbolic System of Equations

There are two numerical techniques for the solution of partial differential equations: explicit and implicit methods. The explicit method is the one that yields an explicit expression for each value at time t_{n+1} in terms of nearby values at time t_n . An implicit method couples together values at different grid points and time t_{n+1} and hence an algebraic system of equations must be solved in each time step in order to advance the solution.

Explicit finite difference methods integrate the basic partial difference equations by considering the changes in the dependant variables (P , u and ρ in our case) along directions of the independent variables (x and t).

A problem is said to be stiff if there are a variety of different time scales in the solution. The conservation equations along with the equation of state are essentially Euler equations with stiff source terms due to the friction terms in the momentum equation and heat transfer equation in the energy equation.

The system of conservation equations (3.5-3.7) cannot be solved analytically as they

contain terms that are unknown or complex functions of their dependent and independent variables (see Flatt, 1986; Mahgerefteh et al., 1999).

In this work, the Method of Characteristics (MOC) is employed as the numerical technique for the resolution of the governing conservation equations. This is because the method gives simpler, more precise and more accurate numerical representation and solution of wave like transient characteristics of the governing system of conservation equations when compared with other solution methods.

MOC is the natural method for quasi-linear hyperbolic systems with two independent variables. It is an explicit finite difference scheme with a sufficiently different approach to warrant separate treatment.

3.5 Method of Characteristics (MOC)

The Method of Characteristics is a general mathematical technique that is particularly suited to the solution of systems of quasi-linear hyperbolic partial differential equations with two independent variables. The method resolves partial differential equations into ordinary differential equations, which are then solved using an explicit finite-difference technique. The method is particularly suitable for systems containing complex boundary conditions, as each node point and boundary condition is analysed individually at each time step.

There are two main grid discretisation methods for the MOC. These are the Characteristic Grid method (CG) which is also known as the natural method of characteristics (Wylie and Streeter, 1993) or the Wave Tracing method (Chen et al., 1993), and the Inverse Marching method, which is also known as the Rectangular Grid method (Wylie and Streeter, 1993) or the Method of Specified Time Intervals (ST) (Flatt, 1986).

In the characteristic grid method, the position of the new solution point is not specified a priori, but is determined from the intersection of left and right running characteristics with origins located at known solution points or initial data. Hence a free-floating grid is developed in the $x-t$ plane as shown in figure 3.1. This method is

particularly accurate since the solution progresses naturally along the characteristic lines. However, where three characteristic lines are employed, such as when an energy equation is solved in addition to the mass and momentum conservation equations, the location of the intersection of the path line (C_0) characteristic between previously known solution points requires some interpolation (Chen et al., 1993).

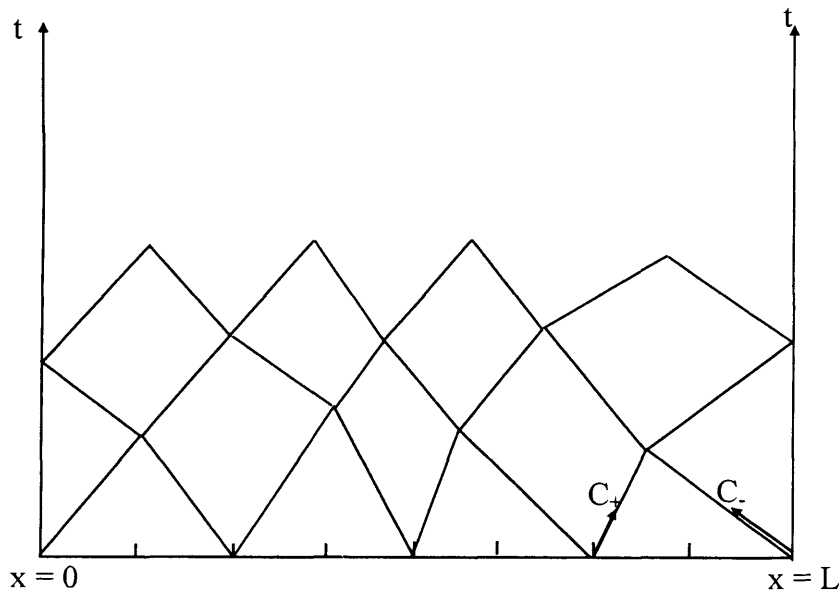


Figure 3.1: The Characteristic Grid.

In the method of specified time intervals (see figure 3.2), the location of the solution points in the space-time grid is specified a priori and the characteristic lines are extended backwards in time to intersect a time line on which initial data points are known from a previous solution. This necessitates interpolation to locate the intersection of all three characteristic lines on the previous time line and as a result can lead to a greater loss of accuracy than the CG method.

The CG method is found to be more accurate than the ST method but due to the drawback of no direct control on the time input variables, makes the method quite burdensome in modelling systems. For this purpose the ST method of discretisation is used throughout this work.

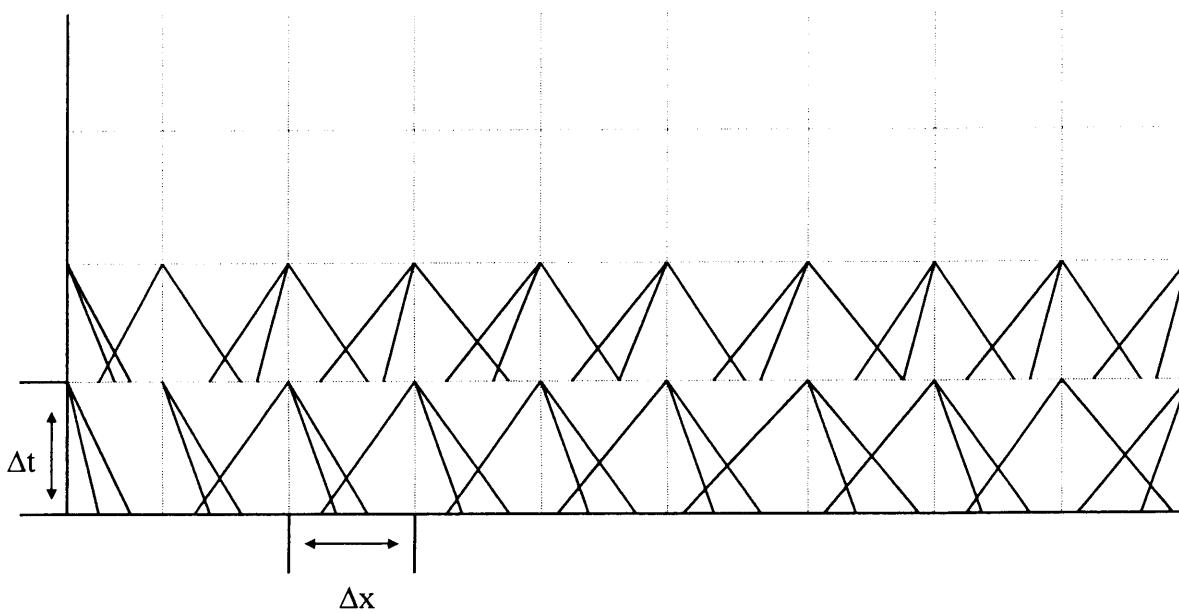


Figure 3.2: The Method of Specified Time Intervals.

3.5.1 Mathematical Formulation of MOC

The MOC involves the definition of an appropriate set of coordinates (characteristic lines), in terms of the system's independent variables (e.g., distance and time), along which the system of partial differential equations is resolved. These characteristic lines are defined such that for each one, the system of partial differential equation is converted into an ordinary differential equation (compatibility equation) which is only valid along that coordinate (characteristic line). The MOC is based on the principle of propagation of characteristic waves along characteristic lines and is therefore well suited to handling fast transient flows as each disturbance is captured along the propagating characteristic (Mach) lines.

To adequately resolve a system of partial differential equations in terms of three dependent variables (e.g., P , h and u), three characteristic lines (i.e., the path line (C_0) plus the positive (C_+) and negative (C_-) mach lines) need to be defined. These in essence govern the speed at which expansion and compression waves propagate from the low and high-pressure ends of the pipeline respectively (positive and negative Mach lines), while the path line dictates the rate of flow through any given point along the pipeline.

MOC solution involves the conversion of the basic partial differential equations of flow into ordinary differential equations (compatibility equations). The most common method of converting the PDEs to ODEs is the matrix transformation method (see Tiley, 1989) and that of multiplying the basic equations by an unknown parameter and subsequent summation.

Following Oke (2004), and introducing $1/\lambda$ to represent the slope of the characteristic lines, the conservation equations may be replaced by 3 compatibility equations, which are valid along 3 characteristic equations given below:

$$\rho d_0 h - d_0 P = \psi d_0 t \quad \text{along} \quad \frac{d_0 t}{d_0 x} = \frac{1}{u} = \frac{1}{\lambda_0} \quad (3.17)$$

(Path line compatibility equation along the Path line characteristic)

$$d_+ P + [\rho a] d_+ u = \left[\frac{\phi \psi}{\rho T} + a \alpha \right] d_+ t \quad \text{along} \quad \frac{d_+ t}{d_+ x} = \frac{1}{u+a} = \frac{1}{\lambda_+} \quad (3.18)$$

(Positive Mach line compatibility equation along the Positive Mach line characteristic)

$$d_- P + [\rho a] d_- u = \left[\frac{\phi \psi}{\rho T} - a \alpha \right] d_- t \quad \text{along} \quad \frac{d_- t}{d_- x} = \frac{1}{u-a} = \frac{1}{\lambda_-} \quad (3.19)$$

(Negative Mach line compatibility equation along the Negative Mach line characteristic)

The compatibility equations may be solved by standard, single step finite-difference methods for ordinary differential equations. Figure 3.3 is a schematic representation of the characteristic lines at a grid point along the space (x) and time (t) independent coordinates.

criterion ensures the stability of the numerical scheme employed and the solution obtained for the entire system under consideration. It is given by:

$$\Delta t \leq \frac{\Delta x}{(|u + a|_{\max})} \quad (3.20)$$

As flow properties (u and a) may vary in each time step, it is important to maintain the numerical stability of solutions obtained in subsequent time steps.

3.5.2 Finite Difference Solution of the Compatibility and Characteristic Equations

A finite difference method is used to numerically solve the compatibility and characteristic equations (3.17-3.19), which are total differentials, using the Euler predictor-corrector algorithm. The method comprises of a predictor step (first order approximation), which is used to estimate the approximate value of the flow properties at the solution point. On the other hand, the corrector step, based on second order approximation improves on the initial approximation of the predictor step.

Following Atti (2006) the procedure is briefly reviewed below.

The finite difference form of the equations (3.17-3.19) given above can be shown as:

$$(\rho)_0 (h_j - h_0) - (P_j - P_0) = \psi_0 (t_j - t_0) \quad (3.21)$$

$$(P_j - P_p) + (\rho a)_p (u_j - u_p) = \left(\frac{\varphi \psi}{\rho T} + a\alpha \right)_p (t_j - t_p) \quad (3.22)$$

$$(P_j - P_n) - (\rho a)_n (u_j - u_n) = \left(\frac{\varphi \psi}{\rho T} - a\alpha \right)_n (t_j - t_n) \quad (3.23)$$

The subscripts in equations (3.21-3.23) assigned to the various properties denote the location in space and time, as shown in figure 3.3.

To calculate the flow properties (P , h , u , ρ , etc) at the solution point j , it is necessary

that the positions (x_p , x_o and x_n) and fluid properties at the intersection of the characteristic lines at the previous time level (t_l) be determined. This can be determined from the knowledge of the slope of the characteristics lines and by linear interpolation between points $i-1$, i and $i+1$ whose conditions are known at time t_l .

Using linear interpolation formulas, expressions for the velocity (u) and speed of sound (a) can be obtained at points p , o , and n . These expressions can then be substituted back into the characteristic equations. The locations of x_p , x_n and x_o can be obtained by substituting the calculated values for u_p , a_p , u_n , a_n and u_o into their corresponding equations.

Similarly the values of P and h at the initial points p , o , and n are calculated from relevant linear interpolation formulas. Hence, at this stage all the initial point flow variables can be evaluated to compute the flow conditions at the solution point (j) in the predictor step.

Thus by linear interpolation, relevant substitution and manipulating of the equations, pressure at the solution point P_j , can be given as gives:

$$P_j = K_1 - (\rho a)_p (u_j - u_p) + P_p \quad (3.24)$$

$$P_j = K_2 + (\rho a)_n (u_j - u_n) + P_n \quad (3.25)$$

Where K_1 and K_2 are given by:

$$K_1 = \left(\frac{\phi \psi}{\rho T} + a\alpha \right)_p \Delta t \quad (3.26)$$

$$K_2 = \left(\frac{\phi \psi}{\rho T} - a\alpha \right)_n \Delta t \quad (3.27)$$

Solving the equations (3.24) and (3.25) simultaneously for u_j gives:

$$u_j = \frac{K_1 - K_2 + (\rho a)_p u_p + (\rho a)_n u_n + P_p + P_n}{(\rho a)_n + (\rho a)_p} \quad (3.28)$$

Hence, the pressure at the solution point, P_j can be calculated by the direct substitution of u_j into either equation (3.24) or (3.25).

The enthalpy at the solution point can subsequently be obtained from the path line compatibility (i.e., equation (3.21)) as:

$$h_j = \frac{\psi_0 \Delta t + (P_j - P_0) + \rho_0 h_0}{\rho_0} \quad (3.29)$$

Once the pressure and enthalpy are determined, other thermodynamic properties at the solution point (e.g. ρ , φ , and T) are obtained from a pressure-enthalpy flash calculation at a defined time step, Δt (time step is chosen according to the CFL criteria described earlier).

The procedure in which the tentative values are obtained at the solution point “ j ” constitutes the predictor step.

To improve on the first order solution, a second order approximation to the compatibility and characteristic is required.

As with the predictor step, the positions x_p , x_o and x_n , and fluid properties at these corresponding locations need to be determined. This is achieved by expressing the characteristic equations in second order form and interpolating between points $i-1$, i and $i+1$.

The second order finite difference form of the compatibility equations (equations 3.17-3.19) can be expressed as:

Path line compatibility;

$$\frac{1}{2} [(\rho)_0 + (\rho)_j] (h_j - h_0) - (P_j - P_0) = \frac{1}{2} [\psi_0 + \psi_j] (t_j - t_0) \quad (3.30)$$

Positive Mach line compatibility;

$$(P_j - P_p) + \frac{1}{2} [(\rho a)_p + (\rho a)_j] (u_j - u_p) = \frac{1}{2} \left[\left(\frac{\phi \psi}{\rho T} + a\alpha \right)_p + \left(\frac{\phi \psi}{\rho T} + a\alpha \right)_j \right] (t_j - t_p) \quad (3.31)$$

Negative Mach line compatibility;

$$(P_j - P_n) - \frac{1}{2} [(\rho a)_n + (\rho a)_j] (u_j - u_n) = \frac{1}{2} \left[\left(\frac{\phi \psi}{\rho T} - a\alpha \right)_n + \left(\frac{\phi \psi}{\rho T} - a\alpha \right)_j \right] (t_j - t_n) \quad (3.32)$$

Following the same approach employed for the predictor step the dependent flow variables at the solution point can now be calculated at the next iteration ($r+1$) step.

The subscript j together with superscript r refer to the solution condition at the previous iteration step, r .

Manipulating equations (3.31) and (3.32) respectively to solve for P_j gives:

$$P_j^{r+1} = K_1 - \frac{1}{2} [(\rho a)_p + (\rho a)_j^r] (u_j^{r+1} - u_p) + P_p \quad (3.33)$$

$$P_j^{r+1} = K_2 + \frac{1}{2} [(\rho a)_n + (\rho a)_j^r] (u_j^{r+1} - u_n) + P_n \quad (3.34)$$

Where K_1 and K_2 are given by:

$$K_1 = \frac{1}{2} \left[\left(\frac{\phi \psi}{\rho T} + a\alpha \right)_p + \left(\frac{\phi \psi}{\rho T} + a\alpha \right)_j^r \right] \Delta t \quad (3.35)$$

$$K_2 = \frac{1}{2} \left[\left(\frac{\phi \psi}{\rho T} - a\alpha \right)_n + \left(\frac{\phi \psi}{\rho T} - a\alpha \right)_j^r \right] \Delta t \quad (3.36)$$

Solving the equations (3.33) and (3.34) simultaneously for yields P_j^{r+1} and u_j^{r+1}

$$u_j^{r+1} = \frac{K_1 - K_2 + \frac{1}{2}[(\rho a)_p + (\rho a)_j^r]u_p + \frac{1}{2}[(\rho a)_n + (\rho a)_j^r]u_n + P_p - P_n}{\frac{1}{2}[(\rho a)_p + (\rho a)_j^r] + \frac{1}{2}[(\rho a)_n + (\rho a)_j^r]} \quad (3.37)$$

P_j^{r+1} is then obtained from equation (3.33), and the enthalpy at the solution point is obtained from the path line compatibility (i.e., equation (3.30)) as:

$$h_j^{r+1} = \frac{[\psi_0 + \psi_j^r]\Delta t + 2(P_j^{r+1} - P_0)}{\rho_o + \rho_j^r} + h_o \quad (3.38)$$

The above second order calculation procedure is repeated until a certain tolerance (*ca.* 10^{-5}) is satisfied for the three dependent variables, i.e. P , h and u .

All the initial point flow variables are now available to compute the flow conditions at the solution point j by employing the predictor-corrector algorithm.

The procedure for calculating the flow variables is only applicable when the 3 characteristic equations are active, i.e. within the interior of the pipeline only. At the closed end of the pipeline (where only 2 characteristics are active), and at the rupture plane, special treatment and the imposition of suitable boundary conditions are required.

The section below deals with modelling the fluid dynamics at the closed end or upstream section, and the rupture plane (downstream) of the pipeline.

3.6 The Intact Point Calculation

In modelling the intact end flow properties, the C_+ is non-existent, and the slope of the path line characteristic (C_o) is infinity since the velocity at all times (u_j) is zero. Figure 3.4 shows the grid scheme for the intact end point.

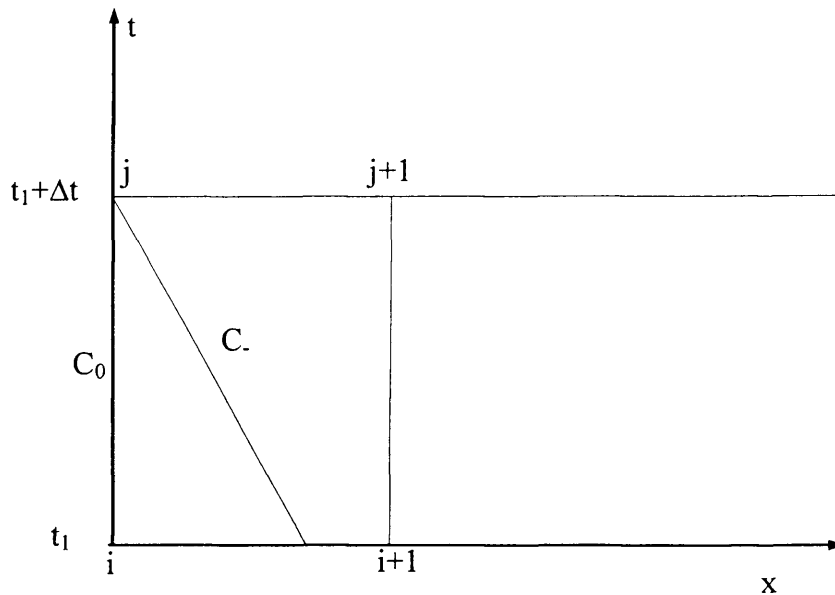


Figure 3.4: Grid scheme showing the active characteristic lines (C_0 and C_-) at the closed end point.

As can be seen from the figure 3.4 above, only the path line and negative characteristics are active.

The corrector step as described earlier is then subsequently employed to yield the flow variables at the intact end.

For scenarios where a pump or reservoir is present upstream, specifying the characteristics of the upstream source, for example pressure or flow rate, allows for the closure of the characteristic equations.

3.7 Rupture Plane Calculation

There are two time domains for discharge at the failure/release plane. The first is the choked/critical flow time domain. Its duration depends on how quickly the pressure at the failure plane drops down to the external pressure. Under this flow regime, the fluid expands and discharges at a critical pressure, which is higher than the ambient pressure, and at which the release rate is maximum. The release velocity corresponds to the sonic velocity at the prevailing release pressure, and conditions downstream of the release plane have no influence on the discharge process. Thus, during critical flow, no disturbance downstream of the release plane can propagate upstream. However, once the external pressure is reached at the release plane, the second time domain is initiated, and in this period the outflow is subsonic.

For both full-bore rupture and puncture at pipe end, the fluid approaching the rupture plane (i.e., the solution point fluid with properties P_j , h_j , s_j , ρ_j , u_j) is assumed to undergo an isentropic expansion on exposure to ambient conditions.

In modelling the rupture plane conditions only the C_+ and C_0 characteristics are applicable. However, the absence of a simple algebraic relationship expressing the expansion process across the release plane as a function of one or more of the flow variables renders the simultaneous solution of the positive and path line compatibility equations impossible. This necessitates the introduction of a “ghost” cell adjacent to the boundary cell as depicted in figure 3.5 within which expressions for the negative compatibility can be formulated. The ghost cell is a form of fictitious node with the node $(i+1)$ lying on node (i) as illustrated in figure 3.5 below.

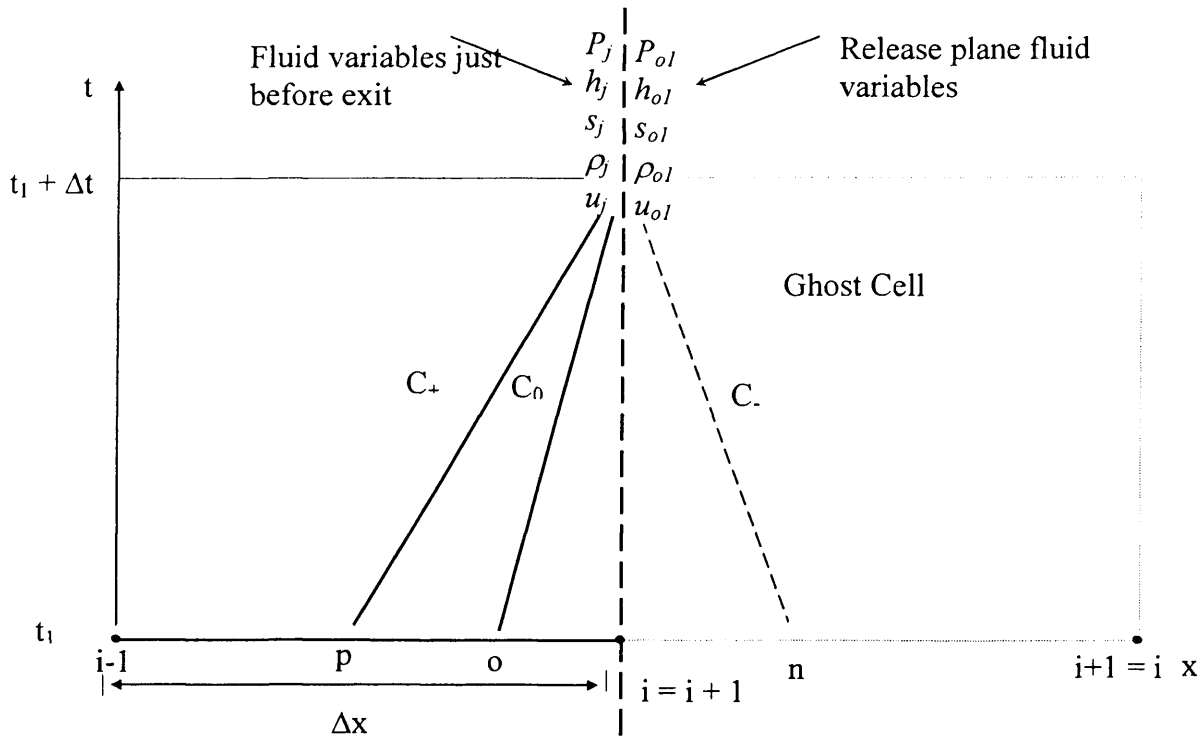


Figure 3.5: Diagram illustrating characteristic lines at the rupture plane based on the concept of a ghost cell.

With the introduction of the negative characteristics, the flow properties at point j can be obtained just as it is done for the interior point calculation shown earlier in figure 3.3. It should be noted that interpolation is not required within the ghost cell as all the properties within it are space invariant.

The flow variables at the release plane (P_{o1}, h_{o1}, u_{o1}) are calculated using a discharge rate algorithm described later.

For discharge across the release plane, there is no accumulation of mass; thus the mass flow rate across the release plane is conserved. Furthermore, although the expansion process across the release plane is assumed to be isentropic, resistance posed by the release plane to the exiting fluid (as is the case with a puncture at the end of a pipeline) introduces irreversibility and hence non-isentropic conditions.

Accordingly, the actual flow rate of the exiting fluid at the release plane is smaller than the isentropic flow rate and the ratio between both flow rates is given by the

discharge coefficient, C_d . Thus, the relationship between the mass flow rate approaching and that leaving the release plane can be expressed as:

$$u_j \times \rho_j \times A_{pipe} = C_d \times \rho_{o1} \times u_{o1} \times A_{o1} \quad (3.39)$$

Where ρ_{o1} , u_{o1} , A_{o1} and A_{pipe} are the fluid density, fluid velocity, orifice area, and pipe area respectively.

The values of ρ_{o1} and u_{o1} (and all other fluid properties at the release plane) are obtained from the discharge rate calculation algorithm described below.

3.8 Discharge Rate Calculation

Figure 3.6 is a schematic representation of the pertinent pressures at the release plane governing the discharge process. P_d is the downstream or ambient pressure. For critical/choked release, the discharge pressure, P_{o1} is higher than the downstream pressure P_d . Under such condition, the discharge rate through the release plane is maximum, and no disturbance can be propagated upstream of the failure plane.

However, under non-critical or no choking conditions, the fluid discharge pressure, P_{o1} is equal to the downstream pressure, P_d and the release rate is calculated accordingly.

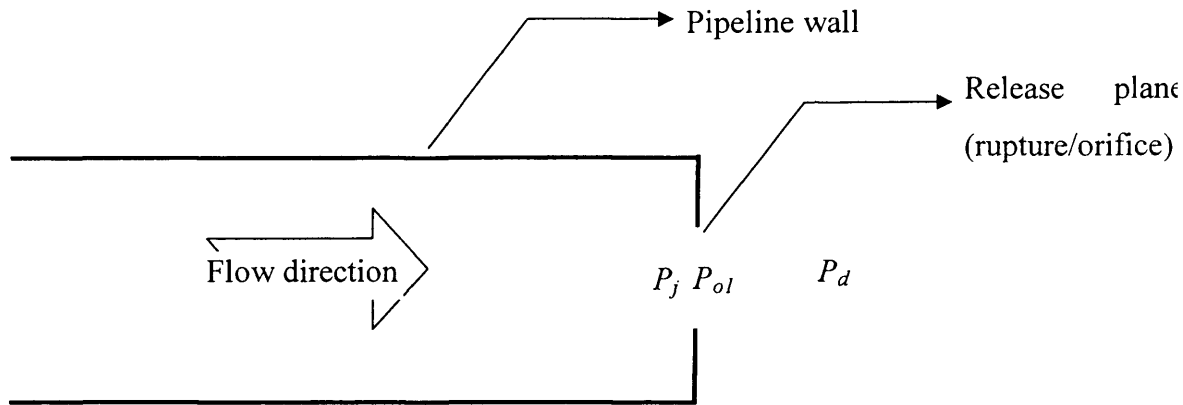


Figure 3.6: Schematic representation of pertinent pressures at the failure plane governing the discharge rate.

The calculations of the choked and non-choked velocities and hence the subsequent discharge rate requires the application of an energy balance across the release plane. The expansion process and hence the energy balance written across the release plane is based on isentropic flow assumption. Furthermore, for two-phase release, both phases are assumed to be in thermodynamic equilibrium, and travel at the same velocity.

Thus, at any time (t_j), and ignoring changes in potential energies between the flow approaching and the flow exiting the release plane, the corresponding energy balance across the release plane is given by:

$$H_j = h_{o1} + \frac{1}{2}u_{o1}^2 \quad (3.40)$$

Where:

$$H_j = h_j + \frac{1}{2}u_j^2 \quad (3.41)$$

In the case of choked/critical flow, equation (3.40) is solved iteratively using the Brent iteration method (Press et al., 1992), and the velocity, u_{o1} replaced by the local single/two-phase speed of sound, a_{o1} . The iterative solution of equation (3.40) involves guessing and updating guessed discharge pressures (P_{o1}) in conjunction with pressure-entropy (isentropic) flash calculations until equation (3.40) is satisfied. Once a solution is obtained, other flow variables at the release plane (ρ_{o1} , T_{o1} , h_{o1}) are determined from a corresponding pressure-entropy (P_{o1} - S_j) flash calculation.

On the other hand, for non-critical flow, the release pressure (P_{o1}) is equal to the ambient pressure (P_d). Thus, from a pressure-entropy (P_{o1} - S_j) flash calculation, the release enthalpy (h_{o1}) is determined and substituted in equation (3.40) to obtain the release velocity (u_{o1}). Unlike critical discharge, no iteration is required in determining flow conditions at the release plane.

Following the solution of equation (3.40), u_j is updated using equation (3.39) and employed in the corrector steps.

3.9 Cubic Equation of State (CEoS)

An equation of state is a constitutive equation describing the state of matter under a given set of physical conditions. The Peng-Robinson equation of state (PR-EoS) has been shown by Walas (1987) to be applicable to high-pressure hydrocarbon mixtures; hence it is used to calculate vapour-liquids thermodynamic data in this study.

The Peng-Robinson equation of state is given by (Walas, 1987):

$$P = \frac{RT}{V - b_v} - \frac{a_v \alpha}{V^2 + 2b_v V - (b_v)^2} \quad (3.42)$$

Where:

$$a_v = \frac{k_1 R^2 T_c^2}{P_c^2} \quad (3.43)$$

$$b_V = \frac{k_2 RT_c}{P_c} \quad (3.44)$$

For mixtures,

$$a_V \alpha = \sum \sum y_i y_j (a_V \alpha)_{ij} \quad (3.45)$$

$$(a_V \alpha)_{ij} = (1 - K_{ij}) \sqrt{(a_V \alpha)_i (a_V \alpha)_j} \quad (3.46)$$

$$b_{V,i} = \sum y_i b_{V,i} \quad (3.47)$$

Where,

- P, P_c = absolute and critical pressures of the fluid respectively (kN/m²)
- T, T_c = absolute and critical temperatures of the fluid respectively (K)
- V = fluid's molar volume (m³/kmol)
- R = universal gas constant (kJ/(kmol-K))
- k_1, k_2 = constants specific to the equations of state
- α = alpha function
- K_{ij} = binary interaction parameter
- y_i, y_j = component mole fractions

3.10 Hydrodynamic and Thermodynamic relations

In case of the homogeneous equilibrium model assumption equation (3.48) below gives the pseudo-mixture density, (ρ), based on pure liquid and gas densities. It is calculated using the EoS:

$$\rho = \frac{\rho_g \rho_l}{\rho_g (1 - \chi) + \rho_l \chi} \quad (3.48)$$

where the subscripts, g and l denote gas and liquid phase respectively. The term, χ refers to the fluid quality, and is the mass of vapour per unit mass of bulk fluid. The values of the respective phase densities can be calculated according to the following

equations:

$$\rho_g = \frac{PM_g}{Z_g RT} \quad (3.49)$$

$$\rho_l = \frac{PM_l}{Z_l RT} \quad (3.50)$$

Where Z is the fluid compressibility and M is the molecular weight.

For single-phase real fluids, the speed of sound through the fluid can be expressed analytically as (Picard and Bishnoi, 1987):

$$a^2 = \frac{\gamma}{k\rho} \quad (3.51)$$

Where, γ is the ratio of specific heats, and k is the isothermal coefficient of volumetric expansion.

For two-phase flows, the analytical determination of γ and c_p becomes complex (Mahgerefteh et al., 1999). Hence the speed of sound is evaluated numerically at a given temperature and pressure as (Mahgerefteh et al., 1999):

$$a^2 = \left(\frac{\Delta P}{\rho(T, P) - \rho(T^*, P - \Delta P)} \right)_s \quad (3.52)$$

Where the subscript, s denotes a constant entropy condition and T , P , ΔP and ρ , denote temperature, pressure, infinitesimal change in pressure ($\Delta P = 1 \times 10^{-6}$ bar) and density of the fluid respectively. T^* represents the corresponding fluid temperature obtained by performing a $(P - \Delta P)/s$ flash.

For single-phase fluids, the isochoric thermodynamic function φ is given (Picard and Bishnoi, 1988) as:

$$\varphi = \left(\frac{\partial P}{\partial s} \right)_\rho = \frac{\rho \cdot \xi \cdot T \cdot a^2}{C_p} \quad (3.53)$$

Where, ξ is the isobaric coefficients of volumetric expansion i.e. $\frac{1}{V} \left(\frac{\partial V}{\partial T} \right)_p$ and C_p , is the specific heat capacity at constant pressure.

For two-phase flows, φ is determined numerically in the following manner.

Given that

$$\varphi = \left(\frac{\partial P}{\partial s} \right)_\rho \equiv \left(\frac{\partial P}{\partial s} \right)_V \quad (3.54)$$

From Maxwell's relations (Walas, 1987):

$$\left(\frac{\partial P}{\partial s} \right)_V = - \left(\frac{\partial T}{\partial V} \right)_s \quad (3.55)$$

The fanning friction factor, f_w is required for calculating the contribution of frictional force to the momentum equation (equation 3.2). It is a function of the flow Reynolds number.

For turbulent flow in smooth pipelines, Rohsenow et al., (1998) recommend the correlation proposed by Techo et al., (1965). The authors assert that the equation gives predictions within ± 2 % of extensive experimental measurements (Rohsenow et al., 1998). It is given by:

$$\frac{1}{\sqrt{f_w}} = 1.7372 \ln \frac{\text{Re}}{1.964 \ln \text{Re} - 3.8215} \quad (3.56)$$

In the laminar region, the evaluation of the fanning friction factor is independent of the pipe roughness. Thus in general, the fanning friction factor for laminar fully

developed flow is given by (Ouyang and Aziz, 1996; Rohsenow et al., 1998):

$$f_w = \frac{16}{\text{Re}} \quad (3.57)$$

The vapour thermal conductivity and viscosity used in calculating the Nusselt, Reynolds and Prandtl numbers are determined from the Ely and Hanley's method (Ely and Hanley, 1981, 1983) for non-polar gaseous mixtures. The method is based on the principle of corresponding states with methane as the reference fluid. Assael et al., (1996) claim that Ely and Hanley's (1981) method is one of the few schemes that is able to predict, with reasonable accuracy, the viscosity and thermal conductivity of a large number of non-polar components and their mixtures.

Viscosities and thermal conductivities for liquid mixtures containing alkanes (methane to n-dodecane) are determined from a semi-empirical scheme proposed by Dymond and Assael (Assael et al., 1996). The scheme generally applies between temperatures ranging from 280K to 400K and pressures from saturation up to 990atm. and has an uncertainty in predictions not greater than 5 per cent (Assael et al., 1996). The authors employed over 2,000 measurements of viscosity and thermal conductivity to optimise the coefficients used in the scheme.

For mixtures containing different classes of compounds, correlations proposed by DIPPR (Design Institute for Physical Property Data) (Daubert and Danner, 1990) are employed due to their accuracy and ease of use.

For two-phase fluids, the mixture thermal conductivity and viscosity is employed as given by:

$$\frac{1}{c_m} = \frac{\chi}{c_g} + \frac{1-\chi}{c} \quad (3.58)$$

Where χ and c respectively represent the fluid quality and the property to be determined.

3.11 Calculation of Fluid and Wall Temperature

Newton's cooling law (Picard and Bishnoi, 1989; Chen et al., 1995b; Fairuzov, 1998; Mahgerefteh et al., 1999) is commonly employed for determining the heat transferred to a fluid flowing in a pipe (q_h). In a given time step, this is given by:

$$q_h = \frac{4}{D_{in}} h_f^{i-1} (T_w - T_f) \quad (3.59)$$

Where D_{in} , is the pipeline inner diameter, T_f the fluid temperature, T_w is the wall temperature at the end of a given time step Δt . $i-1$, refers to property values at the beginning of the given time step.

To calculate the wall temperature for the determination of the heat transferred to the fluid, a 2-D finite difference method is employed for determining the transient temperature profile within the pipewall. The two dimensions taken into account are the radial and longitudinal axis of the pipeline.

Within the pipewall where conduction governs the mode of heat transfer, the differential equation that governs the heat flow is given by (Osizik, 1980):

$$\kappa \left(\frac{\partial^2 T}{\partial x^2} + \frac{\partial^2 T}{\partial y^2} \right) = \rho c \frac{\partial T}{\partial \tau} \quad (3.60)$$

The partial derivatives can be approximated thus (using the nomenclature in Figure 3.7).

$$\frac{\partial^2 T}{\partial x^2} \approx \frac{1}{(\Delta x^2)} (T_{m+1,n} + T_{m-1,n} - 2T_{m,n}) \quad (3.61)$$

$$\frac{\partial^2 T}{\partial y^2} \approx \frac{1}{(\Delta y^2)} (T_{m,n+1} + T_{m,n-1} - 2T_{m,n}) \quad (3.62)$$

The methodology described here is based on Cartesian coordinates; the application of these equations to cylindrical coordinates is based on the assumption of fluid

properties being uniform along the diameter of the inner pipewall. The curvature of the pipewall is assumed to be large so that each discretised section may be treated as a rectangular plate. The time derivative in equation (3.60) is approximated by:

$$\frac{\partial T}{\partial \tau} \approx \frac{T_{m,n}^{p+1} - T_{m,n}^p}{\Delta \tau} \quad (3.63)$$

Combining the above relations and rearranging, yields the following equation;

$$\frac{T_{m+1,n}^p + T_{m-1,n}^p - 2T_{m,n}^p}{(\Delta x^2)} + \frac{T_{m,n+1}^p + T_{m,n-1}^p - 2T_{m,n}^p}{(\Delta y^2)} = \frac{1}{\alpha} \frac{T_{m,n}^{p+1} - T_{m,n}^p}{\Delta \tau} \quad (3.64)$$

Where

- τ = time in seconds
- α = thermal diffusivity = $\frac{k}{\rho c}$
- k = thermal conductivity (W/(m²K))
- c = specific heat capacity (J/(kgK))
- ρ = density (kg/m³)

$T_{m,n}^p$ represents the nodal temperature at the previous time step, while $T_{m,n}^{p+1}$ represents the nodal temperature after the time increment.

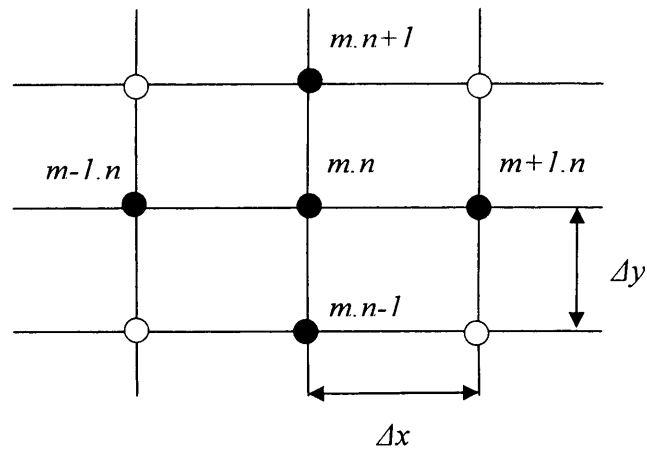


Figure 3.7: Nomenclature for nodal equation during conduction heat transfer.

The above relation is only valid if conduction is the mode of heat transfer. When a solid is exposed to some convection boundary, the temperature at the surface must be computed differently from above.

For the convection boundary (see Figure 3.8), the transient energy balance at the node (m, n) is made by setting the sum of energy conducted and convected into the node equal to the increase in the internal energy of the node. It can be shown (Holman, 1986) that for the convection boundary,

$$k\Delta y \frac{T_{m+1,n}^p + T_{m-1,n}^p}{\Delta x} + k \frac{\Delta x}{2} \frac{T_{m+1,n}^p + T_{m-1,n}^p}{\Delta y} + k \frac{\Delta x}{2} \frac{T_{m+1,n}^p + T_{m-1,n}^p}{\Delta y} + h\Delta y(T_\alpha - T_{m,n}^p) = \rho c \frac{\Delta x}{2} \Delta y \frac{T_{m+1,n}^p + T_{m-1,n}^p}{\Delta \tau} \quad (3.65)$$

In case of a heat flux value equation (3.65) can be modified as:

$$k\Delta y \frac{T_{m+1,n}^p + T_{m-1,n}^p}{\Delta x} + k \frac{\Delta x}{2} \frac{T_{m+1,n}^p + T_{m-1,n}^p}{\Delta y} + k \frac{\Delta x}{2} \frac{T_{m+1,n}^p + T_{m-1,n}^p}{\Delta y} + \Delta y \frac{q}{k} = \rho c \frac{\Delta x}{2} \Delta y \frac{T_{m+1,n}^p + T_{m-1,n}^p}{\Delta \tau} \quad (3.66)$$

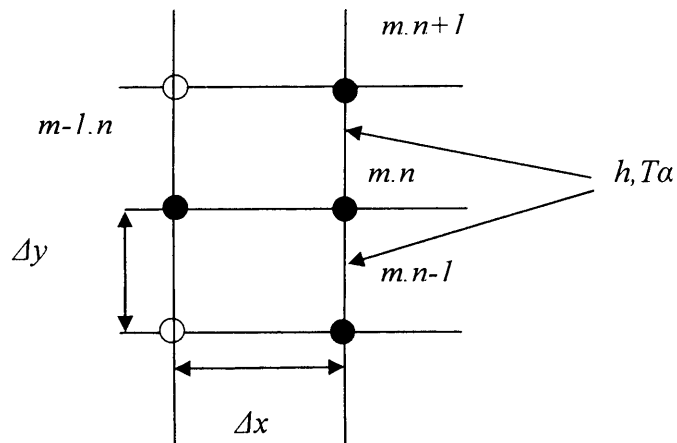


Figure 3.8: Nomenclature for nodal equation with convective boundary condition.

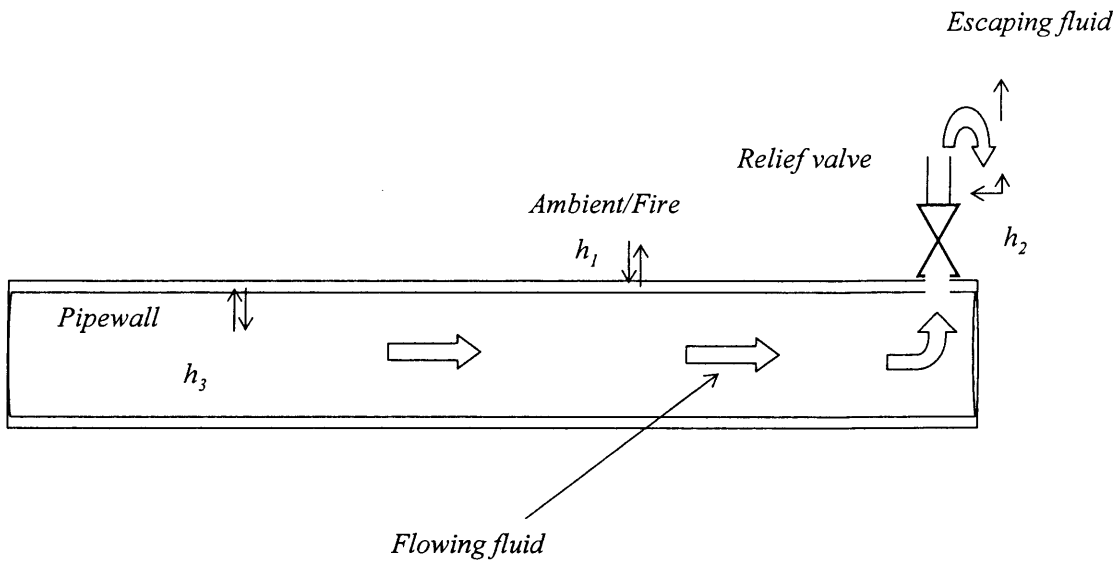


Figure 3.9: Schematic presentation of various convective boundaries.

The modelling of the heat transfer process along the convective boundaries requires the determination of various heat transfer coefficients as dictated by the fluid phase or flow characteristics. However in case of a fire impinging on the outer surface, the heat transferred is obtained from equation (3.66). The different correlations employed at various fluid-wall boundaries are given below.

3.11.1 Fluid/ Pipeline Wall Heat Transfer: h_2/h_3

This section deals with the heat transfer coefficients used in the model. It is assumed that flow through the orifice following pipeline failure is fully developed and turbulent. This is a reasonable assumption considering the relatively high Reynolds numbers ($>10^6$) following outflow. Consequently, heat exchange between the discharging fluid and the pipewall is due to forced, as opposed to natural convection.

For single-phase fully developed flow in pipes, the correlation proposed by Gnielinski (1976) is used to calculate the fluid/wall heat transfer coefficient due to its wide range of applicability and accuracy (Rohsenow et al., 1998). It is given by:

$$Nu = \frac{(Re-1000)Pr(f/2)}{1+12.7(f/2)^{0.5} [Pr^{2/3}-1]} \quad (3.67)$$

Where Nu , Pr and Re are the Nusselt, Prandtl and Reynolds numbers respectively (defined later).

The fanning friction factor, f in equation (3.67), is calculated from the equation (3.56) shown earlier.

For laminar flows, the relation proposed by Holman (1986) is employed

$$Nu = 3.66 + \frac{0.0668(d/L) Re Pr}{1 + 0.04 [(d/L) Re Pr]^{2/3}} \quad (3.68)$$

Where d and L are the pipeline diameter and length respectively.

In the case of two-phase flows, the correlation proposed by Steiner and Taborek, (1992) is employed for calculating heat transfer coefficient (h_3) within the pipeline. Apart from its relative simplicity and ease of use, the correlation has been shown (Rohsenow et al., 1998) to produce good agreement with experimental data for a wide range of flow regimes. It is given by:

$$\frac{h_f}{h_l} = \left[(1-x)^{1.5} + 1.9x^{0.6} \left(\frac{\rho_l}{\rho_g} \right)^{0.35} \right]^{1.1} \quad (3.69)$$

Where, x is the fluid quality, ρ_g and ρ_l are the vapour and liquid densities respectively. h_l is the heat transfer coefficient for the liquid phase in turn given by:

$$\frac{h_l D_{in}}{\kappa_l} = 0.023 \left[\frac{\rho_{mix} u (1-x) D_{in}}{\mu_l} \right]^{0.8} \left[\frac{\mu_l C_{pl}}{\kappa_l} \right]^{0.4} \quad (3.70)$$

Where k_l is the liquid thermal conductivity (W/(mK)), μ_l is the liquid viscosity (Ns/m²), C_{pl} the liquid specific heat capacity at constant pressure (J/(kgK)). ρ_{mix} represents the two-phase mixture density presented earlier (equation 3.48).

3.11.2 Ambient/ Pipeline Wall Heat Transfer: h_l

This section describes the equations employed for heat transfer between the external and the pipewall exposed to the ambient only. In the event of a fire engulfing the pipe, a heat flux value is used to calculate the pipewall/fluid temperature as given in equation (3.66). The heat transfer coefficient, h_{amb} (h_l) between the pipewall and the surrounding ambient is given by (Incropera and DeWitt, 1996; Rohsenow et al., 1998):

$$h_{amb} = \left(h_{nat}^3 + h_{for}^3 \right)^{1/3} \quad (3.71)$$

Where, h_{nat} and h_{for} are the natural and forced heat transfer coefficients respectively.

For natural convection, the correlation proposed by Churchill and Chu (1975) is used:

$$\frac{h_{nat} D_{out}}{\kappa_{film}} = \left[0.60 + \frac{0.387 Ra_D^{1/6}}{\left[1 + (0.559/Pr_{film})^{9/16} \right]^{8/27}} \right]^2 \quad (3.72)$$

The dimensionless groups are defined as:

$$Ra_D = Gr_{film} Pr_{film} \quad (\text{Rayleigh number}) \quad (3.73)$$

$$Gr_{film} = \frac{\rho_{film}^2 g \xi_{film} (T_s - T_{amb}) D_{out}^3}{\mu_{film}^2} \quad (\text{Grashof number}) \quad (3.74)$$

$$Pr_{film} = \frac{C_{pfilm} \mu_{film}}{\kappa_{film}} \quad (\text{Prandtl number}) \quad (3.75)$$

Where, g represents the gravitational acceleration, k and μ being the thermal conductivity and viscosity respectively. The subscript, $film$ represents ambient properties evaluated at the film temperature $[T_{film} = (T_s + T_{amb})/2]$, T_s the surface temperature, and ξ_{film} the isobaric volumetric expansion coefficient. ξ_{film} is a thermodynamic property which can be obtained from the equation of state. It is given by (Incropera and DeWitt, 1996):

$$\xi_{film} = -\frac{1}{\rho_{film}} \left(\frac{\partial \rho_{film}}{\partial T_{film}} \right)_p \quad (3.76)$$

For forced convection, the heat transfer correlation proposed by Churchill and Bernstein (1977) is employed. The correlation is said to cover the entire range of Reynolds number for which data are available as well as a wide range of Prandtl numbers.

$$\frac{h_{for} D_{out}}{\kappa_{film}} = \left[0.30 + \frac{0.62 \text{Re}_{film}^{1/2} \text{Pr}_{film}^{1/3}}{\left[1 + (0.4/\text{Pr}_{film})^{2/3} \right]^{1/4}} \left[1 + \left(\frac{\text{Re}_{film}}{282,000} \right)^{5/8} \right]^{4/5} \right] \quad (3.77)$$

Once the heat transfer coefficients for the fluid h_3 and wall temperature T_w are evaluated, heat transferred to the fluid at the next time step is determined using equation (3.59).

3.12 Validation

In this section the validation of the outflow model by comparison against experimental data is presented. This exercise is limited to outflow under ambient conditions as there are no comparative data available relating to the failure of pressurised pipelines under fire attack.

The Isle of Grain (IOG) pipeline rupture test results, P40 and P42 are chosen for validation. These data are the results of experiments carried out by Shell and BP on the Isle of Grain (Chen, 1993).

In the tests, two 100m instrumented parallel carbon steel pipelines were used. The pipelines were of 154mm nominal diameter with a wall thickness of 7.3mm. Pressure transducers and thermocouples measuring fluid temperature were attached along each line. Inventory and hold-up were measured using load-cells and neutron back scattering.

The pipelines contained commercial propane or LPG. This usually comprises a mixture of propane and other low molecular weight hydrocarbons, such as butane and ethane. The exact fluid composition is not given, but Chen (1993) assumes a mixture of 95-mole % propane and 5-mole % butane.

Transient tests conducted were initiated by rupture of a disc at the downstream end of the pipeline. Table 3.1 is a summary of the prevailing conditions in both tests prior to

rupture.

Parameter	Test P40	Test P42
Initial pressure (bara)	21.6	11.3
Inventory temperature (°C)	20.0	20.0
Ambient temperature (°C)	19.1	18.6
Pipeline roughness (m)	0.00005	0.00005
Rupture diameter (m)	0.154	0.154
Discharge coefficient	1.0	1.0
Wall thickness (m)	0.0073	0.0073

Table 3.1: Prevailing conditions in tests P40 and P42 prior to rupture.

3.12.1 P40 Simulation (FBR)

Figure 3.10 shows pressure-time histories for the LPG mixture. Curve A shows the measured data, while curve B presents the predicted data. From the figure, it can be observed that the simulated and test data are in good agreement.

Figure 3.11 shows the predicted temperature (curve A) and the measured (curves B) temperature-time profiles at the rupture plane for test P40. The rapid expansion of the inventory at the rupture plane results in a significant decrease in its temperature to ca. 238K at 20s following rupture. The subsequent rapid recovery in the fluid temperature is due to the cessation of two-phase flow, with the onset of gas phase flow at the rupture plane. This effect is however not observed by other workers (Chen, 1993; Fairuzov, 1998) using a constant heat transfer coefficient.

Figure 3.12 shows the measured inventory discharged profile for test P40 (curve A) in comparison to the model predictions (curves B). Once again the simulated data (curves B) is in excellent accord with the experimental data.

3.12.2 P42 Simulation (FBR)

The model parameters for test P42 are given in table 3.1.

Figure 3.13 shows the FBR data for the open end pressure-time predictions for the LPG mixture as compared to measured test P42 data. Curves A show the measured data, whilst curve B represents the predicted data.

Figures 3.14 and 3.15 respectively show the corresponding variations of rupture plane temperature and mass discharged with time. In both figures, curves A represent the measured data, while curves B represent the predicted data. Again, good agreement between the measured and experimental data is observed.

As it may be observed in all cases, the model predictions are in agreement with experimental data.

3.13 Conclusion

In this chapter, the equations describing mass, momentum and energy conservation were derived to develop a rigorous outflow model for pressurised pipelines. These equations together with the Peng-Robinson equation of state constitute the building blocks for modelling the outflow process. The thermodynamic correlations used in the model were also shown along with a 2-dimensional heat conduction approach employed in the model. The conservation equations were shown to be quasilinear hyperbolic in nature.

The MOC was chosen to solve these, as it is well suited for handling fast transients during depressurisation. The resolving of the conservation equations using the MOC yields the compatibility equations. These equations together with the appropriate boundary conditions are then used to derive expressions for simulating the fluid dynamics following full bore ruptures and punctures in pipelines.

Various other data such as those recorded during the Piper Alpha tragedy as used

previously by Mahgerefteh et al., (1997-2000) are also available for validation. However, the Isle of Grain data are chosen in preference due to the fact that these were obtained under highly controlled experimental condition and hence may be considered to be more reliable.

The finite disagreement between the model as compared to the experimental data may be considered to be due to the assumptions adopted in developing the pertaining theory, particularly that relating to the applicability of the homogeneous equilibrium model.

The extension of the outflow model for accounting the effect of thermal loading due to fire is presented in chapters 4 and 5.

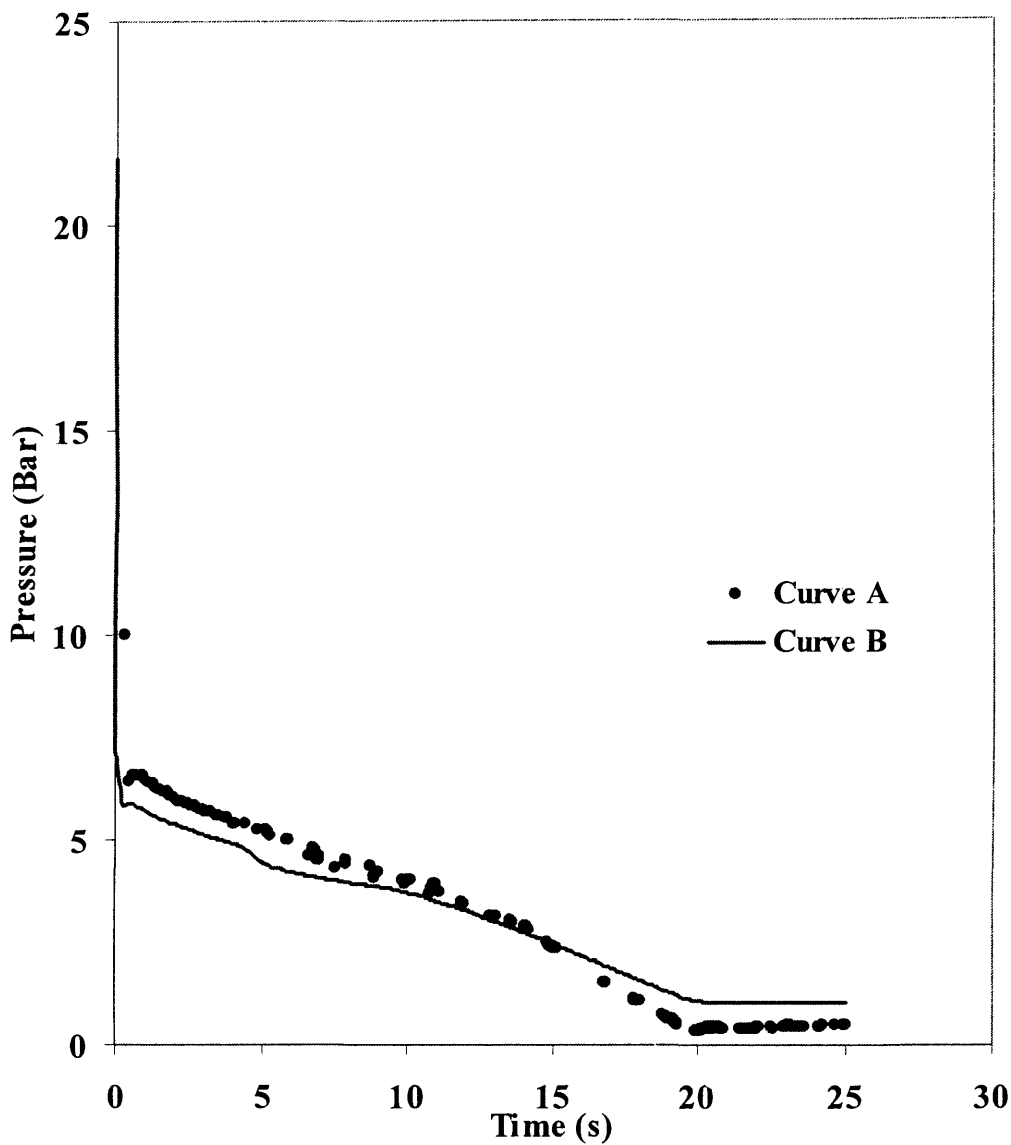


**Figure 3.10: FBR open end pressure-time profiles for test P40 (LPG)
Simulation data are obtained.**

Curve A: Measurement (Richardson and Saville, 1996a,b).

Curve B: 2-D Outflow model

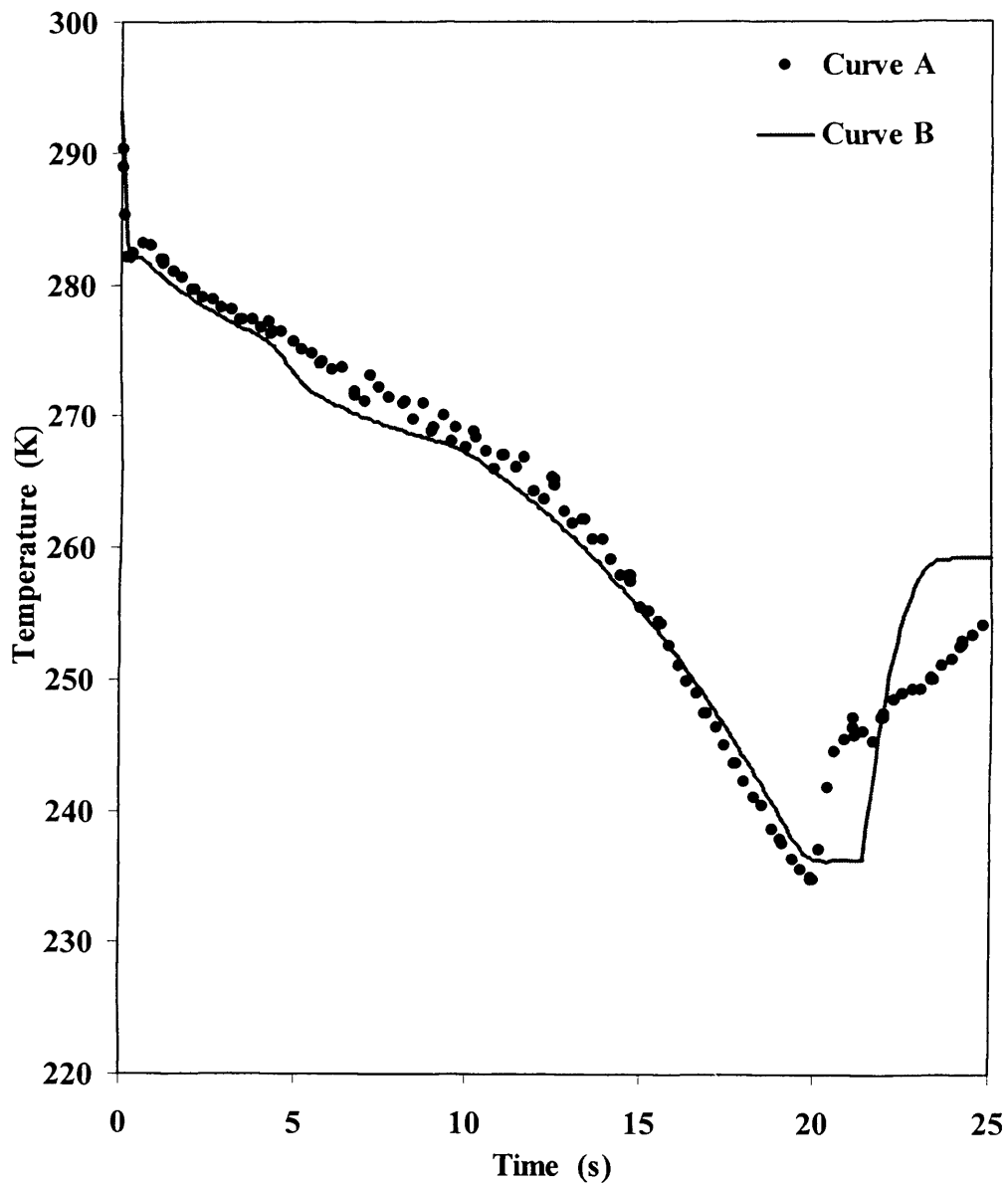


Figure 3.11: FBR open end temperature -time profiles for test P40 (LPG)

Curve A: Measurement (Richardson and Saville, 1996a,b).
Curve B: 2-D Outflow model

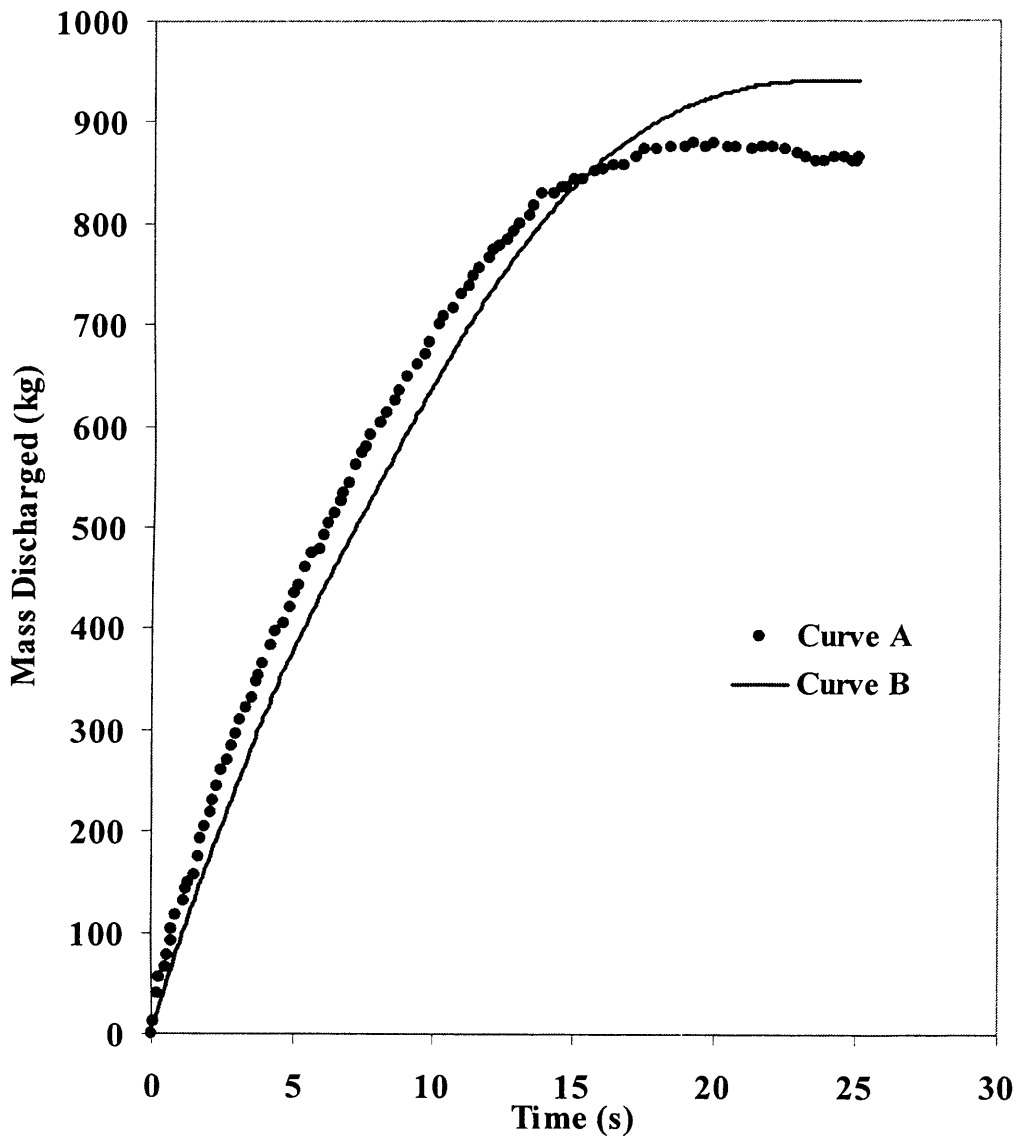


Figure 3.12: FBR mass discharge-time profiles for test P40 (LPG)

Curve A: Measurement (Richardson and Saville, 1996a,b).

Curve B: 2-D Outflow model.

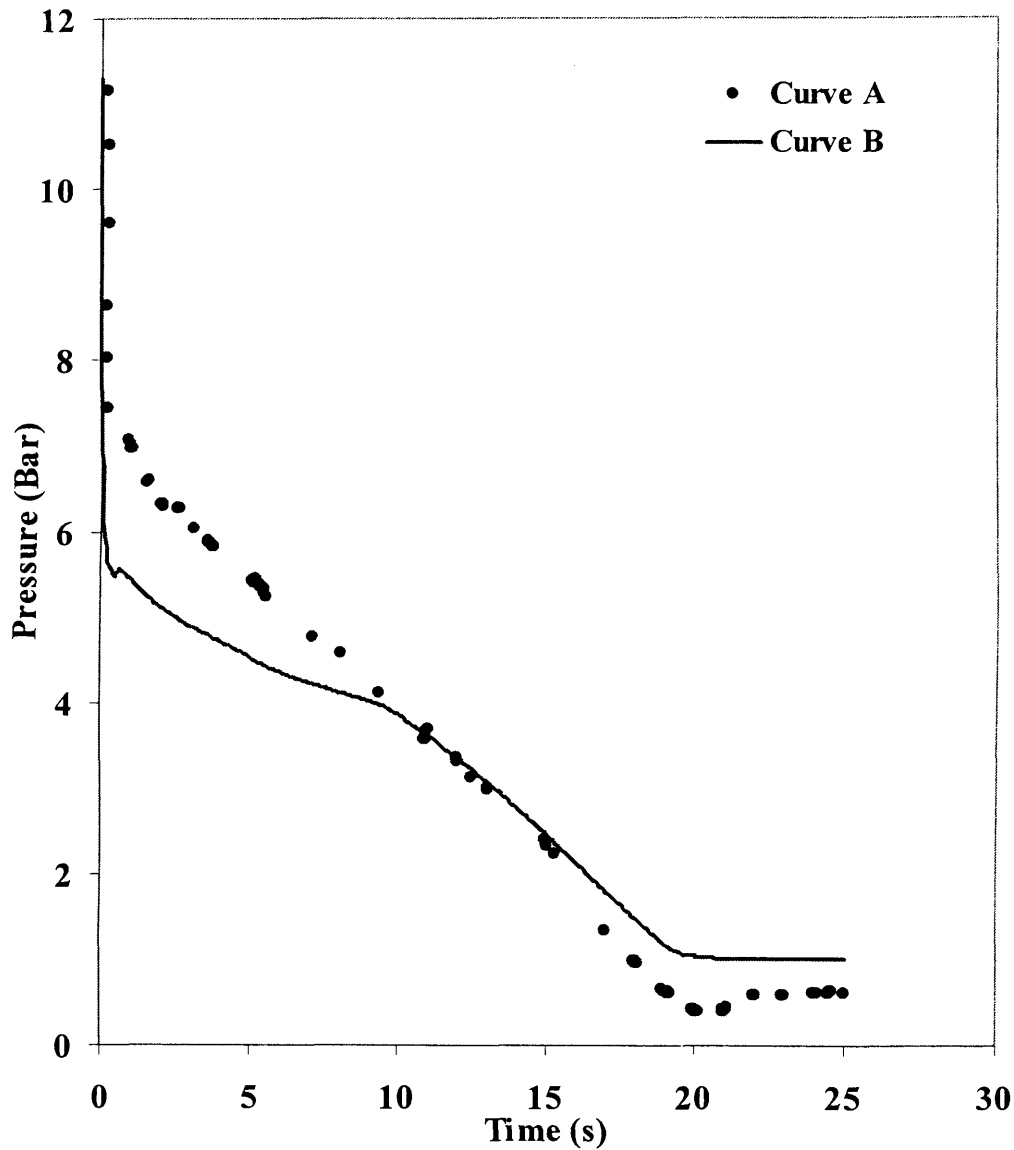


Figure 3.13: FBR open end pressure-time profiles for test P42 (LPG)
Simulation data are obtained.

Curve A: Measurement (Richardson and Saville, 1996a,b).
Curve B: 2-D Outflow model

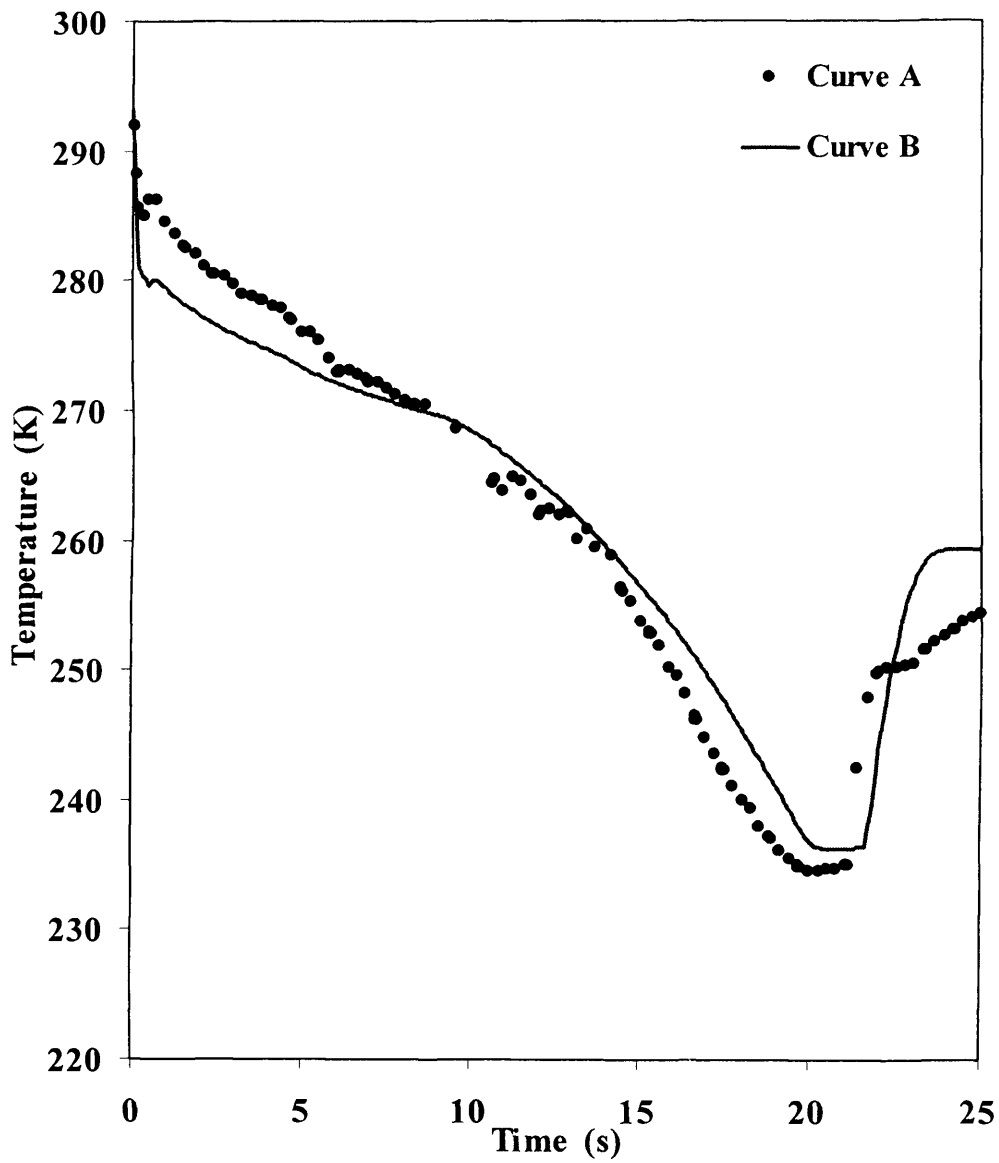


Figure 3.14: FBR open end temperature -time profiles for test P42 (LPG)

Curve A: Measurement (Richardson and Saville, 1996a,b).

Curve B: 2-D Outflow model

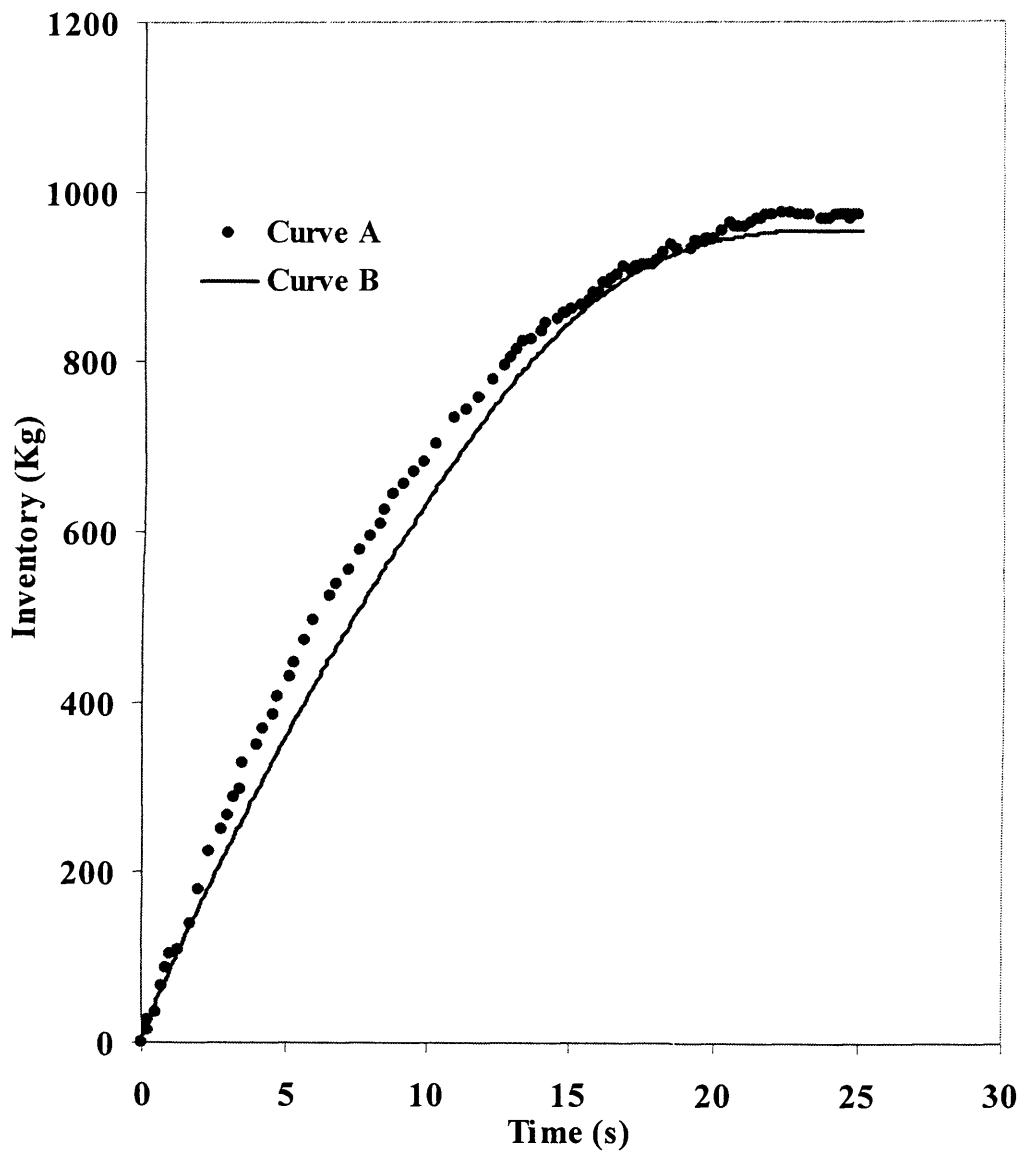


Figure 3.15: FBR mass discharge-time profiles for test P42 (LPG)

Curve A: Measurement (Richardson and Saville, 1996a,b).

Curve B: 2-D Outflow model

4.3 Wall Resident Stresses

Heat from a fire is conducted through the pipewall at a rate dependent on the pipewall material's thermal diffusivity; the ratio of thermal conductivity to the product of density and specific heat capacity. The heat input from the fire, in conjunction with the heat removal from the pipeline results in a temperature gradient across the pipewall.

Due to the wall temperature gradient and internal pipeline pressure, thermal and pressure stresses co-exist during blowdown under fire attack.

Thermal stresses result from non-uniform heating of a material. A metal expands on the application of heat and contracts upon its extraction. For example, during blowdown under fire, the heating on the outside of the wall by the fire causes the outer wall metal to expand. This coupled with the cooling on the inside wall results in a bending moment referred to as thermal stresses (Popov, 1999). These may either be compressive or tensile in action and are transient during blowdown under fire attack.

Pressure stresses exist as a result of the force exerted by the contained pressure on the pipewall. These are the most commonly considered cause for pipeline failure and therefore often used for design specification. The tangential stress (often referred to as the hoop or circumferential stress) is used to determine the safe wall thickness of pressurised pipelines and vessels. On fire impingement, the pressure stresses are dictated by the pressure history within the pipeline and are accounted for in most of the models existing in the literature. The modelling of pressure stresses in thick walled pipelines are well established and easily determined analytically.

An addition of triaxial thermal and pressure stresses give the total resident stresses within the pipewall at any point in time during blowdown under fire attack. A comparison between the total stress and the yield and ultimate tensile strength of the pipewall material at the prevailing integral temperature enables a precise determination of the ductile-failure process.

4.4 Effect of Thermal Impact

Fire attack will result in the thermal weakening of the dry wall leading to metal degradation. This coupled with the combined thermal and pressure stresses has been shown to cause failure (Birk, 1989).

A pressurised pipeline will fail (rupture), when it is subjected to a stress in excess of the strength of material from which it is fabricated. For vessels or pipelines under normal conditions, this is usually taken as the ultimate tensile strength.

As a first approximation, one might expect the pipeline to fail at the point at which the total stresses exceed the material's strength. In practice the plastic deformation and hence stress relaxation that will have occurred before failure is reached will make this calculation of failure mechanism difficult.

At elevated temperatures, the combination of mechanical stress, thermal stress and stress concentrations due to stress risers and associated strains lead to a local exceedence of the ultimate tensile strength and rupture strain. A ductile rupture occurs and an initial crack is formed. The local stress around the crack re-distributes with a very high stress concentration at the crack tip. The conditions at the crack tip are such that fracture criteria are exceeded and the vessel 'unzips' in a trajectory that is approximately normal to the direction of principal stress (Fire and Explosion Guidance, HSE, 2006).

4.5 Model Development

The following processes/effects during blowdown under fire attack are accounted for in the modelling work:

- Fluid dynamics following outflow
- Pipewall/fluid/ambient heat transfer
- Wall transient thermal and pressure stresses
- Failure mode and consequence

The fluid dynamics and heat transfer modelling has been shown earlier in the thesis (see chapter 3). The following assumptions are made in deriving the above model:

- Spatially uniform pressure within the pipeline
- No temperature stratification within the vapour and liquid phases (homogeneous equilibrium)
- Depressurisation/blowdown is assumed to commence upon thermal impingement

4.5.1 Pressure and Thermal Stresses

The pertinent tangential, radial and longitudinal thermal and pressure stresses for a pressurised pipeline are presented in this section. For thick-walled cylinders experiencing non-uniform heating, failure is assumed to occur when any one of the above triaxial total normal pressure and thermal stresses exceed the vessel material's yield stress (Popov, 1999). Furthermore for ductile materials (e.g. carbon steel) permanently deforming failure occurs after the yield stress is exceeded while 'total' failure occurs when the ultimate tensile strength of the material is exceeded. In this chapter, failure is assumed to be the latter.

4.5.1.1 Thermal Stresses Across Pipewall

During blowdown under fire attack, thermal stresses are expected to be significant due to the temperature gradients within the pipewall. This is due to the heating of the outside wall of the pipeline as opposed to cooling on the inner wall due to depressurisation of the escaping fluid.

The equations for 3-D thermal stresses in a cylinder are obtained from the radial temperature profile $T(r)$ as given by Timoshenko and Goodier (1987) in the following form

$$\sigma_t^T = \frac{M_1}{r^2} \left[\frac{r^2 + a^2}{b^2 - a^2} \int_a^b T(r) r dr + \int_a^r T(r) r dr - T(r) r^2 \right] \quad (4.1)$$

$$\sigma_r^T = \frac{M_1}{r^2} \left[\frac{r^2 - a^2}{b^2 - a^2} \int_a^b T(r) r dr - \int_a^r T(r) r dr \right] \quad (4.2)$$

$$\sigma_l^T = M_1 \left[\frac{2}{b^2 - a^2} \int_a^b T(r) r dr - T(r) \right] \quad (4.3)$$

where $M_1 = \frac{\tau E}{1 - \mu}$

- and
- a = pipeline internal radius
 - b = pipeline external radius
 - τ = coefficient of thermal expansion
 - E = modulus of elasticity
 - μ = Poisson's ratio

Superscript T refers to 'thermal' and subscripts t, r, l and tangential, radial and longitudinal stresses respectively.

As can be seen by comparing tables 4.1 and 4.2, carbon steel BS3100 AM1 is more resistant to yielding and hence ultimate failure at elevated temperatures. This will be demonstrated in this study by using the two types of material of construction for the pipeline experiencing jet fire torching during blowdown.

Table 4.1 Ultimate tensile strength for Carbon Steel BS3100 AM1 (composition: 14% C, 29% Si, 45% Mn; annealed) (Brandes, 1983).

Temperature (°C)	Ultimate tensile strength (MPa)
Room temp (293 K)	385
100	352
200	400
300	414
400	372
500	201

Table 4.2 Ultimate tensile strength for Carbon Steel BS3100 A2 (composition: 28% C, 35% Si, 66% Mn; normalised and tempered) (Brandes, 1983).

Temperature (°C)	Ultimate tensile strength (MPa)
Room temp (293 K)	524
100	486
200	480
300	463
400	448
500	324

Figure 4.1 below represents the pipeline failure calculation algorithm during fire attack.

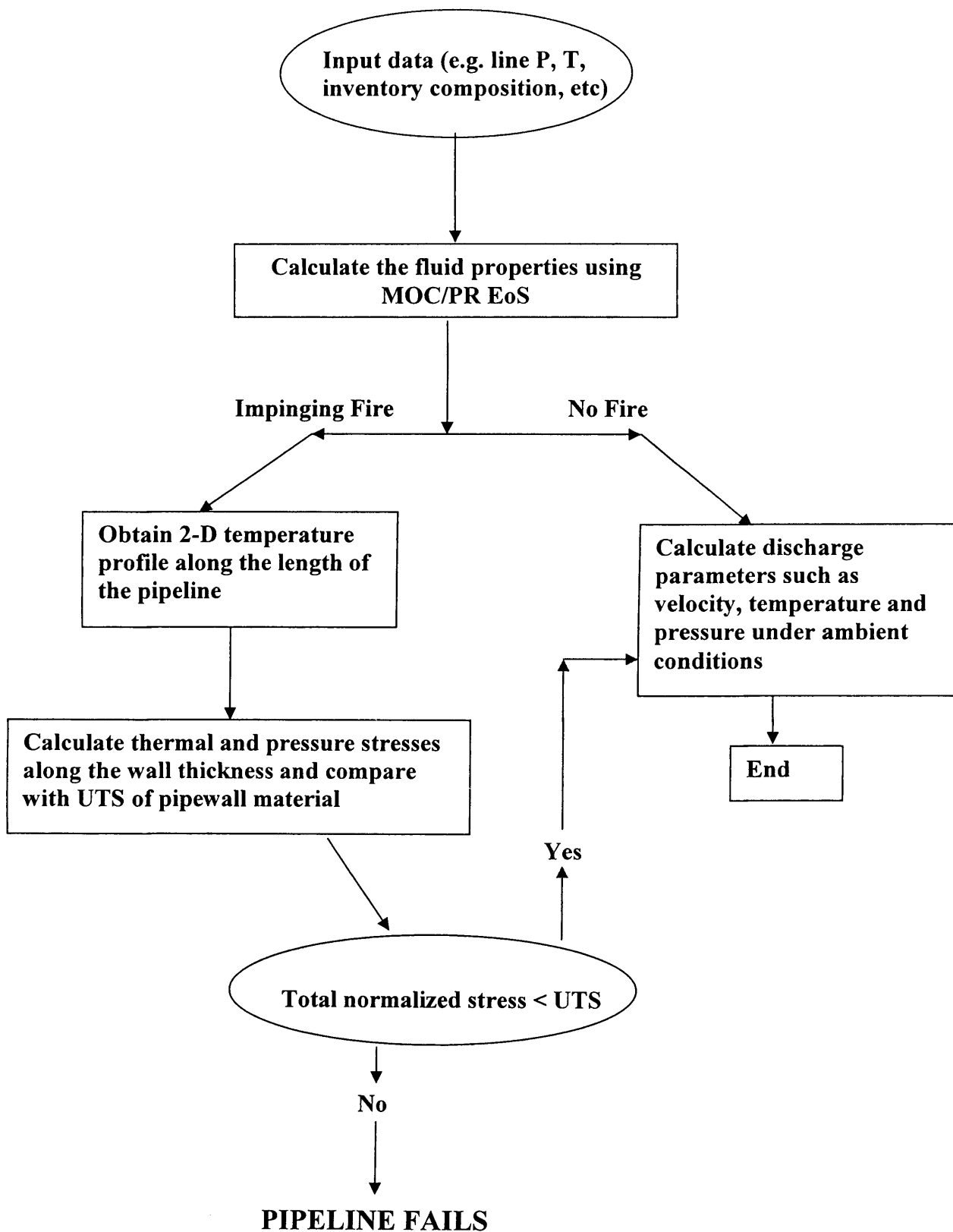


Figure 4.1: Calculation algorithm for predicting pipeline failure following fire attack.

4.6 Case Study

This section presents the results of the application of above model to a hypothetical example involving a carbon steel pipeline containing pressurised natural gas under localised jet fire attack.

As mentioned earlier, two types of failure scenarios are simulated. The first deals with the impact of direct jet fire impingent on an intact pipeline. For reference purposes, this is referred to as 'isolated pipeline failure'. In the second case, hereby referred to 'unisolated pipeline failure', the effect of emergency depressurisation using various diameter relief valves on the pipeline mechanical integrity during fire attack is simulated.

4.6.1 Isolated Pipeline

Table 4.3 shows the pipeline characteristics and the prevailing conditions for the case study. The 1km long 0.419m i.d carbon steel pipeline is assumed to contain natural gas at 117bara. The simulated pipeline is carbon steel type BS3100 AM1. Comparative data for a different pipeline made of BS3100 A2 carbon steel (see tables 4.1 and 4.2) selected in order to demonstrate the effect of pipeline material of construction is given later.

For the sake of an example, it is assumed that a 10m section of the pressurised pipeline is completely enveloped by a jet fire at a distance of 390m from one of its ends. A typical jet fire heat flux of 400kW/m^2 is assumed (Roberts et al., 2000).

The isolated pipeline failure is simulated by placing a nominal 0.001 mm puncture at the end of the pipeline for calculation convenience. Figures 4.4 and 4.5 respectively show the corresponding variations of line pressure and temperature with time. As it may be observed there are no discernable changes in either of these two parameters throughout the simulation. As such approximating the intact pipeline with that having a 0.001mm puncture may be considered to be a fair assumption.

Pipeline length (km)	1
Feed pressure (bara)	117
Feed temperature (K)	293.15
Pipeline thickness (mm)	19
Pipeline inner diameter (m)	0.419
Pipeline density (kg/m ³)	7854
Pipeline thermal conductivity (W/mK)	53.6
Ambient temperature (K)	292.15
Heat Flux (kW/m ²)	400
Pipe roughness (mm)	0.05

Table 4.3: Pipeline conditions; Inventory (mol %): CH₄ (90.0) and C₃H₈ (10.0)

Figure 4.6 shows the variation of the outer (curve A) and inner wall (curve B) temperatures as a function of time for the 10m section of the pipeline under jet fire attack. As it may be observed, the outer wall temperature exposed to fire reaches a maximum temperature 494K some 300s following thermal loading. Given the inner wall temperature of 294K, the corresponding temperature gradient across the pipewall is ca. 190K. A comparison of the resulting thermal and pressure stresses with the pipeline ultimate tensile strength will dictate if and when the pipeline would fail during fire attack. This will be demonstrated later.

Figures 4.7 - 4.9 respectively show the corresponding time dependent variations of the total normalised radial, tangential and longitudinal stresses across the pipewall for the isolated pipeline section exposed to fire attack.

The various stress profiles have been normalised with respect to the pipeline material of construction's UTS data for carbon steel (Brandes, 1983) at the prevailing pipewall integral temperature $\Psi(K)$. The latter is given by

$$\Psi(K) = \frac{\int_a^b T(r, t)}{b - a} \quad (4.7)$$

Normalised stress values equal or greater than unity indicate pipeline failure. Positive and negative values on the other hand represent tensile and compressive stresses respectively.

Referring to figure 4.7, it is clear that pipeline failure in the radial direction in the time domain under consideration (300s) is impossible since the normalised stress values remain well below unity throughout.

Figures 4.8 and 4.9 on the other hand reveal much larger normalised tangential and longitudinal stresses. The relatively low normalised compressive stresses at the inner wall rapidly transform into tensile stresses towards the outer wall. Comparing the data given in figures 4.8 and 4.9 it is clear that the pipeline fails in the tangential direction due to prevailing tensile stresses some 160s following fire attack.

The type of failure demonstrated above, is termed as bulging and buckling. It occurs due to the outer wall exposed to the jet fire being at a higher temperature than the inner wall in contact with the cooler pressurised inventory thus resulting in differential thermal expansion.

The buckling is attributed to the compressive stresses in the inner pipewall whereas the bulging is due to the outer wall experiencing tensile stresses. The pipeline deformation is observed in the tangential direction. This is highlighted in the trends observed in figure 4.6 where the inside compressive stresses (negative) progress across the pipewall becoming tensile (positive) in nature. The compressive stresses are observed to be more in the case of an unisolated pipeline due to the effect of the expansion induced cooling of the inventory. Figure 4.2 is a schematic representation of the bulging and buckling failure.

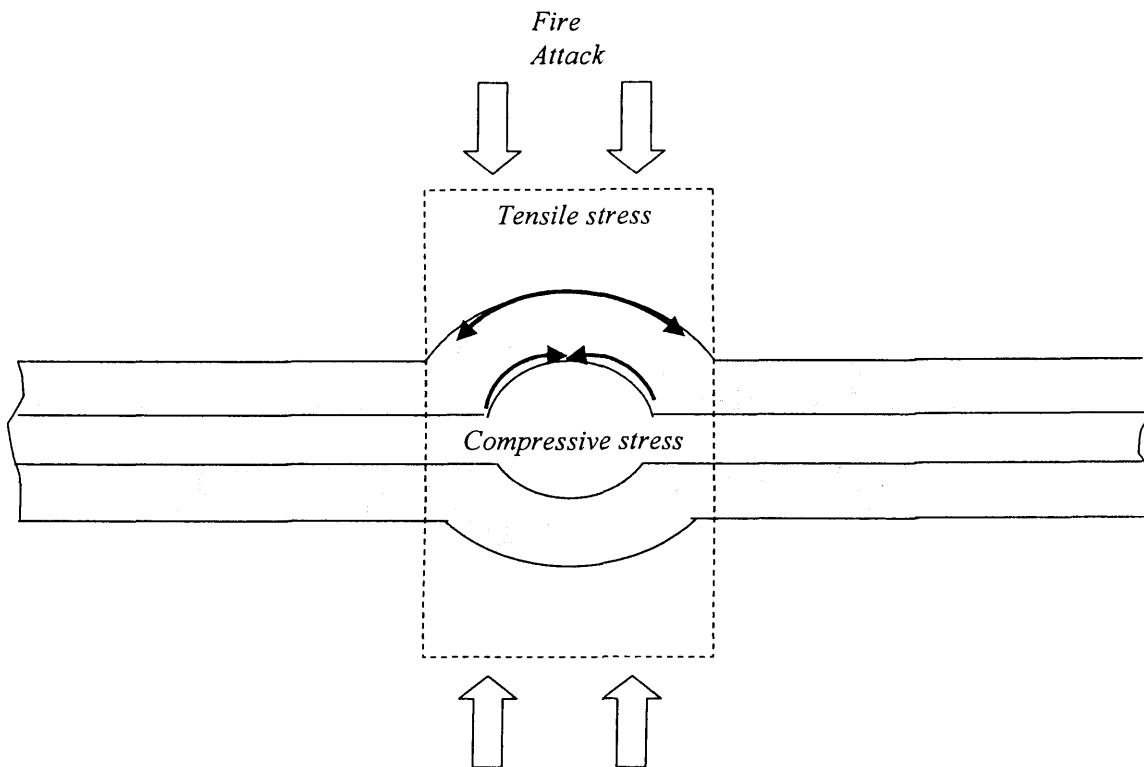


Figure 4.2 schematic representation of bulging and buckling pipeline failure during fire attack.

Order of figures changed

Figure 4.10 shows the transient variations of pipewall total stress ($\sigma_T + \sigma_p$, curve A) and (UTS data, curve B). Curves C and D on the other hand show the corresponding thermal (σ_T) and pressure stresses (σ_p) in the outer pipewall section during fire attack. As may be observed, the dominant failure mechanism for the pipeline is due to thermal stresses. These, in contrast to the pressure stresses, rapidly increase with time during fire loading. The pipeline fails at the intersection of curves A and B; 160s following jet fire attack.

4.6.2 Pressure Relief Valve

In an emergency situation, it is important to choose the correct size of a relief valve in order to provide the desired depressurisation rate. Most risk analysis calculations are made on the basis of the assumption of round holes and sharp edges. These assumptions are made for simplicity and lack of better information.

Chapter 4 *Modelling the Thermal Response of Pressurised Pipelines under Jet Fire Impingement*

Health and Safety Executive (www.hse.gov.uk) categorizes relief valve size distribution as follows:

<10mm, 10-25mm, 25-50mm, 50-75 mm, 75-100mm, >100mm

In this study emergency depressurisation is assumed to occur through 10mm, 25mm and 50mm relief valves. A discharge coefficient of unity is taken.

4.6.3 Unisolated Pipeline

The simulation conditions for the unisolated pipeline failure are the same as those for isolated failure. However, in the unisolated case, the pipeline is assumed to be depressurising by opening a relief valve placed at one of its ends. Figure 4.3 shows a schematic representation of this arrangement showing the various distances and dimensions.

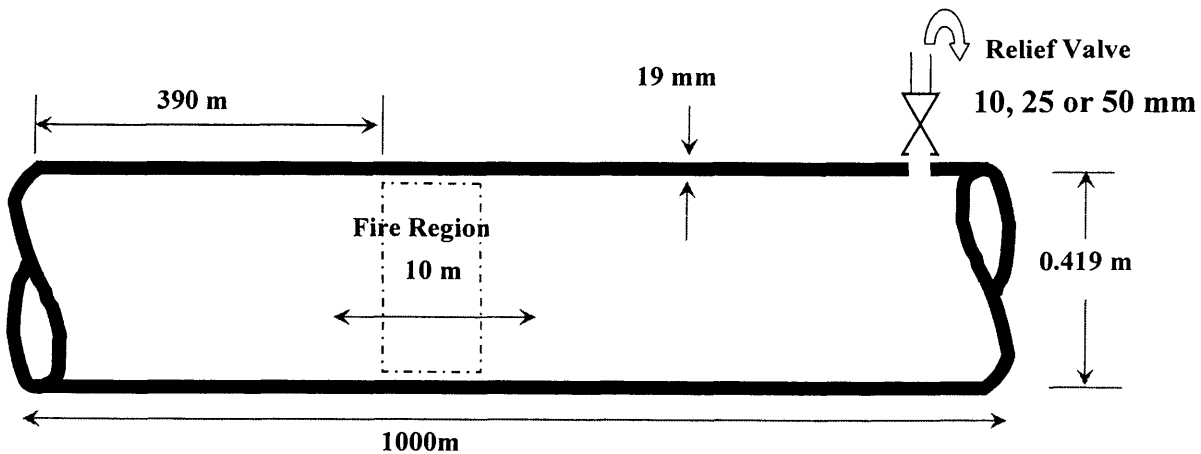


Figure 4.3 Schematic representation of the unisolated pipeline arrangement under fire attack (not to scale).

Figure 4.11 - 4.13 respectively show the temperature variation with time for the outer (curve A) and inner walls (curve B) of the pipeline using 10, 25 and 50mm relief valves.

Figure 4.14 shows the corresponding variation of the difference between the outer and inner wall temperatures extracted from the above data plotted against relief valve

diameter at 300s following depressurisation. The data for the isolated pipeline are also included for comparison. As it may be observed, the pipewall temperature gradient increases with increase in relief valve diameter. The corresponding temperature gradients for 0, 10, 25 and 50 mm relief valve diameters are 190K, 200K, 208K and 222K respectively. The above observed phenomenon is due to the depressurisation induced expansion cooling of the inner wall the extent of which directly increases with increase in the relief valve diameter.

Figure 4.15 shows the comparison of pipeline pressure with time for the isolated and unisolated pipelines using various size relief valves. As it may be observed, increase in the relief valve diameter results in a significant increase in the depressurisation rate. This is to be expected as the discharge rate through the relief valve increases with the square of the orifice diameter.

Figures 4.16-4.24 respectively show the corresponding variations of the total radial, tangential, and longitudinal stresses for the 10m section of the unisolated pipeline exposed to fire using 10, 25 and 50mm diameter relief valves.

Same as the earlier observation, the maximum stress is in the tangential direction for all of the three pipeline depressurisation scenarios; figures 4.17, 4.20 and 4.23.

Figure 4.25 shows the corresponding variation of the normalised tangential stresses versus pipewall thickness at 300s following depressurisation using different diameter relief valves. In all cases, the compressive tangential stresses at the inner pipeline wall rapidly transform into tensile stresses towards the outer pipeline wall. Also, the inner wall compressive stresses significantly increase with increases in relief valve diameter in response to the impact of the depressurisation induced cooling of the inventory. This is in contrast to the outer wall tensile stresses, which decrease with increase in relief valve diameter.

A comparison of total stress (curve A, $\sigma_T + \sigma_p$) with the UTS data (curve B) for the different relief valve diameters is shown in figures 4.26-4.28. Thermal stresses (curve C, σ_T) and pressure stresses (curve D, σ_p) and time of failure are determined from the

intersection of the total stresses (curve A) and UTS data (curve B). The corresponding failure times are 170s, 220s for the 10mm and 25mm relief valves respectively. In case of a 50mm relief valve (figure 4.28) the pipeline does not fail due to the small contribution of pressure stresses (curve B) to the total stresses (curve C).

Figure 4.29 represents the variation of the total tangential stresses as a function of time during emergency depressurisation using different relief valve diameters under fire attack. Curve A shows the time dependent variation of the UTS, curves B, C and D respectively show the total (pressure + thermal) outer wall stresses for 50, 25 and 10mm relief valve diameters. Curve E shows the corresponding data for the isolated intact pipeline (no pressure relief).

As it may be observed from the data, emergency depressurisation has a significant impact on delaying the time for pipeline failure. The corresponding failure times for the isolated, 10mm and 25mm relief valve diameters are 160s, 170s and 220s respectively. There is no possibility of pipeline failure using the 50mm relief valve due to significantly faster depressurisation rate, which relieves the pressure stresses.

4.7 Effect of Pipe Material of Construction

The effect of material of construction is evaluated by the use of two different types of pipelines experiencing jet fire impingement. Failure in the isolated pipeline made of BS 3100 AMI under jet fire torching was shown in figure 4.10. Figure 4.30 (normalised tangential stress with wall thickness) and 4.31 (stresses versus UTS) show the analogous data for the isolated pipeline made of BS3100 A2 (see table 4.2). Remarkably, as it may be observed the time of failure increases by approximately 120s using this new pipeline material. This comparison demonstrates the significant effect of the pipeline material of construction on its resistance to jet fire attack.

4.8 Conclusion

This chapter presented the development of a mathematical model for simulating the loss in the mechanical integrity of pressurised pipelines under fire attack.

Chapter 4 Modelling the Thermal Response of Pressurised Pipelines under Jet Fire Impingement

The governing theory for predicting the fluid dynamics within the pipeline and that of the escaping fluid was presented in the previous chapter. The above coupled with the simulated triaxial thermal and pressure stresses within the pipeline wall form the basis for a comprehensive model for producing a timeline presentation of the failure mechanism of pressurised pipelines during fire attack.

Using a hypothetical example involving a pressurised natural gas pipeline, two types of failure scenarios were quantitatively analysed. The first involved direct jet fire impingement on an isolated pipeline. Secondly the likelihood of failure is assessed by the effect of fire impingement on a pipeline depressurising through a relief valve (unisolated pipeline).

Examination of the resulting triaxial stress data revealed that during thermal loading, the prevailing tangential compressive stresses in the inner pipewall rapidly transform into much larger tensile forces towards the outer wall. Once these stresses exceed the pipewall material yield stress, the pipeline begins to deform by buckling (inner wall) and bulging (outer wall).

With the passage of time, further rise in the temperature of the pipewall results in an increase in the tensile stress at the outer wall. The pipeline catastrophically fails through rupture when this stress exceeds the pipewall material ultimate tensile strength.

Emergency depressurisation is found to have a significant impact on delaying the time to failure with the effect increasing with increasing relief valve diameter. Much the same as that for the isolated pipeline, the prevailing failure mode is found to be due to tangential tensile stresses at the outer pipewall surface. Such failure may however be altogether circumvented using a sufficiently large relief valve diameter. The failure time may also be significantly delayed by changing the pipeline material of construction.

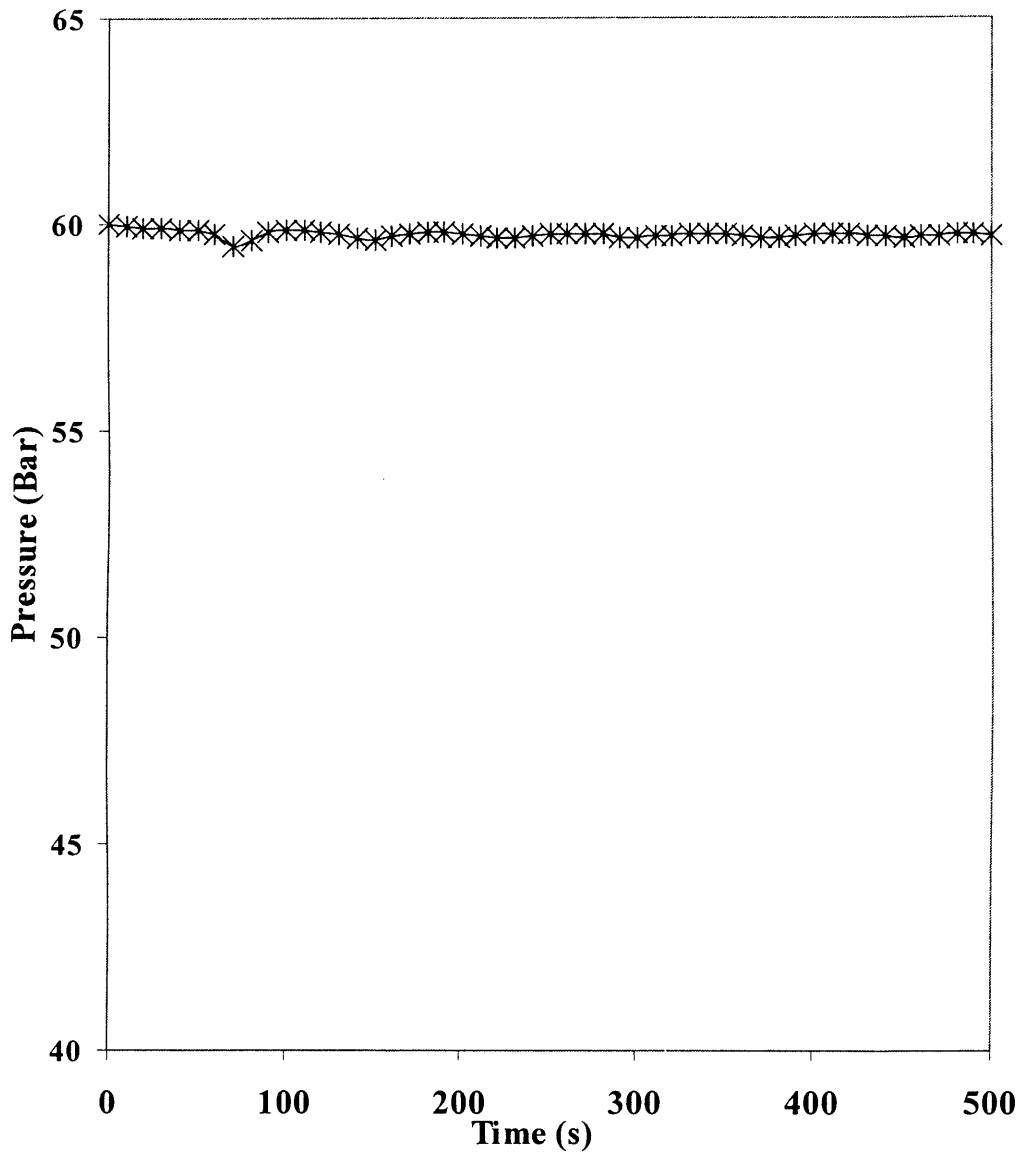


Figure 4.4: Variation of pressure with time for the isolated pipeline.

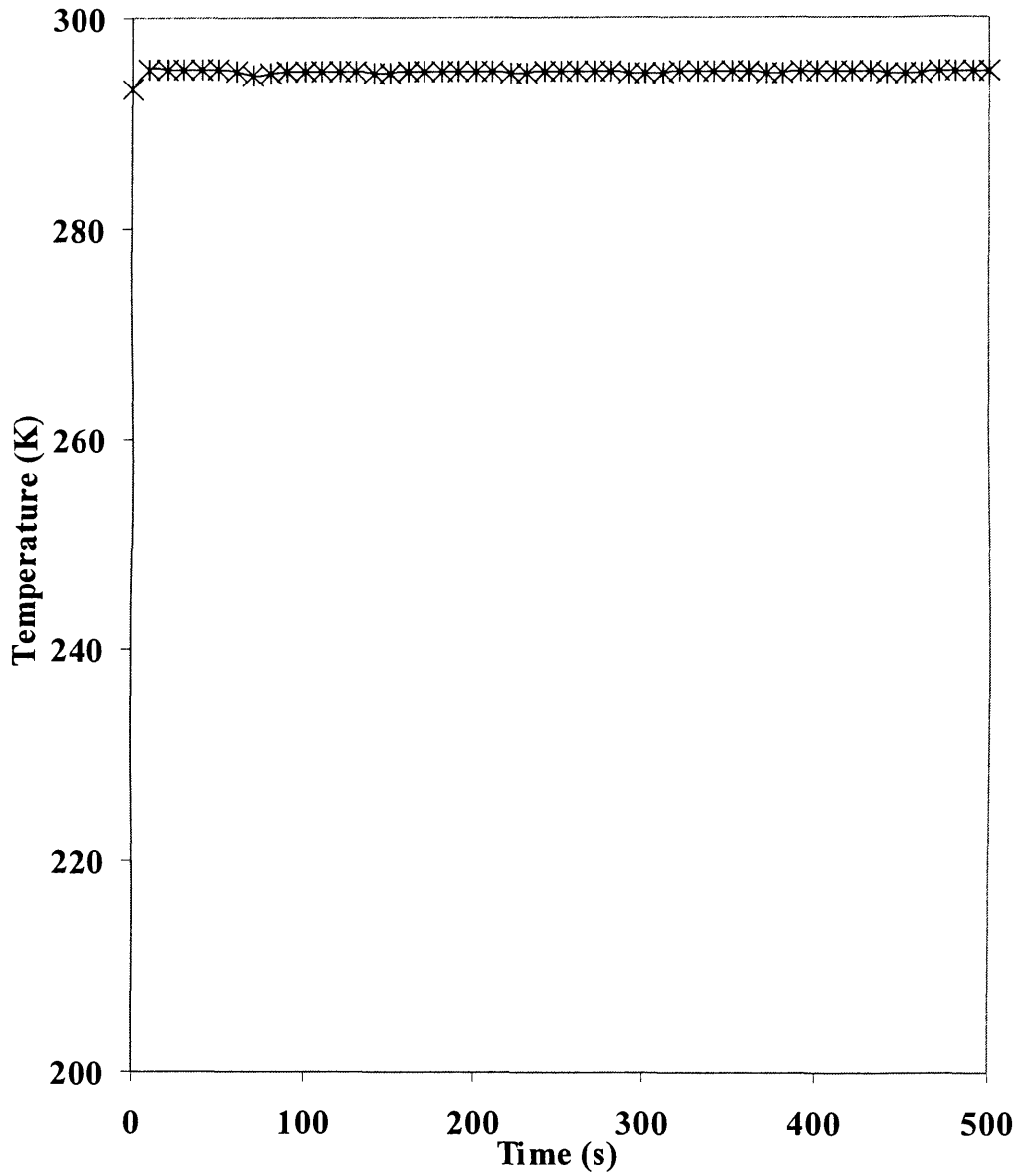


Figure 4.5: Variation of temperature with time for the isolated pipeline.

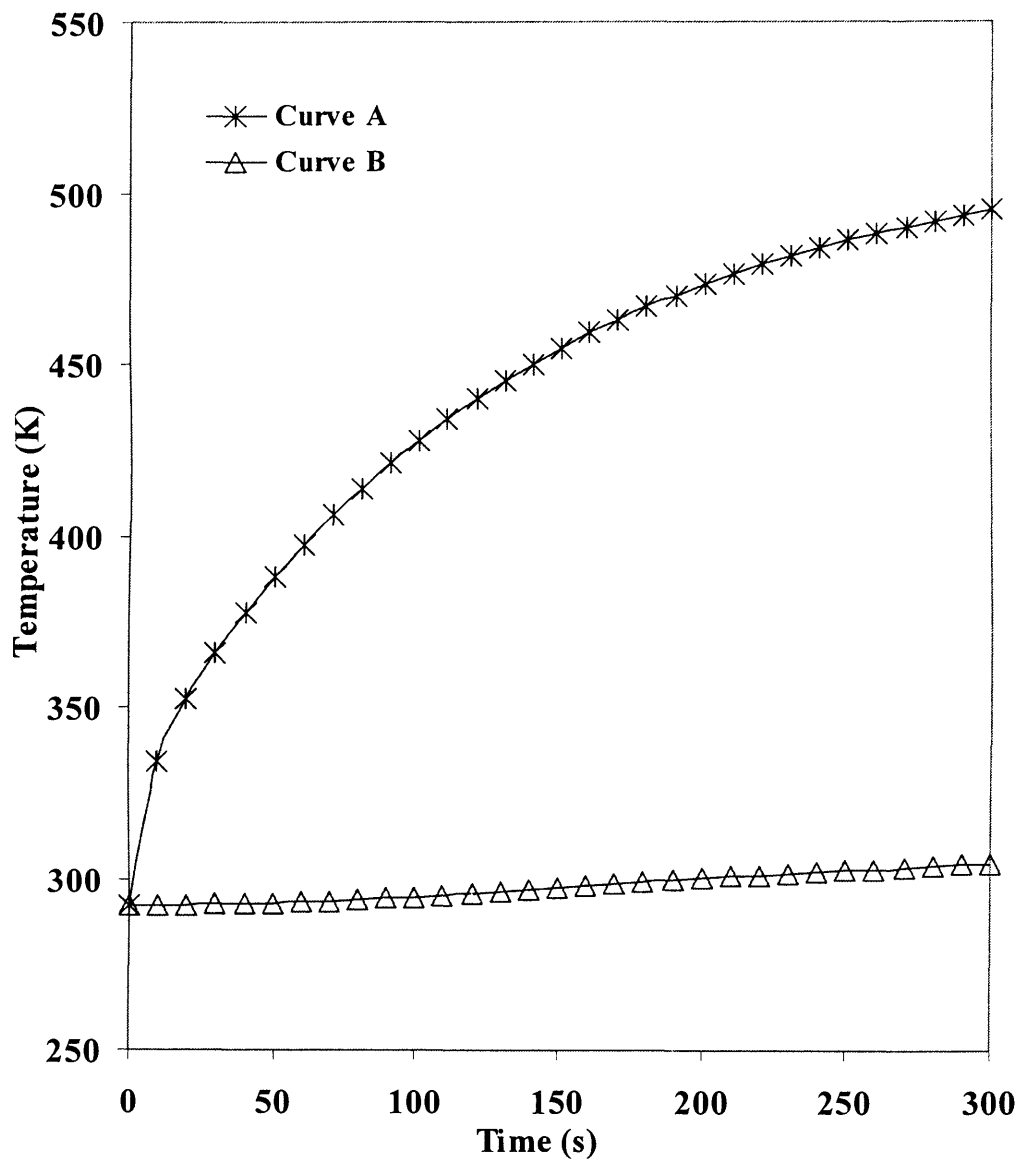


Figure 4.6: Variation of wall temperature with time at the region of fire for the isolated pipeline.

Curve A: Outer wall

Curve B: Inner wall

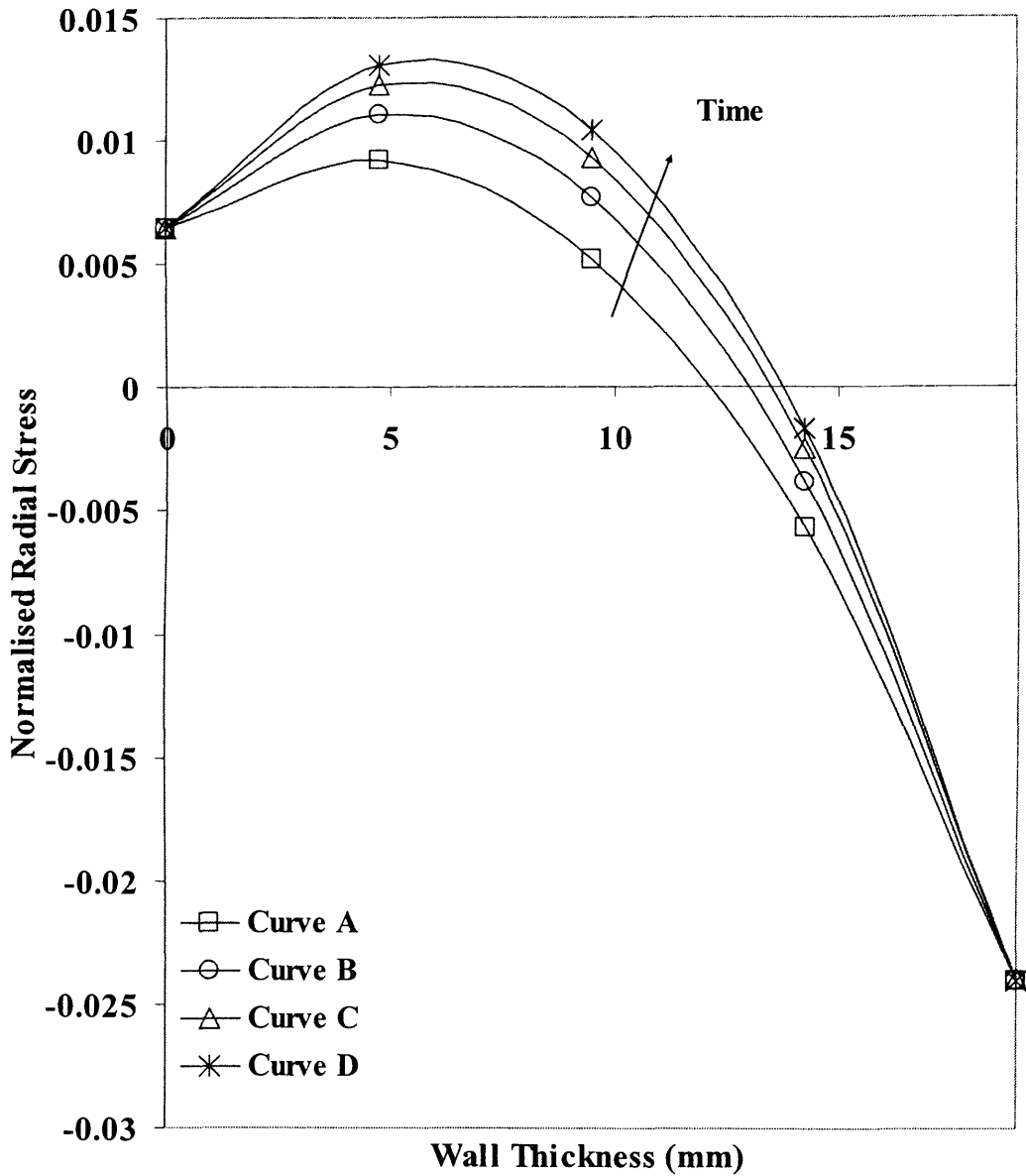


Figure 4.7: Total normalised radial stresses with time across the pipewall thickness for the isolated pipeline during fire attack.

Curve A: 100s, $\Psi(K) = 340.40$

Curve B: 150s, $\Psi(K) = 361.30$

Curve C: 200s, $\Psi(K) = 376.16$

Curve D: 300s, $\Psi(K) = 386.78$

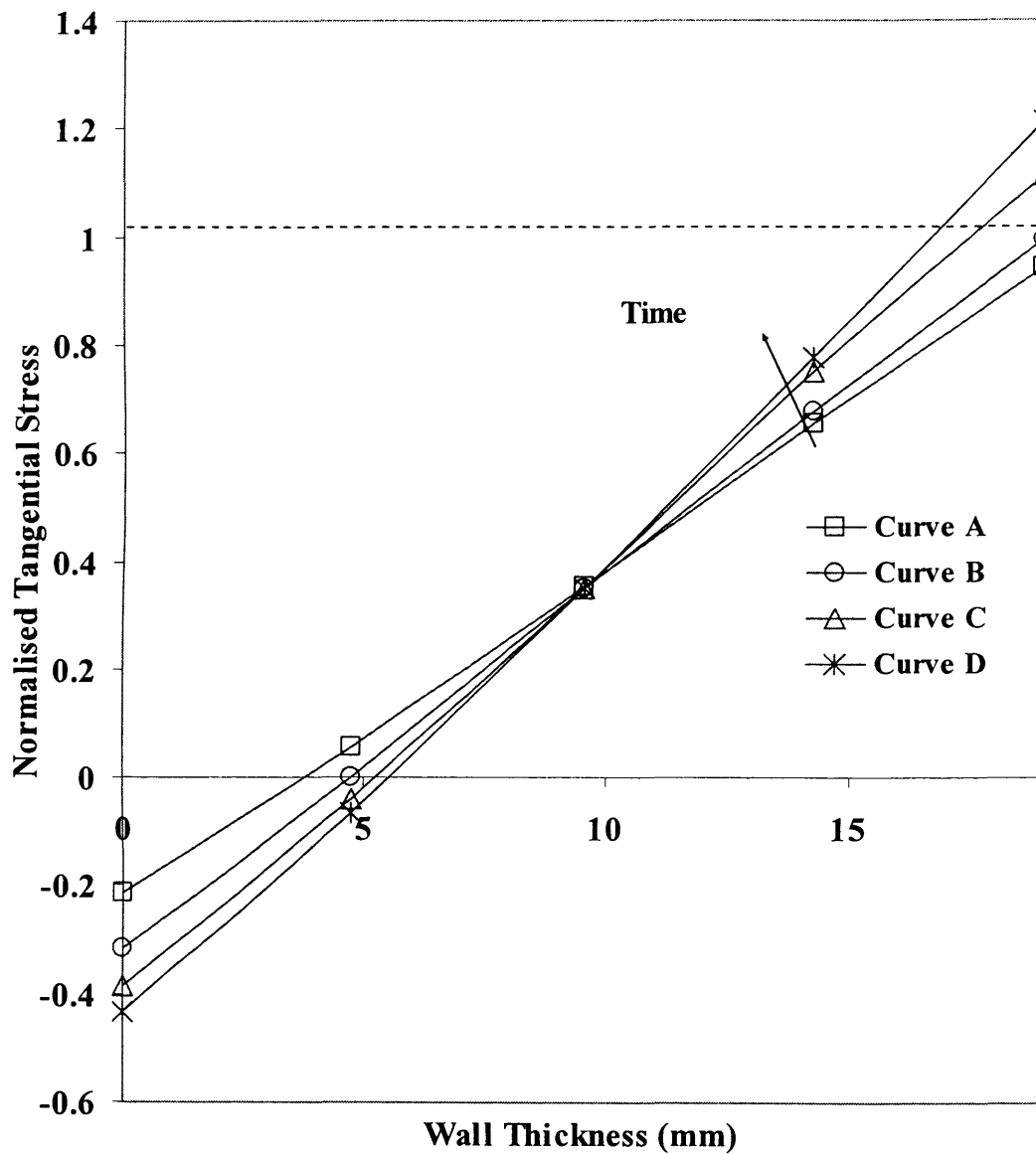


Figure 4.8: Total normalised tangential stresses with time across the pipewall thickness for the isolated pipeline during fire attack.

Curve A: 100s, $\Psi(K) = 340.40$

Curve B: 150s, $\Psi(K) = 361.30$

Curve C: 200s, $\Psi(K) = 376.16$

Curve D: 300s, $\Psi(K) = 386.78$

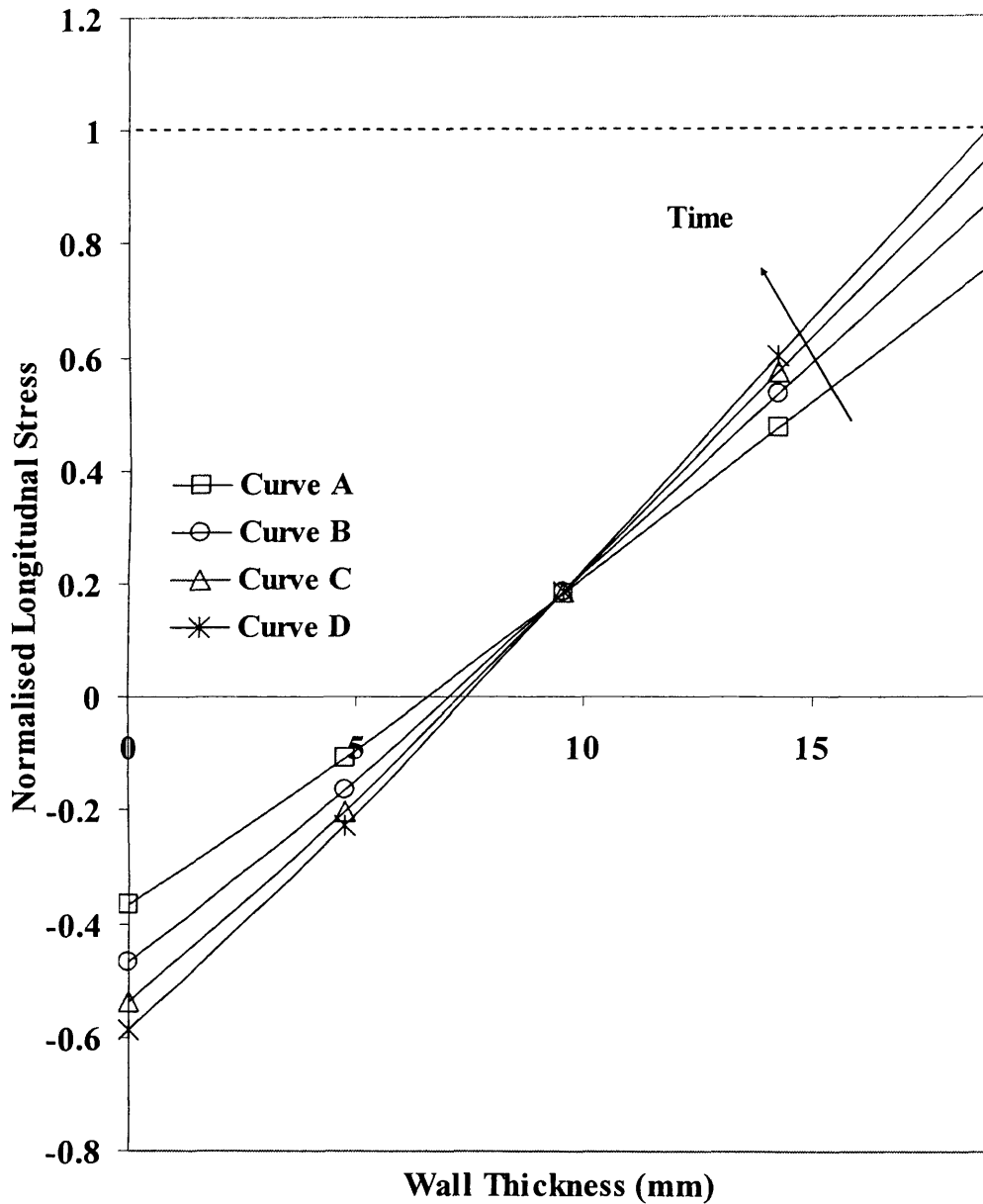


Figure 4.9: Total normalised longitudinal stresses with time across the pipewall thickness for the isolated pipeline during fire attack.

Curve A: 100s, $\Psi(K) = 340.40$

Curve B: 150s, $\Psi(K) = 361.30$

Curve C: 200s, $\Psi(K) = 376.16$

Curve D: 300s, $\Psi(K) = 386.78$

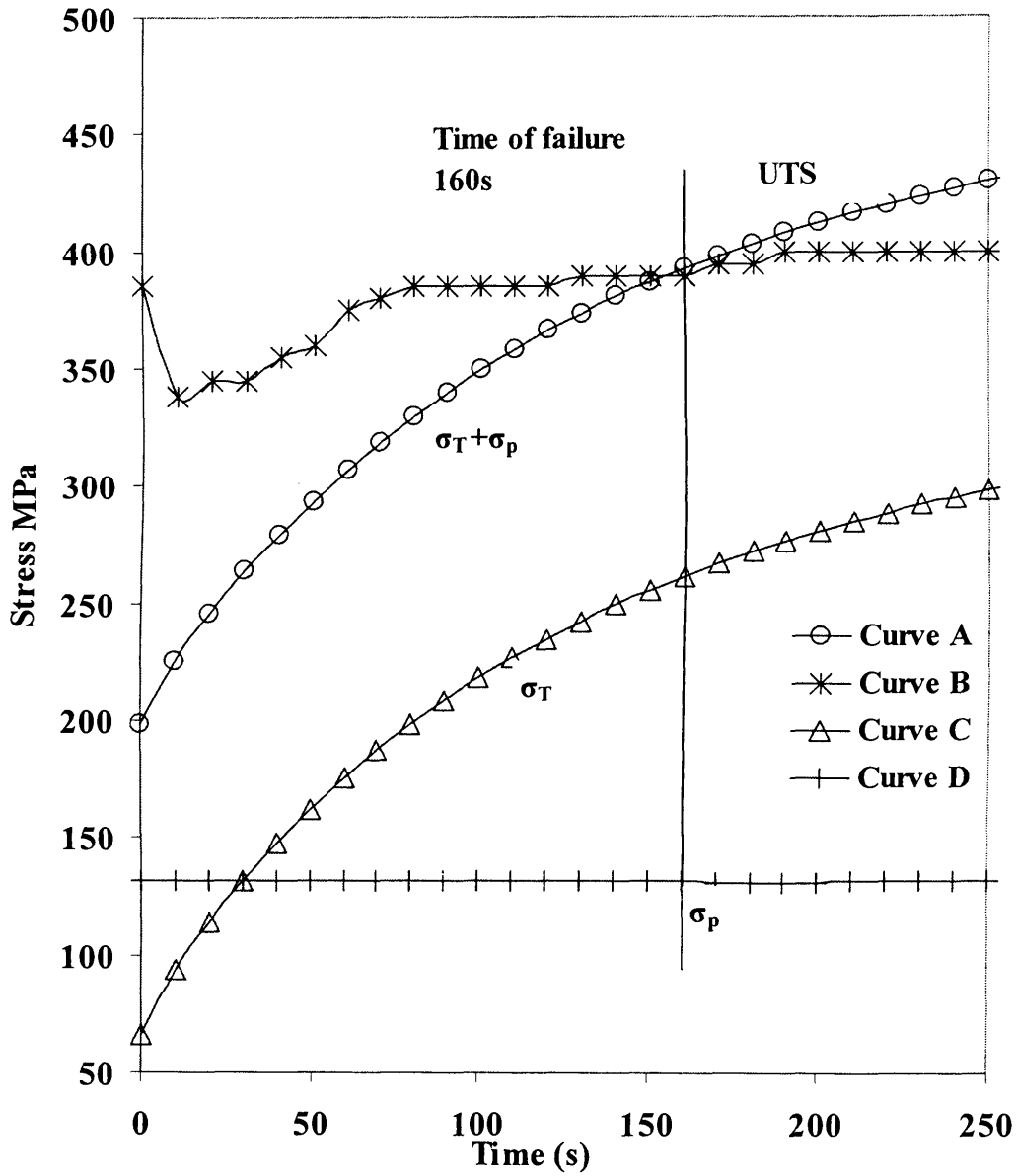


Figure 4.10: The variation of the various outer wall tangential stresses as a function of time for the isolated pipeline under fire attack.

- Curve A: Total Stresses $\sigma_T + \sigma_p$
- Curve B: Ultimate tensile stress (Carbon steel)
- Curve C: Thermal stress σ_T
- Curve D: Pressure stress σ_p

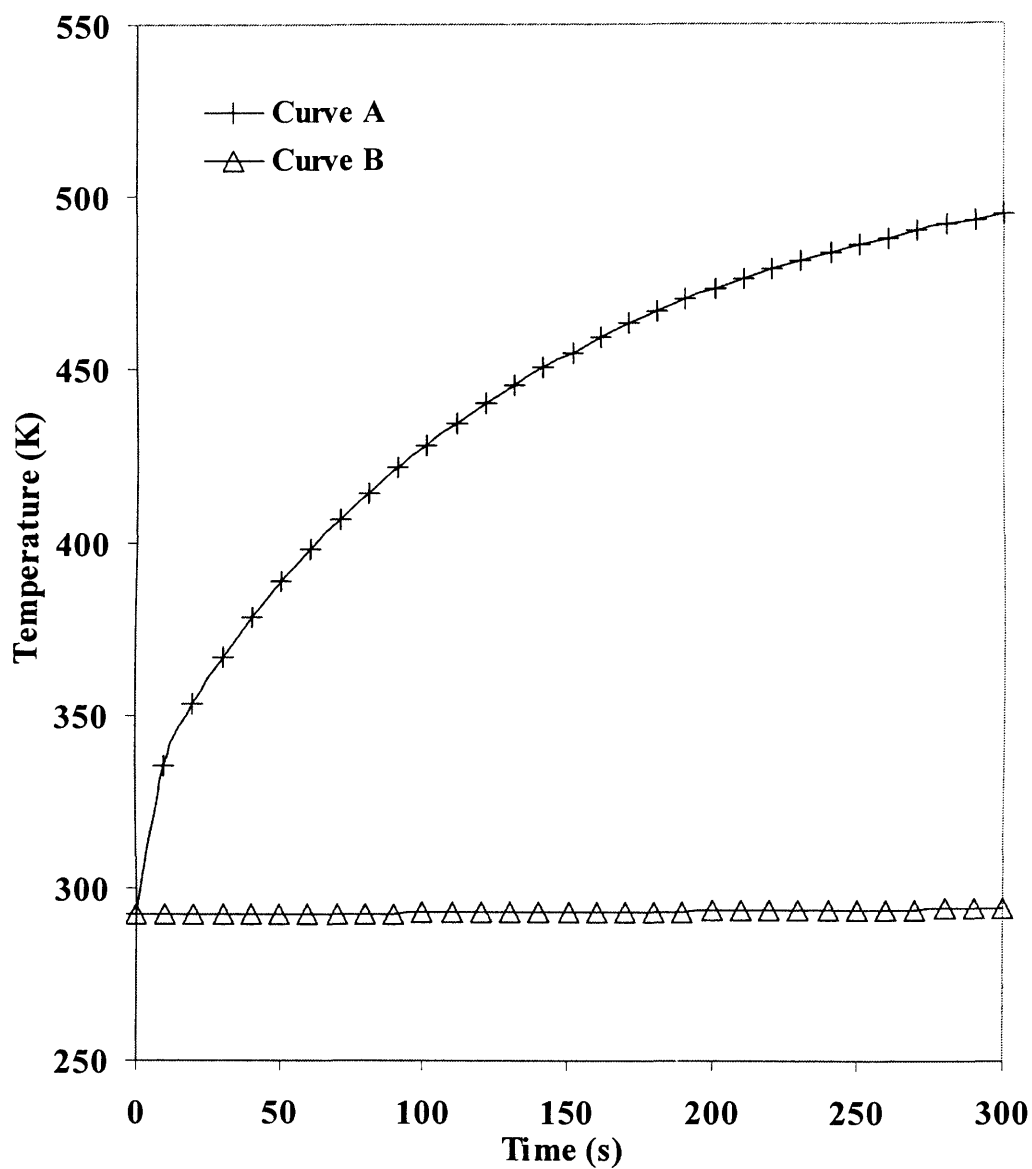


Figure 4.11: Variation of wall temperature with time at the region of fire for the unisolated pipeline depressurising through a 10mm relief valve.

Curve A: Outer wall

Curve B: Inner wall

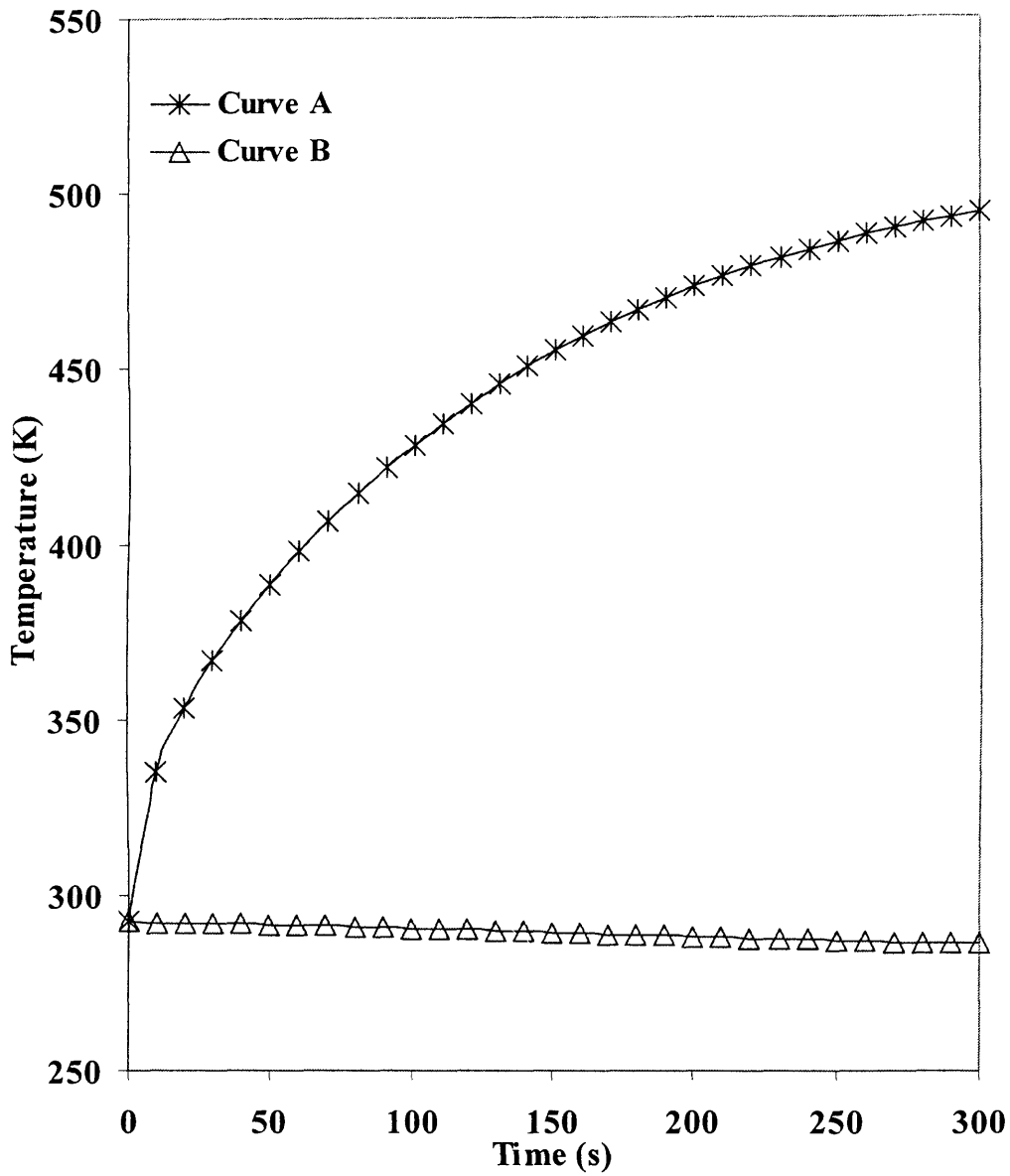


Figure 4.12: Variation of temperature with time at the region of fire for the unisolated pipeline depressurising through a 25mm relief valve.

Curve A: Outer wall

Curve B: Inner wall

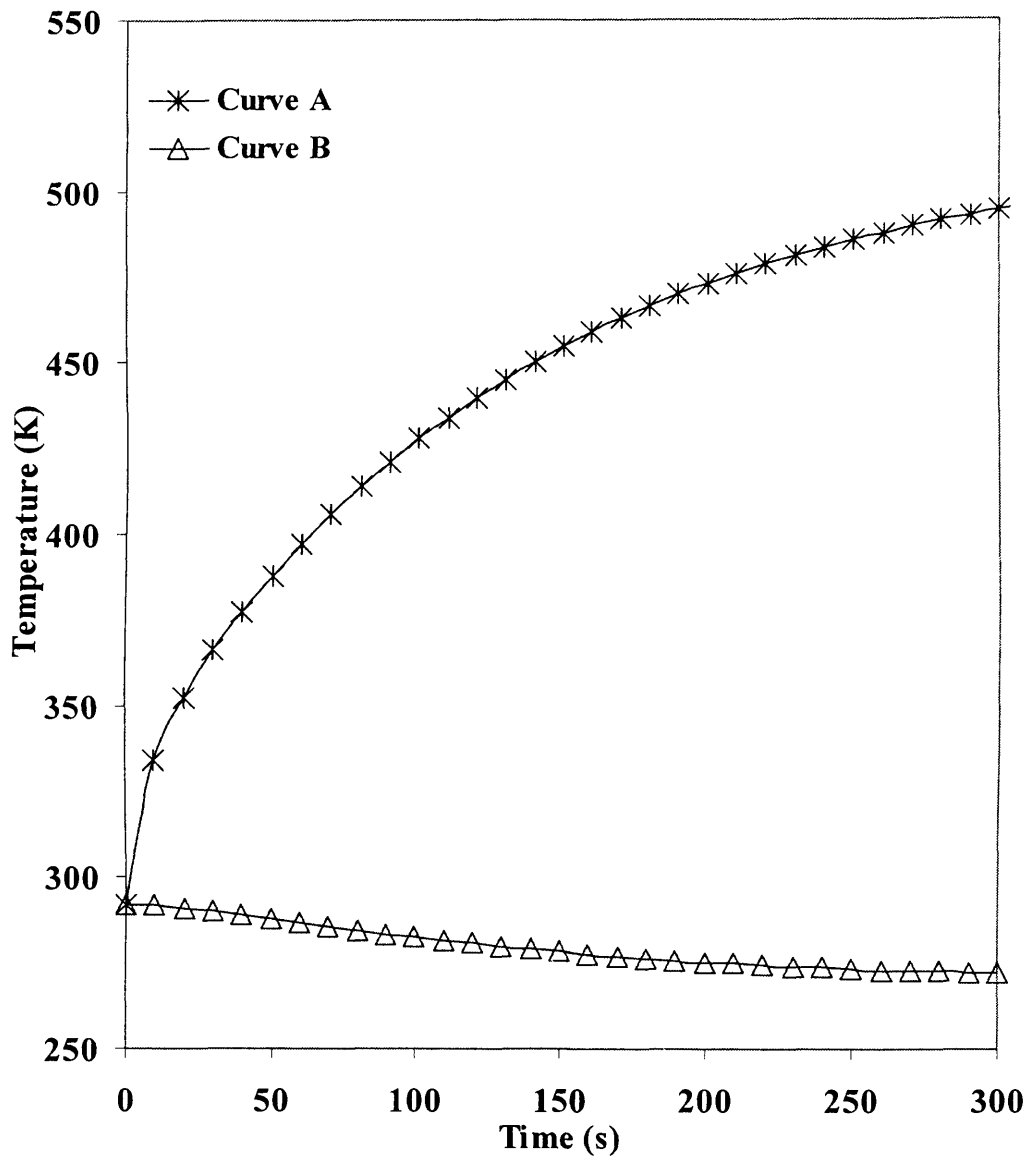


Figure 4.13: Variation of temperature with time at the region of fire for the unisolated pipeline depressurising through a 50mm relief valve.

Curve A: Outer wall

Curve B: Inner wall

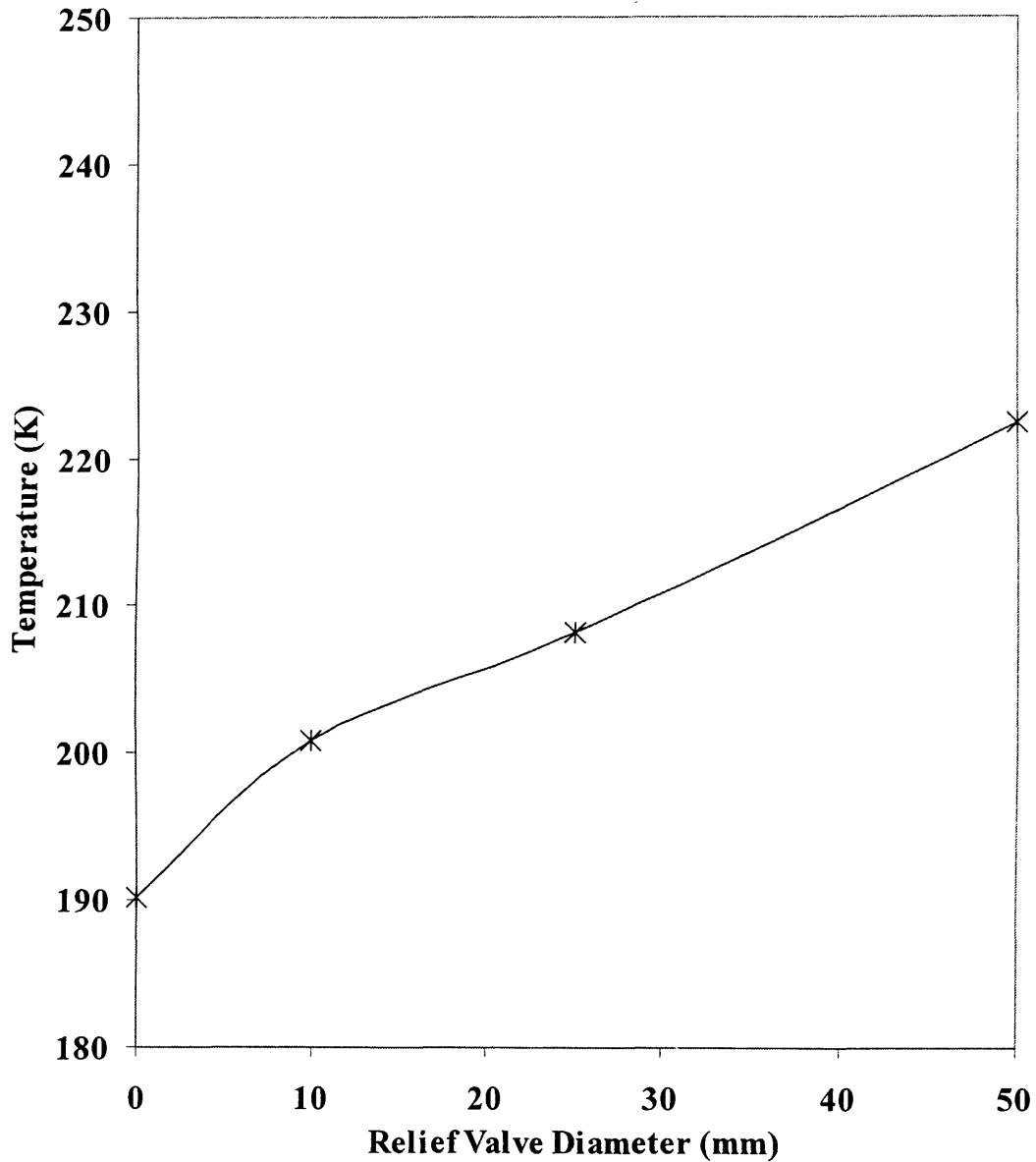


Figure 4.14: Variation of outer and inner wall temperatures difference against relief valve diameter at 300s following depressurisation.

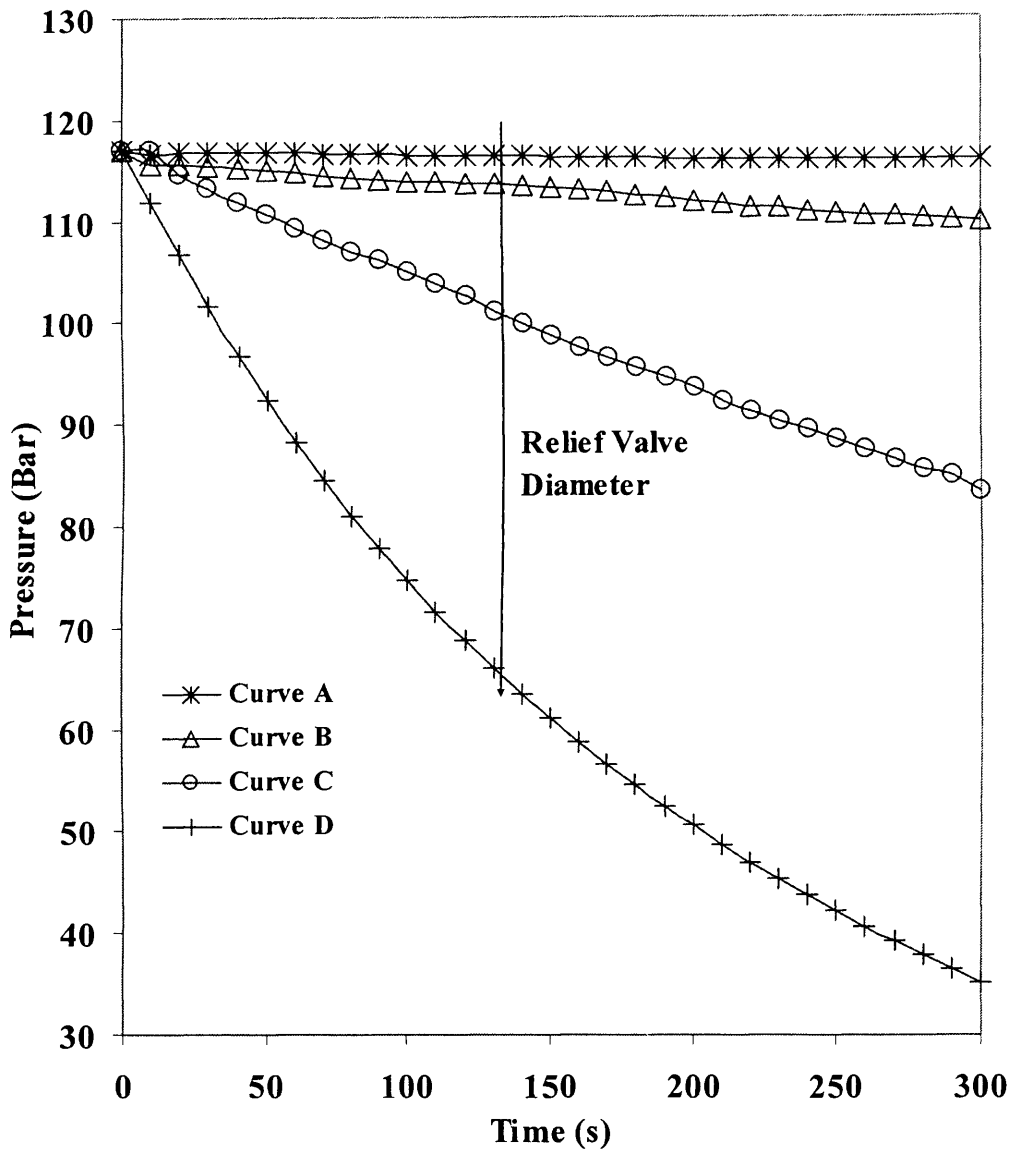


Figure 4.15: Variation of pressure at the orifice for the pipeline under different depressurising conditions.

Curve A: Isolated pipeline

Curve B: Pipeline depressurising through a 10mm relief valve

Curve C: Pipeline depressurising through a 25mm relief valve

Curve D: Pipeline depressurising through a 50mm relief valve

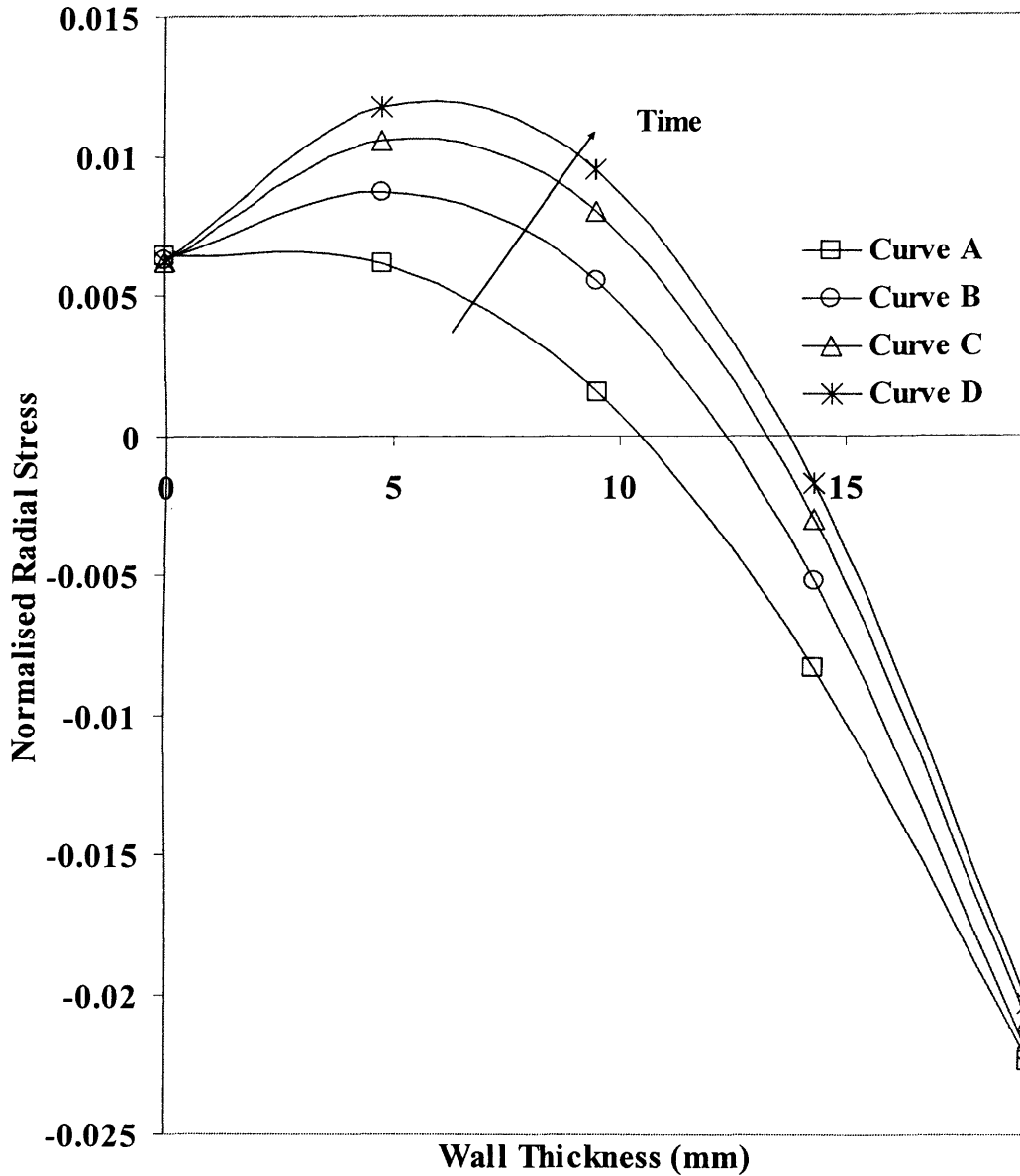


Figure 4.16: Total normalised radial stresses with time across the pipewall thickness for the pipeline depressurising through a 10mm relief valve during fire attack.

Curve A: 100s, $\Psi(K) = 340.48$

Curve B: 150s, $\Psi(K) = 360.47$

Curve C: 200s, $\Psi(K) = 373.99$

Curve D: 300s, $\Psi(K) = 383.33$

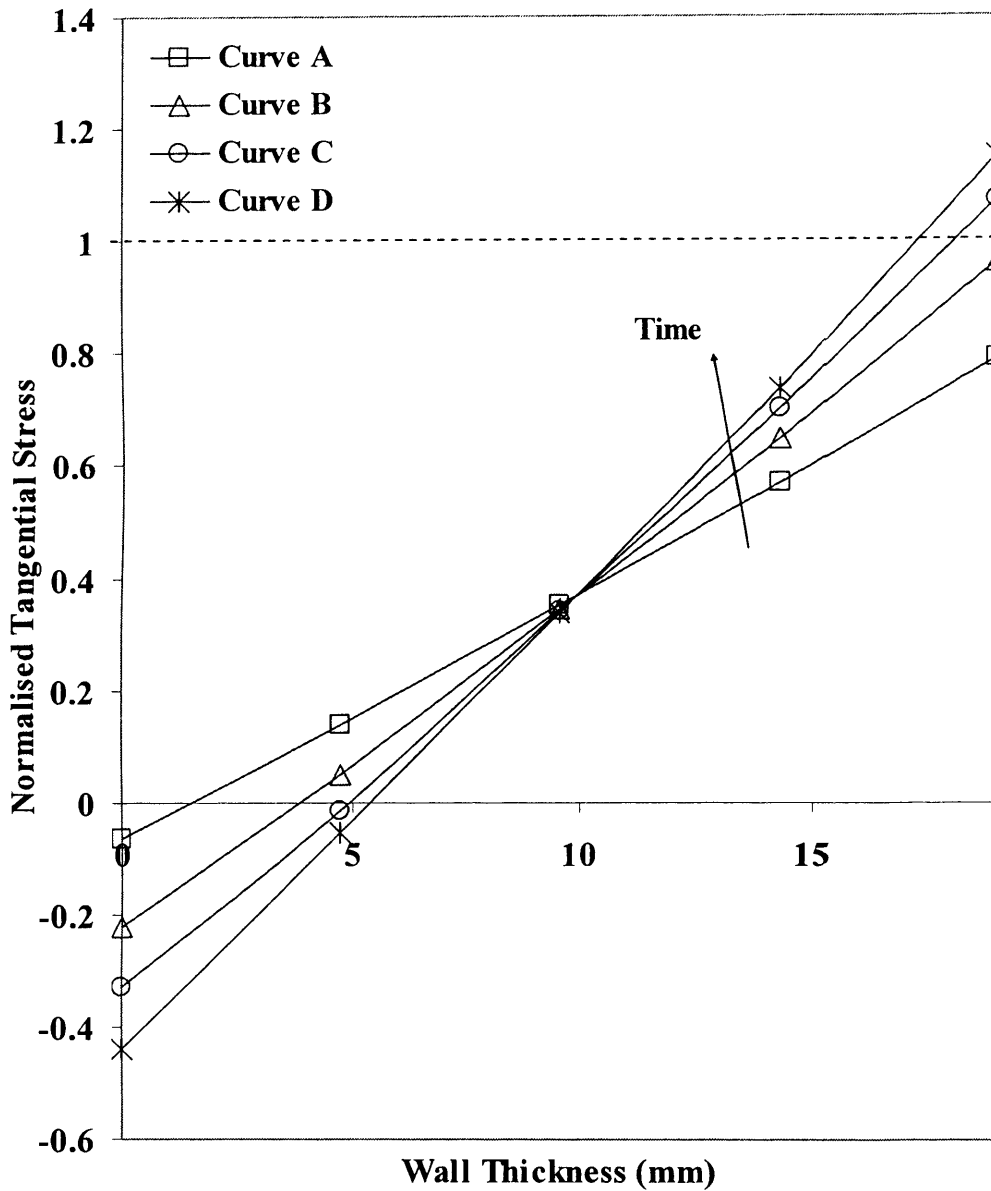


Figure 4.17: Total normalised tangential stresses with time along the pipewall thickness for the pipeline depressurising through a 10mm relief valve during fire attack.

Curve A: 100s, $\Psi(K) = 340.48$

Curve B: 150s, $\Psi(K) = 360.47$

Curve C: 200s, $\Psi(K) = 373.99$

Curve D: 300s, $\Psi(K) = 383.33$

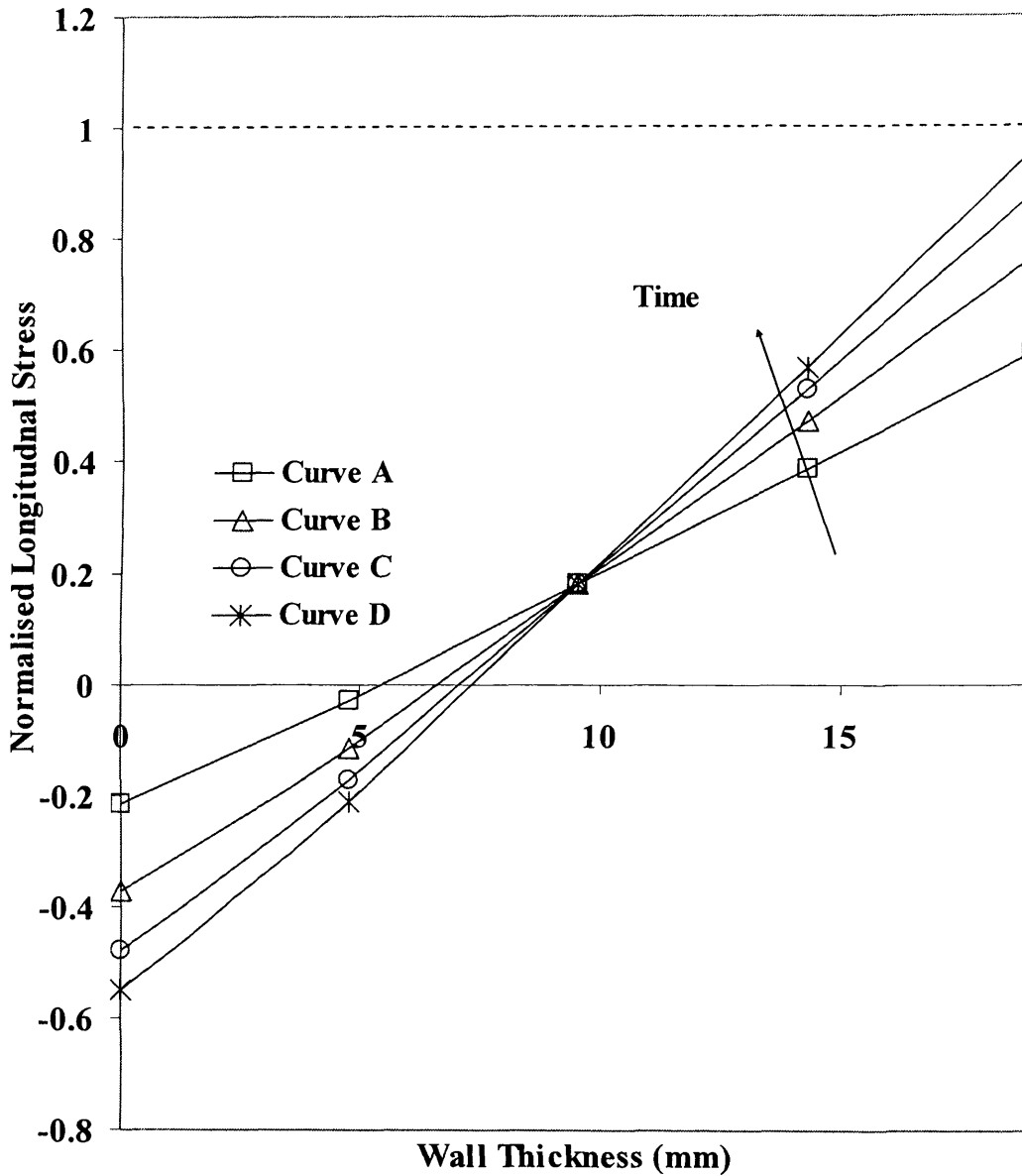


Figure 4.18: Total normalised longitudinal stresses with time across the pipewall thickness for the pipeline depressurising through a 10mm relief valve during fire attack.

Curve A: 100s, $\Psi(K)=340.48$

Curve B: 150s, $\Psi(K)=360.47$

Curve C: 200s, $\Psi(K)=373.99$

Curve D: 300s, $\Psi(K)=383.33$

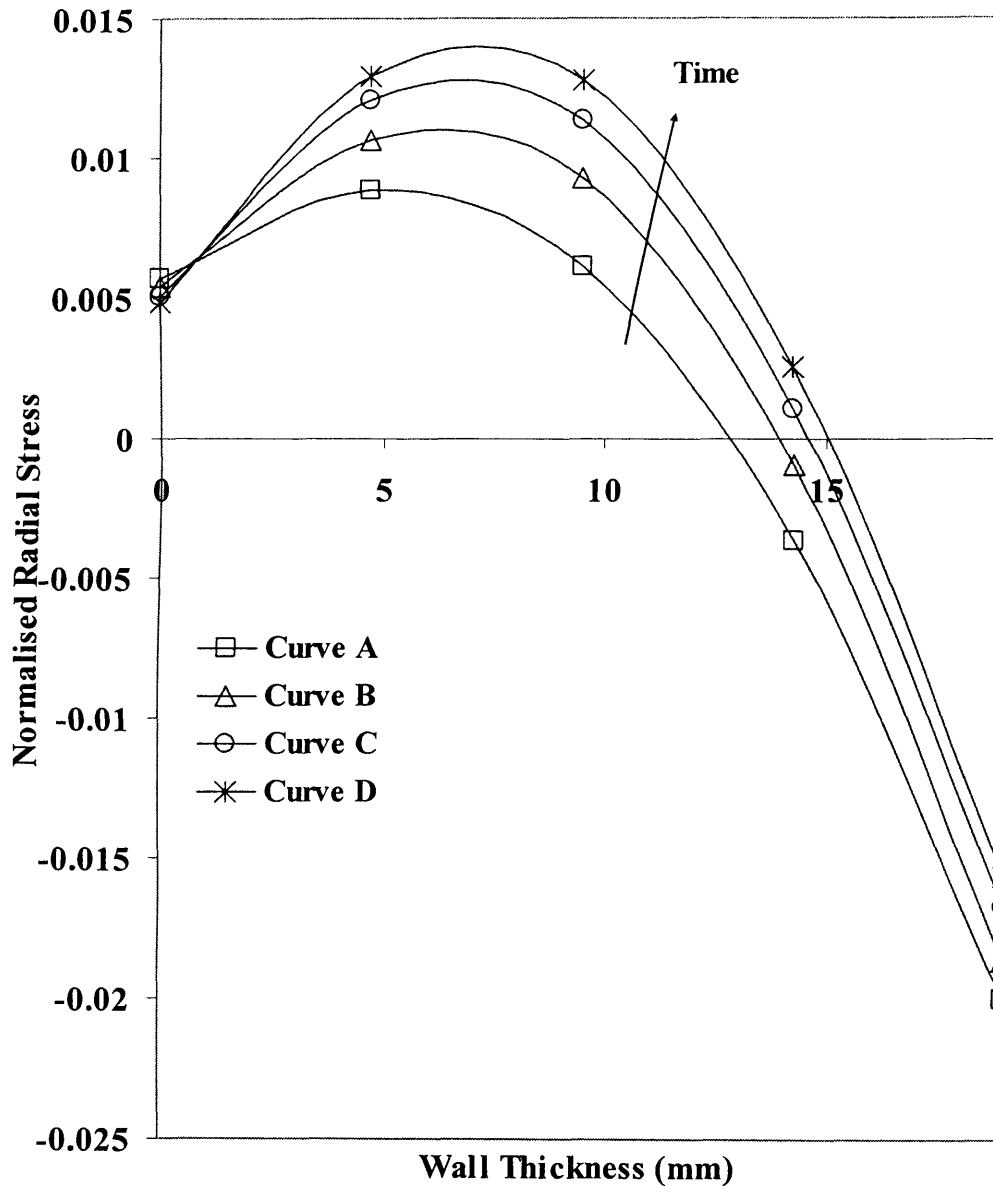


Figure 4.19: Total normalised radial stresses with time across the pipewall thickness for the pipeline depressurising through a 25mm relief valve during fire attack.

Curve A: 100s, $\Psi(K) = 359.37$

Curve B: 150s, $\Psi(K) = 372.19$

Curve C: 200s, $\Psi(K) = 380.77$

Curve D: 300s, $\Psi(K) = 386.48$

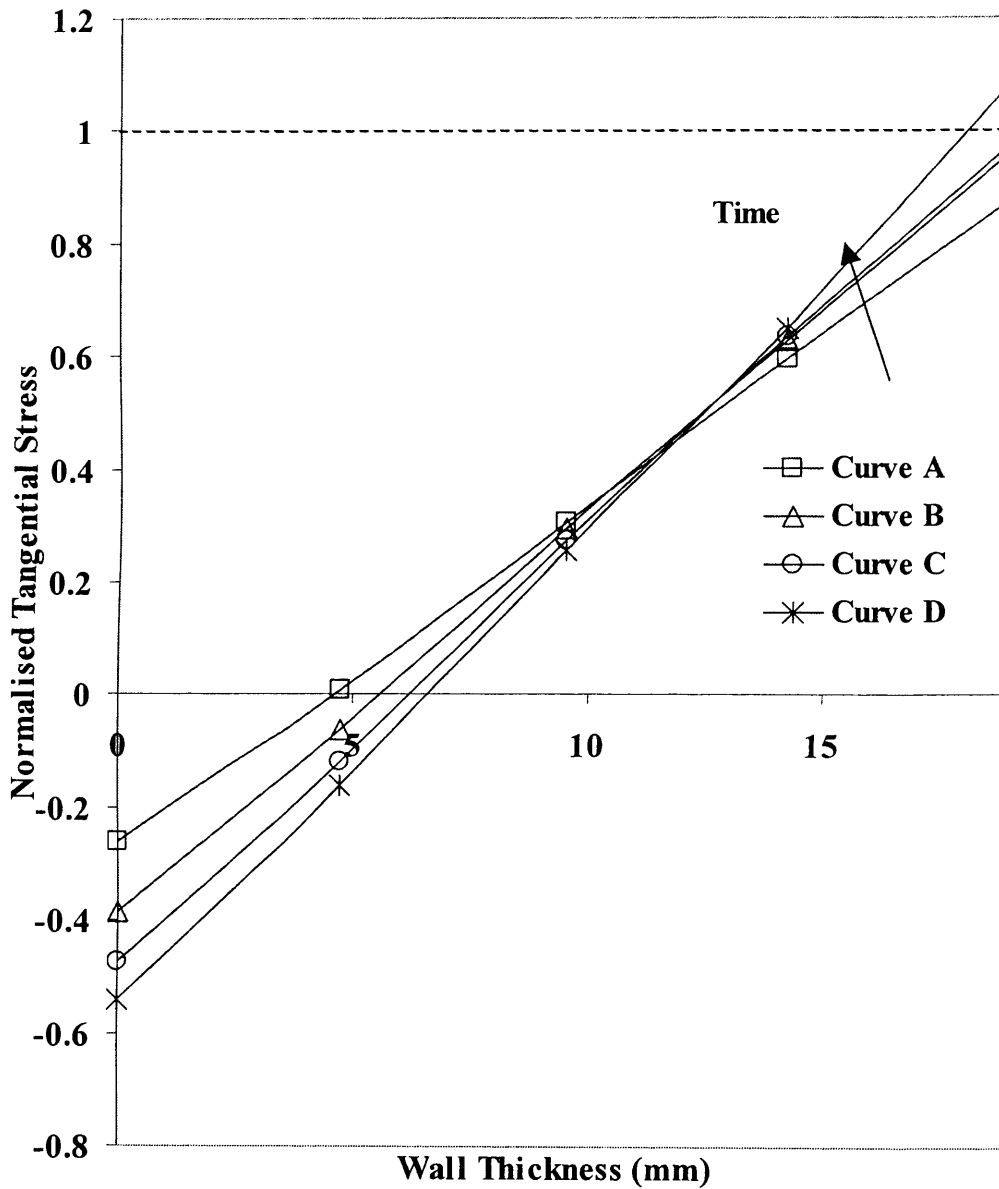


Figure 4.20: Total normalised tangential stresses with time across the pipewall thickness for the pipeline depressurising through a 25mm relief valve during fire attack.

Curve A: 100s, $\Psi(K) = 359.37$

Curve B: 150s, $\Psi(K) = 372.19$

Curve C: 200s, $\Psi(K) = 380.77$

Curve D: 300s, $\Psi(K) = 386.48$

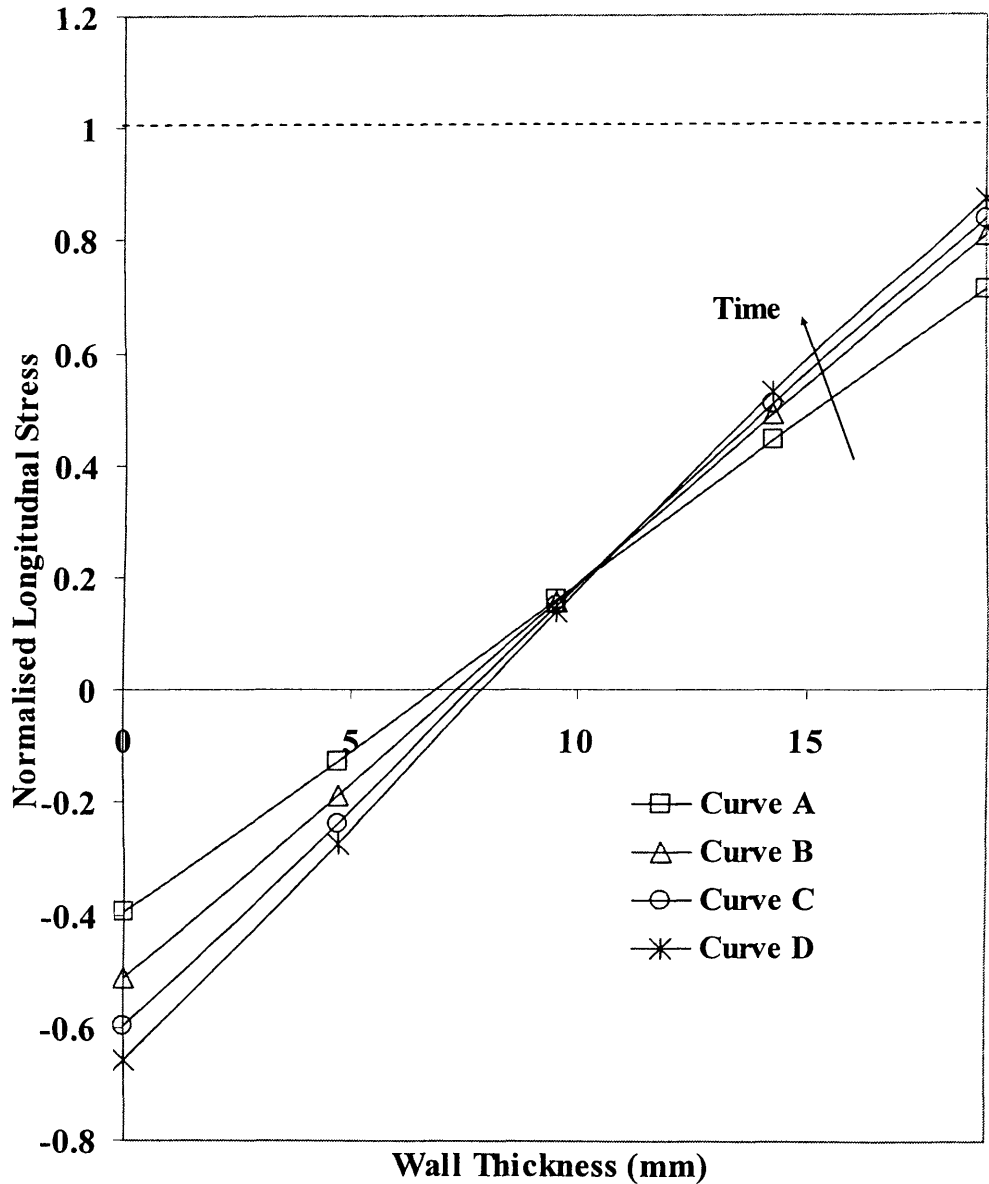


Figure 4.21: Total normalised longitudinal stresses with time across the pipewall thickness for the pipeline depressurising through a 25mm relief valve during fire attack.

Curve A: 100s, $\Psi(K) = 359.37$

Curve B: 150s, $\Psi(K) = 372.19$

Curve C: 200s, $\Psi(K) = 380.77$

Curve D: 300s, $\Psi(K) = 386.48$

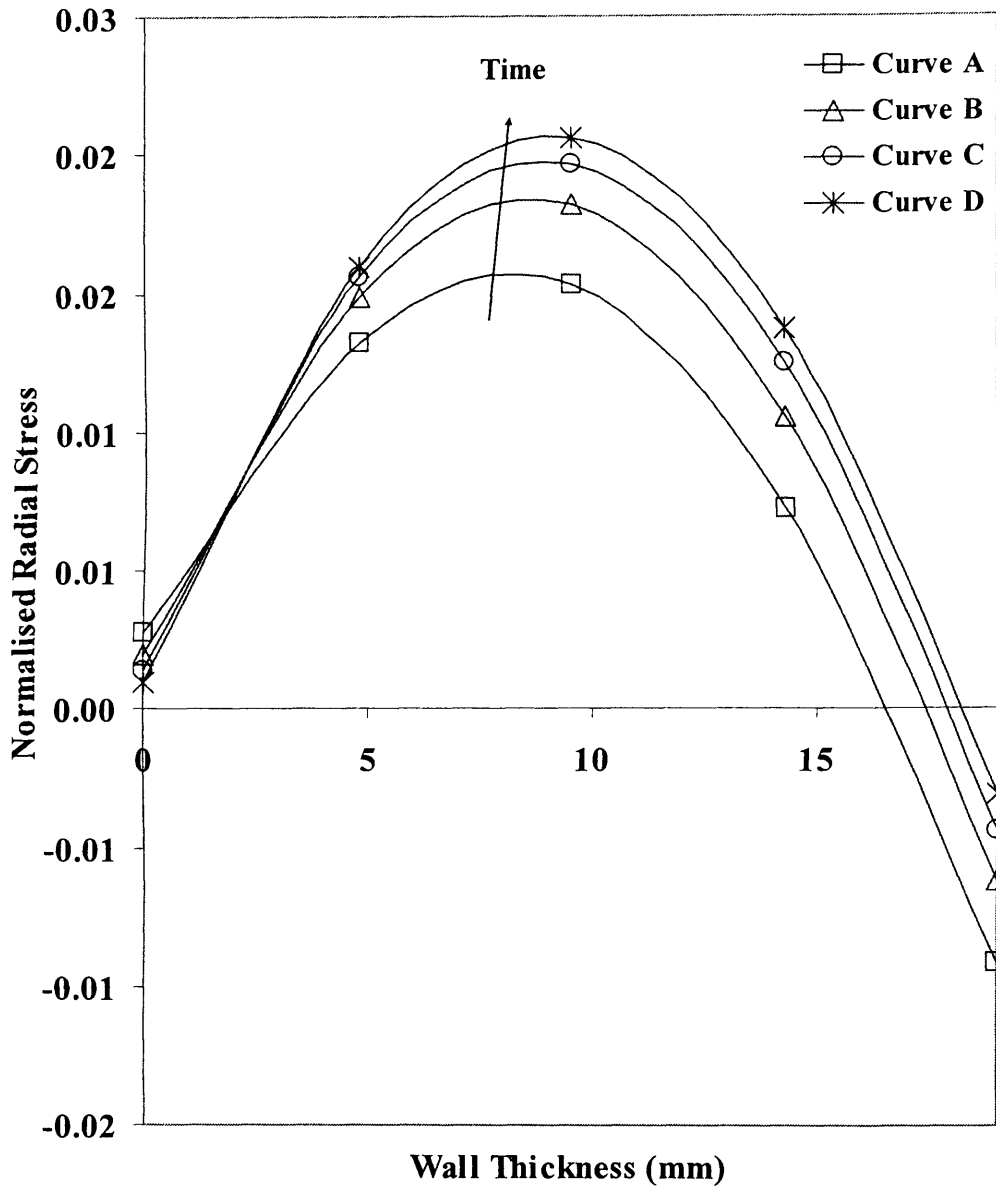


Figure 4.22: Total normalised radial stresses with time across the pipewall thickness for the pipeline depressurising through a 50mm relief valve during fire attack.

Curve A: After 200s, $\Psi(K) = 374.20$

Curve B: After 300s, $\Psi(K) = 383.24$

Curve C: After 400s, $\Psi(K) = 387.58$

Curve D: After 500s, $\Psi(K) = 389.76$

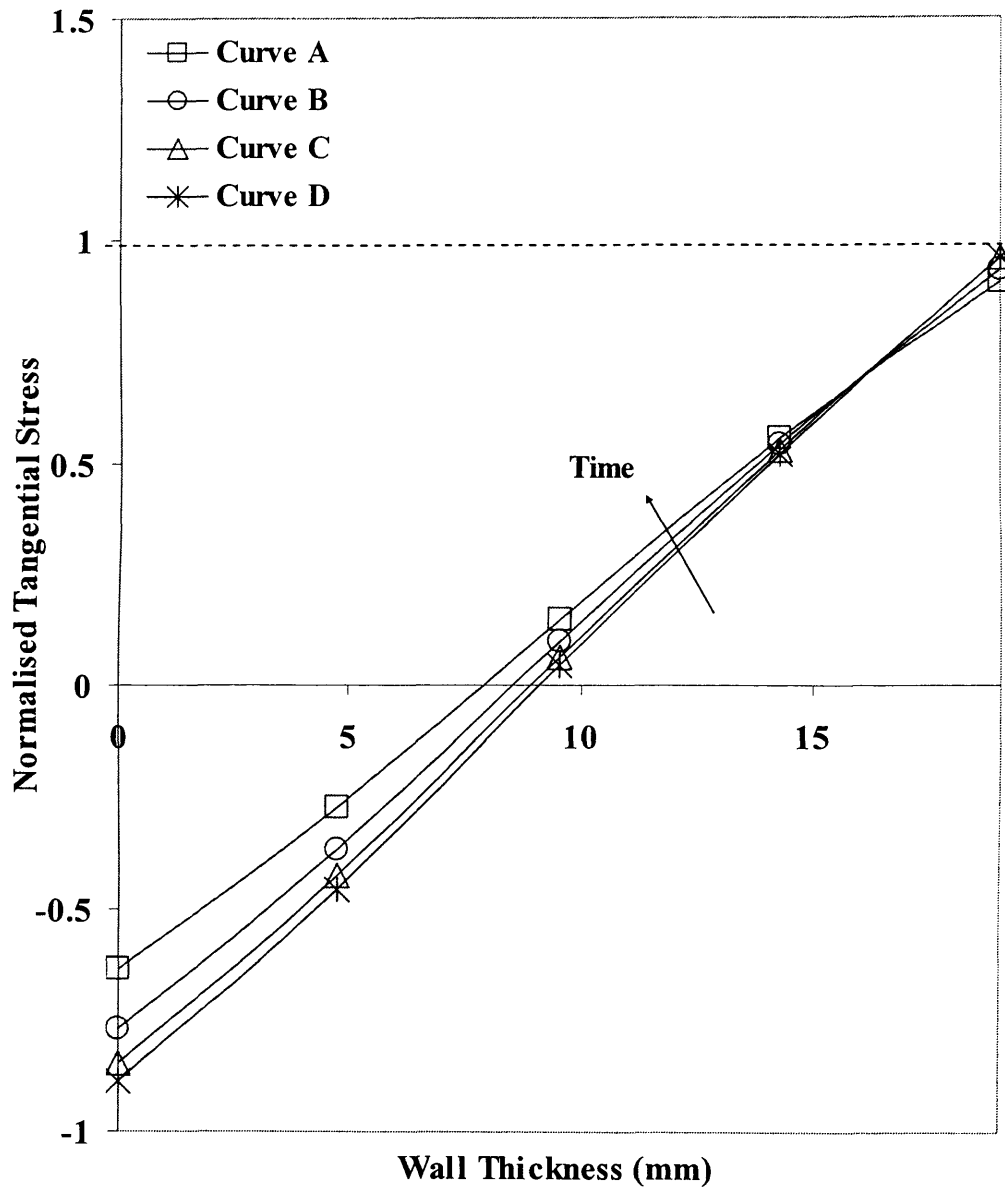


Figure 4.23: Total normalised tangential stresses with time across the pipewall thickness for the pipeline depressurising through a 50mm relief valve during fire attack.

Curve A: After 200s, $\Psi(K) = 374.20$

Curve B: After 300s, $\Psi(K) = 383.24$

Curve C: After 400s, $\Psi(K) = 387.58$

Curve D: After 500s, $\Psi(K) = 389.76$

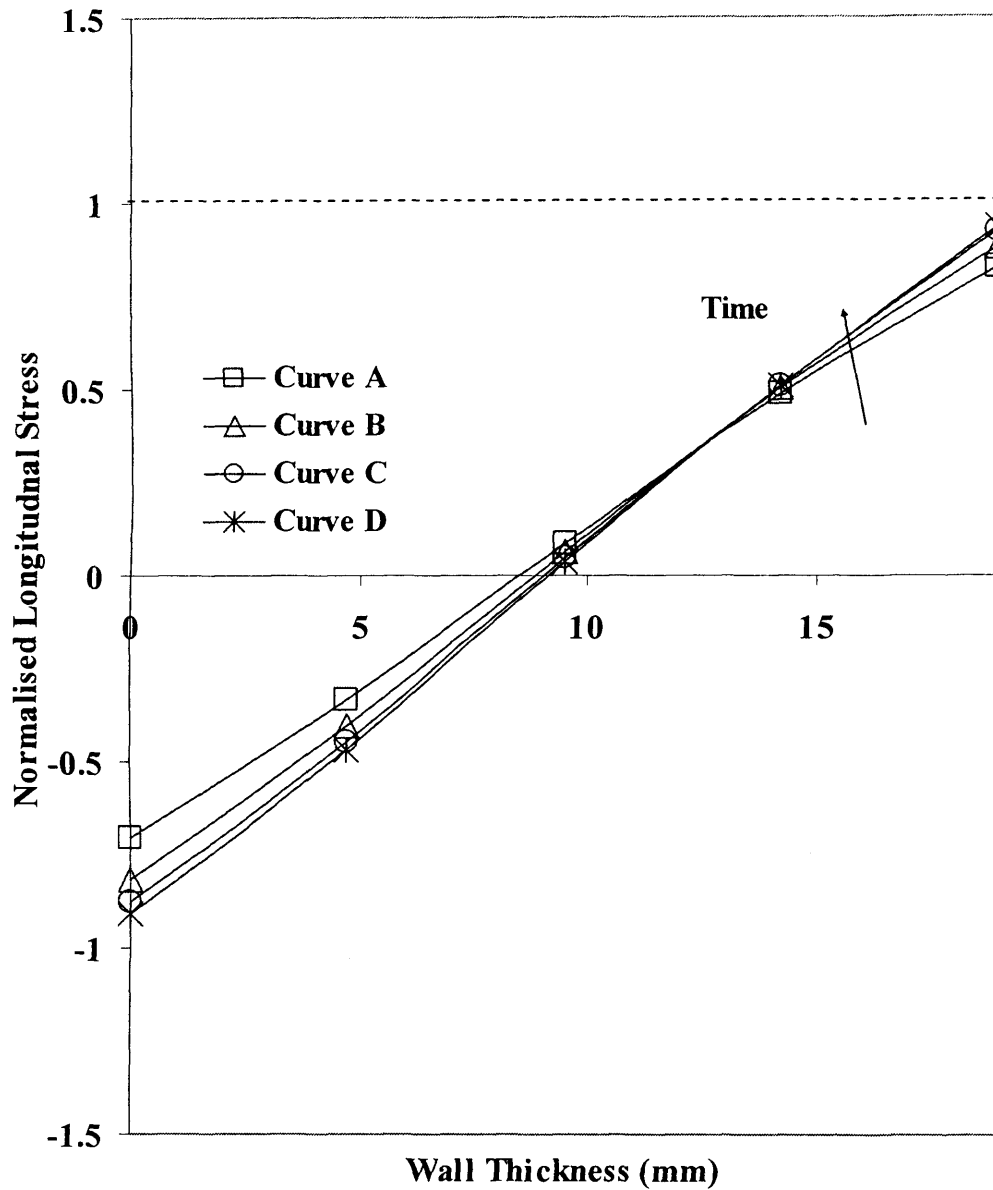


Figure 4.24: Total normalised longitudinal stresses with time across the pipewall thickness for the pipeline depressurising through a 50 mm relief valve during fire attack.

Curve A: After 200s, $\Psi(K) = 374.20$

Curve B: After 300s, $\Psi(K) = 383.24$

Curve C: After 400s, $\Psi(K) = 387.58$

Curve D: After 500s, $\Psi(K) = 389.76$

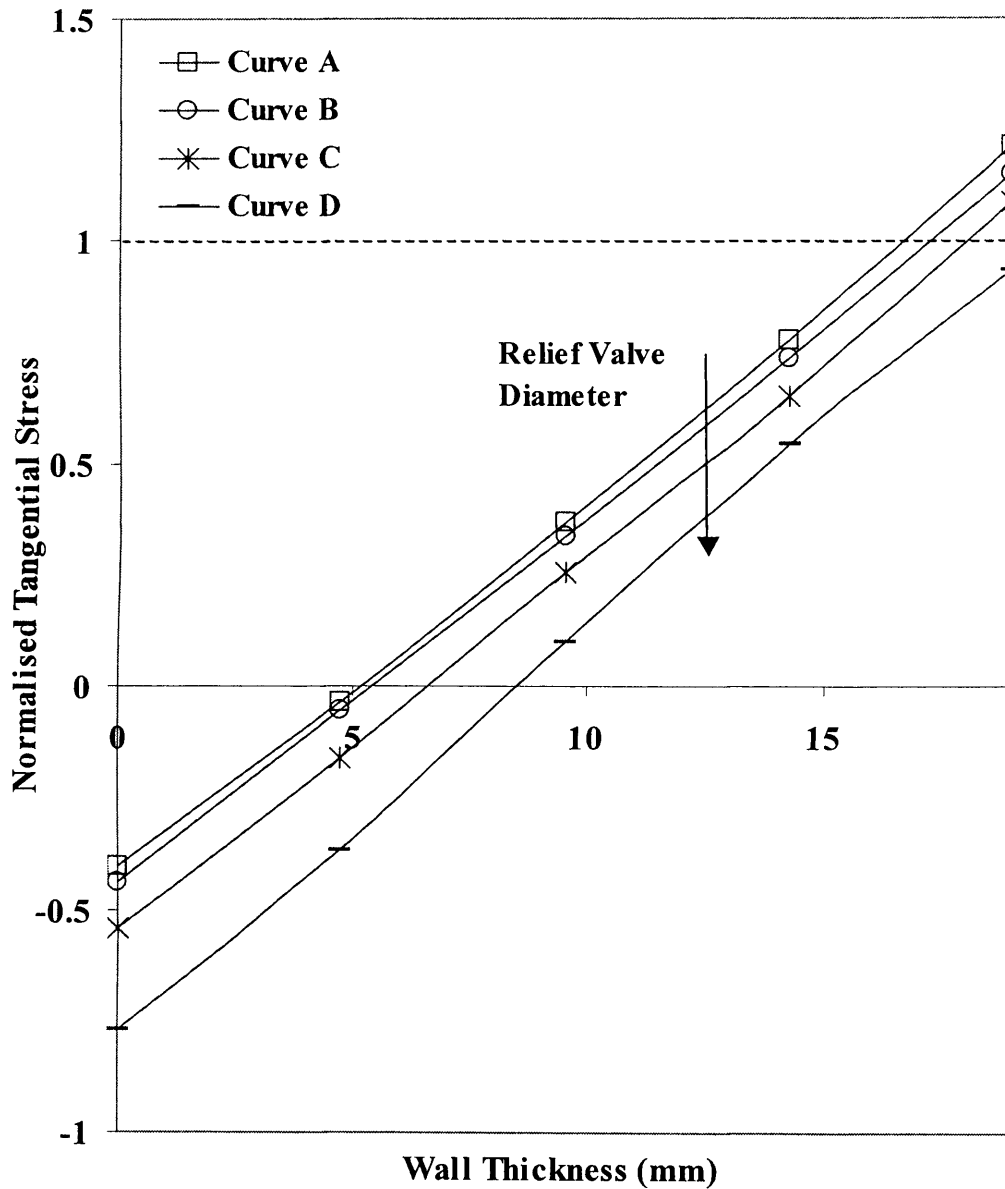


Figure 4.25: Variation of outer wall normalised tangential stresses across pipewall thickness during fire attack depressurisation through various relief valve diameters.

- Curve A: Isolated pipeline
- Curve B: 10mm relief valve
- Curve C: 25mm relief valve
- Curve D: 50mm relief valve

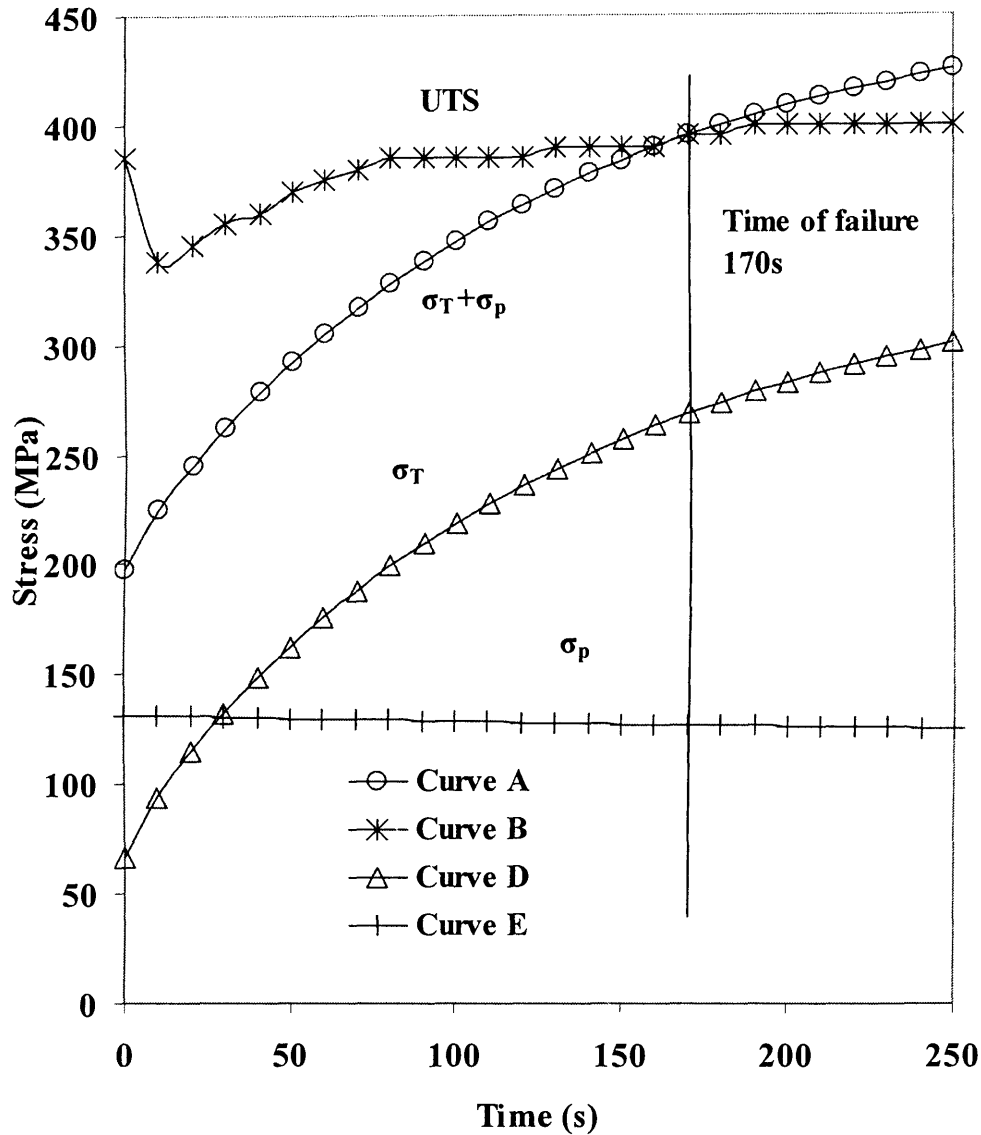


Figure 4.26: The variation of the various outer wall tangential stresses as a function of time for the pipeline depressurising through a 10mm relief valve under fire attack.

- Curve A: Total Stresses $\sigma_T + \sigma_p$
- Curve B: Ultimate tensile stress (Carbon steel)
- Curve C: Thermal stress σ_T
- Curve D: Pressure stress σ_p

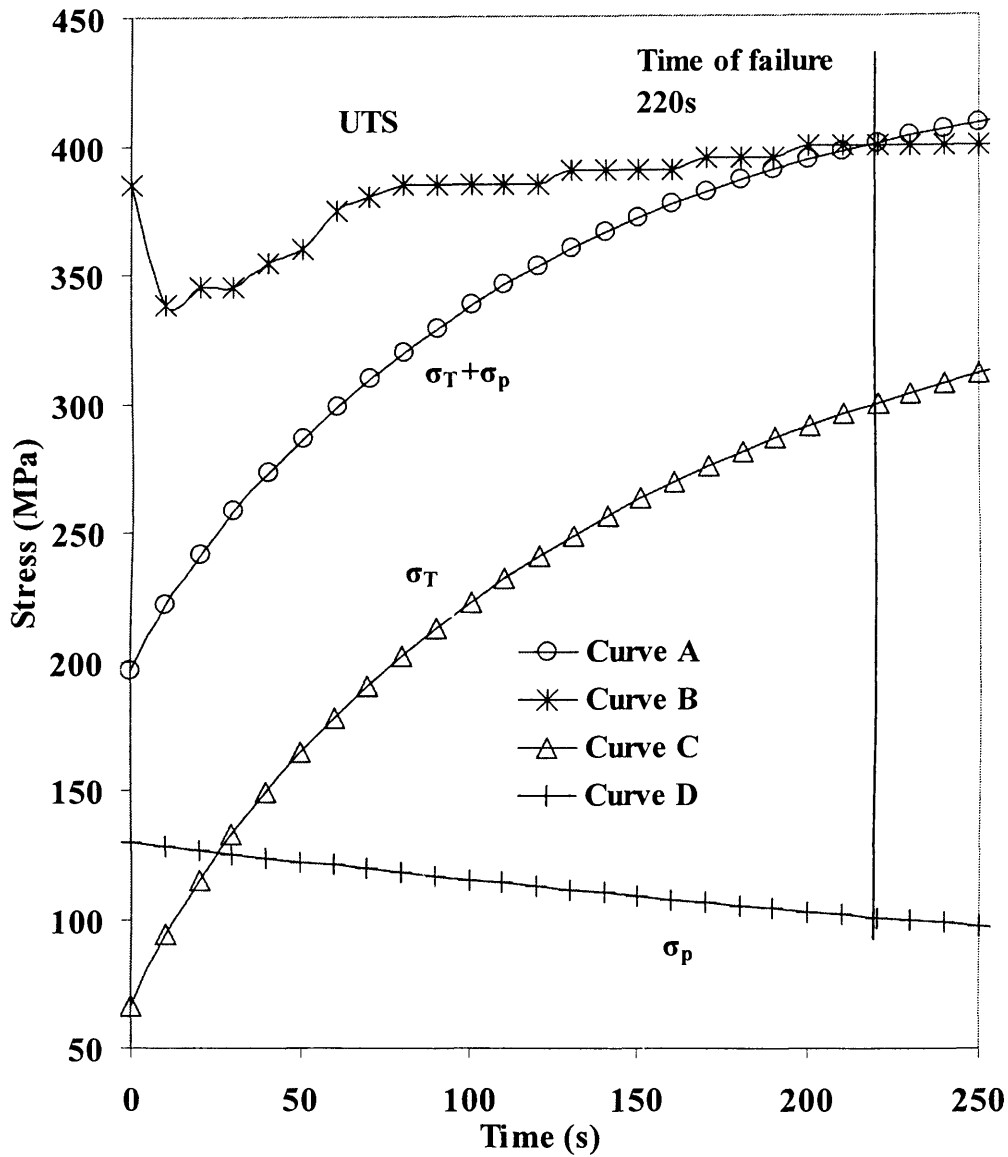


Figure 4.27: The variation of the various outer wall tangential stresses as a function of time for the pipeline depressurising through a 25mm relief valve under fire attack.

- Curve A: Total Stresses $\sigma_T + \sigma_p$
- Curve B: Ultimate tensile stress (Carbon steel)
- Curve C: Thermal stress σ_T
- Curve D: Pressure stress σ_p

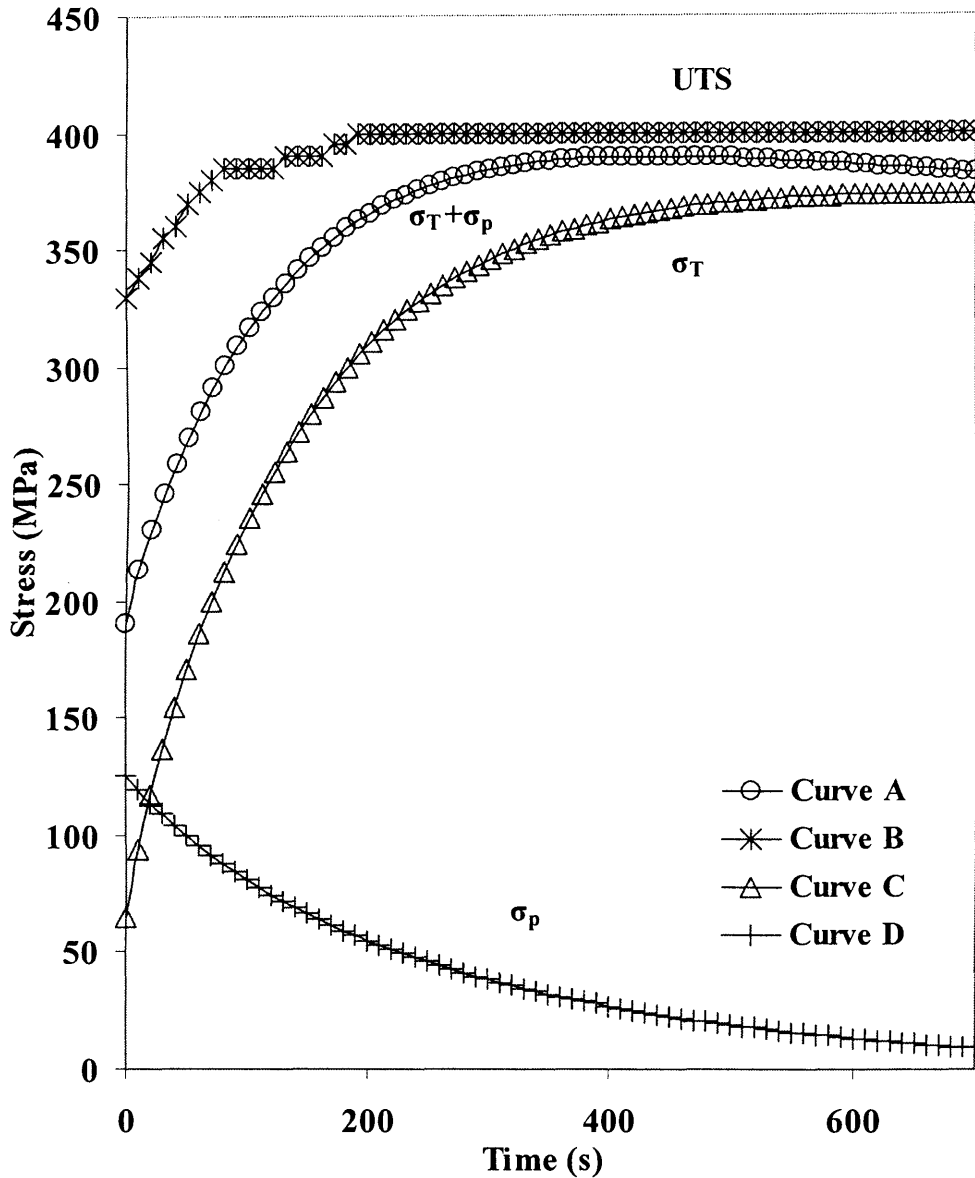


Figure 4.28: The variation of the various outer wall tangential stresses as a function of time for the pipeline depressurising through a 50mm relief valve under fire attack.

- Curve A: Total Stresses $\sigma_T + \sigma_p$
- Curve B: Ultimate tensile stress (Carbon steel)
- Curve C: Thermal stress σ_T
- Curve D: Pressure stress σ_p

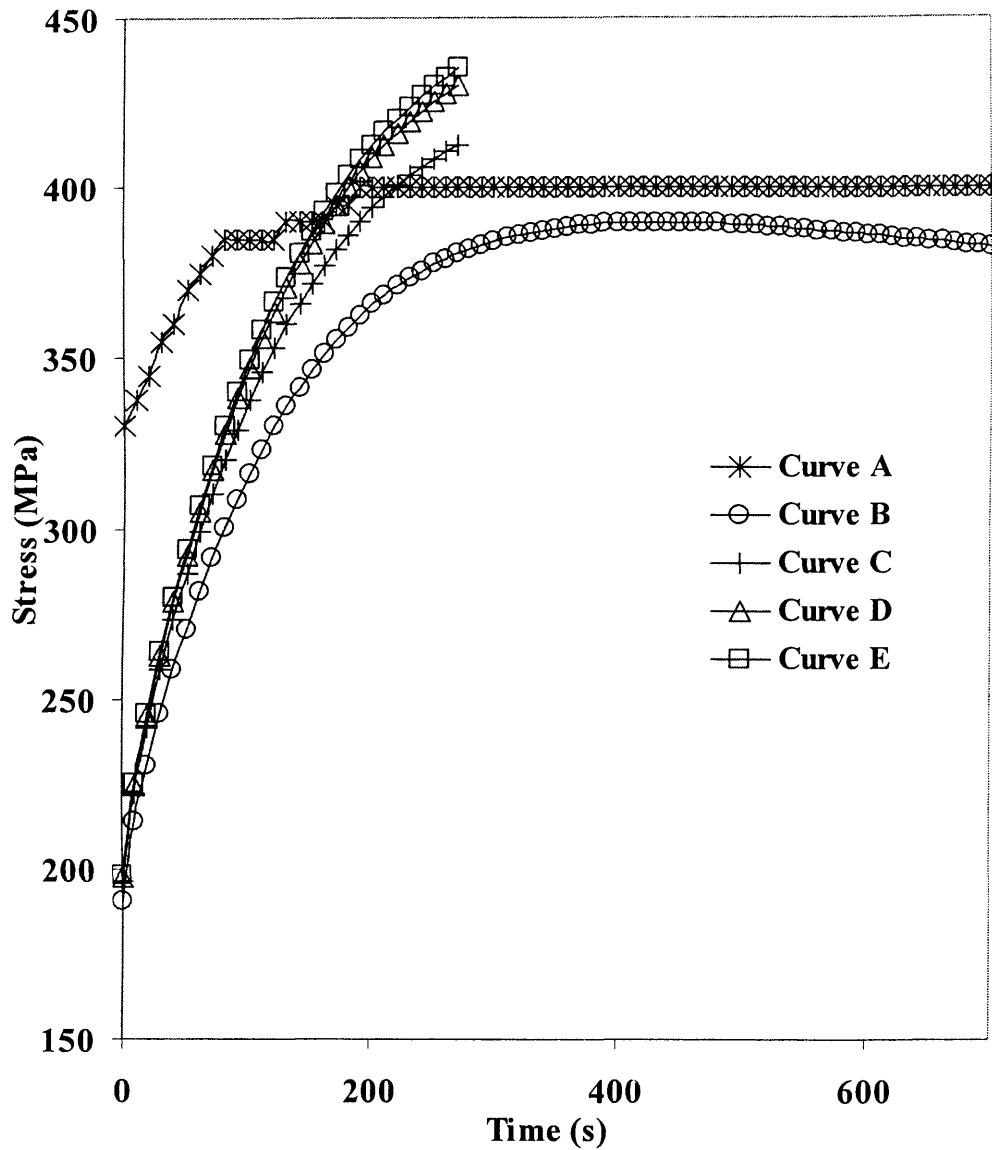


Figure 4.29: Comparison of UTS with total outer wall tangential stress during fire attack.

- Curve A: Ultimate tensile stress (Carbon steel)
- Curve B: Total Stresses (50mm relief valve)
- Curve C: Total Stresses (25mm relief valve)
- Curve D: Total Stresses (10mm relief valve)
- Curve E: Total Stresses for an isolated pipeline

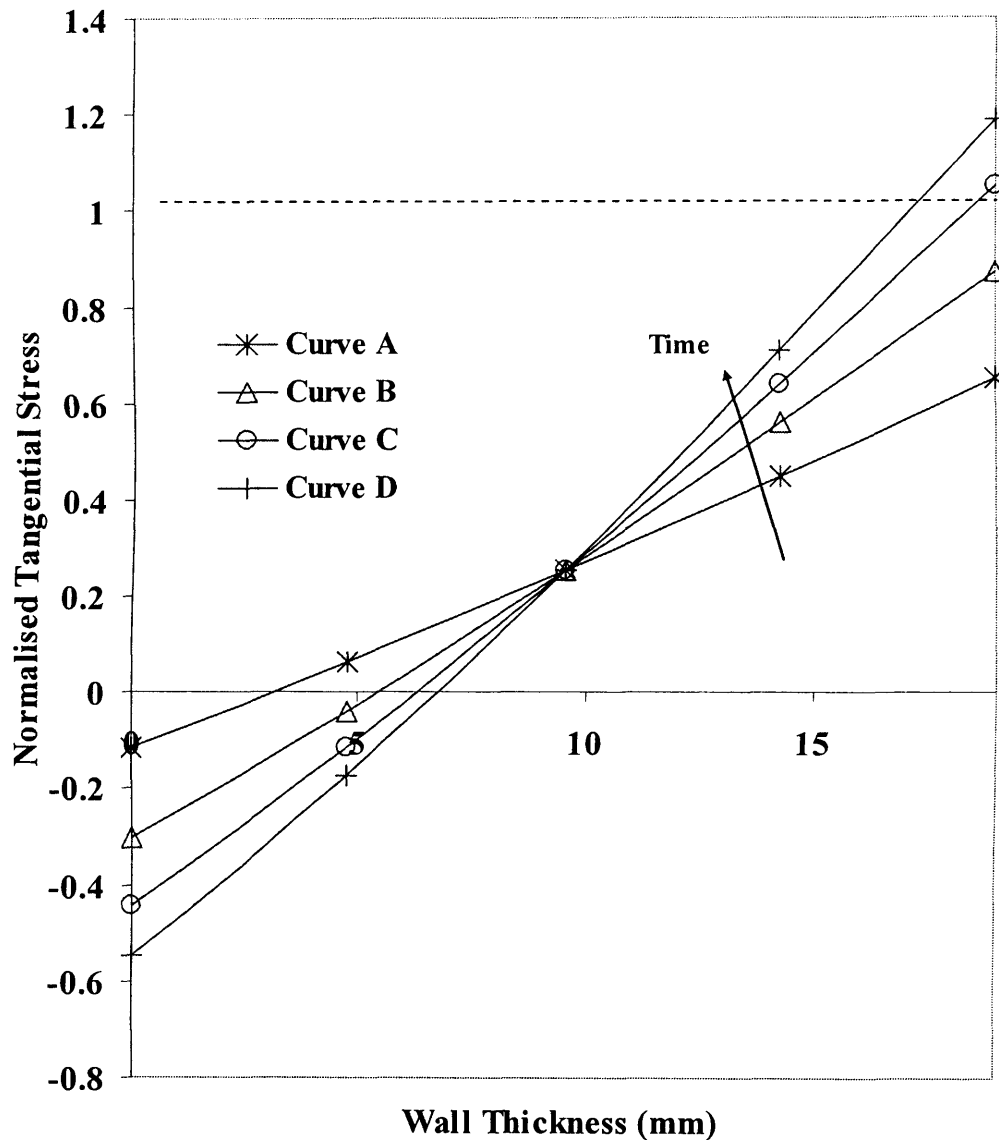


Figure 4.30: Total normalised tangential stresses with time across the pipewall thickness for the isolated pipeline under fire attack (material of construction, carbon steel BS 3100 A2)

Curve A: 100s, $\Psi(K) = 353$

Curve B: 200s, $\Psi(K) = 387$

Curve C: 300s, $\Psi(K) = 413$

Curve D: 400s, $\Psi(K) = 433$

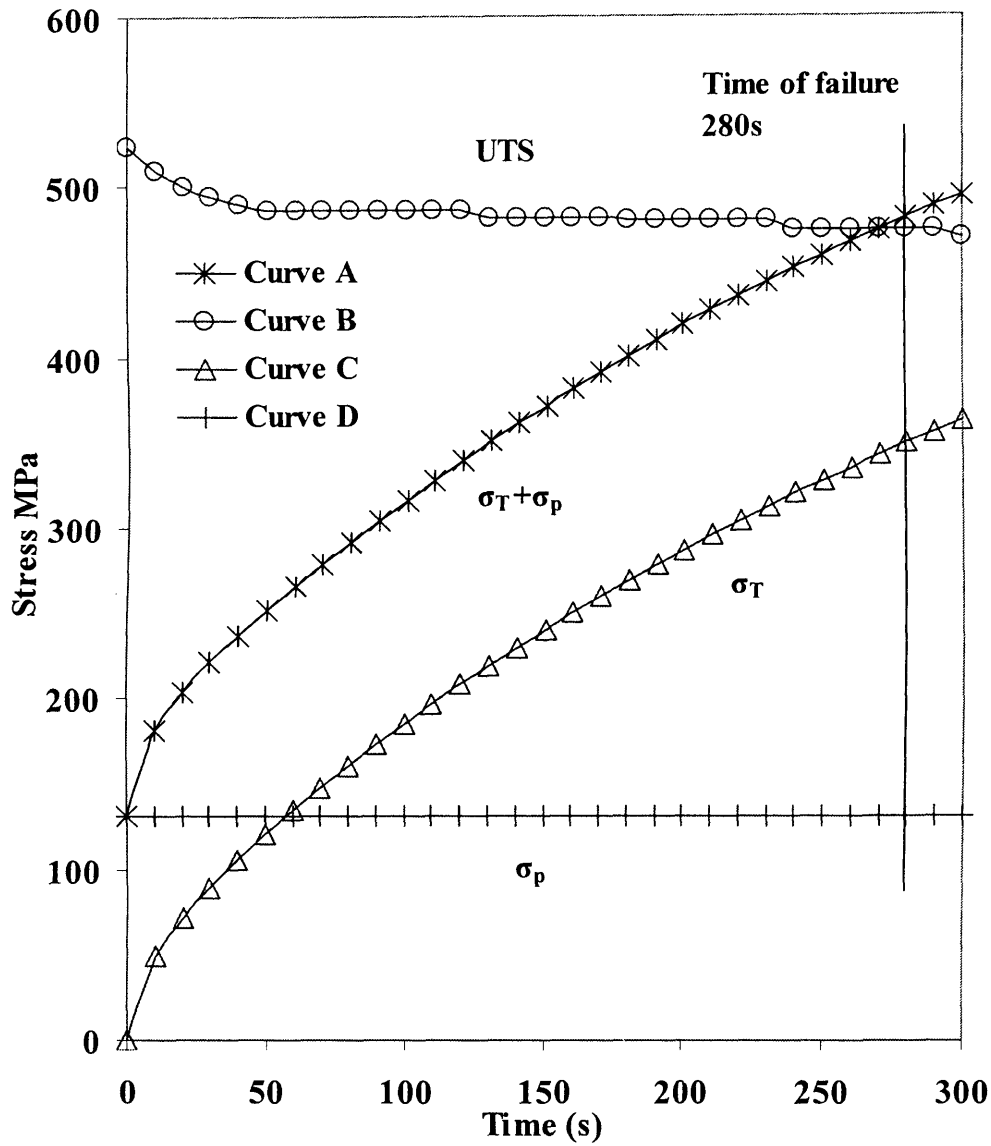


Figure 4.31: The variation of the various outer wall tangential stresses as a function of time for the isolated pipeline, (carbon steel, BS 3100 A2).

- Curve A: Total Stresses $\sigma_T + \sigma_p$
- Curve B: Ultimate tensile stress (Carbon steel, BS 3100 A2)
- Curve C: Thermal stress σ_T
- Curve D: Pressure stress σ_p

CHAPTER 5

MODELLING SECONDARY FAILURES IN PRESSURISED PIPELINES FOLLOWING THE IGNITION OF A RELEASED INVENTORY

5.1 Introduction

In the previous chapter, the modelling of loss in the mechanical integrity of a pressurised pipeline following direct jet fire impingement was presented. In this chapter, an alternative failure scenario involving the puncture of the pressurised pipeline and the immediate ignition of the released inventory is considered. The impact of the resulting jet fire back radiation on the mechanical integrity of the depressurising pipeline is then modelled. An important precursor to the above is the presentation followed by utilisation of an appropriate model based on published literature simulating the transient jet fire characteristics including its overall dimensions and radiation heat flux.

The chapter concludes with the comprehensive analysis of the results relating to the application of the transient jet fire model to the hypothetical failure of a natural gas pipeline.

5.2 Diffusion Flame

A jet flame resulting from the ignition of flammable fluid at the leak aperture is a diffusion flame. The behaviour, in particular the dimensions, of a diffusion flame is a function of the discharge rate.

5.3 Radiation

The three basic mechanisms of heat transfer are conduction, convection and radiation. Fires are hazardous both because of their direct heating effect, by convection within

the fire itself and because of the radiation from the fire. Radiative heat transfer requires no intervening medium between the heat source and the receiver. It is the transfer of energy by electromagnetic waves.

The thermal radiation of a flame of any hydrocarbon comes from two sources. Firstly, hot CO₂ and H₂O, which emit mainly in the near infrared and do not contribute to the visible light emitted from the flame (non-luminous radiation). Secondly, from solid particles, usually coke or soot, burning in the flame and emitting continuous radiation in the wavelength range from the visible to the infrared. These particles emit most of the visible light from the flame (luminous-radiation). Most of the radiation from flames is emitted by minute solid particles of soot, which are formed in almost all diffusion flames. The thermal radiation from the blue chemiluminescent region, characteristic of well-mixed hydrocarbon-air reaction zones, is small compared to that from the luminous yellow flame region. (Flame lift statement removed)

Jet flames can give significant levels of heat radiation. In order to calculate the radiation level, it is usual to distribute the heat release rate over the area of the flame. Not all the heat produced is emitted as radiation. This is taken into account by the fraction of heat radiated by jet flame. This fraction is the ratio of the rate of radiative energy release to the power that would be released if all the fuel supplied to the flame were to burn stoichiometrically and adiabatically. It is a function of the fuel, since it depends on the efficiency of the combustion and of the orifice diameter. It tends to increase as diameter increases, reaching a maximum. It also depends on the amount of energy lost by convection to entrained air and on radiative properties of the combustion products. Soot is a much more efficient radiator than gaseous products. Flames fuelled by heavier hydrocarbons contain relatively higher concentration of soot particles than natural gas flames.

The degree of sophistication used in determining the magnitude of thermal radiation field around a fire depends on the specific application of the results. In developing siting criteria, such as the spacing of other plant equipment around the pipeline, it is desirable to use as accurate a model as possible. There are two basic thermal radiation models: the point source model and the solid flame model. In the point source model,

the flame is represented as a small source of thermal energy. It is a simple but crude means of estimating thermal radiation intensity where the effects of flame geometry are not significant or for a conservative estimate of the hazard to personnel.

The radiation flux from the flames of a fire can be calculated using the Stefan-Boltzmann equation, if the temperature of the flame is known. The problem with this procedure is the uncertainty of the flame temperature, which can give rise to important errors because of the sensitivity of the Stefan-Boltzmann equation to temperature.

An alternative method (Chamberlain, 1987 and Johnson et al., 1995) is to calculate the surface emissive power of the flame, based on the heat release rate and the radiation fraction and dividing by the surface area. The received radiative heat flux is then obtained as the product of the surface emissive power, the atmospheric transmissivity and the view factor. This method assumes that there is no reflection from the receiving surface, a conservative hypothesis, which is adequate in most cases.

The method described above is used in conjunction with relations for the geometry of the flame and for the heat radiated per unit area of the flame surface (Lees, 1996).

5.4 Flame Emissivity

The emissivity of a flame depends on the type of fuel and on the nature of the combustion. The heat radiated from a flame is emitted by gases, in particular the products of combustion CO_2 , H_2O , N_2 , CO and O_2 , and soot. Hot CO_2 and H_2O emit mainly in the near infrared and do not contribute to the visible light emitted from the flame (non-luminous radiation). Coke or soot, burning in the flame emits continuous radiation in the wavelength range from the visible to the infrared. These particles emit most of the visible light from the flame (luminous radiation) (Lees, 1996).

5.5 Atmospheric Transmissivity

The atmospheric transmissivity, τ is defined as the fraction of emitted energy not absorbed or scattered by the atmosphere. The value of τ represents an effective atmospheric transmissivity for all the possible paths through the atmosphere, from points on the flame surface to the receiving surface. Wayne (Wayne, 1991) developed an efficient method for calculating τ . The polynomial expression can be used to calculate atmospheric transmissivities, subject to the restriction of assuming fire temperature of 1500K. The expression can be used for any relative humidity, for path lengths of between 10 and 1000m through atmospheres at temperatures between 253K and 313K.

5.6 View Factor

The view factor VF quantifies the geometric relationship between the model flame shape and the receiving surface. It describes how much of the field of view of the receiving surface is filled by the flame. The view factor equals 1 if the flame fills the field of view of the receiving surface completely; otherwise it is less than one (Johnson et al., 1995). Calculation of the geometric view factor requires knowledge of the geometry of the fire and of the receiving surface, and their relative positions. Then the view factor for a receiver area, dA_2 from emitting area dA_1 is given as:

$$VF = \int_{A_1} \frac{\cos\theta_1 \cos\theta_2}{\pi r^2} dA_1 \quad (5.1)$$

where

θ_1 = angle between local normal to surface elements dA_1 and line joining dA_1 and dA_2

θ_2 = angle between normal to surface elements dA_2 and line joining dA_1 and dA_2

r = length of line joining dA_1 and dA_2

Since it has been observed through various simulations that the angle between the orifice and flame axes (α), (shown later) remains relatively constant hence this study assumes a constant value of 0.5 for the view factor throughout the application of the

Chapter 5 Modelling Secondary Failures in Pressurised Pipelines Following the Ignition of a Released Inventory

model. This is also due to the meticulous computation calculations required to determine the value of the view factor.

The development of a jet flame model and the resulting pressure and thermal loading effects on the pipewall section under the influence of thermal radiation is described next.

5.7 Model Development

This section presents the development of a jet flame model for predicting the characteristics and radiation effects following the ignition of the escaping inventory.

The behaviour of flames is an important factor in the consideration of both the causes and effects of fires and explosions in chemical plants. A complete model of a flame includes information on (Lees, 1996):

- Flame length and dimensions
- Heat release rate
- Fraction of heat radiated
- Flame temperature
- Surface emissive power
- View factor

It is, however not necessary to obtain all the flame characteristics listed above. If the flame is treated as a point source, it may be characterised by the heat release rate and the fraction of heat radiated, with a simple point source view factor used. Methods requiring the flame dimensions may need more accurate estimates of discharge rate, the duration of the release and the total quantity released as essential inputs into jet flame models. Such important inputs have been modelled and described earlier in the thesis (see chapter 3).

In the present study, the jet fire is assumed to emanate following the ignition of the escaping hydrocarbon from the pipeline following its rupture. The jet flame model is primarily based on modification of the Chamberlain's (1987) jet fire correlations.

The Johnson et al., (1995) model is an extension to the Chamberlain's (1987) model and is used specifically for modelling jet fires issuing horizontally. Chamberlain's (1987) model is more suitable for modelling vertical and inclined flares. In this study, the relevant parts from each model will be used to provide a representation of the flame characteristics. The flame shape is assumed to be of a cone, the geometrical aspects are shown in Figure 5.1.

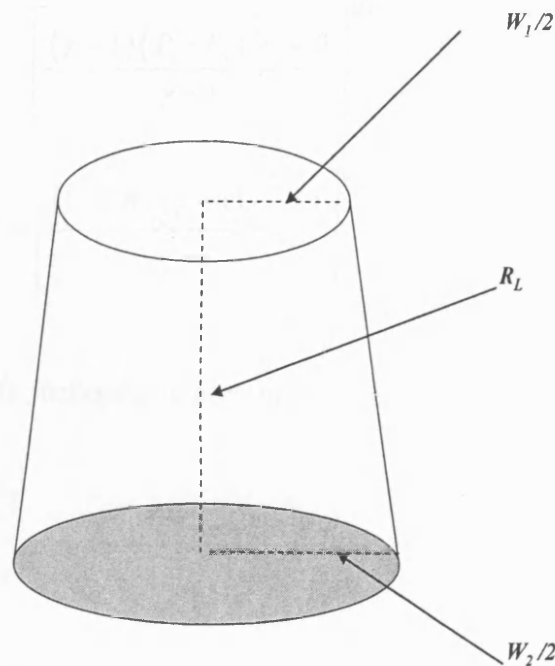


Figure 5.1: Geometrical aspects of the flame cone frustum.

Chapter 5 Modelling Secondary Failures in Pressurised Pipelines Following the Ignition of a Released Inventory

Expanded Jet Temperature (Chamberlain, 1987)

The equation for the expanded jet temperature, T_j is

$$T_j = \frac{2T_s}{2 + (\gamma - 1)M_j^2} \quad (5.2)$$

Where T_s is the stagnation temperature (K), M_j is the Mach number of the expanded jet and γ is ratio of specific heats.

The equations for calculating the Mach flow are:

$$\text{For choked flow } M_j = \left[\frac{(\gamma - 1)(P_c / P_o)^{\frac{\gamma - 1}{\gamma}} - 2}{\gamma - 1} \right]^{1/2} \quad (5.3)$$

$$\text{For unchoked flow } M_j = \left[\frac{(1 + 2F^2(\gamma + 1))^{1/2} - 1}{\gamma - 1} \right]^{1/2} \quad (5.4)$$

Where P_o is the absolute atmospheric pressure,

$$P_c = 3.6713 \frac{m}{d_o^2} \sqrt{\frac{T_c}{\gamma W_{gk}}} \quad (5.5)$$

$$F = 3.6233 \times 10^{-5} \frac{m}{d_o^2} \sqrt{\frac{T_s}{\gamma W_{gk}}} \quad (5.6)$$

m is the mass flow rate of released fluid (kg/s), d_o is the diameter of the puncture or hole in pipeline (m) and W_{gk} is the kilogram molecular weight of fluid (kg/mol). T_c is the static temperature at hole exit plane (K) and is calculated by:

$$T_c = \frac{2T_s}{1 + \gamma} \quad (5.7)$$

Chapter 5 Modelling Secondary Failures in Pressurised Pipelines Following the Ignition of a Released Inventory

Effective Source Diameter (Chamberlain, 1987)

In combustion modelling, a widely used concept is that of the effective source diameter D_s . This is the throat diameter of a nozzle from air of density, ρ_a issuing at a mass flow rate, m .

The effective source diameter, D_s is given by:

$$\text{For unchoked flow: } D_s = d_o \left(\frac{\rho_j}{\rho_a} \right)^{1/2} \quad (5.8)$$

$$\text{For choked flow: } D_s = d_j \left(\frac{\rho_j}{\rho_a} \right)^{1/2} \quad (5.9)$$

where ρ_j is the density of the fluid (kg/m^3) and is given by

$$\rho_j = \rho_g^o (273/T_j) \quad (5.10)$$

Subscripts g and o represent the gas condition and standard conditions respectively. For the choked flow cases, the jet expands to atmospheric pressure at a plane downstream of the exit hole and this plane then acts as a virtual source of diameter d_j , given by

$$d_j = \left(\frac{4m}{\pi u_j \rho_j} \right)^{1/2} \quad (5.11)$$

where u_j is the velocity of the fluid in the expanded jet (m/s), which is given by

$$u_j = M_j \sqrt{\frac{\gamma R T_j}{W_{gk}}} \quad (5.12)$$

R is the ratio of wind speed to jet velocity v/u_j .

Chapter 5 Modelling Secondary Failures in Pressurised Pipelines Following the Ignition of a Released Inventory

Momentum Flux (Johnson et al., 1995)

The initial jet behaviour, when the gas expands down to atmospheric pressure is calculated in the same manner as that described by Chamberlain (1987). Hence the momentum flux of expanded jet is given by:

$$G = \frac{\pi \rho_j u_j^2 d_j^2}{4} \quad (5.13)$$

Richardson's Number, ξ , (Johnson et al., 1995)

Richardson's number characterises the balance between jet momentum flux and buoyancy and measures the importance of buoyancy in determining flame size. It is the cube root of the ratio of the buoyancy to the momentum flux used in combustion studies. The length scale used is the flame length for a vertical flame in still air, L_o

$$\xi(L_o) = \left(\frac{\pi \rho_a g}{4G} \right)^{1/3} L_o \quad (5.14)$$

Vertical Flame in Still Air, L_{BO} , (Chamberlain, 1987)

The flame length in still air, L_{BO} , is determined implicitly from the Kalghatgi's (1984) equation

$$\left(\frac{D_s \beta}{L_{BO} W} \right)^2 = 0.2 + 0.024 \xi(L_{BO}) \quad (5.15)$$

$$\text{With } \beta = \left(\frac{M_a T_1}{M_p T_a} \right)^{1/2} \quad (5.16)$$

Chapter 5 Modelling Secondary Failures in Pressurised Pipelines Following the Ignition of a Released Inventory

Where M_p is the molecular weight of mean product (g/mol), T_I is the temperature under adiabatic conditions (K), T_a is the absolute air temperature (K) and W is the mass fraction of fuel in the stoichiometric mixture with air.

Actual Length of Flame L_B ((Johnson et al., 1995)

For a tilted jet, the general correlation for L_B , assuming that it scales similarly with the angle between the horizontal and the hole axis for all wind speeds and directions:

$$L_B = L_{BO} (0.51 \exp(-0.41w) + 0.49) (1 - 0.67 \times 10^{-3} (\theta_{jw} - 90)) \quad (5.17)$$

Where w is the wind speed (m/s), θ_{jw} is the angle between hole axis and wind vector in the plane containing hole axis, flame axis and wind vector.

Flame Shape (Johnson et al., 1995)

The flame shape is defined relative to the x , y and z coordinates

- x -coordinate: release direction
- y -coordinate: vertical direction
- z - direction: crosswind direction (perpendicular to flame)

The relative effects of the initial jet momentum determine the position of the flame flux, and the wind momentum fluxes in the x - and z -directions. The balance of these momentum fluxes is expressed by the two parameters:

$$\Omega_x = \left(\frac{\pi \rho_a}{4G} \right)^{\frac{1}{2}} L_{BO} u_a \quad \Omega_z = \left(\frac{\pi \rho_a}{4G} \right)^{\frac{1}{2}} L_{BO} v_a \quad (5.18 \text{ a, b})$$

Where u_a is the wind speed in the release direction (m/s), v_a is the wind speed in the perpendicular to the release and Ω_x and Ω_z are parameters.

Chapter 5 Modelling Secondary Failures in Pressurised Pipelines Following the Ignition of a Released Inventory

Position of Flame in x-direction X

It has been found (Johnson et al., 1995) experimentally that the crosswind has little effect on the flame position in the x-direction so the Ω_z parameter can be neglected. For the x- position of the flame, X

$$\frac{X}{L_{BO}} = f(\xi) [1 + r(\xi)\Omega_x], \quad \frac{X}{L_{BO}} \leq 1.0 \quad (5.19)$$

With

$$f(\xi) = 0.55 + (1 - 0.55)\exp(-0.168\xi) \quad \xi \leq 5.11 \quad (5.20a)$$

$$f(\xi) = 0.55 + (1 - 0.55)\exp(-0.168\xi - 0.3(\xi - 5.11)^2) \quad \xi > 5.11 \quad (5.20b)$$

$$r(\xi) = 0 \quad \xi \leq 3.30 \quad (5.21a)$$

$$r(\xi) = 0.82 \{1 - \exp[-0.5(\xi - 3.3)]\} \quad \xi > 3.30 \quad (5.21b)$$

Position of Flame in y-direction Y

$$\frac{Y}{L_{BO}} = h(\xi) [1 + c(\xi)\Omega_x] \quad 0 \leq \frac{Y}{L_{BO}} \leq 1.0 \quad (5.22)$$

with

$$h(\xi) = (1 + 1/\xi)^{-8.78} \quad (5.23)$$

$$c(\xi) = 0.02\xi \quad (5.24)$$

Chapter 5 Modelling Secondary Failures in Pressurised Pipelines Following the Ignition of a Released Inventory

Flame Lift-off Distance

Jets with high initial momentum entrain more air per unit length, in the initial convection dominated part of the jet, and burn more as a premixed blue flame, than jets with lower initial momentum. Further down the jet, less air is entrained per unit length, the combustion is less efficient, and sooting occurs, leading to a luminous flame. The luminous flame lift-off, b , is thus found to be given as:

$$b = 0.141 (G \rho_a)^{\frac{1}{2}} \quad (5.25)$$

Position of Flame in Z-direction, Z

$$\frac{Z}{X-b} = 0.178 \Omega_z \quad (5.26)$$

Angle between Orifice and Flame axes, α

$$\alpha = \frac{1}{\xi(L_{BO})} \left\{ 8000 R_v + \xi(L_{BO}) (\theta_{jw} - 90) [1 - \exp(-25.6 R_v)] \right\} \quad R_v \leq 0.05 \quad (5.27)$$

$$\alpha = \frac{1}{\xi(L_{BO})} \left\{ 1726 (R_v - 0.026)^{1/2} + 134 + \xi(L_{BO}) (\theta_{jw} - 90) [1 - \exp(-25.6 R_v)] \right\} \quad (5.28)$$

$R_v > 0.05$

with $R_v = \frac{w}{u_j}$ (5.29)

Minimum Diameter of Flame, W_1 (width of base of frustum)

$$\frac{W_1}{b} = -0.18 + 0.081 \xi \quad (5.30)$$

where W_1 is the minimum diameter of the flame (m).

Chapter 5 Modelling Secondary Failures in Pressurised Pipelines Following the Ignition of a Released Inventory

Maximum Diameter of Flame at the Point Furthest from the Origin, W_2 (width of top of frustum)

$$\frac{W_2}{L_{xy}} = -0.004 + 0.0396\xi - \Omega_x (0.0094 + 9.5 \times 10^{-7} \xi^5) \quad (5.31)$$

with L_{xy} being the projection of actual flame length onto x, y -plane and is given by the equation $L_{xy} = (X^2 + Y^2)^{1/2}$ (5.32)

For a realistic flame shape W_2 must be greater than W_1 and less than L_{xy} . If W_2 is less than W_1 , then assume that $W_2 = W_1$.

Length of Frustum, R_L (Chamberlain, 1987)

From geometric considerations: $R_L = \sqrt{(L_B^2 - b^2 \sin^2 \alpha)} - b \cos \alpha$ (5.33)

Flame Surface Area, A , (including two end discs)

$$A = \frac{\pi}{4} (W_1^2 + W_2^2) + \frac{\pi}{2} (W_1 + W_2) s \quad (5.34)$$

Where s is the slant length of the frustum (m), and is given by

$$s = \sqrt{R_L^2 + \left(\frac{W_2 - W_1}{2} \right)^2} \quad (5.35)$$

Surface Emissive Power, SEP , (Chamberlain, 1987)

The surface emissive power of the flame is then

$$SEP = \frac{F_r Q}{A} \quad (5.36)$$

$$\text{with } F_r = 0.21 \exp(-0.00323u_j) + 0.14 \quad (5.37)$$

where F_r is the fraction of heat radiated, SEP is the surface emissive power (kW/m^2) and Q is the net heat release rate (kW). Q is calculated using

$$Q = m \times \Delta H_c \times x_{fluid} \quad (5.38)$$

ΔH_c is the heat of combustion of fluid (kJ/kg) and x_{fluid} is the mass fraction of fluid in discharge.

Thermal Radiation Incident on Target, I, (Wayne, 1991)

The incident received flux on the target is given as:

$$I = \tau \times VF \times SEP \quad (5.39)$$

where VF is the view factor, I is the radiation incident on the target (kW/m^2) and τ is the atmospheric transmissivity which is given by Wayne (1991);

$$\begin{aligned} \tau = & 1.006 - 0.0117(\log_{10} \chi(H_2O)) - 0.02368(\log_{10} \chi(H_2O))^2 \\ & - 0.03188(\log_{10} \chi(CO_2)) + 0.001164(\log_{10} \chi(CO_2))^2 \end{aligned} \quad (5.40)$$

$$\chi(CO_2) = D_{path} \left(\frac{273}{T_a} \right) \quad (5.41)$$

$$\chi(H_2O) = \frac{288.651 \times D_{path} \times R_H \times S_w}{T_a} \quad (5.42)$$

Where

- $\chi(CO_2)$ = amount of CO_2 in path between flame and target
- $\chi(H_2O)$ = amount of H_2O in path between flame and target
- D_{path} = path distance (from flame to target)

Chapter 5 *Modelling Secondary Failures in Pressurised Pipelines Following the Ignition of a Released Inventory*

R_H	=	fractional relative humidity
S_w	=	saturated water vapour pressure (mmHg)

Wall Temperature with Incident Received Flux

Using an incident-received-flux, a 2-D pipewall temperature profile is generated using the procedure described earlier in the thesis (see chapter 3). The corresponding thermal and pressure stresses are then evaluated using equations presented in chapter 4. The calculation algorithm relating the jet flame thermal impact to the transient thermal and pressure stresses in the pipewall is shown in figure 5.2 below.

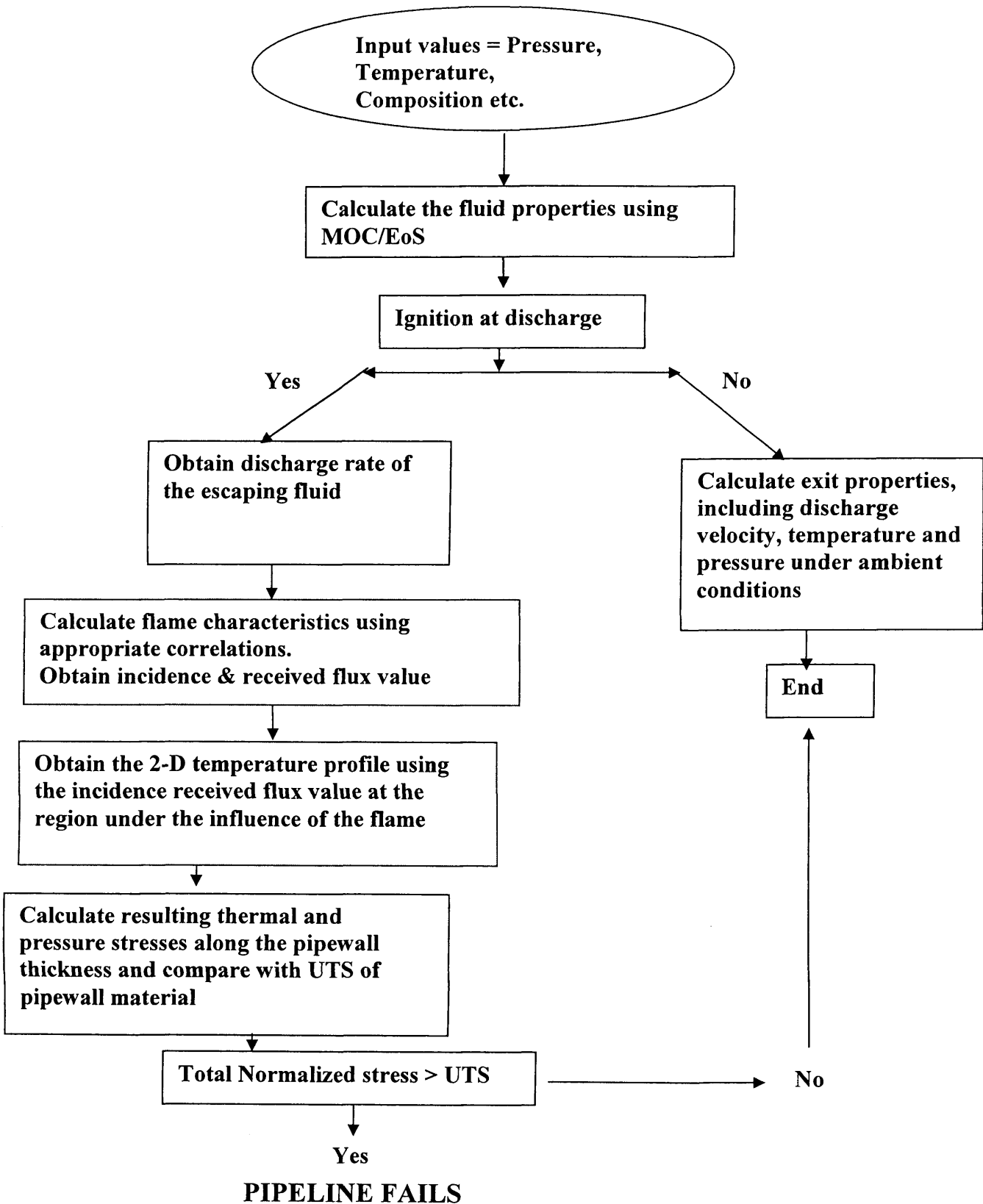


Figure 5.2 Pipeline failure calculation algorithm for ignition of released inventory.

5.8 Validation of Chamberlain (1987) Jet Flame Model

Chamberlain's (1987) jet fire model validation involved wind tunnel experiments and field trials both on and offshore. The effect of flaring a given mass flow of natural gas at progressively higher velocities was observed by comparing data obtained for a release of 10.7 kg/s through flare tips of diameters 0.152m (Mach 0.45) and 0.203m (Mach 1.03). Average values at wind speed of 6m/s were considered. The data obtained by the author along with the comparison of the model explained above is shown in table 5.1. A reasonably good agreement is observed.

Hole diameter, d_o , m	0.152		0.203	
	Experimental data	Model data	Experimental data	Model data
Mach number	1.41	1.46	1.03	1.02
Flame length, R_L , m	19.2	23.7	19.3	20.2
Flame Width, W_2 , m	7.3	6.8	9.6	8.2
Flame tilt, α , deg	14	12.9	29	21.6
Fraction radiated, Fr	0.12	0.17	0.17	0.2
Surface emissive power, kW/m ²	208	230	223	245

Table 5.1 Comparison of data obtained from jet fire model results with experimental data; Chamberlain (1987).

5.9 Case Study

For the purpose of the case study, we assume that a 0.5km methane pipeline is leaking due to an initial defect in the form of a 10mm (1cm) diameter circular puncture at the low pressure end. It is further assumed that the escaping inventory is ignited immediately upon release and the pumping of the feed ceases 160s after the initial leak.

The failure scenario is schematically presented in figure 5.3. The length of the pipewall, x exposed to thermal radiation under consideration is assumed equal to the projection of the actual flame length on the pipewall as indicated by the thick line

Chapter 5 Modelling Secondary Failures in Pressurised Pipelines Following the Ignition of a Released Inventory

drawn in figure 5.3. The prevailing conditions and the pipeline characteristics are shown in table 5.2.

Pipeline length (km)	0.5
Feed pressure (bara)	110
Feed temperature (K)	293.15
Pipewall thickness (mm)	19
Pipeline inner diameter (m)	0.357
Pipeline density (kg/m ³)	7854
Pipeline thermal conductivity (W/mK)	53.6
Ambient temperature (K)	292.25
Initial Puncture (mm)	10
Cross wind velocity (m/s)	6.5
Pipe roughness (mm)	0.05
Feed flow rate prior to failure (kg/s)	34.5

Table 5.2: Pipeline conditions for jet fire analysis; Inventory, 100 % CH₄

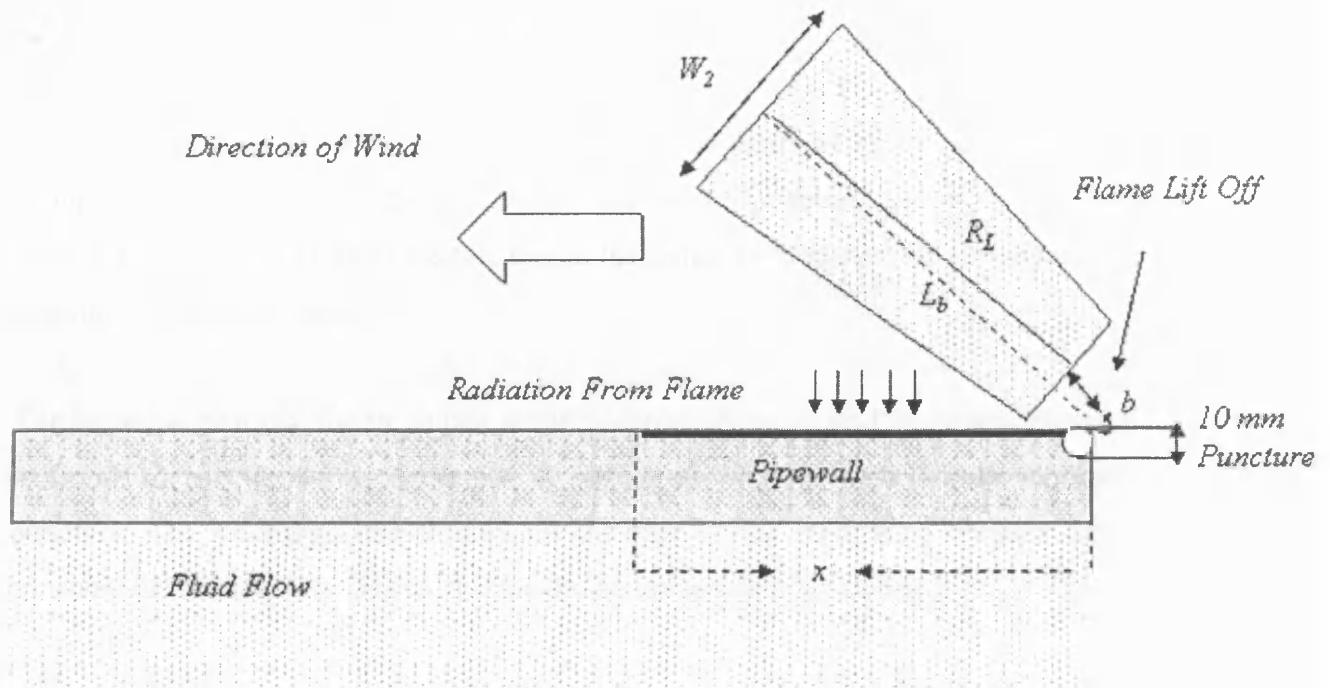


Figure 5.3: Schematic representation of thermal radiation loading following pipeline puncture and ignition of the released inventory. The distance x denotes the pipeline length under consideration.

Figure 5.4 shows the variation of inventory pressure with time at the puncture plane. The data show an initial rapid rise in pressure from the line pressure to 200bar. The termination of pumping some 160s later is marked by a comparatively gradual drop in pressure. The observed rapid pressure surge is due to the impact of the high velocity fluid with the intact end of the pipeline. This rise in pressure is quickly dissipated due to the reflection of the expansion waves from the pipe end and the loss in inventory.

The above explanation is further supported based on the data shown in figure 5.5. In this case the puncture is assumed to occur at mid point along the length of the pipeline. All the other conditions are exactly the same as those relating to figure 5.4. In this case no pressure surge in the data may be observed. This is because the puncture location is well away from the intact end of the pipeline, resulting in flow both through the puncture and towards the intact end of the pipeline. Although the

Chapter 5 Modelling Secondary Failures in Pressurised Pipelines Following the Ignition of a Released Inventory

latter may well result in a pressure surge at the intact end of the pipeline, this pressure surge is dissipated by the time it reaches the puncture location some 250m away from the down stream intact end of the pipeline.

Other simulations were also performed with various puncture sizes such as 30mm, 50mm and 75mm. No failure was observed as the puncture size was increased beyond 10mm. This is due to the fact that as the hole size increases the accompanying pressure stresses decrease.

The variation of mass discharge rate at the puncture plane located at the low pressure end with time is shown in figure 5.6. A sudden drop in the data is observed upon puncture. The discharge rate throughout the rest of the simulation remains fairly constant, decreasing very gradually once the pumping has been stopped.

Figures 5.7 and 5.8 respectively show the variation of the flame length and area with time during depressurisation. As expected both of these parameters follow the pressure/time trends. The initial flame length is ca. 5.7m rapidly growing to a maximum value of ca. 14m before gradually dropping. The respective corresponding flame areas are ca. 20 and 62m².

Figures 5.9 and 5.10 respectively present the variation of the Fraction of heat radiated (Fr) and Surface Emissive Power (SEP) of the flame with time. The fraction of heat radiated is found to correlate with gas discharge rate; as the discharge rate increases the fraction of heat-radiated decreases, because a progressively larger fraction of heat is lost by convection to the entrained air. As the fraction of heat radiated corresponds to the SEP, hence the SEP also decreases with the increasing release pressure.

The incident received flux variation with time is shown in figure 5.11. The data shows the amount of incident heat received on the outer pipewall through radiation from the flame. The incident received flux is the product of the view factor (assumed value of 0.5) and the fraction of heat radiated over flame area. Hence its magnitude increases with an increase in the fraction of heat radiated as shown in figure 5.9. The incidence flux is used to obtain the temperature profile and hence the resulting thermal stresses

using the methodology presented in chapters 3 and 4 to assess the likelihood of a failure.

Figure 5.12 shows the comparison of outer (curve A) and inner pipewall (curve B) temperatures along the pipeline length under consideration (see figure 5.3). The outer pipewall (curve A) temperature rises to a maximum value of 493K some 1000s following puncture due to the impact of heat radiation from the jet fire. The inner wall (curve B) however experiences a marginal drop in its temperature after an initial increase (302K) due to the depressurisation expansion induced cooling of the inventory. The resulting temperature gradient across the pipewall is ca. 464K.

Figures 5.13-5.15 respectively show the normalised radial, tangential and longitudinal stress profiles across the pipewall thickness at different time intervals. The data in figure 5.14 shows that the pipeline fails in the tangential direction (normalised stress value exceeds unity).

The comparison of total (thermal and pressure) tangential stresses (curve A, $\sigma_T + \sigma_p$) with the Ultimate Tensile Stress (UTS) of the pipeline (curve B) during depressurisation and thermal radiation is presented in figure 5.16. The total tangential stress data is used for comparison as it is observed from figure 5.14 that the pipeline would fail in the tangential direction.

According to the data in figure 5.16, the pipeline fails 1070s after puncture; shown from the point of intersection of curves A and B. The pipeline failure mode would be due to the bulging and buckling as explained earlier in the thesis (see chapter 4).

Figure 5.17 shows the variation of the calculated angle (α) using equation (5.27) and (5.28) with time. The data justifies the assumption of a constant value for the view factor. The view factor would change with a change in the angle between the orifice and flame axes (α), which from the data (figure 5.17) is observed to remain relatively unchanged. The angle changes slightly from a value of ca. 3.9° to 4.7°.

5.10 Conclusion

The modelling of the catastrophic loss in the mechanical integrity of pressurised pipelines following puncture and the ignition of the ensuing inventory was presented.

The above involved the simulation of the following time variant interactive processes:

- i) The simulation of the escaping inventory mass discharge rate and pressure at the puncture plane
- ii) The prediction of the ensuing jet flame characteristics including its overall dimensions, the incident and the received heat fluxes using a suitable jet flame model
- iii) The generation of the corresponding 2-D temperature profile within the pipewall as a result of thermal radiation and the resulting tri-axial thermal and pressure stresses
- iv) Comparison of the total stresses with the ultimate tensile stress of the pipeline material in order to ascertain the likelihood and if applicable the time and mode of catastrophic pipeline failure

Application of the model to a 10mm puncture positioned at the downstream end of an hypothetical 0.5km, 0.395m dia. pipeline conveying natural gas at 110bara showed that the pipeline fails in the tangential direction some 1070seconds following the initial release.

The size and location of the puncture during unisolated release were found to have a profound effect on delaying or circumventing catastrophic pipeline failure. The former is to be expected as increasing the puncture diameter results in a more rapid depressurisation rate thus resulting in a faster reduction of the accompanied pressure stresses that contribute to the pipeline failure. The significant effect of the location of

the puncture on the fate of the pipeline was however somewhat unexpected requiring a more detailed examination.

In the case of the puncture at the low pressure end of the pipeline, the pressure-time data indicated a rapid and significant rise in the puncture plane pressure well above the line pressure. This was followed by a gradual reduction back to the line pressure some 1000s following the initial puncture. This initial pressure rise was attributed to the reflection of the expansion waves from the intact end of the pipeline.

No pressure surge was observed in the case of puncture along the length of the pipeline. In this case upon puncture, the puncture plane pressure was observed to instantaneously drop from the line pressure to a much lower choke pressure which gradually dropped with the passage of time.

Comparison of the two failure scenarios revealed that in the first 1000s following discharge, the puncture plane pressure for puncture at the downstream end of the pipeline was approximately double that for the puncture along the pipeline length. The above is consistent with the absence of catastrophic pipeline failure in the case of mid point puncture as the jet flame dimensions including its length, diameter and area directly increase with the discharge pressure. The resulting thermal loading was found to be insufficient to cause secondary pipeline failure.

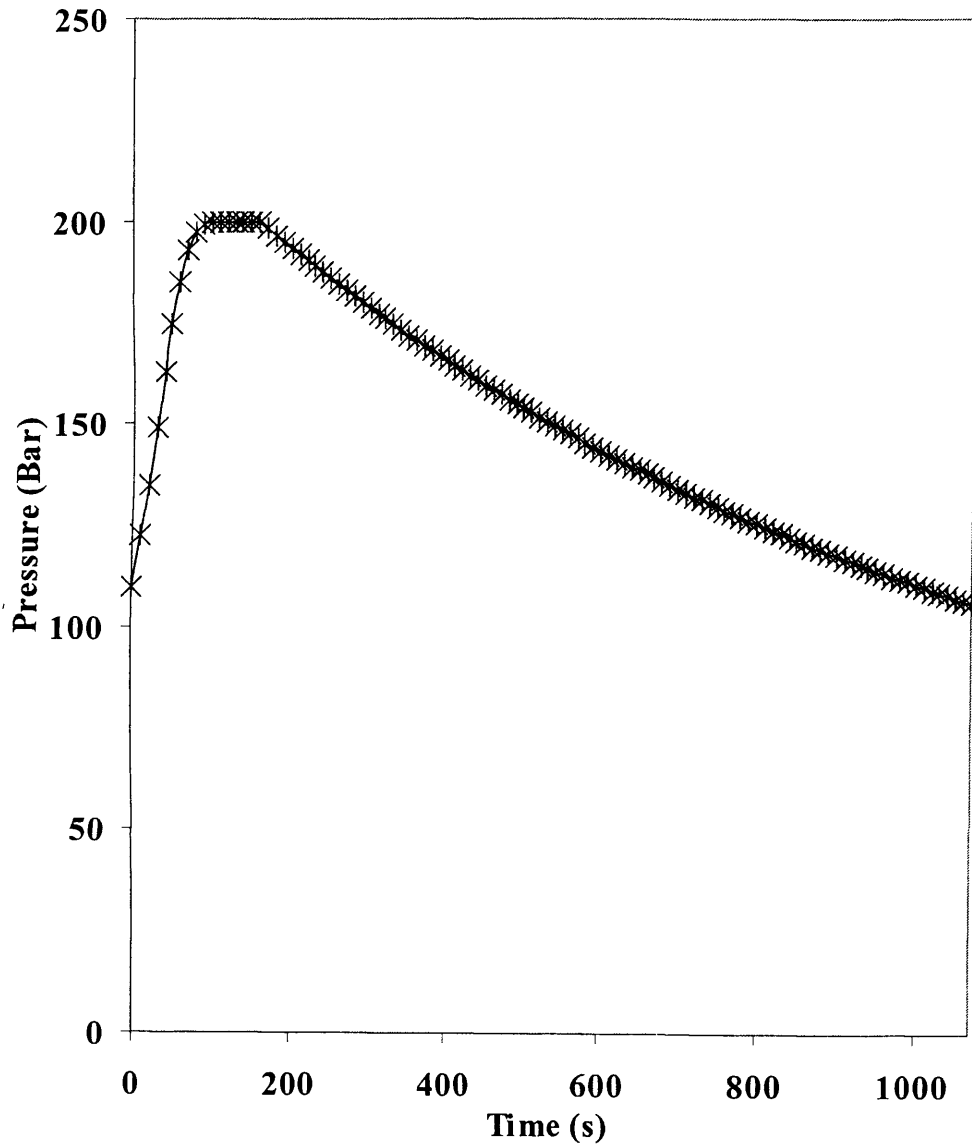


Figure 5.4 Variation of pressure with time following the ignition of releasing inventory through a puncture at the low pressure end of the pipeline.

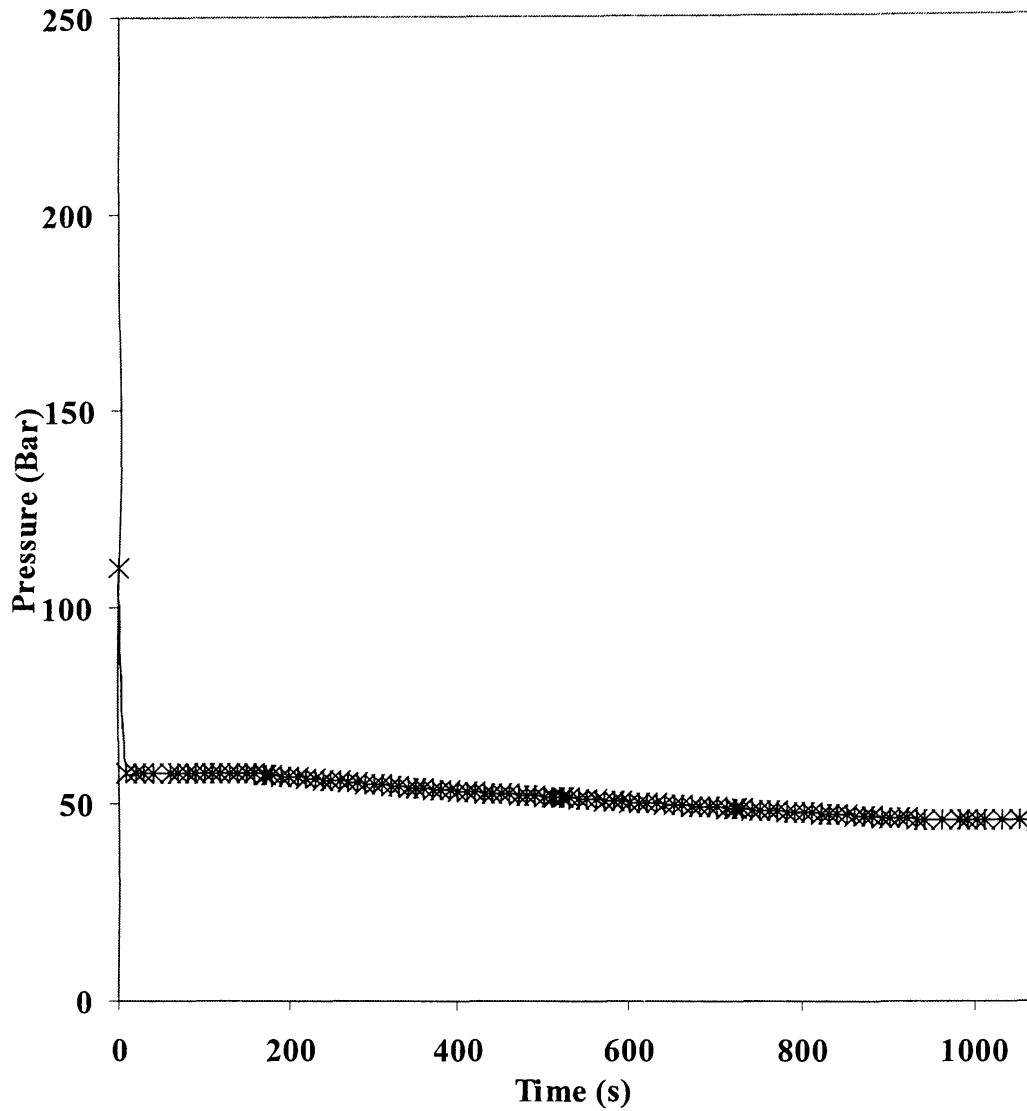


Figure 5.5 Variation of pressure with time following the ignition of releasing inventory through a puncture along the mid point of the pipeline.

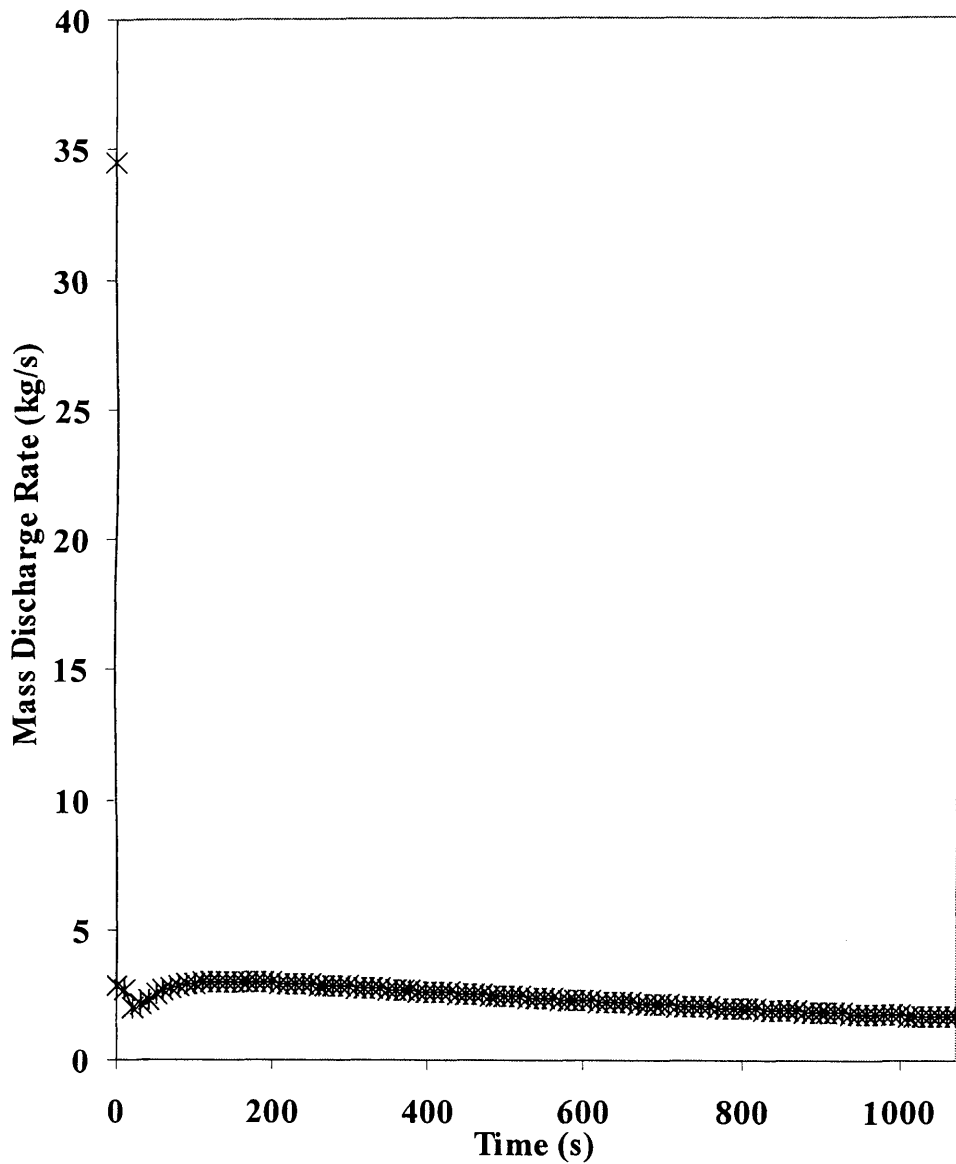


Figure 5.6 Variation of mass discharge rate with time following the ignition of releasing inventory through a 10mm puncture located at the low pressure end of the pipeline.

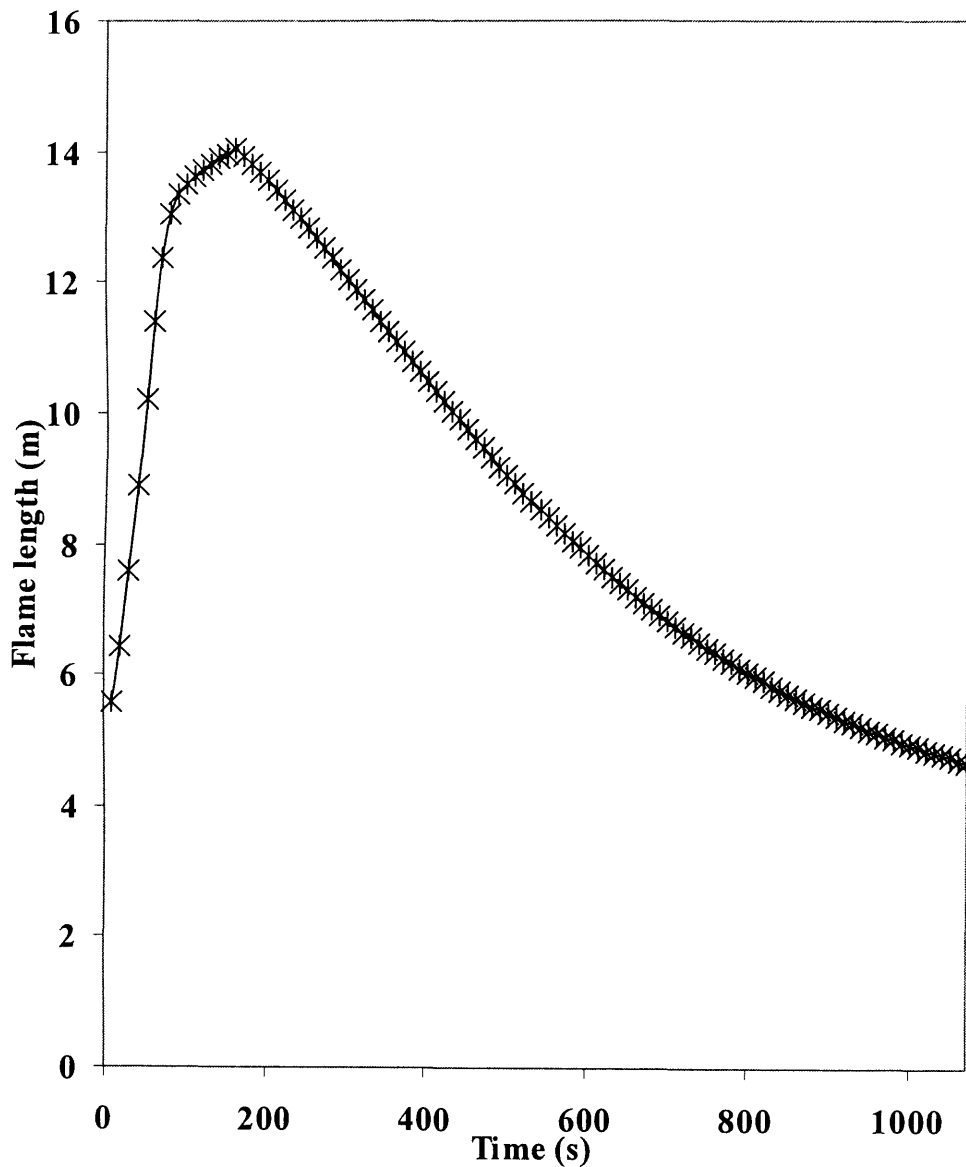


Figure 5.7 Variation of flame length with time following the ignition of releasing inventory.

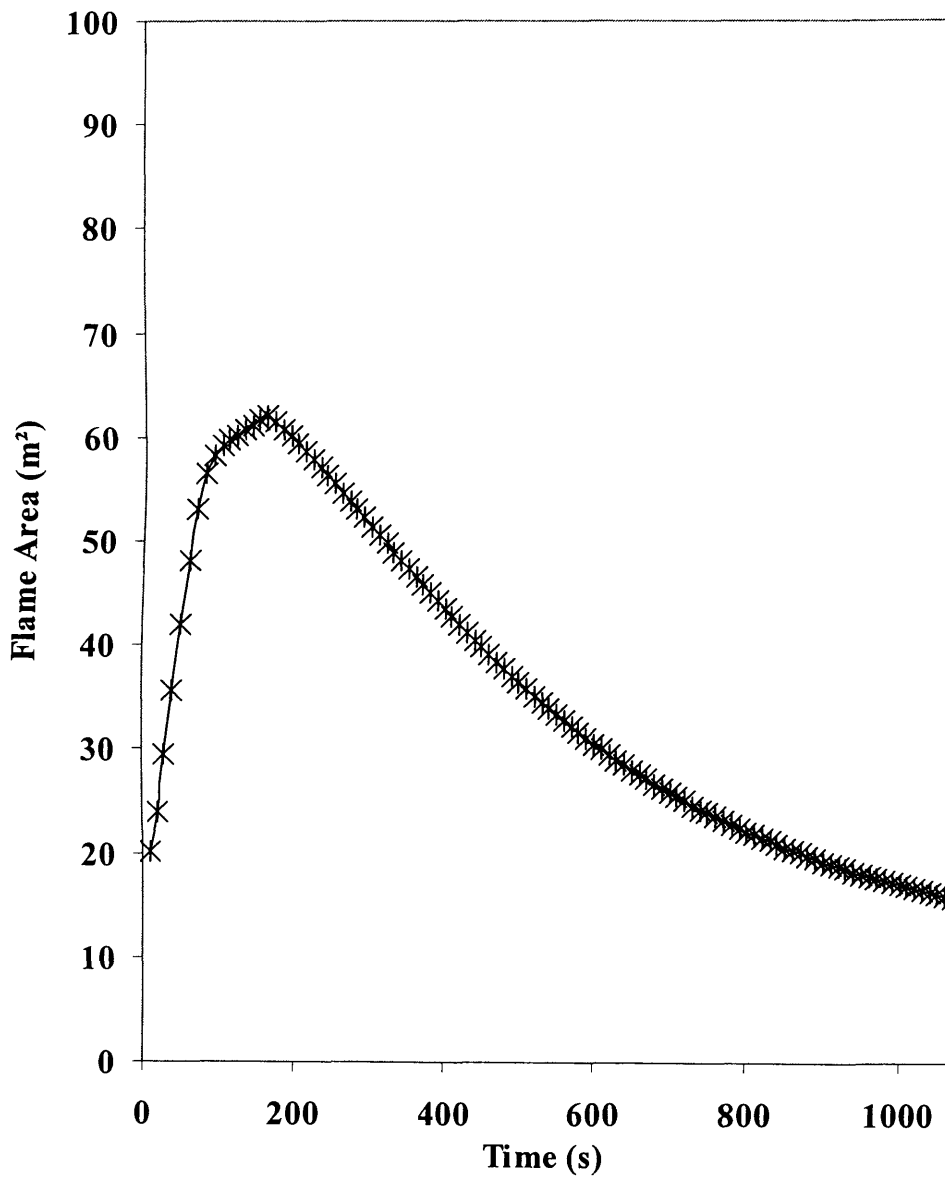


Figure 5.8 Variation of flame area with time following the ignition of releasing inventory.

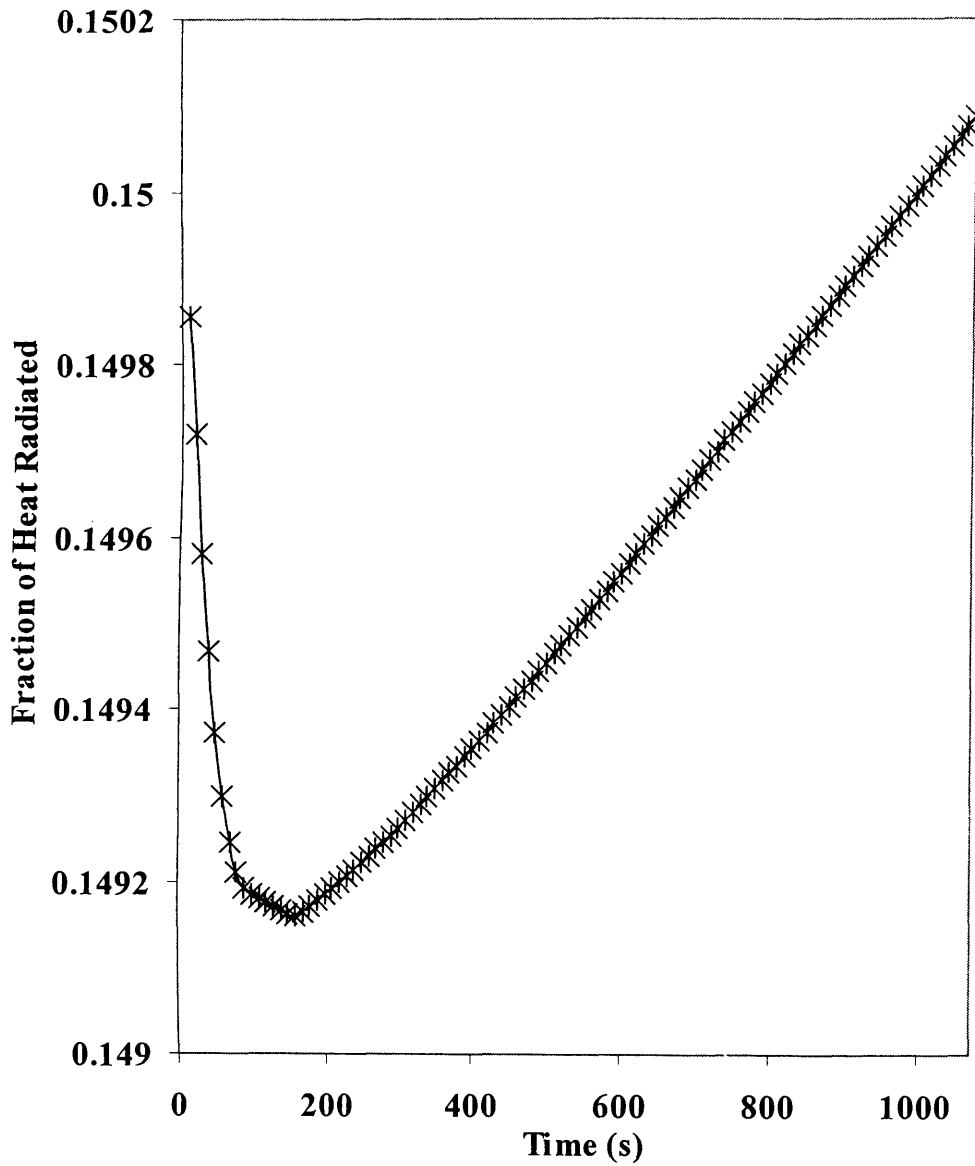


Figure 5.9 Fraction of heat radiated from the flame with time following the ignition of releasing inventory.

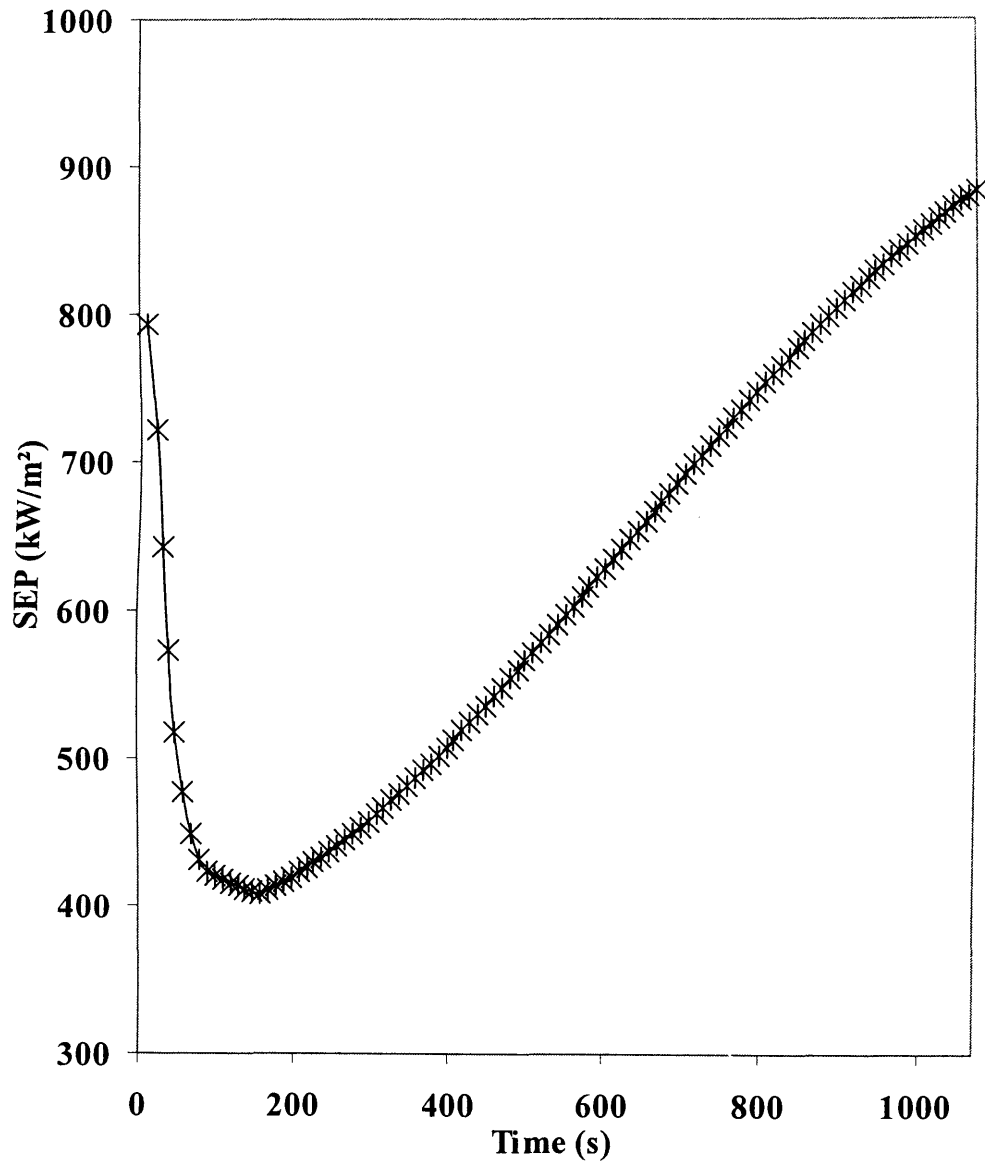


Figure 5.10 Variation of Surface Emissive Power (SEP) of the flame with time following the ignition of releasing inventory.

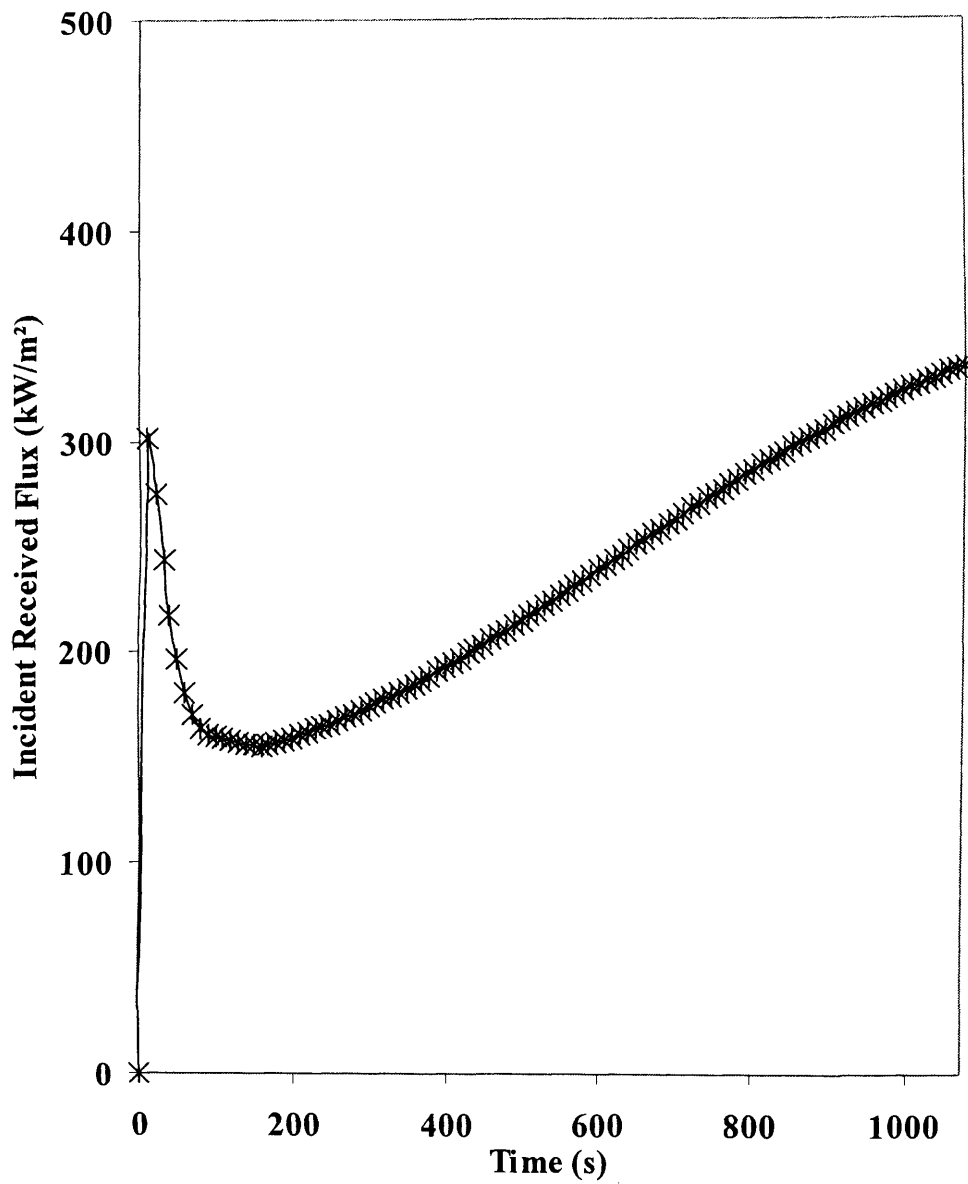


Figure 5.11 Variation of incident received flux on the outer pipewall with time following the ignition of releasing inventory.

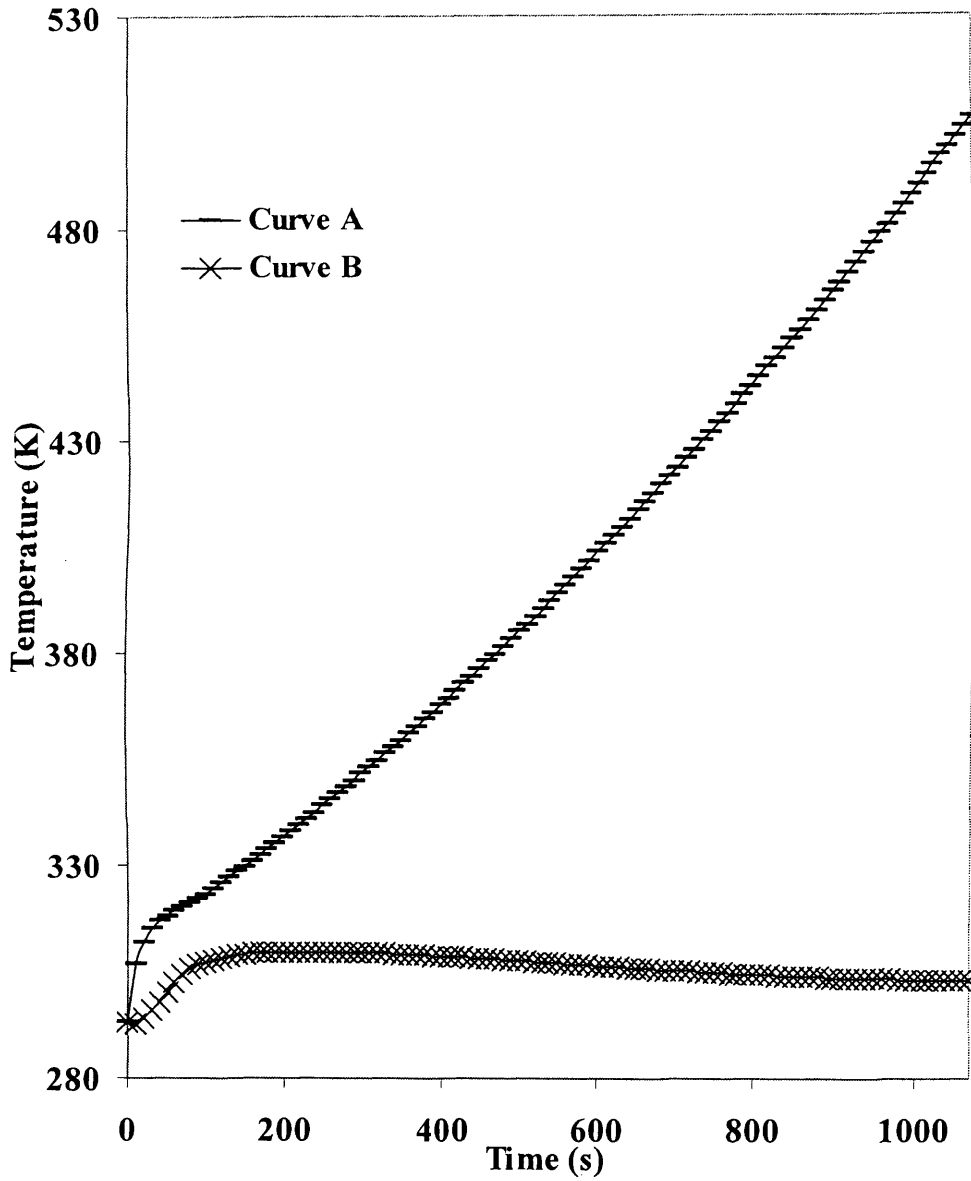


Figure 5.12 Variation of pipewall temperature with time during thermal loading due to radiation from the flame occurring due to ignition of the releasing inventory.

Curve A: Outer wall
Curve B: Inner wall

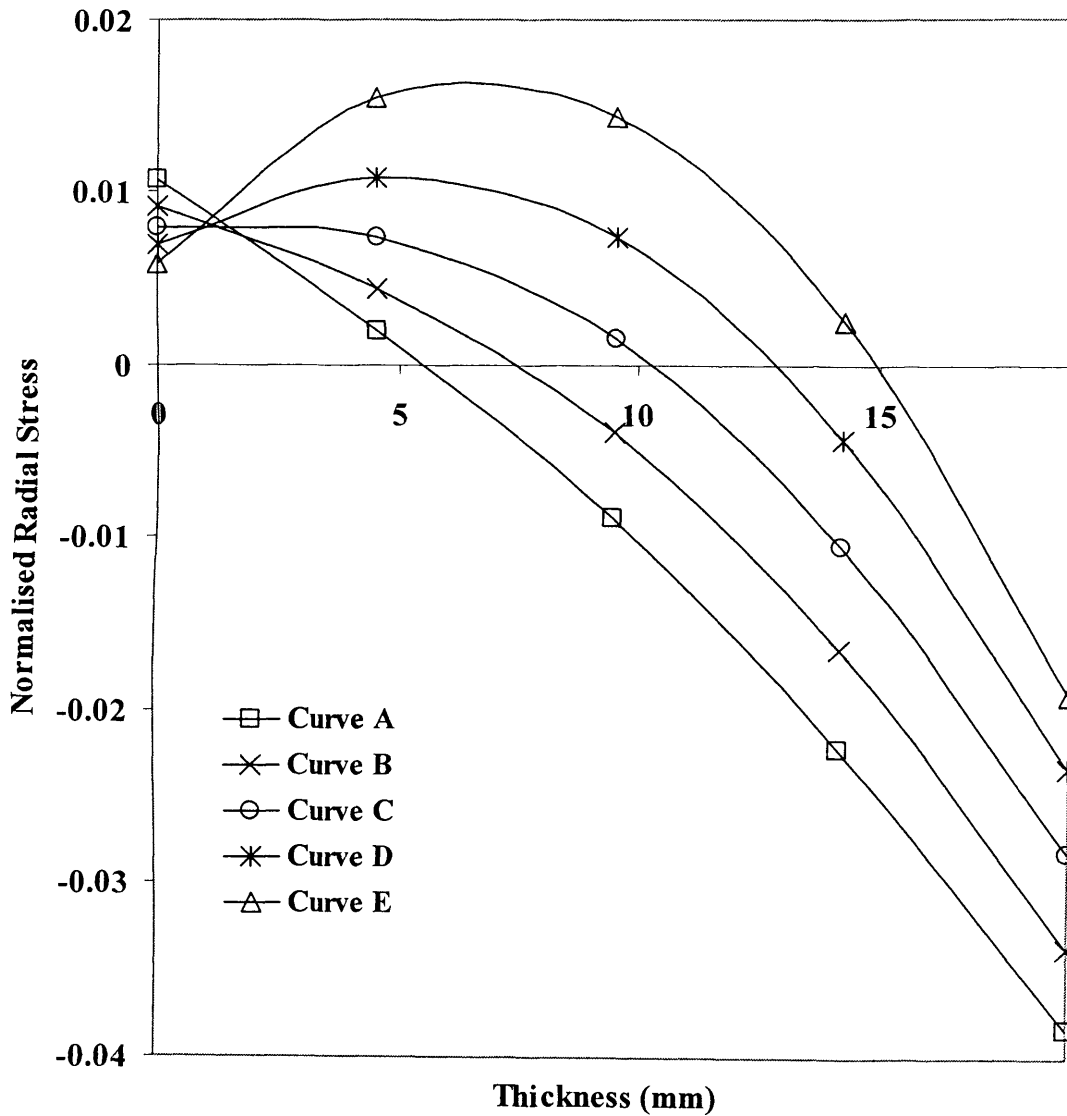


Figure 5.13 Variation of the normalised radial stress across the pipewall under the impact of radiation from a flame occurring due to ignition of releasing inventory.

- Curve A: 200s, $\Psi(K) = 323.21$
- Curve B: 400s, $\Psi(K) = 338.17$
- Curve C: 600s, $\Psi(K) = 355.02$
- Curve D: 800s, $\Psi(K) = 374.70$
- Curve E: 1070s, $\Psi(K) = 402.23$

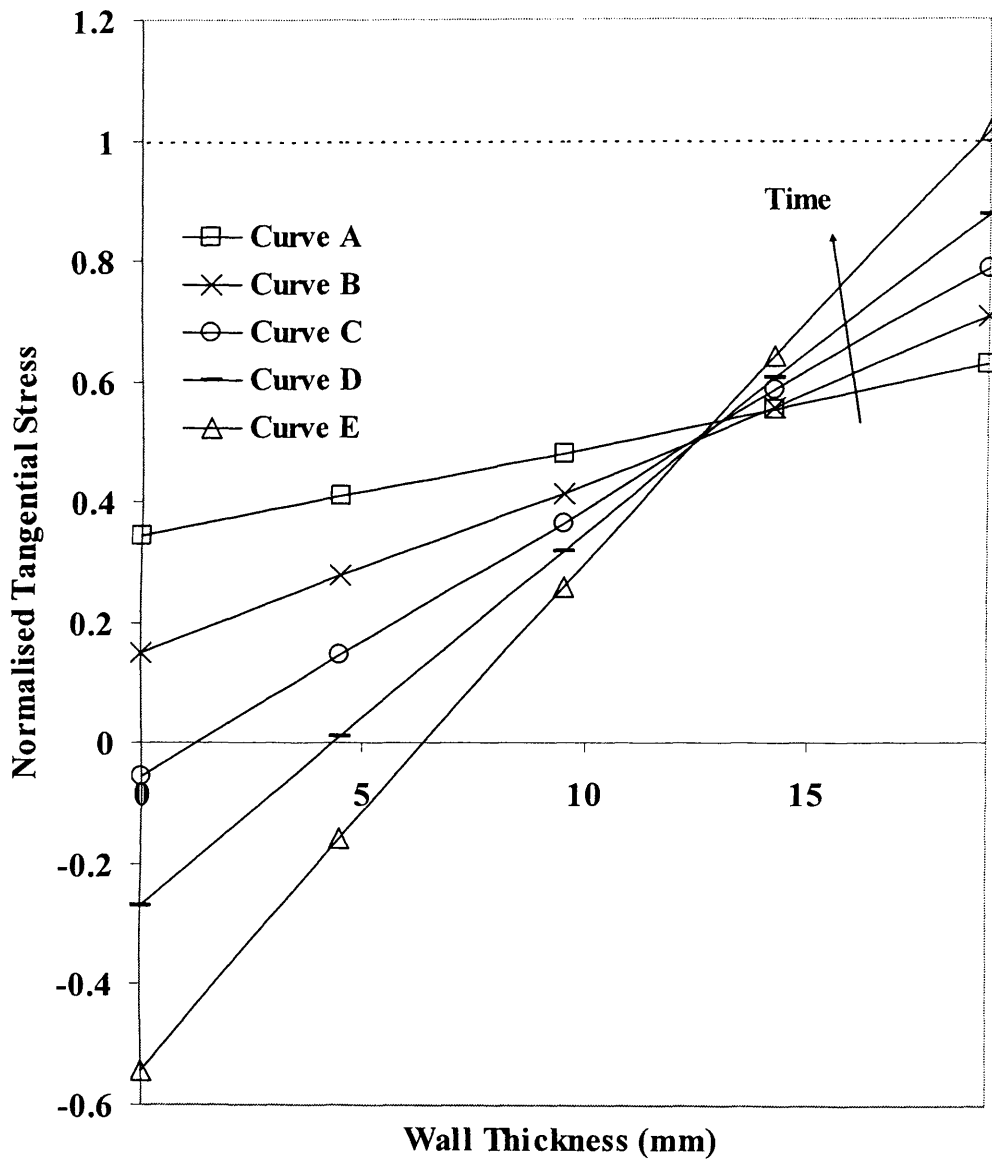


Figure 5.14 Variation of the normalised tangential stress across the pipewall under the impact of radiation from the flame occurring due to ignition of releasing inventory.

- Curve A: 200s, $\Psi(K) = 323.21$
- Curve B: 400s, $\Psi(K) = 338.17$
- Curve C: 600s, $\Psi(K) = 355.02$
- Curve D: 800s, $\Psi(K) = 374.70$
- Curve E: 1070s, $\Psi(K) = 402.23$

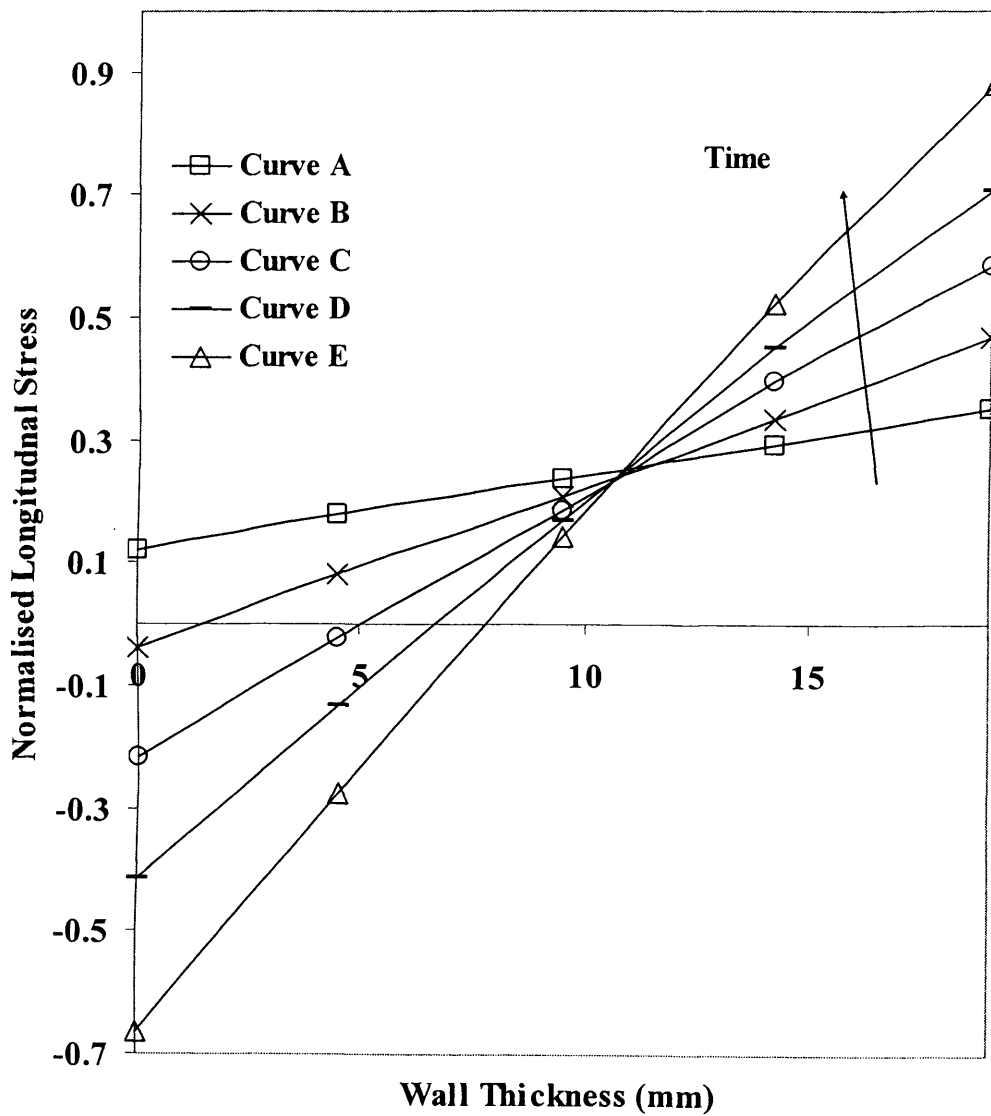


Figure 5.15 Variation of the normalised longitudinal stress across the pipewall under the impact of radiation from the flame occurring due to ignition of releasing inventory.

- Curve A: 200s, $\Psi(K) = 323.21$
- Curve B: 400s, $\Psi(K) = 338.17$
- Curve C: 600s, $\Psi(K) = 355.02$
- Curve D: 800s, $\Psi(K) = 374.70$
- Curve E: 1070s, $\Psi(K) = 402.23$

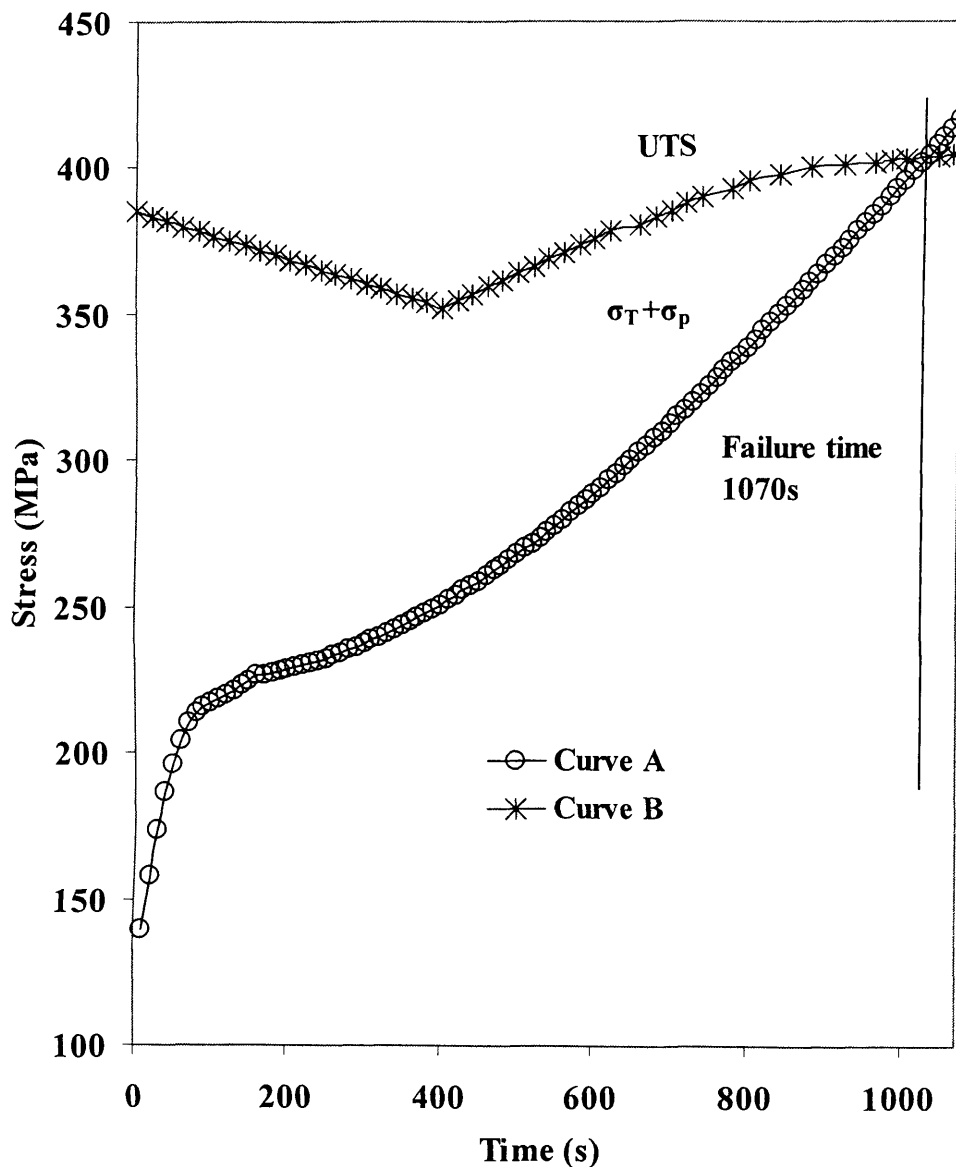


Figure 5.16 Comparison of UTS with total tangential stress in the outer pipewall during formation of a jet flame due to the ignition of the released inventory.

Curve A: Total stress, $\sigma_T + \sigma_P$

Curve B: UTS

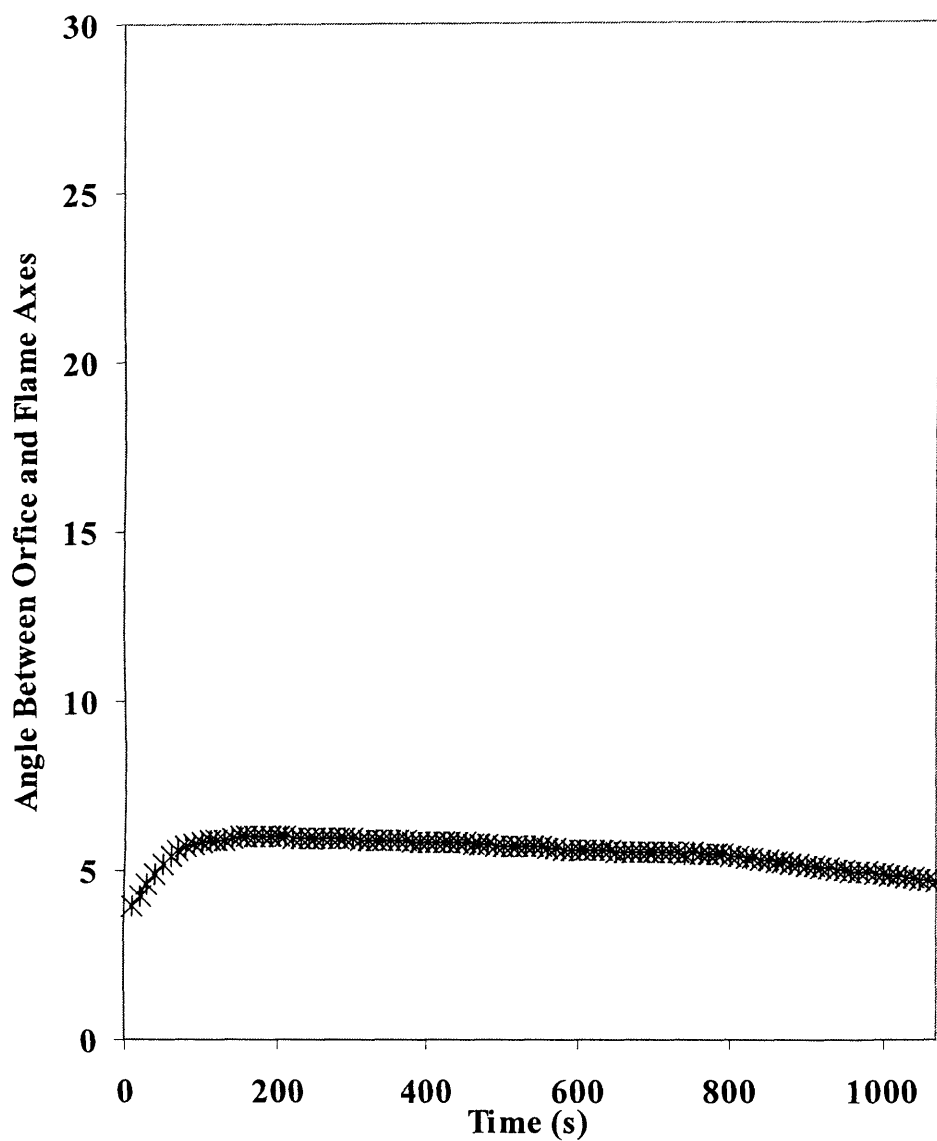


Figure 5.17 Variation of angle between orifice and flame axes with time following the ignition of releasing inventory.

CHAPTER 6

CONCLUSION AND SUGGESTED FUTURE WORK

6.1 Conclusion

This thesis presented the development of a mathematical model for simulating the loss in the mechanical integrity of pipelines conveying high pressure hydrocarbons under fire attack.

Although the thermal response of pressurised vessels following fire attack has been extensively reported, very little comparative studies of a similar nature have been reported for pressurised pipelines. This is despite the fact that the rupture of a pressurised pipeline poses a significantly more serious safety hazard as opposed to a vessel due to the considerably larger amount of inventory involved.

Two types of fire loadings were considered in this study. The first dealt with direct jet fire impingement on the pressurised pipeline by an external source of constant heat intensity. The second scenario assumed the puncture of the pipeline was followed by the immediate ignition of the released inventory.

This work is reported in five chapters.

Chapter 2 dealt with a literature review of some of the pertinent experimental studies conducted in the past 3 decades, which elucidate the important processes taking place during outflow from pipelines, effect of fire attack on vessels and pipework and jet flame modelling. The findings of this chapter formed the basis of the modelling work presented in chapters 4 and 5.

In chapter 3, the equations describing mass, momentum and energy conservation were presented. Of important note was the presentation of the mass conservation equation in

terms of pressure, enthalpy and flow velocity as opposed to the conventional pressure, density and velocity approach. The former formulation has been shown to significantly reduce the computational run time and produce improved accuracy as compared to real data (Oke, 2004). The conservation equations derived were shown to be quasi-linear and hyperbolic in nature. The MOC was chosen to solve these, as it is well suited to handling the fast transients at the rupture plane.

The various hydrodynamic and thermodynamic correlations required for predicting important parameters including the speed of sound, fluid viscosity as well as fluid flow and phase dependent friction coefficient were presented. In addition, the mathematical expression for the quantity of heat transferred to the fluid from the ambient through the pipewall was derived. The above involved the utilization of appropriate phase dependent heat transfer coefficients for both convective and conductive heat transfer and the development of a 2-D finite difference model for predicting the transient pipewall temperature. In the absence of real data for failure of pipelines under fire loading, the resulting model was successfully validated against Isle of Grain (IOG) full bore rupture experimental data obtained under ambient conditions.

Chapter 4 dealt with the development of the methodology for predicting the likelihood of failure of pressurised pipelines under the impact of jet fire impingement. Both unisolated and isolated flow scenarios were assessed. The former was based on the assumption of depressurisation through various size relief valves throughout fire loading. The isolated case on the other hand assumed an intact pipeline with no depressurisation following fire attack. The chapter presented appropriate expressions for predicting the triaxial thermal and pressure stresses in the pressurised pipeline. The sum of these stresses was in turn used to assess the pipewall mechanical integrity by comparison with the material of construction ultimate stress/temperature data.

The model was next applied to a hypothetical case study involving a natural gas pipeline under jet fire attack. A permanent gas was selected as the pipeline inventory as opposed

to a liquid or a two-phase fluid in view of the inferior ability of the former in absorbing heat thus representing the worse case scenario.

The following observations were made based on the results obtained:

- Pipeline depressurisation during fire loading results in significant temperature gradients across the pipewall. This is due to the high temperature of the pipeline outer wall due to direct contact with the fire and the relatively low inner wall temperature due to the expansion induced cooling effect of the depressurising inventory
- Examination of the resulting stress data revealed that during thermal loading, the prevailing tangential compressive thermal stresses in the inner pipewall rapidly transform into much larger tensile forces towards the outer wall. Once these stresses exceed the pipewall material yield stress, the pipeline begins to deform by buckling (inner wall) and bulging (outer wall)
- Further rise in the temperature of the pipewall results in an increase in the tensile stress at the outer wall. The pipeline catastrophically fails through rupture when this stress exceeds the pipewall material ultimate tensile strength
- Emergency depressurisation is found to have a significant impact on delaying the time to failure with the effect increasing with increasing relief valve diameter. Much the same as that for the isolated pipeline, the prevailing failure mode is found to be due to tangential tensile stresses at the outer pipewall surface
- A comparison of the effect of using different grades of carbon steel pipelines revealed the significant impact of the pipeline metallurgical composition on delaying the time to failure

The extension of the model for predicting the ensuing jet flame characteristics following pipeline puncture and the resulting thermal impact in the pipeline was presented in chapter 5.

The above involved the simulation of the following time variant interactive processes:

- The simulation of the escaping inventory mass discharge rate and pressure at the puncture plane
- The prediction of the ensuing jet flame characteristics including its overall dimensions, the incident and the received heat fluxes using a suitable jet flame model
- The generation of the corresponding 2-D temperature profile within the pipewall as a result of thermal radiation and the resulting triaxial thermal and pressure stresses
- Comparison of the total stresses with the ultimate tensile stress of the pipeline material in order to ascertain the likelihood and if applicable the time and mode of catastrophic pipeline failure

Application of the model to a 10mm puncture positioned at the downstream end of a hypothetical 0.5km, 0.395m dia pipeline conveying natural gas at 110bara showed that the pipeline fails in the tangential direction some 1070s following the initial release.

The size and location of the puncture during unisolated release were found to have a profound effect on delaying or circumventing catastrophic pipeline failure. The former is to be expected as increasing the puncture diameter results in a more rapid depressurisation rate thus resulting in a faster reduction of the accompanied pressure stresses which contribute to the pipeline failure. The significant effect of the location of

the puncture on the fate of the pipeline was however somewhat unexpected requiring a more detailed examination.

In the case of the puncture at the low-pressure end of the pipeline, the pressure-time data indicated a rapid and significant rise in the puncture plane pressure well above the line pressure. This was followed by a gradual reduction back to the line pressure some 1000s following the initial puncture. This initial pressure rise was attributed to the reflection of the expansion waves from the intact end of the pipeline.

No pressure surge was observed in the case of puncture along the length of the pipeline. In this case upon puncture, the puncture plane pressure was observed to instantaneously drop from the line pressure to a much lower choke pressure which gradually dropped with the passage of time.

Comparison of the two failure scenarios revealed that in the first 1000s following discharge, the puncture plane pressure for puncture at the downstream end of the pipeline was approximately double that for the puncture along the pipeline length. The above is consistent with the absence of catastrophic pipeline failure in the case of mid point puncture as the jet flame dimensions including its length, diameter and area directly increase with the discharge pressure. The resulting thermal loading was found to be insufficient to cause secondary pipeline failure.

In conclusion, it is hoped that the results of this work will make an important contribution to the quantitative hazard assessment of pressurised pipelines by enabling the evaluation of the likelihood of their catastrophic failure under fire attack. Although such kind of work has received a great deal of attention in the case of pressurised vessels, it is the first time that such analysis has been conducted for pressurised pipelines despite their significantly higher hazard potential.

6.2 Suggested Future Work

The following is a summary of suggested future work aimed at improving the accuracy and the scope of the pipeline safety assessment model reported in this thesis.

Point source modelling

The jet flame modelling in this study approximated the ensuing jet flame from a puncture in the pipeline as a solid flame body emitting a constant heat flux. This will have an impact on the predicted pipeline temperature exposed to the fire. The errors associated with this approximation may be reduced by using a multiple point source model such as that proposed by Carter (1991) (see chapter 2) which accounts for the variation incident heat flux with distance along the length of the flame

Limitation of the homogeneous equilibrium model

The outflow model presented here is based on the homogenous equilibrium assumption in which during the depressurisation process, the constituent liquid and vapour phases are at thermal equilibrium, travelling at the same velocity. Although in the case of permanent gases, such assumption is valid, for two-phase flow, phase-slip is likely. Such effect may be accounted for using a heterogeneous equilibrium model in which separate conservation equations accounting for interface heat and mass transfer are ascribed to each of the constituent phases.

Pipewall heat loss at elevated temperatures due to back-radiation

In this work, a constant heat flux was assumed to impinge on the pipeline without consideration for the reduction in impinging heat flux due to radiation from the heated wall surface. This is believed to be responsible for the relatively high outer wall temperatures obtained in chapter 4 (figure 4.4, curve A) involving localized jet fire

heating of the pipewall. An additional radiation term needs to be incorporated into the outside wall boundary condition when a set temperature is reached.

Investigation of deformation of pipeline prior to failure

In this study pipeline failure was evaluated by comparison of total stresses within the pipewall with the UTS of the pipeline material. This was attributed to the bulging and buckling due to the tensile and compressive stress loading shown through various stress data obtained (chapter 4). In the event of such a failure situation, the pipeline will deform before it reaches a point of failure. The deformation of the pipeline due to thermal loading needs to be investigated with further validation of the bulging and buckling phenomenon.

Modelling other transient flow scenarios

The present model can easily be extended to deal with other transient fluid flow scenarios such as pipeline networks, the effect of operating in line valves and pumps during failure. The outflow model has been extended to account for punctures in pipeline networks (Oke, 2004). The fire model can be incorporated in the network model to assess the situations where a fire impingement can result from another line within the network.

Computational run time

A significant amount of work has been carried out by Oke (2003) and Atti (2006) to reduce the computational run time for the pipeline outflow model. The incorporation of a 2-D approach in this study has increased the computational work load. Further work needs to be done to assess various ways of reducing computational run time.

REFERENCES

Assael, M. J., J. P. M., Trusler, and T. F., Tsolakis, *Thermophysical Properties of Fluids: an Introduction to their Prediction*, Imperial College Press, London (1996).

Atti, F.O, “Modelling Outflow and Low Temperature Induced Crack Propagation in Pressurised Pipelines,” PhD Thesis, University College London (2006).

Aydemir, N. U., V. K. Magapu, A. C. M. Sousa, J. E. S. Venart, “Thermal Response Analysis of LPG Tanks Exposed to Fire”, *Journal of Hazardous Materials*, **20**, 239 (1988).

Andritsos, N., “Effect of Pipe Diameter and Liquid Viscosity on Horizontal Stratified Flow (Two-Phase, Wave Generation)”, PhD. Thesis, University of Illinois at Urbana Champaign (1986).

Baum, H. R. and McGrattan, K. B, “Simulation of Oil Tank Fires”, *National Institute of Standards and Technology, USA*, Vol 2 (1999).

Bejan, A., *Convection Heat Transfer*, John Wiley & Sons, 2nd edition, Chapter 4 (1995a).

Bejan, A., *Convection Heat Transfer*, John Wiley & Sons, 2nd edition, Chapter 10 (1995b).

Bendiksen, K. H., D. Malnes, R. Moe, and S. Nuland, “The Dynamic Two-Fluid Model OLGA: Theory and Applications,” *SPE Production Eng.*, **6**, 171 (1991).

Bergoyne, J.H.. “Oil Storage Tank Fires”. *Oil*, **1** (9), 12, (1950).

Beynon, G. V., L. T. Cowley, L. M. Small, and I. Williams, “Fire Engulfment of LPG Tanks: HEATUP, A Predictive Model”, *Journal of Hazardous Materials*, **20**, 227 (1988).

Birk, A. M., "Modelling the Response of Tankers to External Fire Impingement", *J. Hazard. Mater.*, **20**, 197 (1988).

Birk, A. M. "Internal Wall Cooling in Pressure Vessels Exposed to External Fire Impingement", *Chem. Eng. Comm.*, **80**, 153 (1989).

Birk, A. M. and M. H. Cunningham, "The Boiling Liquid Expanding Vapour Explosion", *J. Loss Prev. Process Ind.* **7**(6) 474 (1994a).

Birk, A. M. and M. H. Cunningham, "A Medium Scale Experimental Study of the Boiling Liquid Expanding Vapour Explosion (BLEVE)", Report TP 11995E, Transportation Development Centre, Montreal, Canada (1994b).

Birk, A. M., "Scale Effects of Fire Exposure of Pressure-Liquefied Gas Tanks", *J. Loss Prev. Process Ind.*, **8**, 275 (1995).

Bond, J., "IChemE accidents database," IChemE, Rugby, UK (2002).

Brandes, E. A., (Editor), *Smithells Metals Reference Book*, Butterworths, London, (1983).

Burmeister, L.C., *Convective Heat Transfer*, John Wiley & Sons, INC., 1st edition, Chapter 11 (1993).

Carter, D A., "Aspects of Risk Assessment for Hazardous Pipelines Containing Flammable Substances", *J Loss Prev Ind.*, **4** (1991).

Chamberlain, G. A., "Developments in Design Methods for Predicting Thermal Radiation from Flares", *Chem. Eng. Res. Design*, **65**, 299 (1987).

Chen, J. R., S. M. Richardson, and G. Saville, "Numerical Simulation of Full-Bore Ruptures of Pipelines Containing Perfect Gases," *Trans. Inst. Chem. Eng. Part B*, **70**, 59 (1992).

- Chen, J. R., "Modelling of Transient Flow in Pipeline Blowdown Problems," PhD Thesis, University of London, (1993).
- Chen, J. R., S. M. Richardson, and G. Saville, "A Simplified Numerical Method for Transient Two-Phase Pipe Flow," *Trans IChemE*, **71A**, 304 (1993).
- Chen, J. R., S. M. Richardson, and G. Saville, "Modelling of Two-Phase Blowdown from Pipelines – I. A Hyperbolic Model Based on Variational Principles," *Chem. Eng. Sci.*, **50**, 695 (1995a).
- Chen, J. R., S. M. Richardson, and G. Saville, "Modelling of Two-Phase Blowdown from Pipelines – II. A Simplified Numerical Method for Multi-Component Mixtures," *Chem. Eng. Sci.*, **50**, 2173 (1995b).
- Chen, N. H., "An Explicit Equation for Friction Factor in Pipes," *Ind. Eng. Chem. Fundam.*, **18**, No. 3, 296 (1979).
- Churchill, S. W., and M. Bernstein, "A Correlating Equation for Forced Convection from Gases and Liquids to a Circular Cylinder in Cross-flow," *J. Heat Transfer*, **99**, 300 (1977).
- Churchill, S. W., and H. H. S. Chu, "Correlating Equations for Laminar and Turbulent free Convection from a Horizontal Cylinder," *Int. J. Heat Mass Transfer*, **18**, 1049 (1975).
- Courant, R., K. O. Friedrichs, and H. Lewy, "Über Die Partiellen Differentialgleichungen Der Mathematischen, Physik," *Mathematische Annalen*, **100**, 32 (1926).
- Cunliffe, R. S., "Condensate Flow in a Wet-Gas Line can be Predicted," *Oil and Gas Journal*, Oct 30 (1978).
- Daubert, T.E and Danner, R.P (eds) *Data Compilation Tables of Properties of Pure Compounds* (New York: Ann. Inst. Chem. Engrs), (1985)

Ely, J. F., and H. J. M. Hanley, "Prediction of Transport Properties. 1. Viscosity of Fluids and Mixtures," *Ind. Eng. Chem. Fundam.*, **20**, 323 (1981).

Ely, J. F., and H. J. M. Hanley, "Prediction of Transport Properties. 2. Thermal Conductivity of Pure Fluids and Mixtures," *Ind. Eng. Chem. Fundam.*, **22**, 90 (1983).

Environmental Defence, News Release, 3 Feb 1999, New York.

Fairuzov, Y. V., "Blowdown of Pipelines Carrying Flashing Liquids," *AIChE J.*, **44**, No. 5, 245 (1998).

Falope, O.B., "Modelling the Transient Thermal Response of Pressurised Vessels During Blowdown under Fire Attack," PhD Thesis, University College London (2002).

Fannelop, T. K., and I. L. Ryhming, "Massive Release of Gas from Long Pipelines," *J. Energy*, **6**, 132 (1982).

Fire and Explosion Guidance, Part-2 Avoidance and Mitigation of Fires Final Draft *UKOOA/HSE* (2006)

Flatt, R., "A Singly-Iterative Second Order Method of Characteristics for Unsteady Compressible One-Dimensional Flows," *Comm. in Applied Num. Meth.*, **1**, 269 (1985a).

Flatt, R., "On the Application of Numerical Methods of Fluid Mechanics to the Dynamics of Real Gases," *Forschung im Ingenieurwesen*, **51(2)**, 41, in German (English translation: British Gas Translation No. T07823/BG/LRS/LRST817/86), (1985b).

Flatt, R., "Unsteady Compressible Flow in Long Pipelines Following a Rupture," *Int. J. Num. Meth. Fluids*, **6**, 83 (1986).

Flatt, R., "Unified Approach of Calculation of Mono-phase and Bi-Phase/Homogeneous Flows of Condensable Pure Fluids," *Revue Entropie*, **149**, 48 (French), (1989).

Gnielinski, V., "New Equations for Heat and Mass Transfer in Turbulent Pipe and Channel Flow," *Int. Chem. Eng.*, **16**, 359 (1976).

Hall, A. R. W., E. R. Butcher, and C. E. Teh, "Transient Simulation of Two-Phase Hydrocarbon Flows in Pipelines," *Proceedings of the European Two-Phase Flow Group Meeting*, Hannover (1993).

Haque, M. A., S. M. Richardson, and G. Saville, "Blowdown of Pressure Vessels. I. Computer model," *Trans IChemE Part B: Process Safety Environmental Protection*, **70 (BI)**, 1 (1992a).

Haque, M. A., S. M. Richardson, G. Saville, G. Chamberlain, and L. Shirvill, "Blowdown of pressure vessels. II. Experimental Validation of Computer Model and Case Studies," *Trans IChemE Part B: Process Safety Environmental Protection*, **70 (BI)**, 10 (1992b).

HInt Dossier, *Hazards Intelligence*, Näsilinnankatu 30-B32, 33200 Tampere, Finland, (2005)

Holman, J.P., *Heat Transfer*, New York. McGraw Hill Inc. (1986).

Hyprotech, *PROFES-Transient user manual*, Aspentech, Houston (2001).

Incropera, F. P., and D. P. De Witt, *Fundamentals of Heat and Mass Transfer*, 4th Ed., John Wiley and Sons, New York (1996).

Johnson, A. D., H. M. Brightwell, and A. J. Carsley, "A Model for Predicting the Thermal Radiation Hazards from Large-scale Horizontally Released Natural Gas Jet Fires", *Trans. I.Chem. E.* **72(B)**, 157 (1995).

References

- Jones, D. G., and D. W. Gough, "Rich Gas Decompression Behaviour in Pipelines," *AGA-EPRG Pipeline Research Seminar IV*, Duisburg, British Gas, Report No. ERSE 293, (1981).
- Kalghatgi, G. T., "The Visible Shape and Size of a Turbulent Hydrocarbon Jet Diffusion Flame in a Cross-Wind", *Combustion Science and Flame*, **52**, 91 (1983).
- Kalghatgi, G. T., "Lift-off Heights and Visible Lengths of Vertical Turbulent Jet Diffusion Flames in Still Air", *Comb. Sci. Tech*, **41**, 17 (1984).
- Kletz, T.A. "Hazard Analysis – a Quantitative Approach to Safety". *Major Loss Prevention*, p. 111. (1971).
- Lees, F. P. *Loss Prevention in the Process Industries*, Butterworths, (1996).
- Mahgerefteh, H., P. Saha, and I.G. Economou, "A Study of the Dynamic Response of Emergency Shutdown Valves Following Full-Bore Rupture of Gas Pipelines," *Trans. Inst. Chem. Eng., Part B*, **75**, 201 (1997).
- Mahgerefteh, H., P. Saha, and I. G. Economou, "Fast Numerical Simulation for Full Bore Rupture of Pressurized Pipelines", *AIChE*, **45(6)**, 1191 (1999).
- Mahgerefteh, H., and Wong, S.M.A., "A Numerical Blowdown Simulation Incorporating Cubic Equations of State," *Computers in Chemical Engineering*, **23(9)**, 1309 (1999).
- Mahgerefteh, H., Saha, P. and Economou, I. G., "Modelling Fluid Phase Transition Effects on Dynamic Behaviour of ESDV," *AIChE*, **46(5)**, 997 (2000).
- Mahgerefteh, H., G. B. O. Falope, and A. O. Oke, "Modeling Blowdown of Cylindrical Vessels under Fire Attack", *AIChE*, **48(2)**, 1309 (2002).
- Mahgerefteh, H, and G.B.O Falope, 'Modelling Thermal Response of Spherical Vessels During Blowdown Under Fire Attack', *AIChE*, **49(5)**, 1307 (2003)

References

- Mahgerefteh, H., & Oke, A., & Rykov, Y., 'Efficient Numerical Simulation for Highly Transient Flows' *Chem.Eng.Sci.*, **61(15)**,5049 (2006a).
- Mahgerefteh, H., Oke, A., & Atti, O., 'Modelling Outflow Following Rupture in Pipeline Networks', *Chem.Eng.Sci.*, **61(6)** , 1811 (2006b).
- Mahgerefteh, H., Atti, O., and Denton, G., 'An Interpolation Technique for Rapid CFD Simulation of Highly Transient Flows', *Trans.IChemE.*, Part B, Process Safety & Environmental Protection, **84(B6)**, 1 (2006c).
- Mahgerefteh, H. and Atti, O., 'Modeling Low Temperature-Induced Failure of Pressurised Pipelines', *AIChE Journal*, **52(3)**, 10719 (2006)
- Moorehouse, J. and M. J. Pritchard, "Thermal Radiation Hazards from Large Pool Fires and Fireballs. A Literature Review", *IChemE Symposium Series* No 71 (1982).
- Offshore Technology Report, OTO 98 162, *Subsea Hydrocarbon Pipeline Failure: Survey of Available Prediction Schemes*, HSE, (1998).
- Oke, A., H. Mahgerefteh, I. Economou, and Y. Rykov, "A Transient Outflow Model for Pipeline Puncture," *Chem. Eng. Sci.*, **58(20)**, 4591 (2003).
- Oke, A., "An Efficient Numerical Simulation for Modelling Outflow Following Rupture or Puncture of Pressurised Pipeline Networks," PhD Thesis, University College London (2004).
- Ouyang, L., and K. Aziz, "Steady-State Gas Flow in Pipes," *J. Pet. Sci. Eng.*, **14**, 137 (1996).
- Overa, S. J., E. Stange, and P. Salater, "Depressurisation of Temperatures and Flare Rates During Depressurisation and Fire", *Proceedings of the 72nd GPA Annual Convention*, 235 (1994).
- Ozisik, M. N., *Heat conduction*, John Wiley and Sons, New York, (1980).

- Peng, D. Y., and D. B. Robinson, "A New Two-Constant Equation of State," *Ind. Eng. Chem. Fund.*, **15**, 59 (1976).
- Perry, R. H., and D. W. Green, *Perry's Chemical Engineers' handbook*, 7th Ed., McGraw Hill, London (1997).
- Peterson, C.E. Chexal, V.K. and Clements, T.B. "Analysis of a Hot-leg Small Break LOCA in a Three Loop Westinghouse PWR Plant," *Nuc. Tech.*, **70**, No.1, 104 (1985).
- Philbin, M. T., and A. H. Govan, "Pipeline Analysis Code," UKAEA Report AEA-APS-0031 (1990).
- Philbin, M. T., "The Simulation of Transient Phenomena in Multiphase Production Systems," AEA Harwell Report AEA-APS-0177 (1991).
- Picard, D. J., and P. R. Bishnoi, "Calculation of the Thermodynamic Sound Velocity in Two-Phase Multi-Component Fluids," *Int. J. Multiphase Flow*, **13**(3), 295 (1987).
- Picard, D. J., and P. R. Bishnoi, "The Importance of Real-Fluid Behaviour and Non-Isentropic Effects in Modelling Compression Characteristics of Pipeline Fluids for Application in Ductile Fracture Propagation Analysis," *Can. J. Chem. Eng.*, **66**, 3 (1988).
- Picard, D. J., and P. R. Bishnoi, "The Importance of Real-fluid Behaviour in Predicting Release Rates Resulting from High Pressure Sour-Gas Pipeline Ruptures," *Can. J. Chem. Eng.*, **67**, 3 (1989).
- Pipeline Safety Instrument for the Control of Major Accident Hazards Involving Pipelines, Joint Research Centre, European Commission, *Major Accident Hazards Bureau*, Ispra (Va), Italy, (1999).
- Popov, E. P., *Engineering Mechanics of Solids*, Prentice Hall, New Jersey, (1999).

Prasad, P., and R. Ravindran, *Partial differential equations*, Wiley Eastern Limited, New Delhi (1985).

Press, W.H., Teukolsky, S.A., Vetterling, W.T., and Flannery, B.P., *Numerical Recipes in FORTRAN 77: The Art of Scientific Computing*, Cambridge University Press, 2nd edition, Chapter 9 (1992)

Ramskill P. K., "A Description of the 'ENGULF' Computer Codes - Codes to Model the Thermal Response of an LPG Tank either Fully or Partially Engulfed by Fire", *Journal of Hazardous Materials*, **20**, 177 (1988).

Regulatory Benchmark for the Control of Major Accident Hazards Involving Pipelines, European Commission Draft Directive on Pipeline Safety, *Major Accident Hazards Bureau*, Brussels (2004).

Reid, R.C., Prausnitz, J.M., and Sherwood, T.K., *The Properties of Gases and Liquids*, McGraw-Hill Book Company., 4th Edition, 642 (1986).

Richardson, S. M., and G. Saville, "Blowdown of Pipelines," *Society of Petroleum Engineers Europe 91*, paper SPE 23070, Aberdeen, UK, 369 (1991).

Richardson, S. M., and G. Saville, "Isle of Grain pipeline Depressurisation Tests," HSE OTH 94441, HSE Books, HSE, Bootle, U.K. (1996a).

Richardson, S. M., and G. Saville, "Blowdown of LPG Pipelines," *Trans. IChemE*, **74B**, 236 (1996b).

Richardson, S. M., G. Saville, A. Fisher, A. J. Meredith, and M. J. Dix, "Experimental Determination of Two-Phase Flow Rates of Hydrocarbons Through Restrictions," *Trans IChemE, Part B: Process Safety and Environmental Protection*, **84 (B1)**, 40, (2006).

References

Roberts, T. and H. Beckett, "Hazard Consequences of Jet-fire Interactions with Vessels Containing Pressurised Liquids: Project Final Report", HSL Report R04.029, PS/96/03, Buxton, UK (1996).

Roberts, S. G., "Multiscale Phenomena in Plasticity: From Experiments to Phenomenology," *Modelling and Materials Engineering*, 8 Sep.1999 - 19 Sep 1999, Ouranopolis, Greece (1999).

Roberts. T. A., Medonos. S, Shirvill. L.C. "Review of the Response of Pressurised Process Vessels and Equipment to Fire Attack" *HSE Offshore Technology Report, OTO 2000 051* (2000).

Rohsenow, W. M., J. P. Hartnett, and Y. I. Cho, eds., *Handbook of Heat Transfer*, 3rd ed., McGraw-Hill, New York (1998).

Russo E. P., P. D. Herrington, and W. W. St Cyr, "Transient Thermal Stresses in Pressure Vessels and Pipelines", *Proceedings of the fifth International Offshore and Polar Engineering Conference*, Vol II, 102 (1995).

Saha, P., "Modelling the Dynamic Response of Emergency Shutdown Valves Following Full-Bore Rupture of Long Pipelines," PhD Thesis, University College London (1997).

Sens, M., P. Jouve, and R. Pelletier, "Detection of a Break in a Gas Line," *11th International Gas Conference*, Moscow, Paper No. IGU/C37-70, in French, (English Translation: British Gas, Translation No. BG. TRANS 4910) (1970).

Shoup, G., J. J. Xiao, and J. O. Romma, "Multiphase Pipeline Blowdown Simulation and Comparison to Field Data," *1st North American Conference on Multiphase Technology*, BHR Group Conference Series No. 31, Banff, Canada, 3, June 10-11 (1998).

Sparrow, E. W. and R. D. Cess, "*Radiation Heat Transfer*", Brooks-Cole Publishing Company, (1966).

References

- Steiner, D., and J. Taborek, "Flow Boiling Heat Transfer in Vertical Tubes Correlated by an Asymptotic Method," *Heat Transfer Eng.*, **13(2)**, 43 (1992).
- Stroud, K. A., *Engineering Mathematics: Programmes and Problems*, 4th ed., Macmillan, London (1995).
- Taler, J. "Analytical Solution of the Over Determined Inverse Heat Conduction Problem with an Application to Monitoring Thermal Stresses", *Heat and Mass Transfer*, **33**, 209 (1997).
- Tam, V. H. Y., and L.T. Cowley, "Consequences of Pressurised LPG Releases: the Isle of Grain Full Scale Experiments," *Proceedings of GASTECH 88 (13th Int. LNG/LPG Conf.)*, Kuala Lumpur, 2 (1988)
- Tanks: Experiments and Modelling", *Fire Hazard and Fire Risk Assesment*, ASTM STP **1150**, 100 (1992).
- Taylor, J.R. *Risk Analysis for Process Plant Pipelines and Transport* (London: Spon), (1994).
- Techo, R., R. R. Tickner, and R. E. James, "An Accurate Equation for the Computation of the Friction Factor for Smooth Pipes from the Reynolds Number," *J. Appl. Mech.*, **32**, 443 (1965).
- Tiley, C. H., "Pressure Transient in a Ruptured Gas Pipeline with Friction and Thermal Effects Included," PhD Thesis, City University, London (1989).
- Timoshenko S. P., and J. N. Goodier, *Theory of Elasticity*, McGraw-Hill, New York, (1987).
- U.S. Department of Transport, Code of Federation Regulations (CFR) Title 49D, Part 195, *Transportation of hazardous liquids by pipeline*, Accident Report Data Base.3 (1982 – 1997).

References

- Vahedi, S., "Modelling the Effects of Inclination and Pipeline Enlargement on Outflow Following Pipeline Rupture," PhD Thesis, University College London (2003).
- Venart, J.E.S., "Boiling Liquid Expanding Vapour Explosions (BLEVE): Possible Failure Mechanisms and their Consequences", *ICHEME Symposium Series 147*, 121 (2000).
- Vervalin, C.H. *Fire Protection Manual for Hydrocarbon processing Plants* (Houston, TX: Gulf) (1964a).
- Vervalin, C.H. *API/NFPA report on HPI fire losses*. *Hydrocarbon Process.*, **52** (1), 128 . (1974a).
- Walas, S. M., *Phase Equilibrium in Chemical Engineering*, Butterworth Publisher, Boston, (1987).
- Wayne, F. D., "An Economical Formula for Calculating Atmospheric Infrared Transmissivities", *J. Loss Prev. in Proc Ind.*, **4** (2), 86 (1991).
- Wong, S. M. A. PhD Thesis, University College London (1998).
- Wylie, E. B., and V. L. Streeter, *Fluid transients*, McGraw-Hill Inc., New York (1978).
- Wylie E.B., and Streeter V.L., *Fluid Transients in Systems*, Prentice- Hall, New Jersey, 51 (1993).
- Zhou, X.X., C.J. Lea, M. Bilò, and T.E. Maddison, "Three-Dimensional Computational Fluid Dynamic Modelling of Natural Gas Releases from High-Pressure Pipelines," *Pipes & Pipelines International*, Sept-Oct., 13 (1997).
- Zucrow, M. J., and J. D. Hoffman, *Gas dynamics*, volume I and II, Wiley, New York, 297 (1976).